nagra.

TECHNICAL REPORT 24-22 Rev. 1

Synthesis of the Performance Assessment for a Deep Geological Repository for Radioactive Waste

October 2024

Nagra | National Cooperative for the Disposal of Radioactive Waste
Hardstrasse 73 | 5430 Wettingen | Switzerland
T. +41 56 437 11 11 | info@nagra.ch | nagra.ch

nagra.

TECHNICAL REPORT 24-22 Rev. 1

Synthesis of the Performance Assessment for a Deep Geological Repository for Radioactive Waste

October 2024

Nagra | **National Cooperative for the Disposal of Radioactive Waste**
Hardstrasse 73 | 5430 Wettingen | Switzerland
T. +41 56 437 11 11 | info@nagra.ch | nagra.ch

The report "Synthesis of the Performance Assessment for a Deep Geological Repository for Radioactive Waste" has been elaborated by a project team consisting of P. Marschall[1], A. Papafotiou[1], N. Diomidis[1], T. Guillemot[1], O. Leupin[1], L. Martin[1], C. Li[2], M. Hayek[2], U. Lengler[2] & K. Luu[2]

[1] Nagra
[2] Intera

An earlier version of the report has been reviewed and commented on by Paul Smith (SAM). The authors would like to thank him for his valuable contributions.

NTB 24-22, May 2025: Corrigendum

This report was revised in May 2025. The corrections include adding more specific references to related reports, correcting typographical errors, and ensuring consistency.

To maintain consistency with the documents submitted for the general licence applications, the original publication date is retained.

ISSN 1015-2636

Abstract

This synthesis report provides a general overview of the performance assessment workflow pursued in the context of the safety case for a deep geological repository for both high-level waste (HLW) and low- and intermediate-level waste (L/ILW) at the Haberstal site in the Nördlich Lägern siting region.

The Swiss safety concept for deep geological disposal for radioactive waste relies on a staggered system of geological and engineered barriers, representing the so-called "pillars of safety" in the general safety architecture. Founded on a well-established, transparent disposal programme and on a sound scientific and technical basis, each of the seven pillars of safety performs several safety functions. These functions are overarching functional requirements on the multi-barrier system that, taken together, ensure post-closure safety.

Performance assessment represents the first stage in the general safety assessment workflow towards a robust safety case. Following international standards of transparent and traceable assessment workflows, the performance assessment addresses the post-closure safety of the repository at a level of simplification, which bridges the gap between the real repository system and its highly abstracted representation in the analysis of radiological consequences. The performance assessment workflow encompasses four steps:

- Assessment of barrier performance for each element of the multi-barrier system at the component level ("*performance assessment by barrier*");
- Assessment at the level of the entire system ("*total system performance*") to account for any possible thermo-hydro-mechanical interactions between the individual barrier components;
- *Uncertainty quantification* with special focus on parametric and conceptual uncertainties, which are associated with the simplified representation of the realistic repository system in an abstracted performance / safety assessment framework (including uncertainty propagation associated with the abstraction process);
- *Performance screening*, encompassing a probabilistic assessment of the expected repository performance and of deviations thereof to screen the possible paths of repository performance and to identify, bundle and formulate the safety-relevant paths in a format that can be subjected to the next step in the safety assessment workflow.

The auditability of the assessment workflow is ensured with a traceable method of proof. For this, claims are formulated, assigning one or more intended safety functions to each component of the multi-barrier system and to the repository system as a whole. The claims are rationalised by a suite of arguments. A claim can be said to be robust if it is well substantiated using sound arguments and providing convincing evidence. The robustness of a claim is strengthened by seeking multiple lines of argument that can be assigned broadly to the following categories: (i) *empirical knowledge* such as experience from other radioactive waste management programmes, (ii) *dedicated scientific and technical databases* that have been elaborated specifically in the context of the repository project, and (iii) a *safety-oriented repository design*.

Each argument must be supported by convincing evidence along multiple lines of knowledge gain (*empirical evidence*, *experimental evidence* from targeted site investigation programmes, *model-supported evidence* derived from sensitivity and robustness analyses). A balanced evaluation of arguments and evidence provides important insights into the limitations of repository performance when the multi-barrier system is subjected to internal or external perturbations.

Traceable handling of uncertainty is an indispensable element in the assessment workflow. Performance assessment must provide evidence that the modelling tools and approaches applied for quantitative assessment of barrier performance at component and total system level adequately represent the safety-relevant processes and phenomena. Following well-established safety assessment principles, uncertainty is categorised as scenario uncertainty, conceptual uncertainty and parameter uncertainty. The effect, when the uncertainties of the input parameters of a physical system give rise to uncertainties in the system response, is termed propagation of uncertainty. Tracking of uncertainty propagation along the model abstraction chain is a complex process, called uncertainty quantification. It aims to bracket the confidence bounds on the expected system response of the simplified performance assessment model.

It is the role of performance assessment to screen the possible paths of repository performance and to identify, bundle and formulate the safety-relevant deviations from the expected repository performance in a format that can be subjected to radiological consequence analysis. From the performance assessment perspective, the possible paths of repository evolution are classified in terms of expected performance of the multi-barrier system and deviations thereof. Deviations from the expected performance are analysed at the component level and at the level of the entire repository system with emphasis on the likelihood of occurrence and on their relevance for safety. Those PA-Scenarios which are deemed relevant for long-term safety are forwarded to the next safety assessment process, called safety scenario development. Safety scenario development maps the relevant paths of barrier performance to the corresponding branches of the safety scenario event tree, representing the input to the analysis of radiological consequences.

The performance assessments presented in this report reaffirm that the repository design, with its multiple layers of defense, offers significant safety margins and is capable of meeting both national and international safety standards. The systematic book-keeping of claims, arguments and evidence at the component level confirmed the performance of the barrier components with respect to their assigned safety functions. The arguments compiled are comprising empirical knowledge, project specific databases from site investigations, dedicated experiments, and a safety-oriented repository layout, based on model-supported designs. The consistency of different lines of argument and wide-ranging evidence from independent data sources provides confidence in the general safety concept.

The performance assessment at the system level concentrated predominantly on phenomena and processes along the backfilled and sealed underground structures. In particular it was shown that that the HLW and L/ILW sections of the repository are hydraulically and thermally decoupled from each other. The thermal- and gas-induced perturbations in the HLW repository section occur at different times, which means that detrimental superposition of the thermal- and gas-related impacts on the safety functions of the engineered and geological barriers can be excluded. Neither the thermal- nor the gas-related disturbances lead to an increased pore-water flow along the sealed and backfilled repository structures, which could otherwise give rise to increased radionuclide release. Likewise, the impact of thermal- and gas-induced perturbations on the mechanical and chemical integrity of the engineered and geological barriers of the HLW repository is modest. The layout of the repository provides large gas storage volumes, which are crucial for reducing the gas pressure build-up in the L/ILW repository section. The resulting moderate gas overpressures in the repository structures of up to 2 – 3 MPa are not expected to impair the mechanical integrity of the engineered and geological barriers. Volatile radionuclides (mainly ^{14}C) are safely contained until they finally disappear due to radioactive decay. At the same time, the unsaturated conditions in the L/ILW emplacement caverns, with moderate gas overpressures, ensure that the release of dissolved radionuclides from the waste packages into the host rock is strongly retarded for very long times, because the mortar backfill around the waste containers represents a capillary barrier for dissolved radionuclides.

A wide range of potentially relevant deviations from expected barrier performance were specified as part of the performance screening process. The assessment of 23 PA-Scenarios provided clear evidence of the robustness of the repository system. The redundancy and diversity of the individual barrier components were shown to be an important feature of the multi-barrier system. None of scenarios assessed indicated a significant reduction of safety margins of the repository at the system scale. Finally, only a handful of PA-Scenarios were identified as cases worthy of further evaluation in the radiological consequence analysis. The motivation for complementary in-depth analyses is the fact that these scenarios deviate significantly from the expected repository evolution, which formed the basis for the provisional repository design, although there was no evidence of a relevant loss of barrier performance.

It can be concluded that the repository for HLW and L/ILW at the Haberstal site is safe over the entire assessment period, with significant safety margins under both expected and adverse conditions. The concept relying on a multi-barrier system, combined with a robust, evidence-based assessment of its performance, ensures that the repository will meet its safety objectives even considering internal or external perturbations that are even of hypothetical nature. By meticulously addressing uncertainties and thoroughly evaluating each element of the system, the performance assessment builds a strong case for the repository's long-term safety. The transparent and traceable workflow further strengthens the conclusions, ensuring that the safety case is both credible and verifiable and providing a solid foundation for moving forward with the next stages of the safety case and overall repository development.

Zusammenfassung

Der vorliegende Synthesebericht gibt einen Überblick über die sicherheitstechnische Beurteilung der Wirksamkeit der geologischen und technischen Barrieren im Rahmen des Sicherheitsnachweises für ein geologisches Tiefenlager für hochaktive Abfälle (HAA) sowie für schwach- und mittelaktive Abfälle (SMA) am Standort Haberstal in der Standortregion Nördlich Lägern.

Das Schweizer Sicherheitskonzept für die geologische Tiefenlagerung radioaktiver Abfälle beruht auf einem gestaffelten System geologischer und technischer Barrieren, welche als tragende «*Säulen der Sicherheit*» betrachtet werden. Die Sicherheitsarchitektur des Lagersystems basiert auf einem langjährig etablierten und transparenten Entsorgungsprogramm sowie auf einer soliden wissenschaftlichen und technischen Grundlage, jede der sieben Säulen der Sicherheit erfüllt mehrere Sicherheitsfunktionen. Diese Funktionen sind übergreifende sicherheitstechnische Anforderungen an das Multibarrierensystem, die in ihrem Zusammenwirken die Sicherheit des Tiefenlagers nach seinem Verschluss gewährleisten.

Die Prüfung der Barrierenwirksamkeit («*Performance Assessment – PA*») stellt den ersten Schritt im mehrstufigen Prozess zur allgemeinen Beurteilung der Langzeitsicherheit («*Safety Assessment – SA*») dar, der schliesslich zu einem robusten Sicherheitsnachweis führt. Auf der Grundlage internationaler Standards und Empfehlungen für einen transparenten und nachvollziehbaren Sicherheitsnachweis erfolgt die Prüfung der Barrierenwirksamkeit des geologischen Tiefenlagers auf einer Abstraktionsebene, die die Lücke zwischen dem realen Lagersystem und seiner stark vereinfachten Darstellung im Rahmen der radiologischen Konsequenzenanalysen überbrückt. Der Prüfprozess umfasst folgende Schritte:

- Beurteilung der Barrierenwirksamkeit der einzelnen Elemente des Multibarrierensystems («*performance by barrier*»);
- Beurteilung der Barrierenwirksamkeit auf dem Massstab des Gesamtsystems («*total system performance*»), um mögliche thermo-hydro-mechanische Wechselwirkungen zwischen den einzelnen Barrierenkomponenten zu berücksichtigen;
- Analyse der Ungewissheiten («*uncertainty quantification*») unter besonderer Berücksichtigung der parametrischen und konzeptionellen Ungewissheiten, die sich aus dem Prozess der Modellabstraktionen ergeben (Fehlerfortpflanzung infolge von Modellvereinfachungen);
- Systematische Sichtung von Prüfszenarien zur Barrierenwirksamkeit im Rahmen probabilistischer Modellanalysen («*performance screening*»). Dabei wird die erwartete Barrierenwirksamkeit des Lagersystems entsprechend der geplanten Lagerauslegung verglichen mit dem Barrierenverhalten, welches sich ergibt, wenn einzelne Komponenten von der erwarteten Barrierenwirksamkeit abweichen. Sicherheitsrelevante Abweichungen vom erwarteten Verhalten werden erfasst und bewertet, um allenfalls einer weitergehenden Beurteilung im Rahmen der radiologischen Konsequenzenanalyse unterzogen zu werden.

Die Überprüfbarkeit der Bewertungsmethodik wird durch eine transparente Nachweisführung sichergestellt. Dazu werden Thesen («*claims*») formuliert, die jeder Komponente des Multibarrierensystems und dem Tiefenlager als Ganzem eine oder mehrere Sicherheitsfunktionen zuweisen. Die Thesen werden durch eine Reihe von Argumenten («*arguments*») begründet. Eine These kann als robust bezeichnet werden, wenn sie mit stichhaltigen Argumenten gut untermauert und durch überzeugende Nachweise («*evidence*») belegt ist. Die Robustheit einer These wird durch die Entwicklung von mehreren voneinander unabhängigen Argumentationslinien («*lines of arguments*») gestärkt. Argumente werden den folgenden Qualitätskategorien zugeordnet: (i) empirische Erkenntnisse wie zum Beispiel Erfahrungen aus anderen Programmen zur Entsorgung

radioaktiver Abfälle, (ii) spezielle wissenschaftliche und technische Datengrundlagen, welche im Rahmen des eigenen Entsorgungsprogramms erarbeitet wurden, und (iii) eine sicherheitsorientierte Lagerauslegung.

Um eine möglichst breite Abstützung der Argumente zu gewährleisten, muss jedes Argument durch überzeugende Nachweise aus verschiedenen, möglichst unabhängigen Quellen belegt werden (z. B. empirische Nachweise aus Fallstudien, experimentelle Nachweise aus eigenen Standortuntersuchungsprogrammen, modellgestützte Nachweise aus Sensitivitäts- und Robustheitsanalysen). Dabei werden auch wichtige Erkenntnisse gewonnen, um den potenziellen Verlust an Barrierenwirksamkeit zu beurteilen, wenn das Tiefenlager internen oder externen Störungen ausgesetzt ist.

Der nachvollziehbare Umgang mit Ungewissheiten ist eine unverzichtbare Anforderung an den Sicherheitsnachweis. Bei der Prüfung der Barrierenwirksamkeit muss der Nachweis erbracht werden, dass die verwendeten Modellwerkzeuge und Modellansätze die sicherheitsrelevanten Prozesse und Phänomene angemessen darstellen. In der Sicherheitsanalyse ist es üblich, Ungewissheiten in die Kategorien *Szenario-Ungewissheit*, *konzeptionelle Ungewissheit* und *Parameter-Ungewissheit* einzuteilen. Die Tatsache, dass die Unbestimmtheit der Eingangsparameter eines physikalischen Systems zu Ungewissheiten in der Systemantwort führt, wird als «*Fehlerfortpflanzung*» bezeichnet. Die Betrachtung der Fehlerfortpflanzung entlang der Modellabstraktionskette ist ein komplexer Prozess, der im Englischen als «*uncertainty quantification*» bezeichnet wird. Zweck der Fehleranalyse bei der modellunterstützten probabilistischen Prüfung der Barrierenwirksamkeit ist die Ausweisung von Sicherheitsmargen («*safety margins*»).

Die systematische Sichtung der Prüfszenarien zur Barrierenwirksamkeit hat zum Ziel, mögliche Entwicklungspfade des Multibarrierensystems zu analysieren, sicherheitsrelevante Abweichungen von der erwarteten Barrierenwirksamkeit zu identifizieren und diese für die sicherheitstechnischen Szenarienanalysen bereitzustellen. Abweichungen von der erwarteten Barrierenwirksamkeit werden hinsichtlich ihrer Eintrittswahrscheinlichkeit und ihrer Relevanz für die Sicherheit beurteilt. Diejenigen Szenarien, die für die langfristige Sicherheit als relevant erachtet werden, werden an den nächsten Prozess der Sicherheitsanalyse weitergeleitet («*Entwicklung der Sicherheitsszenarien*»). Beim Prozess der Szenarienentwicklung werden die relevanten Pfade der Barrierenwirksamkeit den entsprechenden Verzweigungen des Ereignisbaums der Sicherheitsszenarien zugeordnet, die den Input für die «*radiologische Konsequenzenanalyse*» darstellen.

Die in diesem Bericht vorgestellten Analysen bestätigen, dass die beispielhafte Auslegung des geologischen Tiefenlagers am Standort Haberstal grosse Sicherheitsmargen aufweist. Die systematische Erfassung von Argumenten und Nachweisen auf Komponentenebene bestätigt die Wirksamkeit der einzelnen Barrierenkomponenten im Hinblick auf ihre zugewiesenen Sicherheitsfunktionen. Die aufgeführten Argumente umfassen empirische Erkenntnisse, projektspezifische Datengrundlagen aus Standortuntersuchungen, spezielle Experimente und eine sicherheitsorientierte Lagerauslegung auf Grundlage eines modellgestützten Designs. Die Konsistenz verschiedener Argumentationslinien und umfassende Nachweise aus unabhängigen Datenquellen schaffen Vertrauen in das allgemeine Sicherheitskonzept.

Die Prüfung der Barrierenwirksamkeit auf dem Massstab des Gesamtsystems konzentriert sich auf Phänomene und Prozesse entlang der verfüllten und versiegelten Untertagebauwerke. Insbesondere wird gezeigt, dass die HAA- und SMA-Lagerfelder hydraulisch und thermisch voneinander entkoppelt sind. Die thermischen und gasbedingten Störungen im HAA-Lager treten zu unterschiedlichen Zeiten auf, was bedeutet, dass eine ungünstige Überlagerung der thermischen und gasbedingten Einflüsse auf die Sicherheitsfunktionen der technischen und geologischen Barrieren ausgeschlossen werden kann. Weder die thermischen noch die gasbedingten Störungen führen zu einem erhöhten Porenwasserfluss entlang der verfüllten Untertagebauten, womit eine Freisetzung von Radionukliden über die Schächte ausgeschlossen werden kann. Ebenso ist der Einfluss der thermischen und gasbedingten Störungen auf die mechanische und chemische

Stabilität der technischen und geologischen Barrieren des HAA-Lagers gering. Die Auslegung des Lagers sieht grosse Gasspeichervolumina vor, die für die Reduzierung des Gasdruckaufbaus im SMA-Lager von entscheidender Bedeutung sind. Die daraus resultierenden moderaten Gasüberdrücke in den verfüllten Untertagebauten von maximal 2 – 3 MPa werden die mechanische Stabilität der technischen und geologischen Barrieren nicht beeinträchtigen. Flüchtige Radionuklide (hauptsächlich ^{14}C) werden im Tiefenlager zuverlässig eingeschlossen, bis sie schliesslich durch radioaktiven Zerfall verschwinden. Gleichzeitig sorgen die ungesättigten Bedingungen mit moderaten Gasüberdrücken in den SMA-Einlagerungskavernen dafür, dass die Freisetzung gelöster Radionuklide aus den Abfallgebinden in das Wirtgestein sehr lange stark verzögert wird, da der Verfüllmörtel um die Abfallbehälter eine Kapillarsperre für gelöste Radionuklide darstellt.

Im Rahmen des *performance screenings* wurde eine breite Palette potenziell relevanter Abweichungen vom erwarteten Barrierenverhalten des Tiefenlagers analysiert. Die Bewertung von 23 Szenarien bestätigt die Robustheit des Multibarrierenkonzepts. Keines der analysierten Szenarien deutete auf eine signifikante Verringerung der Sicherheitsmargen auf Systemebene hin. Schliesslich wurde nur eine Handvoll Prüfszenarien identifiziert, für die eine weiterführende Analyse im Rahmen der radiologischen Konsequenzenanalyse sinnvoll wäre. Grund dafür ist, dass diese Szenarien erheblich von der erwarteten Entwicklung des Tiefenlagers abweichen, welche die Grundlage für die aktuelle Lagerauslegung darstellt. Hinweise auf eine signifikante Verringerung der Sicherheitsmargen auf Systemebene gibt es jedoch nicht.

Aus den Ergebnissen der Barrierenwirksamkeitsprüfung kann gefolgert werden, dass das geologische Tiefenlager für HAA und SMA am Standort Haberstal in der Standortregion Nördlich Lägern über den gesamten Bewertungszeitraum hinweg sicher ist und sowohl unter erwarteten als auch unter ungünstigen Bedingungen grosse Sicherheitsreserven aufweist. Durch die systematische Prüfung der Barrierenwirksamkeit, begleitet von einer umfassenden Nachweisführung, wird gewährleistet, dass das geologische Tiefenlager die von den Behörden gestellten Sicherheitsanforderungen auch unter Berücksichtigung von internen oder externen Störungen des Lagersystems erfüllt.

Table of Content

List of Tables

List of Figures

List of Acronyms

asl / a.s.l.	above sea level
ATW	Alpha-toxic waste
b.g.l.	below ground level
CAE	Claims, arguments, evidence (approach)
CEC	Cation exchange capacity
CDF	Cumulative density function
CMP	Compatibility of the components of the repository system (i.e., of the elements of the multi-barrier system and radioactive waste with each other and with other materials)
CON	Complete containment of radionuclides for a period of time
CRZ	Containment-providing rock zone
EDZ	Excavation-damaged zone
EGTS	Engineered gas transport system
FEPs	Features, events and processes
HLW	High-level waste (spent fuel assemblies and high-level waste from reprocessing)
IMS	Immobilisation, retention and slow release of radionuclides
IRF	Instantaneous release fraction
ISO	Isolation of radioactive waste from humans and the environment
JO	Jura Ost (siting region)
KEG	Nuclear Energy Act (*Kernenergiegesetz*)
KEV	Nuclear Energy Ordinance (*Kernenergieverordnung*)
L/ILW	Low- and intermediate-level waste
MIRAM	Model inventory of radioactive materials
NAB	Nagra Work Report (*Nagra Arbeitsbericht*)
N/A	Not applicable
NBT	Normalised bentonite temperature
NL	Nördlich Lägern (siting region)
NPP	Nuclear power plant
NTB	Nagra Technical Report (Nagra Technischer Bericht)
NTF	Normalised tracer flux
OoM	Order of magnitude
OPA	Opalinus Clay

PA	Performance assessment
PDFs	Probability density functions
RBG	General licence application (*Rahmenbewilligungsgesuch*)
RD&D	Research, Development and Demonstration
RP-HLW	(Vitrified) reprocessing of high-level waste
SA	Safety assessment
SATP	Standard Ambient Temperature and Pressure
SF	Spent fuel
SGT	Sectoral Plan for Deep Geological Repositories (*Sachplan geologische Tiefenlager*)
STB	Long-term stability of the barrier system with regard to long-term geological and climatic evolution
TF	Tracer flux
THM-CB	Thermo-hydro-mechanico-chemical and biological (interactions)
V&V	(Code and calculation) verification and (model) validation
ZNO	Zürich Nordost (siting region)
wrt.	with respect to

1 Introduction

1.1 Context

In Switzerland, legal regulations (Nuclear Energy Act, KEG 2003 and Nuclear Energy Ordinance, KEV 2004) and guidelines are in place for the management of radioactive waste. The Nuclear Energy Ordinance (KEV) classifies Switzerland's radioactive waste into low- and intermediate-level waste (L/ILW), alpha-toxic waste[1] (ATW) and high-level waste (HLW), the latter comprising spent fuel (SF) and vitrified HLW from reprocessing (RP-HLW). The Nuclear Energy Act (KEG) requires the disposal of all these types of radioactive waste in deep geological repositories. The feasibility of this disposal solution has been demonstrated for L/ILW in Nagra (1985) and for long-lived intermediate-level waste and HLW in Nagra (2002).

The Sectoral Plan for Deep Geological Repositories (SGT) regulates the search for suitable siting regions for deep geological repositories in Switzerland. This site selection process is conducted in three stages (BFE 2008). Stages 1 and 2 have already been completed and Nagra is currently in Stage 3 (SGT-E3). Clarifications on the safety-related specifications for this stage are provided in ENSI 33/649 (ENSI 2018b), while ENSI Guideline G03 and the corresponding explanatory report (ENSI 2023, ENSI 2020a) specify the protection objective, protection criteria and design principles for deep geological repositories.

In SGT-E3, three siting regions located in Northern Switzerland have been considered – Jura Ost (JO), Nördlich Lägern (NL) and Zürich Nordost (ZNO) – with the objective of selecting one siting region for an HLW repository, one for an L/ILW repository, or one for a combined repository for all waste types.

Following a comparison of these siting regions, Nagra concluded that NL is the safest and most flexible siting region for both repository types and is therefore applying for a general licence for a combined repository for both HLW and L/ILW at the Haberstal site.

The justification for this selection and the safety demonstration for a repository at the proposed site are submitted as part of the general licence application (RBG[2]). The reports relating to post-closure safety, shown in Fig. 1-1, are structured as follows:

- The overall safety-related argumentation, including post-closure and operational safety, is summarised in an overarching safety report ("*Sicherheitsbericht*", NTB 24-01, Nagra 2025b) shown at the top of Fig. 1-1.
- The upper left side of Fig. 1-1 shows the reports supporting Nagra's site comparison. The available options are compared with respect to safety and engineering feasibility and the results are synthesised in Nagra (2025a, NTB 24-03, "*Bericht zur Begründung der Standortwahl*").
- The upper right side of Fig. 1-1 shows the reports documenting the post-closure safety case for the combined repository at the selected site, including its synthesis in the post-closure safety report (NTB 24-10 Rev. 1, Nagra 2024o).
- The lower part of Fig. 1-1 shows a report that presents the safety and repository concept (NAB 24-18 Rev. 1, Nagra 2024s), including the provisional design, and reports providing the assessment basis. In the figure, the present report, which supports the safety assessment and post-closure safety case for a combined repository at the site, is highlighted with a red box.

---

[1] According to Nagra (2024a), ATW can coexist with L/ILW within the same emplacement caverns. As a result, for the sake of simplicity, the term L/ILW encompasses ATW without explicit mention.

[2] From the German *Rahmenbewilligungsgesuch.*

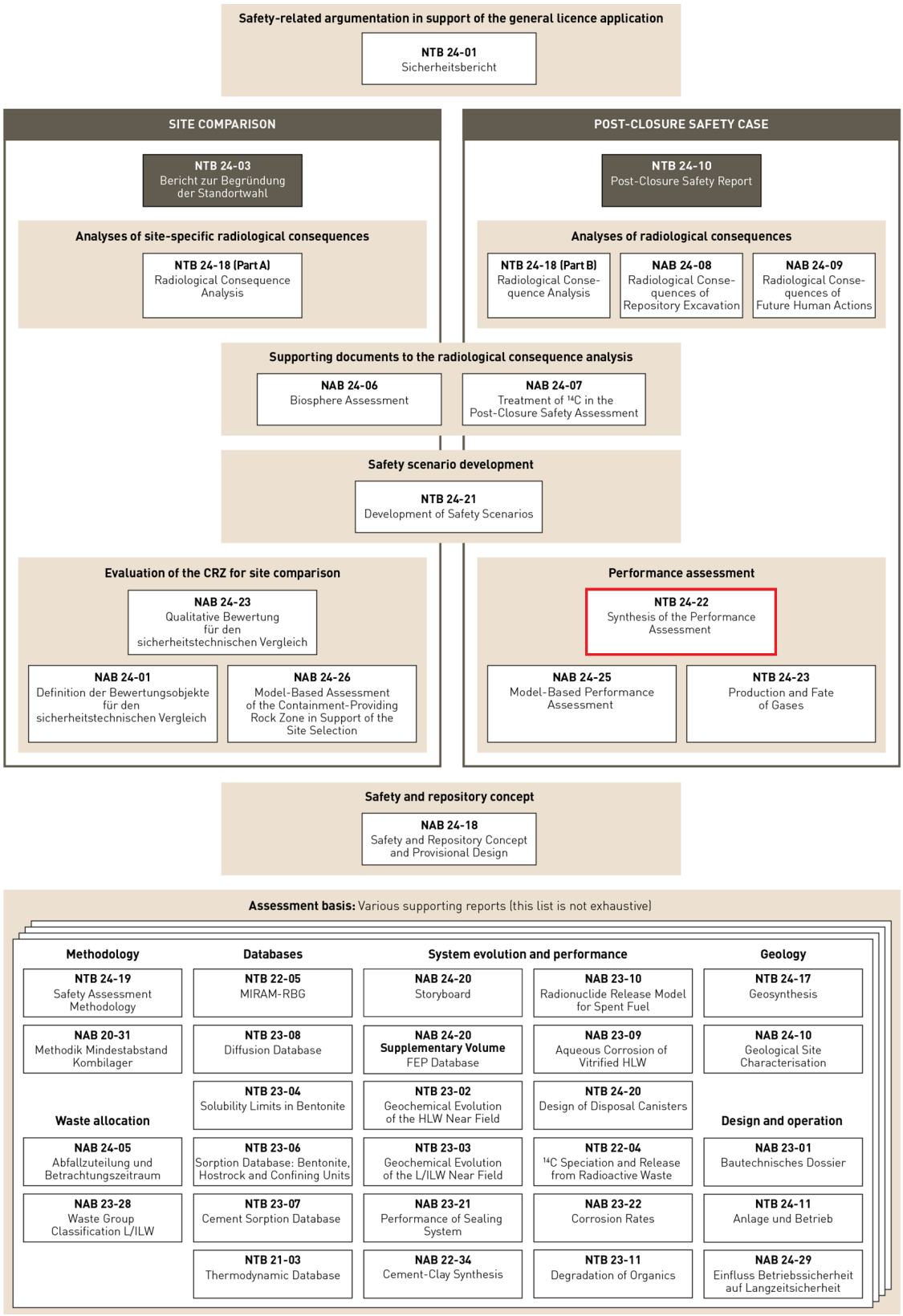

Fig. 1-1: Structure of reports covering post-closure safety aspects of the site comparison and the post-closure safety case

The present report is highlighted with a red box.

The post-closure protection objective for a deep geological repository is the permanent protection of humans and the environment (KEG 2003, ENSI 2023). The protection objective, design principles, protection criteria and the safety and repository concept inform the iterative design development process. This process leads to a provisional design and implementation plan for a deep geological repository for HLW and L/ILW at the Haberstal site, and to serve as the basis for the post-closure safety case and underlying safety assessment (as documented in the reports shown on the upper right side of Fig. 1-1). The safety assessment consists of four main processes:

- **Performance assessment** (PA), the subject of the present report, in which the thermal, hydraulic, mechanical and chemical evolution of the repository system is analysed;
- **Safety scenario development** (NTB 24-21, Nagra 2024e), which entails the identification and description of a set of safety scenarios that capture uncertainty in the initial state and subsequent evolution of the repository system over time;
- **Analysis of radiological consequences** (NTB 24-18, Nagra 2024r), which consists of an evaluation of radionuclide release rates to the surface environment as a function of time; and
- **Demonstration of post-closure safety**, in which evidence, arguments and results from the three previous steps are brought together in the post-closure safety report (NTB 24-10 Rev. 1, Nagra 2024o; Fig. 1-1 and Fig. 1-2).

This workflow is illustrated in Fig. 1-2 where the safety and repository concept leads to the iterative development of a provisional repository design and implementation plan (light blue boxes on the left) for which a safety assessment (dark blue boxes on the right) is then carried out. The full description of the post-closure safety case workflow can be found in the safety assessment methodology report (NTB 24-19, Nagra 2024t).

1.2 Scope and objectives

This report provides a synthesis of performance assessment (PA), which is the first of the four main processes of safety assessment outlined above. A general overview is given of the PA workflow that is carried out as part of the safety case for a deep geological repository for high-level waste (HLW) and low- and intermediate-level waste (L/ILW) at the Haberstal site in the Nördlich Lägern siting region. The workflow encompasses the following steps:

- Assessment of barrier performance for each element of the multi-barrier system at the component level ("*performance by component*"). Systematic book-keeping of claims, arguments and evidence ensures a traceable evaluation process and conveys a clear ranking of the safety relevance of the collected evidence.
- Assessment at the level of the entire system ("*total system performance*"), to account for any possible thermo-hydro-mechanical interactions between the individual barrier components.
- Uncertainty quantification, with special focus on parametric and conceptual uncertainties, which are associated with the simplified representation of the realistic repository system in an abstracted performance / safety assessment framework (i.e., uncertainty propagation associated with the abstraction process).
- *Performance screening*, based on a probabilistic assessment of the expected repository performance and of deviations from the expected performance. Possible paths of repository performance are identified, bundled and formulated in a format that can be subjected to the next step in the performance assessment/safety assessment (PA/SA) workflow.

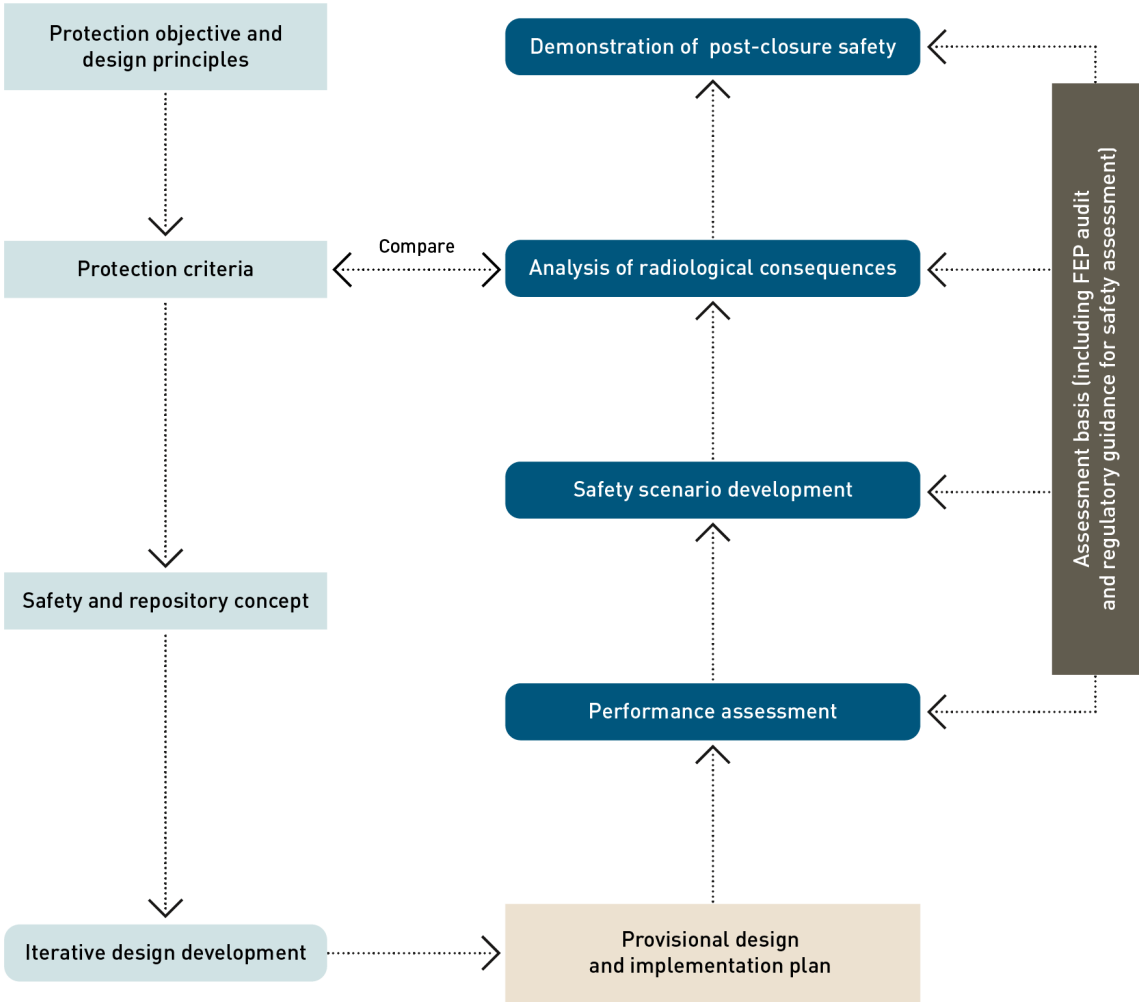

Fig. 1-2: High-level workflow for the safety assessment in support of the post-closure safety case for a repository for HLW and L/ILW in the proposed siting region

See Chapter 5 of NTB 24-19 (Nagra 2024t) for a full description.

PA is based on the evidence, knowledge, assessment tools and methodologies developed or acquired by Nagra in support of the safety assessment, collectively termed the assessment basis, which is depicted in the dark grey box on the right-hand site of Fig. 1-2. Key assessment basis reports are shown at the bottom of Fig. 1-1. The assessment basis includes, for example, current understanding of the geological and climatic evolution of Northern Switzerland, as synthesised in NTB 24-17 (Nagra 2024k), and of the phenomenological evolution of the waste and the repository system, which is brought together in the form of a "storyboard" in NAB 24-20 Rev. 1 (Nagra 2024n).

Together with the assessment basis, the findings of PA form the basis for a set of safety scenarios for the RBG (NTB 24-21, Nagra 2024e), for which the radiological consequences are evaluated (NTB 24-18, Nagra 2024r) and compared with regulatory protection criteria in the form of individual effective dose and risk limits provided in ENSI Guideline G03 (ENSI 2023).

1.3 Report outline

The report is structured as follows:

- Chapter 2 provides a detailed description of the entirety of repository barrier components and their intended functionalities contributing to the multi-barrier system of the deep geological repository, as well as details of the PA methodology.
- Chapter 3 presents an evaluation of the functionality of each component of the multi-barrier system with respect to the specified performance targets/requirements (performance by component).
- Chapter 4 presents an evaluation of the functionality of the entire repository system with respect to the high-level post-closure safety requirements (total system performance).
- Chapter 5 gives an evaluation of uncertainties associated with the simplified representation of the realistic repository system in an abstracted modelling framework (uncertainty propagation associated with the abstraction process).
- Chapter 6 provides an evaluation of deviations from the expected repository performance by barrier and by thermo-hydro-mechanical (THM) interactions between the barrier components ("scenario screening").

A summary and conclusions are presented in Chapter 7. Further details of the modelling work summarised in this report are given in NAB 24-25 (Nagra 2024m).

2 Repository concept and design, and performance assessment methodology

2.1 Concept and design development at a programme level

The objective of deep geological disposal is to ensure the long-term protection of humans and the environment by means of a system of staged, passively functioning engineered and geological barriers, termed the multi-barrier system. This overarching protection objective, as well as design principles and protection criteria, prescribed by Swiss regulations and national and international principles, provide the starting point for concept and design development. These underlie a high-level safety and repository concept for geological disposal, which in turn provides a basis for an iterative design development.

The Swiss repository concept, comprising the safety concept and provisional designs, has been iteratively developed over decades, with a number of major milestones already accomplished and others foreseen over the forthcoming years (NTB 16-01, NTB 21-01, NAB 24-18 Rev. 1: Nagra 2016, 2021a, 2024s).

In Nagra's terminology, the safety concept explains how, through the safety barriers and safety functions they provide, the repository performs its overarching safety functions and ensures the protection of humans and the environment. The repository concept describes the individual safety barriers and their properties, including interactions. The safety concept and repository concept are thus closely intertwined and are referred to collectively as the safety and repository concept. Nagra's current safety and repository concept is mature since it has been iteratively developed over more than 20 years. It is also sufficiently general to be considered stable: It is applicable to a repository in the Opalinus Clay in all the siting regions considered in the general licence applications and robust with respect to remaining uncertainties, i.e., it is not expected to fundamentally change in the future.

By contrast, the more detailed design and implementation plan is provisional and specifically developed for the purposes of the general licence application. Following the high-level workflow (Fig. 1-2), the safety concept and iterative design developments are detailed in Fig. 2-1, representing the current outcome of an ongoing iterative process entailing:

- The identification and development of a set of design requirements to be met, including, but not limited to, those related to post-closure safety,
- The design development itself, whereby solutions are proposed and refined to meet these design requirements in a manner that is compatible with site-specific conditions, feasible to implement with proven technology, and that avoids unnecessary complexity and excessive cost, and
- Analyses of the system as a whole and its various subsystems to test whether the requirements are met and to guide the further modification of the design.

In summary: The protection objective, protection criteria, safety functions, component-specific functions, performance objectives and design requirements together constitute a hierarchy of safety requirements that guide design development.

The key elements of the Swiss repository concept and the corresponding safety concept are described in NAB 24-18 Rev. 1 (Nagra 2024s). The safety concept for the post-closure phase of a deep geological repository ensures the permanent protection of humans and the environment using staged, passive barriers (Art. 3c KEG 2003). In Switzerland, the safety concept for HLW and L/ILW is based on a multi-barrier system optimised with regard to post-closure safety. This includes engineered barriers consisting of the waste matrix, disposal canisters, backfilling and sealing as well as the containment-providing rock zone (CRZ) as a geological barrier.

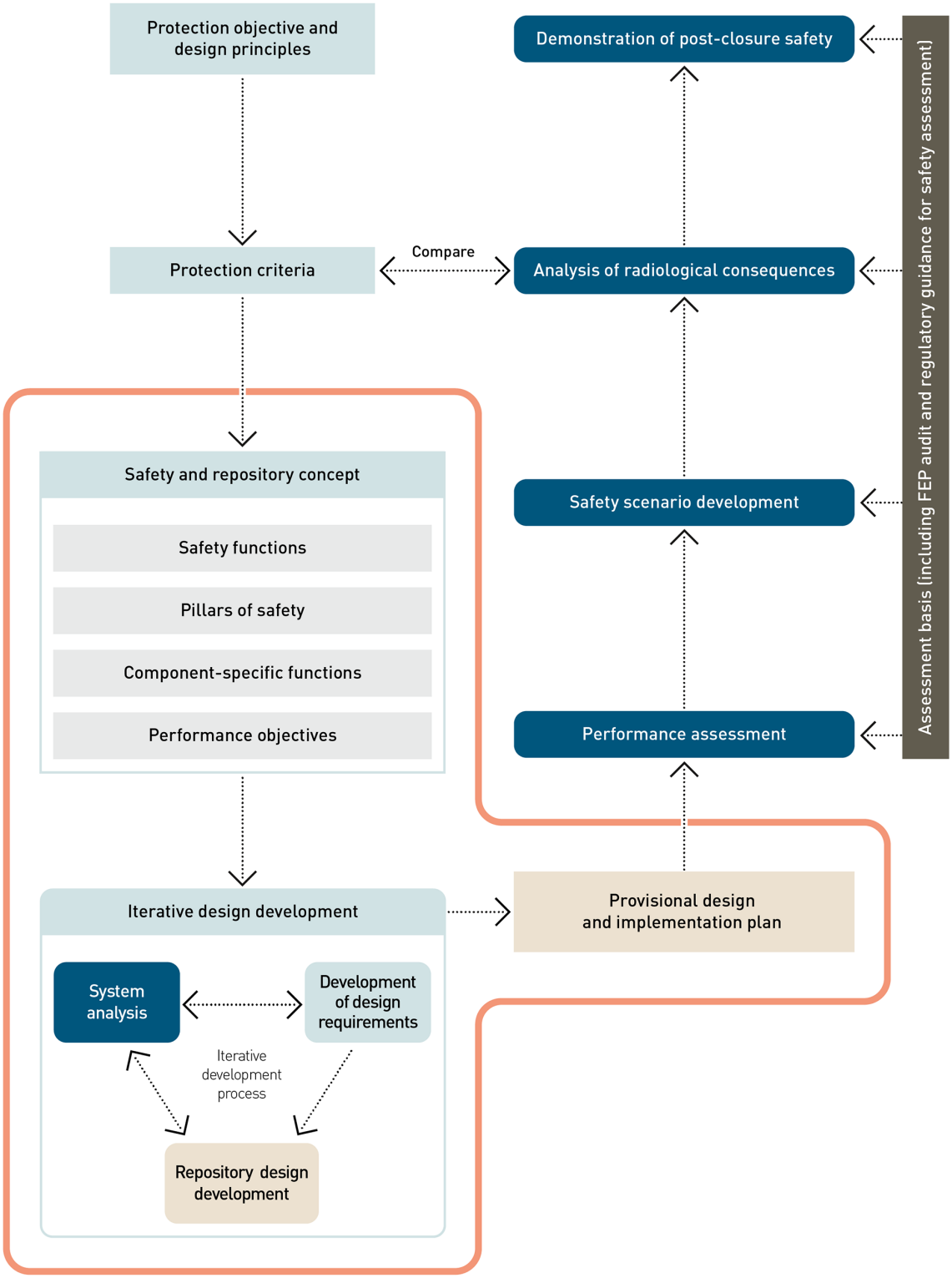

Fig. 2-1: Key elements of the safety concept and detailed design and implementation plan for the post-closure safety case according to the high-level workflow (Fig. 1-2), which then leads to a provisional design and implementation plan

2.2 Safety and repository concept

The safety and repository concept is discussed in detail in NAB 24-18 Rev. 1 (Nagra 2024s). The following paragraphs summarise the main aspects with relevance to post-closure safety.

2.2.1 Overview

In line with the Swiss legal and regulatory framework as well as national and international principles and practice (see Chapter 2 of NTB 24-10 Rev. 1, Nagra 2024o), the repository provides safety by means of multiple geological and engineered barriers, i.e., a multi-barrier system. These barriers operate passively, meaning that, after closure of the repository, no further measures such as for maintenance, control or monitoring, are required to ensure post-closure safety. This relieves future generations of the burden of having to manage or monitor the repository. The individual barriers contribute to so-called safety functions of the repository system, which together ensure a robust system, as discussed below in Section 2.2.2.

Radioactive waste is disposed of in emplacement rooms, located deep underground, roughly in the middle of the layer of the Opalinus Clay host rock and its over- and underlying confining geological units (Fig. 2-2). The innermost engineered barriers for HLW disposal consist of SF assemblies with fuel rods (UO_2 or mixed oxide fuel (MOX) pellets in cladding tubes) and vitrified HLW from reprocessing of SF (RP-HLW), packaged in steel canisters (NTB 24-20, Nagra 2024d). These HLW canisters are emplaced in drifts, which are subsequently backfilled with a compacted bentonite buffer, and sealed. For L/ILW disposal, waste packages for L/ILW are placed inside waste containers, which are in turn emplaced in caverns that are backfilled with cement-based mortar. The inventory of the waste to dispose of is described in detail in NTB 22-05 (Nagra 2023d).

The geological barrier is of primary importance due to the excellent qualities and long-term geological stability of the containment-providing rock zone (CRZ) (Chapter 5 in NTB 24-17, Nagra 2024k). The CRZ includes the Opalinus Clay host rock, as well as the geological units above and below the host rock with similarly favourable properties. The CRZ is delimited in the course of the site selection process according to ENSI 33/649 (ENSI 2018b) and documented in NAB 24-01 Rev. 1 (Nagra 2024c).

The Opalinus Clay is characterised by Nagra (2024k):

- A fine and homogeneous pore structure with a very low hydraulic conductivity. This ensures that water movement in this clay formation is limited, and that radionuclide migration is essentially diffusion-dominated.
- A high clay-mineral content. This results in a high sorption capacity for many radionuclides, thereby delaying their migration through the clay formation.
- A high self-sealing capacity. This means that any fractures that may form in the clay formation will rapidly close.

The geological units above and below the Opalinus Clay, albeit with a lower or more heterogeneous clay-mineral content, contribute further to the retardation and slow transport of radionuclides.

The depth of the geological barrier is sufficient to limit any potential impact of events and processes at the surface, including erosion, on the safety-related properties of the Opalinus Clay itself and its confining geological units.

The geological barrier is complemented by a mutually compatible set of engineered barriers.

A key role of the engineered barriers is the minimisation and mitigation of disturbances to the CRZ. Such disturbances are inevitably caused by the radioactive waste and its emplacement, including, for example, the effects of heat generated by the waste and the disturbance to the rock caused by the excavation and ventilation of underground openings. The engineered barriers around the waste are expected to provide a period of complete containment for at least as long as the heat generated by the waste has a significant potential to affect transport processes in the surrounding rock. After this period of complete containment, an eventual release of radionuclides and migration through the multi-barrier system cannot be excluded. Most radionuclides will, however, remain immobilised in the waste packages and waste containers until they decay (Section 5.4 of NTB 24-10 Rev. 1, Nagra 2024o).

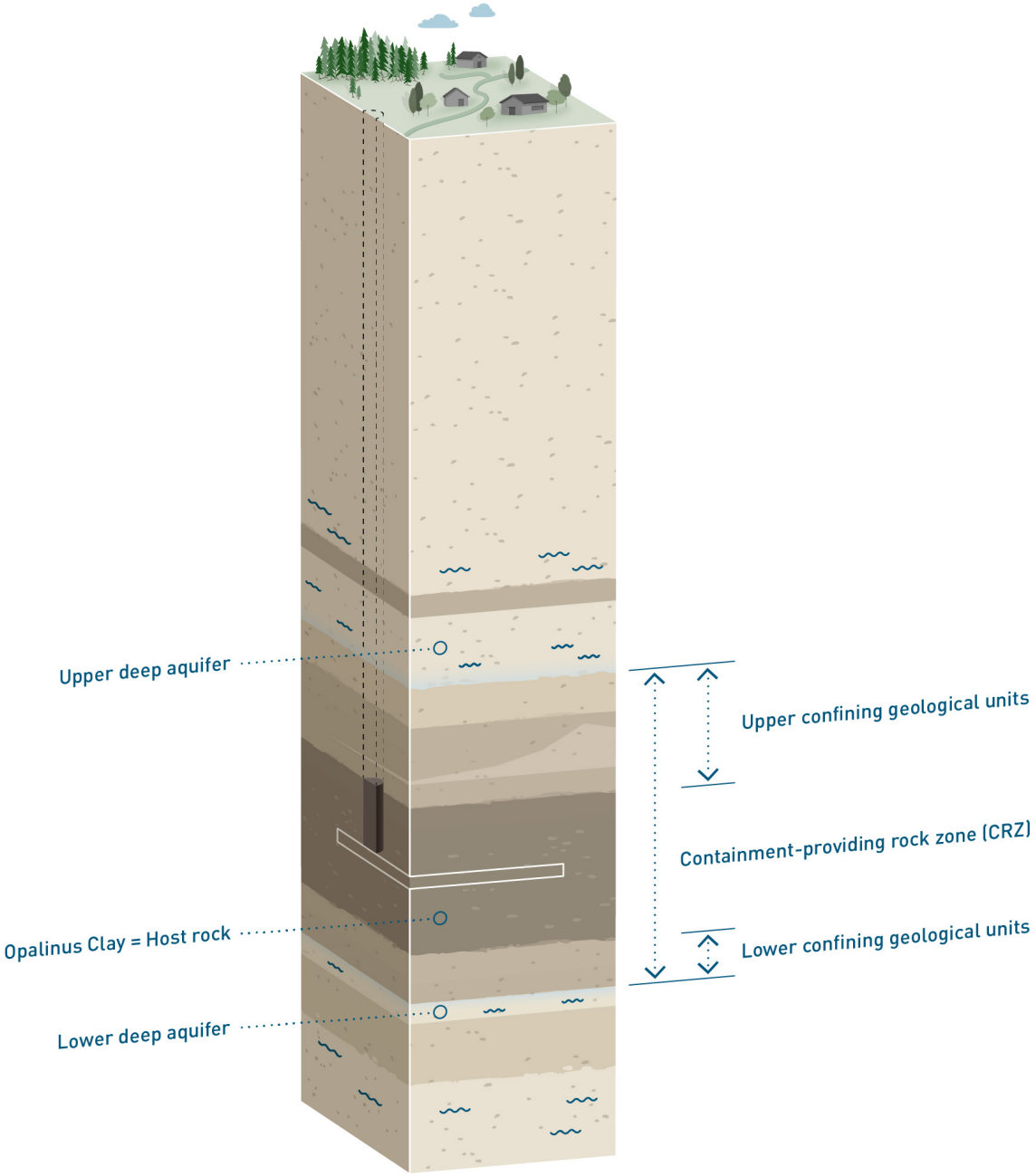

Fig. 2-2: Placement of the repository deep underground within the Opalinus Clay, between its confining units

Furthermore, the radionuclides that are released will migrate only slowly towards the surface environment, with substantial attenuation by radioactive decay, first within the engineered barriers and then, for any that migrate through these barriers, within the surrounding geological barrier. This staggered system of barriers will thus ensure the compliance with the safety criterion set by the regulator.

2.2.2 Safety functions and pillars of safety

In line with ENSI Guideline G01, Appendix 1 (ENSI 2011), safety functions are overarching functional requirements on the multi-barrier system that, taken together, ensure post-closure safety. Collectively, the multi-barrier system provides the following safety functions:

S1: **Isolation** of radioactive waste from humans and the environment (referred to in this report as *ISO safety function*);

S2: **Complete containment** of radionuclides for a period of time (*CON safety function*);

S3: **Immobilisation, retention, and slow release** of radionuclides (*IMS safety function*);

S4: **Compatibility** of the components of the repository system (*CMP safety function*);

S5: **Long-term stability** of the multi-barrier system with regard to long-term geological and climatic evolution (*STB safety function*).

The repository barriers and their properties that are the main contributors to these safety functions are termed “pillars of safety”. As demonstrated by the present performance assessment, they are well understood and insensitive to perturbations. The seven pillars of safety are:

- The **deep underground location of the waste emplacement rooms in a stable geological environment** that lacks underground resources specific to the region that could attract future human exploitation. It ensures that the repository is not susceptible to geological events and processes relevant to post-closure safety and that inadvertent human intrusion remains unlikely.
- The **containment-providing rock zone** (CRZ) includes the host rock as well as the upper and lower confining geological units. The host rock, Opalinus Clay, is characterised by a fine and homogeneous pore structure, extremely low hydraulic permeability, a homogeneous and high clay-mineral content and the associated high sorption capacity for many radionuclides (NTB 24-17, Nagra 2024k). The CRZ is characterised by favourable properties (especially its self-sealing capacity) for long-term stability, forming a very effective and stable barrier against radionuclide transport and a compatible (physical and chemical) environment for the engineered barriers (NAB 24-18 Rev. 1, Nagra 2024s and NTB 24-17, Nagra 2024k).
- Both the **SF and RP-HLW matrices** are chemically stable in the expected environment.
- The **SF and RP-HLW disposal canisters** are mechanically stable and corrosion-resistant in the expected environment. They ensure complete containment of the radionuclides for at least as long as the heat generated by the waste could potentially have a significant impact on transport processes in the surrounding barriers. The canisters satisfy the regulatory requirement of complete containment for at least 1,000 years (ENSI Guideline G03, ENSI 2023).

- The HLW emplacement drifts will be backfilled with a **buffer**. This buffer serves as a suitable physical and chemical environment that enhances the longevity of the HLW disposal canisters. Additionally, the buffer offers mechanical support to the surrounding rock after the degradation of the tunnel support. It compartmentalises the repository by isolating the disposal canisters from one another, thereby mitigating the impact of accidental human intrusion. The buffer reduces the potential effects of heat release on the safety-relevant properties of the CRZ and acts as a barrier against radionuclide transport.
- The **L/ILW cementitious near-field** promotes the sorption of radionuclides, decreases the corrosion of metals and inhibits the degradation of organic materials, which in turn reduces gas generation. The cement-based backfill can also store a significant volume of gas and provides mechanical stability to the host rock, even after the degradation of the tunnel support.
- The **closure system** (backfill and seals) provides retention of radionuclides released from the waste packages, and a transport and storage system for repository-generated gas, which retains gaseous radionuclide species within the underground structures while limiting the build-up of gas pressure. The sealing of both the individual waste emplacement rooms and the HLW and L/ILW repository sections reduces safety-relevant interaction between these two repository sections and the radiological impact of inadvertent human intrusion. The closure system further provides mechanical stabilisation of the host rock after the rock support has degraded.

Each pillar of safety can contribute directly and/or indirectly to the safety functions. For example, the HLW disposal canisters contribute directly to the containment of radionuclides, while the surrounding bentonite buffer contributes indirectly as it helps to protect the canisters. Compatibility between the different pillars of safety is based upon a solid technical and scientific understanding of the geological and engineered components. In accordance with international safety standards (IAEA 2011)[3] redundancy and diversity of the barriers at component level ensure the robustness of the entire multi-barrier system.

The contributions of these seven pillars of safety to the five safety functions are summarised schematically in Fig. 2-3 and are elaborated in the discussion of component-specific functions in Section 3.4 of NAB 24-18 Rev. 1 (Nagra 2024s). The figure shows how the pillars of safety rest on a sound scientific and technical basis, which is itself built upon a well-defined waste-disposal programme, which is updated periodically as the state of knowledge evolves (e.g., NTB 21-01, Nagra 2021a).

[3] *"Containment and isolation of the waste shall be provided by means of a number of physical barriers of the disposal system. The performance of these physical barriers shall be achieved by means of diverse physical and chemical processes together with various operational controls. The capability of the individual barriers and controls together with that of the overall disposal system to perform as assumed in the safety case shall be demonstrated. The overall performance of the disposal system shall not be unduly dependent on a single safety function."* (from IAEA SSR-5, IAEA 2011).

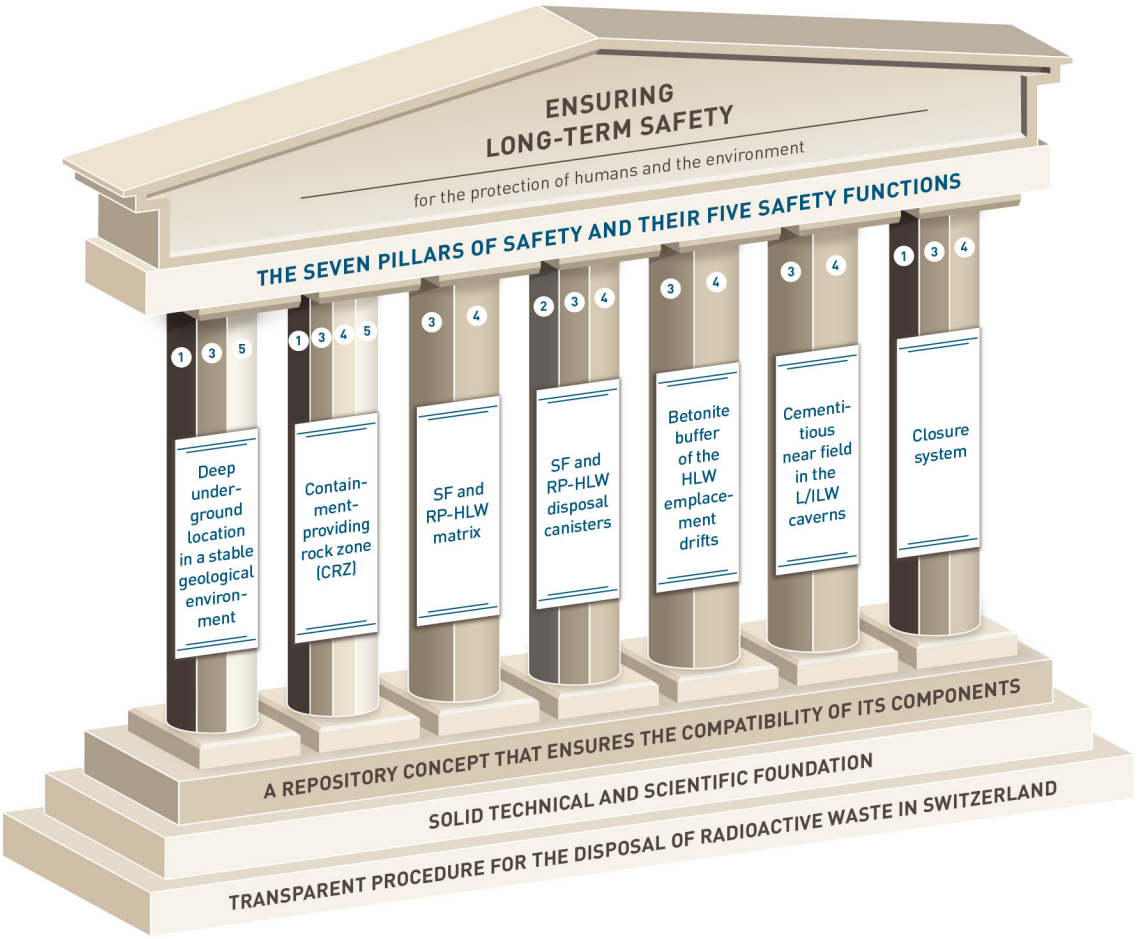

SAFETY FUNCTIONS

1. **Isolation** of the radioactive waste from humans and the environment
2. **Complete containment** of radionuclides for a period of time
3. **Immobilisation, retention, and slow release** of radionuclides
4. **Compatibility** of the components of the repository system
5. **Long-term stability** of the multi-barrier system regarding long-term geological and climatic evolution

Fig. 2-3: Summary of Nagra's safety and repository concept, showing the seven pillars of safety contributing to the five overarching safety functions

A solid scientific and technical basis built on a transparent waste disposal programme forms the foundation of this safety concept.

2.3 Provisional design and implementation plan

The provisional design for the combined repository, i.e., the current implementation of the safety and repository concept, has been developed for the purposes of the current licencing step. An overview is given in the following paragraphs; for more details, see Chapter 4 in NAB 24-18 Rev. 1 (Nagra 2024s) and NTB 24-11 (Nagra 2024b).

As illustrated in Fig. 2-4, the repository is foreseen to consist of two separate sections: one for the disposal of L/ILW (including ATW), and the other one for HLW (including both RP-HLW and SF), constructed roughly in the vertical centre of the Opalinus Clay host rock layer. The HLW and L/ILW repository sections are spatially separated with a respect distance of nearly 2 km.

The HLW emplacement drifts will be supported by pre-cast concrete tubbing elements (i.e., ring elements). The tunnel support for the L/ILW emplacement caverns and other underground openings consists of an outer layer of shotcrete and an inner concrete liner.

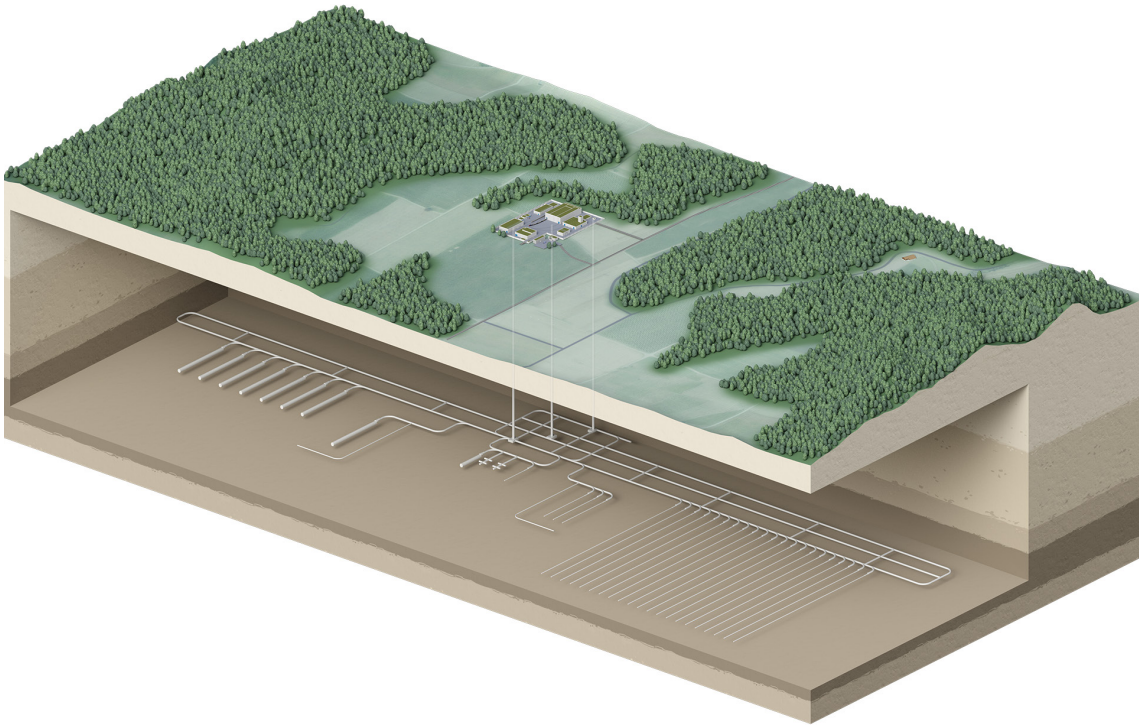

Fig. 2-4: Generic repository layout for a combined repository
NTB 24-01 (Nagra 2025b).

In addition to the main HLW and L/ILW disposal areas, each repository section includes a pilot repository, in which the behaviour of the waste, the backfill, the seals and the host rock is monitored until the end of a monitoring phase.

The engineered barriers are illustrated in Fig. 2-5. Disposal takes place in parallel sets of waste emplacement rooms (HLW emplacement drifts and L/ILW emplacement caverns). HLW is encapsulated in carbon-steel disposal canisters, placed coaxially along the emplacement drifts, with the surrounding space filled with the bentonite buffer. Most of the L/ILW is compacted, embedded in a cement/mortar matrix and placed in standardised 200 L drums, MOSAIK-II-type casks made of cast iron, or steel casks. These waste packages are placed inside containers made of reinforced concrete and infilled with a cement-based mortar. Once the L/ILW containers are emplaced in the caverns, the caverns are backfilled with a cement-based mortar.

The repository is connected to the surface via three shafts: an access shaft, an operations shaft and a ventilation shaft. Elements of the surface infrastructure and of some of the access structures are shared between the two repository sections.

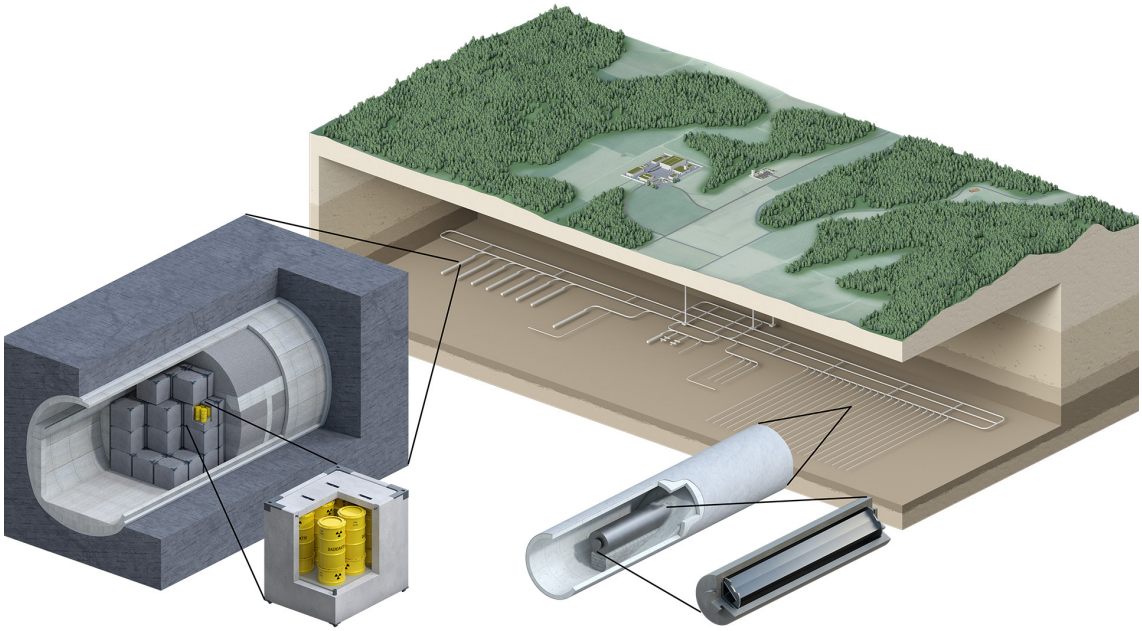

Fig. 2-5: Illustration of the provisional design of the engineered barriers of the combined repository for HLW (right) and L/ILW (left)

The example for HLW (right) is based on spent fuel (SF) assemblies with fuel rods (UO_2 pellets in cladding tubes) packaged in a steel disposal canister. The HLW disposal canisters are placed in an HLW emplacement drift which is then backfilled (for example with bentonite) and sealed. The example for L/ILW (left) is based on a typical waste package type (200 L drum) that is packaged in a disposal container and disposed of in an L/ILW emplacement cavern that, in this example, is backfilled with cement-based reference mortar.

A generic timeline for repository construction and operations was presented in NTB 21-01 (Nagra 2021a) and adapted to the current repository project from the engineering point of view (NTB 24-11, Nagra 2024b). For the model-based analyses presented in this report, some further simplifications have been implemented, as shown in Tab. 2-1.

The repository closure system consists of various clay-based seals and tunnel backfill (see Figure 3-9 from NTB 24-10 Rev. 1, Nagra 2024o and NAB 21-12 Rev. 1, Nagra 2021d). The seals comprise:

- HLW-V1 and L/ILW-V1 seals (waste emplacement room seals) located at the entrance of the HLW emplacement drifts and L/ILW emplacement caverns, respectively. These seals are installed immediately after emplacement of the waste and the complete backfilling of the emplacement rooms.
- HLW-V2 and L/ILW-V2 seals (disposal area access seals) located at the entrance of the disposal area accessways of the HLW repository section (in the construction, operations and ventilation tunnels) and the L/ILW repository section (in the ventilation and operations tunnel), respectively.
- V3 seals (shaft seals) located in the shafts up to the top of the Opalinus Clay host rock. These are the outermost seals.

VF1 and VF2 backfills fill the repository structures up to the V3 seals at the top of the Opalinus Clay. In addition, shaft backfill fills the part of the shafts above the V3 seals up to the surface level.

Tab. 2-1: Generic timeline for the implementation of a repository for HLW and L/ILW, as assumed in the model-based analyses of repository performance

Modified after NTB 21-01 (Nagra 2021a) and NTB 24-11 (Nagra 2024b).

Phase	**Description**
Operational Phase 1	Construction and operation of test area (0 – 21 years)
Operational Phase 1b	Construction of main L/ILW repository (21 – 34 years)
Operational Phase 2a	Construction of main HLW repository and HLW emplacement (34 – 36 years)
Operational Phase 2b	Construction of main HLW repository and SF emplacement (36 – 46 years)
Operational Phase 3	First monitoring phase (46 – 56 years): backfilling of SF emplacement drifts and L/ILW emplacement caverns
Operational Phase 4	Second monitoring phase (56 – 96 years): backfilling of all underground structures except access tunnels to pilot repository
Post-closure phase	All repository components backfilled and sealed (>96 years)

2.4 Foundations of the performance assessment

2.4.1 Assessment basis

The quality of the performance assessment, and of the overall safety assessment, rests on a sound assessment basis. The assessment basis is defined as the evidence, knowledge, assessment tools, and methodologies developed or acquired by Nagra in support of the safety assessment. Key inputs from the assessment basis needed for the assessment of repository performance at the component level and on the scale of the total system are as follows:

- The radionuclide inventory and a description of the waste forms, masses and volumes provided by the Model Inventory of Radioactive Materials (MIRAM) database for the general licence application (NTB 22-05, Nagra 2023d).

  It encompasses the nuclide vector, material balance, geometries related to gas-relevant materials, and the schedule for waste production. Thermal and gas-related source terms, derived from the waste inventory, represent a key input for the assessment of repository-induced effects (NTB 24-23 and NAB 24-27: Nagra 2024p, 2024f). A compilation of important PA inputs from the MIRAM database is given in App. A-1.

- The general layout of the current repository project for HLW and L/ILW at the Haberstal site and the detailed engineering design of the repository components, the waste emplacement rooms for HLW and L/ILW, pilot repositories, operations and ventilation tunnels, central area, experimentation areas and shafts (NTB 24-11, Nagra 2024b).

  A compilation of important PA inputs from the engineering database is given in App. A.2.

- The interpretation of the geoscientific databases gathered during site-specific investigation programmes and the synthesis of the geoscientific interpretations in the context of the regional geological setting (NTB 24-17, Nagra 2024k).

  This process leads to the development of site-specific geoscientific reference datasets. A compilation of important PA inputs from the engineering database is given in App. A.3.

- A comprehensive description of the phenomenological evolution of a combined repository in the Opalinus Clay formation in the NL siting region from the perspective of post-closure safety (NAB 24-20 Rev. 1, Nagra 2024n).

  This includes detailed documentation of the various processes, phenomena, and the corresponding timescales that govern the post-closure repository evolution, including the following periods:

  - Period of thermal disequilibrium in the HLW repository section (typically <10,000 years);
  - Period of chemical disequilibrium in the HLW and L/ILW repository sections (corrosion and degradation of wastes, typically <50,000 years);
  - Period of hydraulic disequilibrium (pore pressure recovery and resaturation of all underground structures (typically <100,000 years);
  - It also discusses the impact of geological long-term evolution (neotectonics, erosion, glaciation) during the entire period for assessment.

The models, codes, and databases that support the present performance assessment are also part of the assessment basis.

2.4.2 Assessment principles

Nagra's safety assessment methodology has been developed in line with international guidance, advancements and publications. Following OECD/NEA (2002), confidence in safety assessment is established by *logical, transparent assessment workflows within an auditable framework*. Based on these and Nagra's own experience, a set of principles and objectives for the safety assessment have been identified, as presented in Section 4.1 of NTB 24-10 Rev. 1 (Nagra 2024o). The following principles are particularly relevant to the performance assessment:

Rigour in consideration and treatment of uncertainty

As far as possible, all potential sources of uncertainty and the various sources of bias are considered and recognised when conducting and interpreting the analyses. In particular, the model-based assessment of long-term repository performance respects all categories of uncertainties introduced by the simplified representation of the repository system in terms of geometry, prevailing processes, parameter assignment, boundary and initial conditions and source terms (see Section 2.5.3 and Chapter 5). A key part of performance assessment is the identification and analysis of uncertain and potentially detrimental phenomena, together with other uncertainties, as input to the formulation of safety scenarios, which are addressed in the analysis of radiological consequences.

Validation and verification of models and databases

Appropriate quality assurance and control measures are adopted to ensure that the models and databases developed and applied in the analyses are suitable for their intended purpose. Each computer code used to perform analyses is subject to a well-planned and executed code and a calculation verification and model validation (V&V) programme, formulated in terms of qualitative and quantitative performance measures.

Multiple lines of argument for safety

In line with, e.g., the recommendations of OECD/NEA (2004) claims related to the performance and safety of the disposal system are supported, as far as possible, by multiple lines of argument and wide-ranging evidence. The development of arguments and evidence supporting a set of high-level claims is a key element of the performance assessment methodology.

Assurance of completeness

The assurance of comprehensiveness, i.e., the minimisation of "completeness uncertainty" is discussed in Section 4.5 of NTB 24-10 Rev. 1 (Nagra 2024o). Although it is impossible to prove beyond all possible doubt the completeness of a safety assessment, measures are taken to ensure the inclusion of a comprehensive set of potentially relevant phenomena. Specifically, the description of the phenomenological evolution of the repository on which the present performance assessment is based has undergone iterative development over many years, with each version having been peer-reviewed and informed by Nagra's extensive RD&D programme (NTB 21-02, Nagra 2021c). The comprehensiveness of this description is further enhanced by effective information exchange among safety assessors, technical experts within Nagra, and the broader scientific community. Section 4.5 of NTB 24-10 Rev. 1 (Nagra 2024o) also describes how an FEP audit is carried out to verify the inclusion of all relevant features, events and processes (FEPs) in the performance assessment and in the wider safety assessment, and to justify the omission of other features.

2.4.3 Claims, arguments and evidence

The need for an auditable assessment framework calls for a traceable method of proof with quantitative performance targets whenever possible. For this, claims are formulated that relate to how the individual repository components and the overall repository system contribute to the different safety functions to satisfy the assigned functional requirements (Fig. 2-3). A suite of arguments, backed-up by evidence, is developed to substantiate each claim. A claim can be said to be robust if it is well substantiated using sound arguments and convincing evidence. In line with the assessment principles, the robustness of a claim is strengthened by seeking multiple lines of argument.

Arguments and evidence can both broadly be grouped according to the following categories (see also Fig. 2-6):

Empirical knowledge and evidence from elsewhere

This includes knowledge from other scientific disciplines, from other radioactive waste programmes and from natural analogues. Arguments based on such knowledge and experience provide confidence in the solid scientific foundation of the safety concept. Empirical evidence derived from desk studies summarising knowledge from other waste disposal programmes or other geoscientific disciplines (e.g., reservoir engineering, CO_2 sequestration, geothermal energy) provides general confidence in the consistency of the arguments with the state of the art. However, the transferability of this general knowledge and experience to the specific conditions of the project under investigation can be limited.

Project-related experimental databases

Dedicated experimental databases are collected in the context of Nagra's RD&D programme (e.g., in-situ experiments in rock laboratories, geotechnical characterisation of the barrier materials) and as part of recent site investigation programmes (e.g., 3-D seismics in the three siting regions and the deep borehole campaign) to provide direct evidence for the performance of the repository project under investigation. Specifically, experimental evidence derived from targeted site investigation programmes provides the specific databases needed to prove the performance of the geosphere as a transport barrier and to demonstrate the robustness of the geological barrier in the context of geological long-term evolution. Dedicated scientific studies of THM-C processes at laboratory and field scale as part of Nagra's RD&D programme provide confidence in the governing phenomena and processes associated with the engineered barrier system.

Safety-oriented and favourable repository layout and design and associated model-supported evidence

The individual barrier components and the entire repository are designed such that the intended safety functions are expected to be provided in most reasonably foreseeable circumstances with large safety margins. Model-supported sensitivity and robustness analyses support the optimisation of the performance of individual barrier components and of the entire repository system (see system analysis as part of the iterative design process in Fig. 2-1). In the context of performance assessment, model-supported evidence provides important insights in the adequacy of repository performance when the multi-barrier system is subjected to internal or external perturbations.

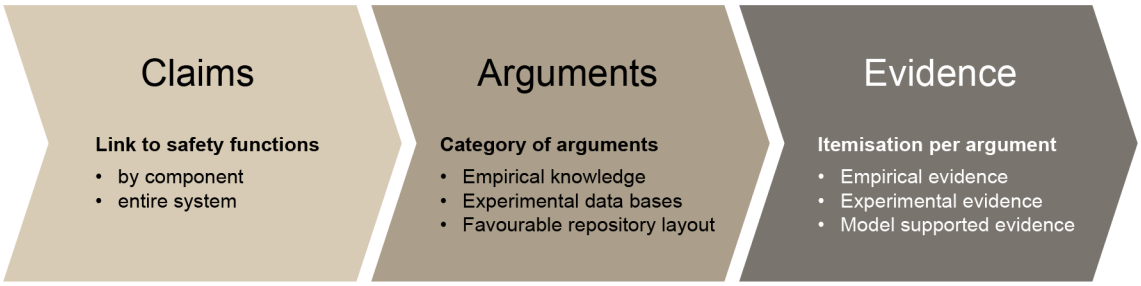

Fig. 2-6: Traceable method of proof, structured as claims, arguments and evidence, aimed at substantiating the performance of the repository system

As part of their substantiation, and in accordance with the assessment principles, claims need to be tested for their robustness with respect to uncertainties, including, for example, uncertainties in the rates or occurrence of processes, the spatial extent of features and the timing of events. Specific arguments can be developed for robustness with respect to some uncertain phenomena (e.g., the self-sealing potential of the host rock provides robustness with respect to phenomena that could give rise to either the creation of fractures or reactivation of existing faults). In addition, model-supported quantitative assessments, including sensitivity and analyses, play a key role in assessing robustness.

Systematic book-keeping of claims, arguments and evidence is carried out to ensure a traceable assessment workflow and to convey a clear ranking of the safety relevance of the collected evidence.

2.4.4 Performance indicators, indices, targets and evaluation scales

Model-supported quantitative assessments apply, wherever possible; a so-called indicator approach is used similar to the criteria-based indicator approach applied in the context of the site comparison in NAB 24-26 (Nagra 2024l). The approach involves the use of numerical models to evaluate a set of performance indicators or indices, which are compared with a set of performance targets. Performance indicators, indices and targets are defined as follows:

Performance indicator

A measurable or calculable quantity that quantifies one or more system components with respect to their expected performance.

Performance index

A calculated, dimensionless quantity derived from the (calculable) performance indicator, generally by dividing the performance indicator by its corresponding performance target, such that, for example, a performance index of less than one indicates favourable performance.

Performance target

A specific target value related to a calculated performance index. A performance target, if met, provides evidence that one or more potentially detrimental phenomena do not compromise the performance of individual components or of the overall repository. This evidence is typically used to substantiate a performance assessment claim.

Performance targets are generally defined based on the known physical and chemical properties of repository materials and general scientific understanding of the behaviour of these materials in the presence of thermal, hydraulic, mechanical, and chemical loads (i.e., they are not tied to the

specific repository concept and design under consideration). The performance indicators, on the other hand, are defined using models that are concept- and design-specific and are used to quantify the loads that will arise in a repository context.

By design, the repository components and the overall repository system are expected to fulfil their safety functions in accordance with the safety concept; this expected performance is deduced from a well-constrained assessment basis (Section 2.4.1) and further supported by probabilistic performance assessment simulations, which account for inherent parametric uncertainties associated with the initial state of the barrier system (Section 6.2). The model-based performance indicators and indices show large safety margins, building confidence in the post-closure safety of the repository as designed, including its robustness with respect to repository-induced effects (e.g., gas and heat). The safety margins represent a measure of barrier performance which can be expressed in terms of evaluation scales, classifying the performance in qualitative terms such as "very favourable", "favourable", "less favourable" or "unfavourable" with respect to potentially detrimental phenomena.

2.5 Performance assessment workflow

The detailed PA workflow as part of the high-level SA workflow (Fig. 1-2) is summarised in Fig. 2-7 and discussed in the following paragraphs. It is guided by the premise that confidence in the assessment of repository performance is created through *logical, transparent assessment workflows within an auditable framework*.

PA, which represents the first stage in the wider safety assessment workflow, is taken to comprise:

- an assessment of barrier performance, expressed as claims at the component level for each of the pillars of safety of the multi-barrier system (Section 2.5.1);
- an assessment of claims related to the performance of the entire system (total system performance), to account especially for THM-C interactions between the individual barrier components (Section 2.5.2);
- an assessment of uncertainties associated with the simplified representation of the realistic repository system in an abstracted PA framework (uncertainty associated with the abstraction process), ensuring that the modelling tools applied for quantitative assessment of barrier performance at component level and at the total system level adequately represent all safety-relevant processes and phenomena (Section 2.5.3); and
- an assessment of deviations from the expected repository performance by barrier and by interaction ("screening of assessment scenarios") as input to safety scenario development (Section 2.5.4). Special emphasis is given to those deviations from expected repository performance that require an in-depth assessment of the radiological consequences.

In each of these steps, PA addresses the geological setting, the provisional repository design and the evolution of the repository at a level of simplification that is between the realistic system and its highly abstracted representation in the analysis of radiological consequences.

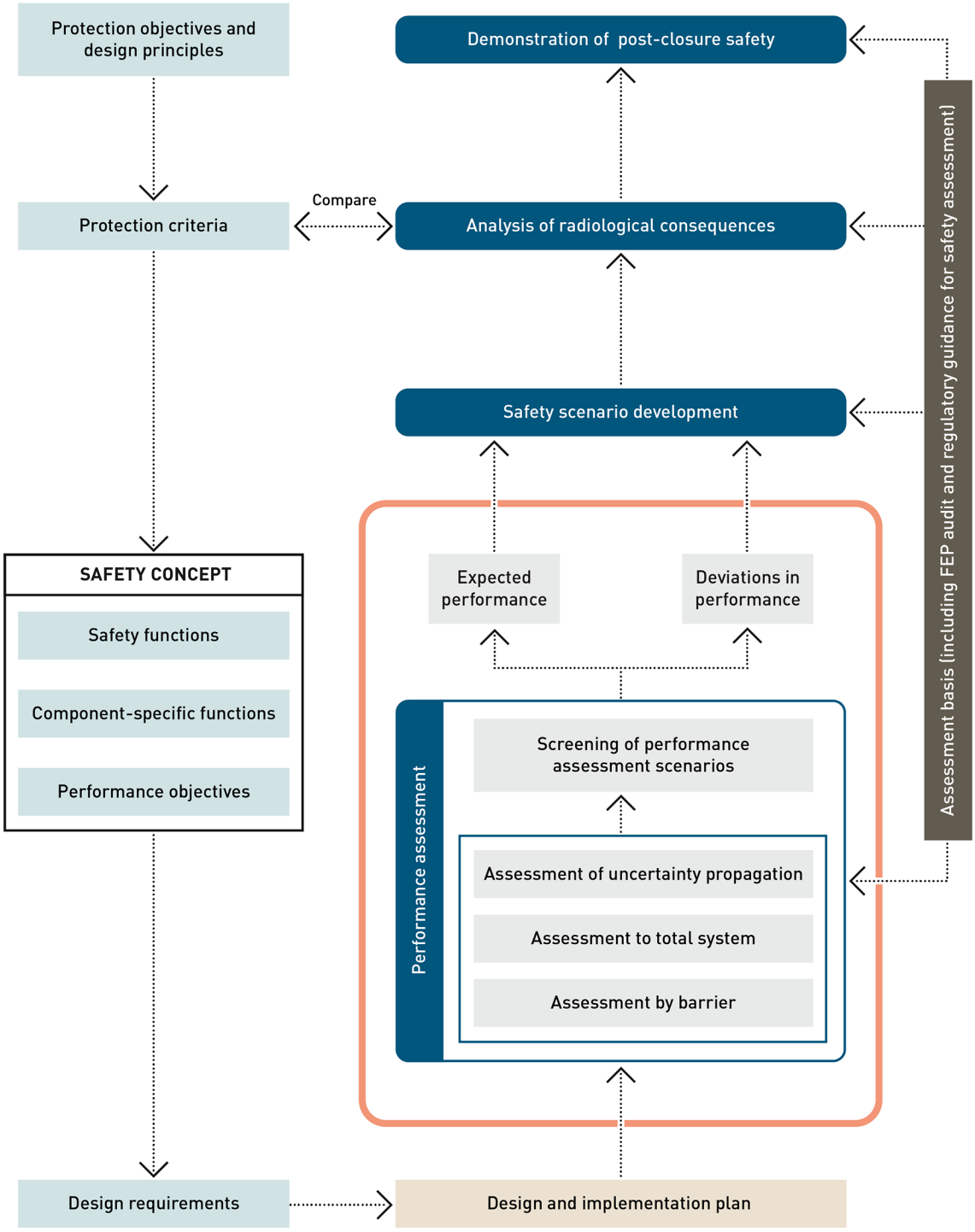

Fig. 2-7: Workflow for the post-closure safety case, highlighting, in the orange box, the main elements of the PA process

2.5.1 Performance assessment by component

Specific properties of, or actions to be performed by one or more system features, including the pillars of safety and other features of the system (such as excavation-damaged zones [EDZ] and the linings used in underground excavations) that contribute directly or indirectly to the safety functions are termed component-specific functions and are described at length in Section 3.4 of NAB 24-18 Rev. 1 (Nagra 2024s). Specific claims inherent in these component-specific functions are examined in the performance assessment at the component level. The claims are statements that express the ways in which the components contribute to the repository safety functions. If the barrier component consists of subcomponents which contribute separately to the safety functions, the claims are assigned specifically to the subcomponents, which are called "assessment objects". For instance, the HLW-V1, HLW-V2 seals of the closure system in the HLW repository section are considered separately from those of the L/ILW repository section (L/ILW-V1, L/ILW-V2), because they perform different safety functions. Tab. 2-2 gives an overview of the safety-relevant repository components, the corresponding assessment objects, the claims and the corresponding safety functions. The PA by component, in which the arguments and evidence that substantiate these claims are presented, is the subject of Chapter 3.

Tab. 2-2: PA of repository components: assessment object, claims and corresponding safety functions

Safety functions: ISO = isolation of radioactive waste from humans and the environment, CON = complete containment of radionuclides for a period of time, IMS = immobilisation, retention and slow release of radionuclides, CMP = compatibility of the components of the repository system, STB: long-term stability of the multi-barrier system with regard to long-term geological and climatic evolution.

Assessment object	**Claim**	**Safety functions**				
		ISO	**CON**	**IMS**	**CMP**	**STB**
SF and RP-HLW matrix						
SF rods (containing SF pellets and cladding)	The SF assemblies experience chemical conditions favourable to their stability for an extended period of time, which ensures the retention and slow release of radionuclides.			✓		
	The SF assemblies are chemically stable and do not impair the chemical integrity of the canister or the bentonite buffer.				✓	
RP-HLW	The glass matrix containing the RP-HLW provides a chemical environment where most radionuclides are immobilised and only very slowly released.			✓		
	The stainless-steel flask containing the RP-HLW is compatible with the glass, the canister and the bentonite porewater.				✓	

Tab. 2-2: Cont.

Assessment object	Claim	Safety functions				
		ISO	CON	IMS	CMP	STB
HLW disposal canister						
Canister	The canister provides complete containment of radionuclides for at least the early post-closure phase, when the canister near-field is exposed to distinct thermal and hydraulic disequilibrium conditions.		✓			
	The products of canister degradation (corrosion) are not detrimental to other engineered and/or geological barriers.				✓	
Bentonite buffer/HLW near-field						
Bentonite	Radionuclides will be retained in the bentonite buffer, limiting the release into the host rock over the entire period for assessment.			✓		
	The bentonite buffer provides favourable chemical and mechanical conditions in the HLW near-field, ensuring compatibility with the other engineered and/or geological barriers.				✓	
Lining and EDZ	The lining and the EDZ around the HLW emplacement drifts do not represent a significant transport pathway for dissolved radionuclides.			✓		
	The lining and the EDZ around the HLW emplacement drifts do not impair the chemical and mechanical integrity of the other components of the barrier system.				✓	
Cementitious L/ILW near-field						
Cement-based L/ILW near-field	The cement-based components of the L/ILW near-field contribute to the retention and slow release of radionuclides.			✓		
	The cement-based components of the L/ILW near-field are compatible with each other.				✓	
Closure system (backfill and seals)						
HLW-V1/V2 seals	The HLW-V1/V2 seals contribute to a retarded release of dissolved and volatile radionuclides.			✓		
	The HLW-V1/V2 seals ensure the mechanical and chemical integrity of the bentonite buffer.				✓	
L/ILW-V1/V2 seals	The L/ILW-V1/V2 seals contribute to a retarded release of radionuclides along the backfilled repository structures.			✓		
	The L/ILW-V1/V2 seals (sand-bentonite mixture) contribute to the compatibility of the barrier components.				✓	

Tab. 2-2: Cont.

Assessment object	Claim	Safety functions				
		ISO	CON	IMS	CMP	STB
Closure system (backfill and seals) *continued*						
VF1 and VF2 backfill	The VF1 and VF2 backfill contributes to retarding the releases of radionuclides along the tunnel system.			✓		
	Backfill contributes to mechanical integrity of the host rock.				✓	
V3 shaft seals	The V3 seals contribute to a retarded release of dissolved and volatile radionuclides.			✓		
	The V3 seals contribute to the isolation of radioactive waste from the earth's surface.	✓				
Geological barrier with the containment-providing rock zone (CRZ)						
Host rock	The host rock at great depth ensures the isolation of radioactive waste from humans and the environment.	✓				
	Radionuclides will be retained in the host rock over the entire period for assessment.			✓		
	The host rock provides a stable geomechanical and geochemical environment which protects efficiently the engineered barriers over the entire period for assessment.				✓	
Confining units	The upper/lower confining units represent an efficient additional transport barrier for dissolved radionuclides.			✓		
Regional-scale groundwater flow	Favourable groundwater flow conditions at the regional scale contribute to the retarded release of radionuclides into the regional aquifer systems.			✓		
Deep underground location (stable geological setting)						
Neotectonics/ seismicity	Neotectonic events will not compromise the radionuclide retention capacity of the engineered and geological barriers of the repository.			✓		
Erosion	The deep underground location of the repository structures ensures the isolation of the radioactive waste from humans and the environment.	✓				
	The long-term geological stability of the site (towards erosion and glaciation) ensures that radionuclides will be retained in the CRZ over the entire period for assessment.			✓		
	The long-term geological stability of the site (towards erosion, glaciation, tectonics) ensures sufficient mechanical integrity of the geological barrier to protect the engineered barriers over the entire period for assessment.					✓

2.5.2 Performance of the total system

The construction and operation of a deep geological repository changes the environmental conditions in the vicinity of the underground structures, creating a thermal, hydraulic, geomechanical and geochemical disequilibrium in the repository near-field over an extended period of time. These perturbations of the physico-chemical conditions could give rise to THM-C interactions between the repository components, which can include microbiological activity. The impact of THM-C interactions on the overall performance of the repository system *("total system performance"*) must also be addressed in the performance assessment framework.

Again, claims are formulated for each type of interaction, each related to one or several safety functions, addressing the corresponding functional requirement at the scale of the entire repository. It should be noted that the safety-relevant interactions between the components of the barrier system can essentially be assigned to two safety functions, namely IMS and CMP. Tab. 2-3 gives an overview of specific assessment issues to be addressed, the claims and the corresponding safety functions.

Phenomena and processes that occur along the backfilled and sealed underground structures are the main drivers for THM-C interactions at the total system level. Model-based analyses of the interactions between the different barrier components require large model set-ups, including complex couplings between the phenomena and processes involved. The computationally intensive simulations allow only a limited number of numerical analyses, addressing deterministic cases of expected repository performance and possible deviations thereof. Performance indicators such as temperature, pore pressure and gas saturation in the repository near-field are used to evaluate the performance of the multi-barrier system and to obtain insight in the interactions between the repository components. The PA of the total system, including these model-based analyses, is the subject of Chapter 4.

Tab. 2-3: PA of the total system: assessment issues, claims and corresponding safety functions

Safety functions: IMS = immobilisation, retention and slow release of radionuclides, CMP = compatibility of the components of the repository system.

Assessment issue	Claim	Safety functions	
		IMS	CMP
General interactions related to repository layout			
Interactions HLW – L/ILW repository sections	HLW and L/ILW repository sections are separated from each other, preventing efficiently any detrimental THM-C interactions between the two repository sections.		✓
Interactions related to the repository-induced effects			
Thermal interactions	Thermal impacts do not enhance radionuclide release along the backfilled and sealed HLW structures.	✓	
	Thermal impacts do not impair the stable geochemical and geomechanical environment.		✓
Gas-related interactions	Gas-related impacts do not impair the stable geochemical and geomechanical environment of the HLW repository.		✓
	Gas-related impacts do not enhance radionuclide release along the backfilled and sealed HLW structures	✓	
	Gas-related impacts do not impair the stable geochemical and geomechanical environment of the L/ILW repository.		✓
	Gas-related impacts do not enhance radionuclide release along the backfilled and sealed L/ILW structures	✓	
Transport of radionuclides as gaseous species	The release of radionuclides as gaseous species (mainly ^{14}C as methane) outside the multi-barrier system is not dose relevant.	✓	

2.5.3 Uncertainty quantification in the model-based PA workflow

Traceable handling of uncertainty is an indispensable element in the confidence-building process contributing to the assessment of post-closure performance and safety of deep geological repositories (NTB 24-19, Nagra 2024t). It is common practice to categorise uncertainty as:

- Data uncertainties, which relate, for example, to deficiencies, incompleteness and inaccuracy in experimental data, field observations, design information, test data and waste specifications (e.g., missing data, missing values, random measurement errors);
- Model uncertainties, which relate, for example, to the lack or plurality of suitable and manageable conceptual and computational models that are consistent with the available data, as well as to the applicability of a given model to a particular situation;
- Scenario uncertainties, which can potentially give rise to alternative paths for the broad evolution of the repository system in terms of its main components and their safety functions, such as the occurrence of a large earthquake.

The model-based quantitative assessments require a traceable management of data, models and scenario uncertainty as a prerequisite for auditability.

The assessments are carried out with a portfolio of numerical models for the simulation of the performance of the multi-barrier system at the component scale and at the scale of the entire repository system. Scenario uncertainties are handled, in general, by exploring discrete, "deterministic" alternative assumptions. Data uncertainties can also be handled in this way. Alternatively, a more comprehensive probabilistic approach can be used, in which uncertainties in parameter values are expressed in terms of probability density functions (PDFs), which are sampled automatically and at random in the model-based analyses. Such probabilistic approaches are applied in Chapter 6 of this report. They are, however, computationally demanding, and require the use of more simplified models than the deterministic approach applied, for example, in Chapter 5.

Model uncertainties are related to this notion of model simplification or abstraction. By nature, a model is an abstraction of a realistic system, gained by eliminating unnecessary details. Consequently, any type of model abstraction or "conceptualisation" introduces inaccuracy and additional uncertainty, in that it involves the reduction of the degrees of freedom of the realistic system. In PA, the "elimination of unnecessary detail" is required and desirable as it improves traceability of the system behaviour. At the same time, it must be proven that the "elimination of unnecessary detail" does not impair the applicability of a model to its intended use, namely an unbiased assessment of repository safety. This calls for a traceable analysis of the types of simplification, and hence potential sources of uncertainty, in the model abstraction process. These include:

- Geometric abstractions, i.e., the simplified representation of geometry, such as the representation of 3-D systems by 2-D models;
- Process abstractions, i.e., the simplified formulation of phenomena and processes, such as the use of Darcy's law as an approximation to the more general Navier-Stokes equation for fluid flow, or the omission of chemical and biological processes that could act as sinks for repository-generated gas;
- Homogenisation / scaling of parameters, e.g., the spatial and temporal averaging of effective material properties;
- Simplification of boundary conditions, initial conditions and source terms, e.g., the assumption of a zero concentration of radionuclides released from the repository at the upper and lower boundaries of the CRZ.

The tracing, quantification and aggregation of uncertainties is a complex process, which starts with the model-supported interpretation of field observations, site characterisation data or dedicated laboratory experiments, and examines how these propagate to the eventual evaluation of safety indicators and indices. This is the subject of Chapter 5 of the present report.

2.5.4 Performance screening

Performance screening is the subject of Chapter 6 of the present report. A probabilistic indicator workflow is presented, which allows the performance margins of selected PA-Scenarios to be evaluated by comparing safety-relevant performance indices with their corresponding performance targets.

By design, the multi-barrier system of the provisional repository project, as specified in the provisional design and implementation plan (see Fig. 2-1), performs all required post-closure safety functions over the entire period for assessment. Accordingly, its evolution under the action of internal and external perturbations corresponds to the PA-Scenario called "Expected Performance – *EXPERF*" (see also Section 6.2.1). Performance screening represents the final step in the PA workflow (Chapter 6), aimed at identifying and evaluating safety-relevant deviations from the expected barrier performance.

A probabilistic approach is followed to evaluate the deviations from the expected barrier performance. Monte Carlo simulations are carried out to identify whether one or more performance targets fail to be met, or whether the safety margins are significantly reduced, possibly with extreme combinations of uncertain parameters. Multiple performance indicators, each with their own performance targets, are used to evaluate the performance of the multi-barrier system (Section 6.2.3). The indicator-based assessment encompasses the PA-Scenario of expected performance (Section 6.2.4) and multiple scenarios addressing deviations from the expected performance (Section 6.3). For each PA-Scenario, the corresponding safety margins are expressed in terms of dimensionless performance indices (see Section 2.4.4). An overview of the performance indicators, performance indices, performance targets and evaluation scales (see below) applied in the performance assessment is given in Tab. 2-4. The performance indicator *tracer flux (TF) of a conservative tracer* is briefly discussed in the following paragraphs. A detailed discussion of each indicator is found in App. C.

The TF of a conservative tracer, representing a dose-relevant, non-sorbing radionuclide from the nuclide inventory of the repository, is used as a performance indicator for the evaluation of the radionuclide retention capacity of the multi-barrier system (Tab. 2-4). It is assumed that the radionuclide is dissolved in the porewater and released as an instantaneous pulse from the near-field into the host rock, from where it migrates towards regional aquifer systems at the top and bottom of the CRZ. The dose-relevant radionuclide for the HLW repository section is ^{129}I, whereas ^{36}Cl is used as the representative nuclide for the L/ILW section. For the L/ILW repository additional tracer simulations are dedicated to the release of the volatile radionuclide ^{14}C.

The pulse-like tracer release in the indicator-based PA calculations must be made consistent with the more accurate source terms which are used in the radiological consequence analysis (NTB 24-18, Nagra 2024r). This ensures that the indicator-based PA simulations provide acceptable approximations to the expected maximum tracer fluxes[4] despite the simplified representation of the source terms (for further details see App. A.1.3 and C.1).

As an illustration, Fig. 2-8 (left column) presents the results of simple, deterministic numerical simulations with a 2-D transport model, showing the diffusive transport of ^{129}I from the HLW emplacement drifts through the CRZ towards the regional aquifer systems. Similarly, Fig. 2-8 (right column) presents the transport of ^{36}Cl released from the L/ILW emplacement caverns.

[4] Note that the tracer flux TF is a simple indicator of barrier performance rather than a precise estimator of dose rates. Reliable estimates of dose rates are obtained in NTB 24-18 (Nagra 2024r), which takes into account the entire radionuclide inventory of the repository and represents the time dependent source terms in a more sophisticated manner. On the other hand, the tracer flux TF used in the performance assessment as an indicator for barrier performance is a first order estimator of dose rates for selected radionuclides (^{129}I, ^{36}Cl, ^{14}C), derived by a simple calibration procedure using the corresponding dose rates from NTB 24-18 (Nagra 2024r).

Contour plots of tracer concentration TC in [Bq/m^3] are presented at four different times. In addition, the transients of the corresponding tracer fluxes, $TF_{CRZ,I\text{-}129}$ and $TF_{CRZ,Cl\text{-}36}$ (sum of tracer fluxes to the underlying Malm aquifer and overlying Keuper aquifer; see App. A.3 are depicted in Fig. 2-8 (top row). For both radionuclides, tracer flux is given in [mSv/a], making use of two nuclide-specific biosphere dose conversion factors which represents the present-day climate (further details are found in App. C.1).

The contour plots of the ^{129}I tracer (Fig. 2-8 left column) indicate that the tracer front reaches the top of the Keuper aquifer after less than 500,000 years and the base of the Malm aquifer after 1 million years. The total tracer flux, $TF_{CRZ,I\text{-}129}$, calculated as the sum of tracer fluxes passing into the overlying Malm aquifer and underlying Keuper aquifer, reaches a peak TF_{max} after around 500,000 years with a maximum dose rate more than 3 orders of magnitude below the regulatory dose limit (Fig. 2-8 top left). The dimensionless performance index NTF is derived from the maximum tracer flux TF_{max} by normalisation with the corresponding performance target, which is set equal to the regulatory dose limit (see Tab. 2-4). A performance index NTF > 1 means simply that the regulatory dose limit has been exceeded, indicating an unacceptable performance of the multi-barrier system. The evaluation scale, introduced in the last column of Tab. 2-4, allows quality levels of barrier performance to be specified (further details are found in App. C.1). For example, an NTF value <0.001 means that the tracer flux remains 3 orders of magnitude below the regulatory dose limit and a very favourable barrier performance is achieved.

The release of ^{36}Cl from the L/ILW emplacement caverns through the host rock towards the regional aquifer systems is illustrated in Fig. 2-8 (right column). The L/ILW caverns are expected to be partially saturated for a period of ten thousand years, which has a strong impact on the transport of ^{36}Cl in the CRZ, significantly retarding and reducing the release into the regional aquifer systems. The contour plots indicate that the ^{36}Cl remains largely within the Opalinus Clay around the L/ILW caverns, finally disappearing due to radioactive decay (the half-life of ^{36}Cl is 3.013×10^5 years). The total tracer flux $TF_{CRZ,Cl\text{-}36}$, reaches a peak TF_{max} after nearly 1 million years with a maximum dose rate more than 6 orders of magnitude below the regulatory dose limit (Fig. 2-8 top right).

The indicator-based evaluation of the PA-Scenario of the expected barrier performance confirms the robustness of the safety concept, revealing large safety margins for all performance indicators addressed in the assessment. Additional PA-Scenarios were defined to analyse the impact of deviations from the expected repository performance in a traceable manner for each barrier component (Section 6.3). These deviations were screened with respect to their likelihood of occurrence and safety relevance (Section 6.4). Both aspects form inputs to safety scenario development, which specifies the safety scenarios for the radiological consequence analysis. In this context, it is worth noting that aspects which are not captured by the performance assessment models (e.g., radionuclide retardation by sorption mechanisms) may also be propagated directly to the formulation of safety scenarios.

Tab. 2-4: Performance indicators, performance indices, performance targets and evaluation scales used in quantitative assessments

The performance indicators are discussed in greater detail in App. E.

Performance indicator	**Source term**	**Performance index**	**Performance target**	**Evaluation scale**[5]
Tracer flux (TF) of a conservative tracer, representing a dose-relevant, non-sorbing radionuclide, dissolved in the porewater and released from the repository system into the regional aquifer systems at the top/bottom of the CRZ				
Variants: tracer flux $TF_{CRZ,\ I\text{-}129}$ tracer flux $TF_{CRZ,Cl\text{-}36}$ tracer flux $TF_{V3\text{-}C14}$ tracer flux $TF_{CRZ\text{-}C14}$	 IR – 10% of total ^{129}I inventory IR – 100% of ^{36}Cl inventory IR – 100 % of ^{14}C (L/ILW only) IR – 100 % of ^{14}C (L/ILW only)	Normalised tracer flux (*NTF*) $NTF = \frac{TF_{max}\ [mSv/a]}{0.1\ [mSv/a]}$	$NTF = 1$	$NTF_{P99} \geq 1$ unacceptable $NTF_{P95} \geq 0.1$ unfavourable $NTF_{P95} \geq 0.01$ less favourable $NTF_{P95} \geq 0.001$ favourable $NTF_{P95} < 0.0001$ very favourable
Temperature in the HLW near-field				
Temperature T_B in the HLW near-field	Heat source term “Kombi” (see App. A.1.2)	Normalised temperature in the buffer (*NBT*): $NBT = \frac{T_B}{150[°C]}$	$NBT = 1$	Percentile of frequency distribution $NBT_{P75} \geq 1$ unacceptable $NBT_{P95} \geq 1$ unfavourable $NBT_{P99} \geq 1$ less favourable $NBT_{P99.9} < 1$ favourable
Pore pressure at a given control point associated with thermal/gaseous impacts in the HLW and the L/ILW repository near-fields.				
Variants $P_{HLW,heat}$ $P_{HLW,gas}$ $P_{L/ILW,gas}$	Gas source terms (see App. A.1.1) HLW L/ILW	Failure potential of intact rock (“slip tendency”): $\begin{Bmatrix} FPH \\ FPG_{HLW} \\ FPG_{L/ILW} \end{Bmatrix} = \frac{\tau}{\tau_{max}}$ τ- shear stress τ_{max} - maximum shear stress	$\begin{Bmatrix} FPH \\ FPG_{HLW} \\ FPG_{L/ILW} \end{Bmatrix} = 1$	Percentile of frequency distribution $FPI_{P75} \geq 1$ unacceptable $FPI_{P95} \geq 1$ unfavourable $FPI_{P99} \geq 1$ less favourable $FPI_{P99.9} < 1$ favourable FPI = {FPH,FPG}

[5] The evaluation scales presented here are based on pragmatic considerations associated with the limited number of Monte Carlo simulations performed. More rigorous estimation of rare event probabilities of overstepping the performance target requires a refined assessment of input uncertainties (extended ranges, complementary probability distributions).

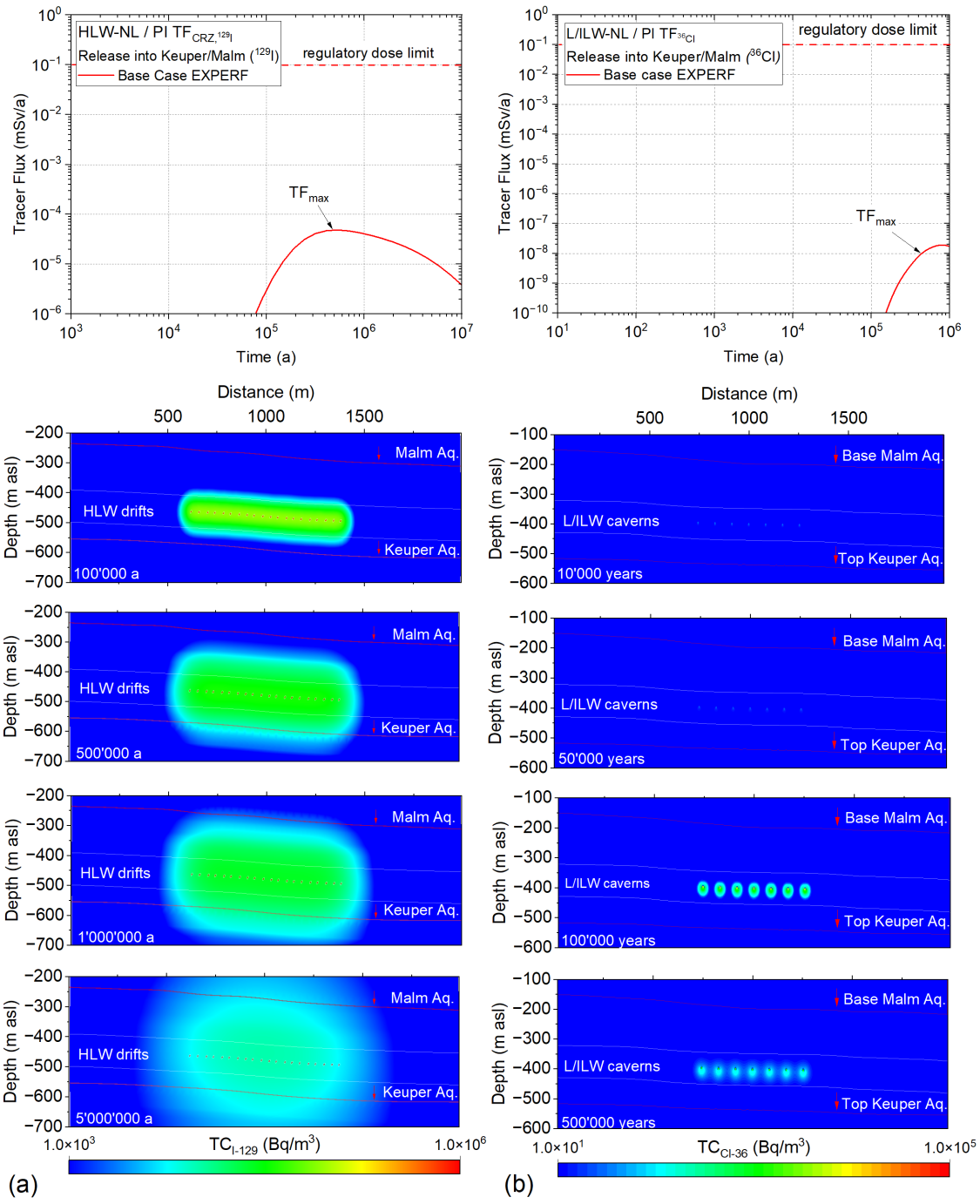

Fig. 2-8: Model-based assessment of the performance indicators, $TF_{CRZ,I\text{-}129}$ and $TF_{CRZ,Cl\text{-}36}$

Simulations correspond to the base case of the PA EXPERF scenario (see Section 6.2.3).

Left column: 2-D simulation of diffusive transport of ^{129}I released from the HLW emplacement drifts. Snapshots of tracer concentration in [Bq/m^3] are presented at the times 100 ka, 500 ka, 1 million a and 5 million a. The top graph presents the transients of the tracer flux $TF_{CRZ,I\text{-}129}$ from the CRZ to the aquifers. Right column: ^{36}Cl released from the L/ILW emplacement caverns. Concentrations in [Bq/m^3], presented at times of 10 ka, 50 ka, 100 ka and 500 ka. The top graph presents the transients of the tracer flux $TF_{CRZ,Cl\text{-}36}$ from the CRZ to the aquifers.

3 Performance assessment by component

Chapter 3 focuses on evaluating the performance of the system of engineered and geological barriers at the level of individual components. Building on the general safety concept of the provisional repository project for HLW and L/ILW (Fig. 2-5), this chapter systematically assesses the seven pillars of safety, with a focus on the specific safety functions assigned to each component. The evaluation begins with the SF/RP-HLW (Section 3.1), followed by an assessment of the HLW disposal canisters (Section 3.2) and the bentonite buffer near-field of the HLW emplacement drifts (Section 3.3). Section 3.4 addresses the cementitious near-field of the L/ILW emplacement caverns. The performance of the closure system, including the HLW and L/ILW seals as well as the backfill of non-disposal repository structures (access, operations and ventilation tunnels, central and test areas), is covered in Section 3.5. Lastly, Sections 3.6 and 3.7 highlight the geological barrier system, comprising the containment-providing rock zone and the general geological setting of the selected site. Finally, Section 3.8 presents the conclusions for the PA by component.

3.1 SF and RP-HLW matrix

3.1.1 Claims, arguments and evidence – overview

The SF assemblies and the glass matrix of the RP-HLW are addressed in PA as separate assessment objects, representing the first barrier of the multi-barrier system (see Tab. 2-2). Each of them contributes to the retarded release of radionuclides (IMS safety function) and ensures compatibility with the other elements of the multi-barrier system (CMP safety function). An overview of the claims made for this barrier, together with the corresponding lines of argument and evidence is given in Tab. 3-1.

Tab. 3-1: Performance of the SF and RP-HLW matrices: overview of arguments and evidence for each claim

Argument	Evidence
Waste matrix for SF and RP-HLW – claim: The SF assemblies experience chemical conditions favourable to their stability for an extended period of time, ensuring the retention and slow release of radionuclides.	
The majority of radionuclides are trapped in the UO_2, MOX mineral phases (fuel matrix).	Activation calculations and dissolution experiments have shown that more than 97% of the total radionuclide inventory is present within the fuel matrix (Chapter 1 in NAB 23-10, Johnson et al. 2023 and references therein).
	Congruent release of the fuel happens with a fractional dissolution rate of 10^{-7} a^{-1}, upper bound 10^{-6}, lower bound 10^{-8} a^{-1} (Section 7.2 in Johnson et al. 2023).
The Instantaneous Release Fraction (IRF) from SF corresponds to only a small fraction of the total radionuclide inventory.	Empirical and experimental evidence has shown that the IRF consists of less than 3% of the total radionuclide inventory and only represents the volatile radionuclides trapped in the gap between the Zircaloy hull and the SF pellets in cracks in the pellets and in void spaces at grain boundaries (Table 4-2 in Johnson et al. 2023).
The SF pellets experience a chemical environment, where most radionuclides are only very slowly released by dissolution after water has entered the canister.	H_2 generated by metal corrosion dissolves in porewater, leading to reducing conditions. Experimental studies have shown that, under such reducing conditions, where hydrogen is dissolved, dissolution of SF is a very slow process (Section 5.6 in Johnson et al. 2023).
	Model-based assessments of the HLW near-field evolution demonstrate that the HLW disposal canisters will remain unsaturated for >100,000 years in a hydrogen atmosphere at gas pressures above hydrostatic (NAB 24-25, Nagra 2024m; this report: Chapters 4 and 6).
Waste matrix for SF – claim: The SF assemblies are chemically stable and do not impair the chemical integrity of the canister or the bentonite buffer.	
The SF matrix mainly consists of UO_2, dissolves at a very slow rate and does not chemically interact with the canister and bentonite or only to a very limited extent.	Thermodynamic models evaluating the chemical interaction between bentonite porewater, canister corrosion products, Zircaloy and the SF matrix demonstrate a very low release of elements from the fuel matrix, implying hardly any chemical interactions between these adjacent materials materials (Sections 3.7 and 3.8 in Johnson et al. 2023).

Tab. 3-1: Cont.

Argument	Evidence
Waste matrix for RP-HLW – claim: The glass matrix containing the RP-HLW provides a chemical environment where most radionuclides are immobilised and are only very slowly released.	
The slow release is attributed to the glass composition employed for the conditioning of RP-HLW.	The extensive miscibility of SiO_2 and B_2O_3 provides a flexible structure for the glass which can accommodate a large amount and variety of network modifiers, including most considered dose-relevant actinides and fission products. This results in a homogeneous distribution of the radionuclides (Sections 2.3 and 2.4 in NAB 23-09, Curti 2022).
	Once water is in contact with the glass, a protective surface layer of gel is formed at the glass – water interface, which can act as a powerful diffusion barrier for the glass. This gel layer is regarded as the main corrosion-rate limiting factor in the long term (Section 3.3 in Curti 2022).
	According to numerous experimental studies, glass dissolution rates are relatively low (derived glass dissolution rates for the MW and SON68 for safety assessment calculations (reference rates: 1.0×10^{-3} and 1.5×10^{-3} $g \cdot m^{-2} \cdot d^{-1}$; see Table 7-1 for all rates in Curti 2022).
Waste matrix for RP-HLW – claim: The stainless-steel flask containing the RP-HLW is compatible with the glass, the canister and the bentonite porewater.	
Chemical interactions between these materials are limited due to their low degradation rates.	Corrosion studies indicate that corrosion rates of stainless steel and metal are very low within a bentonite porewater environment (NAB 23-22, Diomidis et al. 2023).

3.1.2 Spent fuel assemblies

SF comprises sintered fuel pellets consisting of uranium oxide (UO_2(s)) with only a small fraction of other elements (UO_2 fuel). There are also mixed oxide fuel types in the Swiss reactors which are enriched in plutonium (MOX fuel). The fuel pellets are stacked and packed into Zircaloy hulls (Fig. 3-1) that are filled with an inert gas. Several rods are then bundled to an SF assembly.

During irradiation in a nuclear reactor, the temperature within the UO_2 pellets reaches 1,000 – 1,500 °C in the pellet centre and about 400 °C at the pellet boundary. As a result of this thermal gradient, elements representing a fraction of the radionuclide inventory produced in the UO_2 matrix are segregated to grain boundaries, to cracks in the fuel and to the gap between the fuel and the cladding (Fig. 3-1). These elements are the first to be released as part of the instant release fraction (IRF, see below). During irradiation, the Zircaloy cladding itself is activated and can suffer from embrittlement.

After interim storage and cooling, the SF is encapsulated in disposal canisters. When, after thousands of years in the repository, the disposal canisters are breached due to a combination of stress and corrosion, the Zircaloy cladding, which has a very low corrosion rate, prevents water coming in contact with the spent fuel pellets for a period of time. It is to be noted that, for safety assessment calculations, no credit is taken for the intactness of the Zircaloy cladding, as a small fraction of the fuel rods could have suffered from embrittlement in the reactor or during interim storage.

As water gets into contact with the SF matrix, a relatively rapid release of some dose-relevant volatile radionuclides (^{129}I, ^{14}C, ^{36}Cl, ^{135}Cs) occurs. In dose calculation models, this relatively rapid release is treated as instantaneous, and the radionuclides that are released are termed the IRF. The IRF results in a sharp dose peak, even if it represents only a few per cent of the total radionuclide inventory (<3% according to NAB 23-10, Johnson et al. 2023; Fig. 3-1b). It should be noted that ^{129}I, ^{14}C, ^{36}Cl and ^{135}Cs have a high importance in safety assessment due to their relatively long half-lives and high mobility in groundwater due to their low sorption on mineral phases (NTB 24-18, Nagra 2024r).

The majority (>97%) of the radionuclide inventory resides in the uranium dioxide (UO_2) or MOX matrices. UO_2(s) and MOX dissolve in water by releasing U(IV) and Pu species and their fission products in solution. This process occurs with a certain rate, referred to a *non-oxidative dissolution* (NAB 23-10, Johnson et al. 2023). Indeed, a large amount of H_2 is generated by metal corrosion and dissolves partially in porewater, thus contributing to reducing conditions. A large number of studies on fuel dissolution and alpha-doped simulated materials have shown that dissolution of fuel is a very slow process under highly reducing conditions (see NAB 23-10, Johnson et al. 2023 and references therein).

Under repository-like conditions, SF pellets and the Zircaloy cladding are chemically and mechanically stable and compatible with the canister or the bentonite buffer. This is supported by thermodynamic calculations (see NAB 23-10, Johnson et al. 2023 and NTB 23-02 Rev. 1, Nagra 2024v).

The SF dissolution rate recommended to be used in safety assessment is based on multiple lines of argument (these arguments include that conditions in the repository ensure that the H_2 concentration will remain high). Results from experimental studies in solution purged with H_2, catalytic activation of H_2 at the surface of ε-particles, natural analogue studies etc., confirm these rates (for further details, see Section 5.7 from NAB 23-10, Johnson et al. 2023). Based on these arguments, the SF dissolution rate proposed for use in safety assessment calculations is 10^{-7} a^{-1}, with upper and lower limits of 10^{-6} a^{-1} and 10^{-8} a^{-1}, respectively, which is consistent with the congruent release of radionuclides from spent fuel being a very slow process. It should be noted that the cumulative dose of what is released from the near-field is influenced by the solubility limit of the ^{226}Ra dose curve (Fig. 3-1b), which is one of the major daughter nuclides of the radioactive decay chain of ^{238}U.

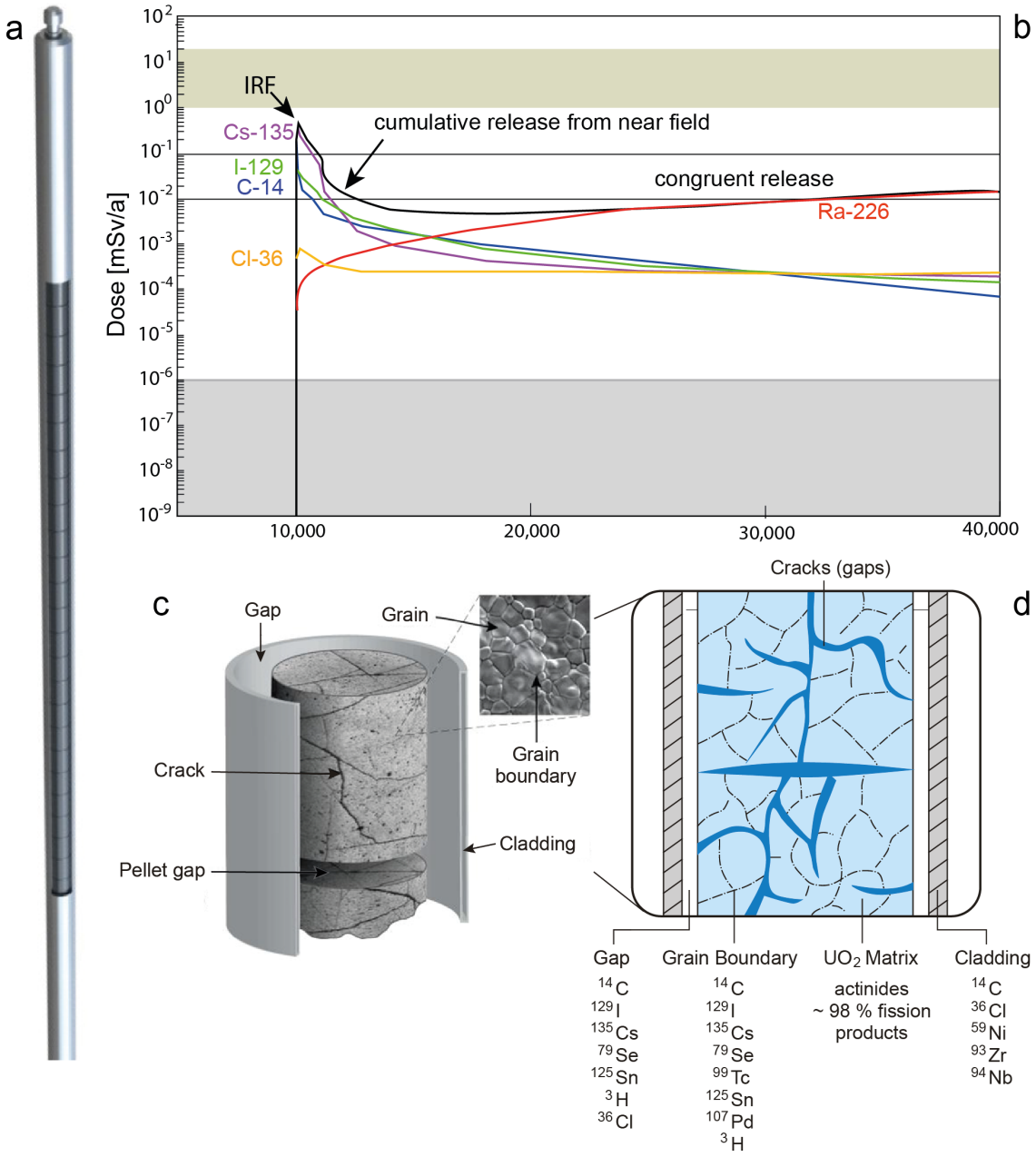

Fig. 3-1: The key elements of the SF assemblies

(a) Schematic view of a fuel rod with fuel pellets in Zircaloy cladding. IRF: Instantaneous Release Fraction. (b) Schematic dose curves for radionuclides released from the SF near-field. (c) The macro- and microstructure of a fuel pellet after its irradation. (d) Conceptual distribution of radionuclides in a spent fuel rod (from NAB 23-10, Johnson et al. 2023, redrawn after Johnson & Tait 1997).

3.1.3 Vitrified high-level waste from reprocessing (RP-HLW)

RP-HLW[6] contributes to the IMS and CMP safety functions. Research on RP-HLW has been performed for decades and has been followed by Nagra, e.g., in the scope of the NF-PRO projects (e.g., Grambow et al. 2008). Detailed information related to the current process understanding of the aqueous dissolution of RP-HLW and the corresponding dissolution rates has been synthesised in NAB 23-09 (Curti 2022). RP-HLW is the product of the treatment and reprocessing of SF, aiming at extracting fissionable U and Pu for re-use in nuclear power plants. The SF is first dissolved to form a highly radioactive liquid, and, after a complex extraction procedure, the liquid is then evaporated, calcined and mixed at high temperatures with a borosilicate glass-forming additive to produce a homogeneous molten glass. The melt is poured into stainless steel flasks of a few mm wall thickness and allowed to solidify before sealing by welding (Fig. 3-2a – b). During cooling, the glass monolith undergoes unavoidable thermal stress cracking, causing an increase of the geometric surface area, as summarised in NAB 23-09 (Curti 2022).

Switzerland's waste has been vitrified in facilities in France and the United Kingdom. Within the scope of the JSS project (Joint Japanese, Swiss, Swedish project) the basis has been set for the empirical understanding of the dissolution kinetics of the two reference borosilicate glasses which are to be disposed of in Switzerland.

The high miscibility of SiO_2 and B_2O_3 has a number of advantages in glass technology (Section 2.3 from NAB 23-09, Curti 2022). In particular, the chemical resistance of borosilicate glasses to aqueous leaching is high and its flexible structure can accommodate a large amount and variety of network modifiers, including most dose-relevant actinides and fission products.

The RP-HLW is protected by the disposal canister and by the stainless-steel flask, which is several mm thick (Fig. 3-2a). When the canister is breached, the stainless-steel flask prevents the contact of water with the RP-HLW for a certain time, until it has corroded and allows water ingress. It is to be noted that, for safety assessment calculations, no credit is taken for this function of the stainless-steel flask.

Once water contacts the glass, a thin reactive layer forms at the glass-water interface due to hydration (Fig. 3-2c), leading to ion exchange of alkalis with protons and to network dissolution (hydrolysis). The interplay of network dissolution and condensation reactions leads to the formation of a protective surface gel layer, a few micrometres in thickness, which can act as a powerful diffusion barrier. The nanostructural properties of gel layers are now regarded to be the main corrosion-rate limiting factor in the long term, as they control the rate of exchange of chemical components between aqueous solutions and corroding glass (Section 3.3 in NAB 23-09, Curti 2022). In general, a densification of the gel via polymerisation of silanol groups (recondensation) will hinder the transport of hydrolysed species and thus reduce the residual dissolution rate. The gel layer can therefore be more or less passivating, depending on leaching conditions. At an advanced stage of glass dissolution, a micrometre-thick sheet of secondary phases can accumulate on top of the gel layer via direct precipitation from the leaching solution.

[6] In 2006, the Swiss government decided to prohibit the export of SF for reprocessing and vitrification. However, the RP-HLW produced up to that date still needs to be disposed of in the HLW repository section.

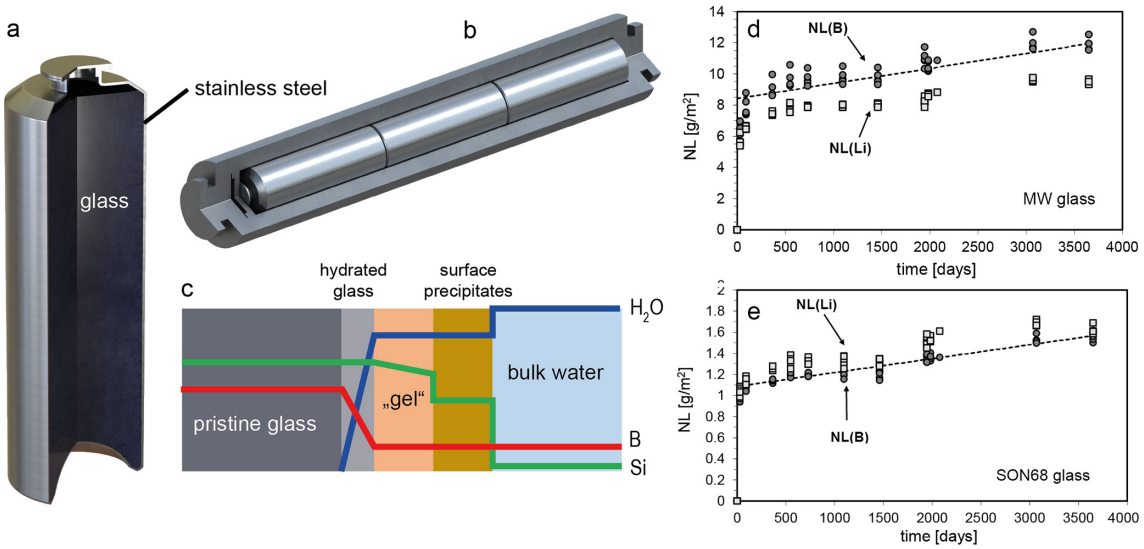

Fig. 3-2: Waste matrix for RP-HLW – arguments and evidence

a) Stainless-steel cask for RP-HLW; b) disposal canister for 3 RP-HLW casks; c) schematic cross-section through altered borosilicate glass in contact with the leaching aqueous solution, showing idealised profiles for Si, B and water concentrations. The diagrams present normalised mass loss (NL) for the MW and SON68 glasses determined from the PSI long-term experiments in initially pure water at Surface/Volume = 1,320 m^{-1} at 90 °C and free pH drift.

From NAB 23-09 (Curti 2022).

Aqueous glass dissolution rates have been derived in a large set of experimental studies on SON68 and MW glass, which have representative compositions for glasses returned to Switzerland after reprocessing in France and the UK. These glasses are subjected to varying conditions in order to study the effect of different fluids, pH, salinities, temperatures, self-irradiation, glass composition, the presence of clay and of iron, as well as its corrosion products, cementitious materials and combined environmental effects (Chapter 4 in NAB 23-09, Curti 2022).

Based on a review by Curti (2022), representative and also very conservative (pessimistic case) glass dissolution rates for the MW and SON68 glasses were derived for safety assessment calculations (reference rates: 1.0×10^{-3} and 1.5×10^{-3} $g \cdot m^{-2} \cdot d^{-1}$; lower bound: 2.0×10^{-5} and 1.5×10^{-4} $g \cdot m^{-2} \cdot d^{-1}$; pessimistic forward rates: 9.3×10^{-2} and 1.7×10^{-1} $g \cdot m^{-2} \cdot d^{-1}$; Section 7.3 in NAB 23-09, Curti 2022). The release of the homogeneously distributed radionuclides from the glass is therefore low for the conditions envisaged in the Swiss HLW repository section.

3.2 HLW disposal canister

3.2.1 Claims, arguments and evidence – overview

The HLW disposal canisters contribute to the CON and CMP safety functions. They must provide complete containment of radionuclides for a minimum of 1,000 years after emplacement (ENSI Guideline G03, ENSI 2023). For the purpose of safety and performance assessment calculations, an HLW disposal canister lifetime of at least 10,000 years is anticipated (NTB 24-20, Nagra 2024d). An overview of the claims, arguments and evidence associated with the canister performance is given in Tab. 3-2.

Tab. 3-2: Performance of the canister: overview of arguments and evidence for each claim

Argument	Evidence
Canister – claim: The canister provides complete containment of radionuclides for at least the early post-closure phase, when the canister near-field is exposed to distinct thermal and hydraulic disequilibrium conditions.	
The canister is designed to ensure mechanical integrity for at least 1,000 years even under the assumption of unfavourable corrosion rates, material degradation and external state conditions (e.g., total stress, temperature and pore pressure).	The evolution of canister wall thickness and relevant canister material properties (e.g., fracture toughness) are calculated based on unfavourable corrosion rates (Table 4-1 in NTB 24-20, Nagra 2024d).
	Model-supported analyses demonstrate that stresses in the canister wall, lid, base and weld region (including the possibility of undetected defects) will not give rise to premature structural failure causing breach of containment (Chapter 5 in NTB 24-20, (Nagra 2024d).
Manufacturing, welding, heat treatment, inspection and handling procedures can be tailored to minimise undetected defects and residual stresses.	The inspection procedures that will be employed ensure that any flaws remaining in the canister after manufacturing and welding are smaller than the critical crack length by a suitable margin. Post-weld heat treatment is employed to reduce residual stresses in the weld region (Chapter 5 in NTB 24-20, (Nagra 2024d).
Canister – claim: The products of canister degradation (corrosion) are not detrimental to other engineered and/or geological barriers.	
The gas production rate due to corrosion is limited compared with the gas transport capacity of the rock and repository structures, such that excessive pressure build-up in the repository, which can affect the properties of the host rock, is avoided.	Dedicated long-term corrosion experiments under conditions representative of the HLW near-field registered low corrosion rates and associated hydrogen generation (Taniguchi et al. 2010, Hesketh et al. 2023 and NAB 23-22, Diomidis et al. 2023).
	Model-based assessments demonstrate that pressure build-up in the HLW near-field does not lead to mechanical failure of the engineered barriers or of the host rock (Case 3 in NTB 24-23, Nagra 2024p).

Tab. 3-2: Cont.

Argument	Evidence
Canister – claim: The products of canister degradation (corrosion) are not detrimental to other engineered and/or geological barriers *(continued)*.	
Gas generated by canister corrosion is transported through the buffer without significant reduction of its function as a hydraulic barrier.	Dedicated laboratory experiments and model-based assessments demonstrate that gas transport through granular bentonite does not impair its performance as a hydraulic barrier (Section 4.1 in NAB 24-27, Nagra 2024f, Figure 3-26 in Levasseur et al. 2021 and Marschall et al. 2024).
	Long-term gas-injection experiments on compacted granular bentonite samples did not reveal any enhancement of intrinsic permeability with time, which could be related to structural changes of the material in response to the gas flow (Sections 3.3 and 3.4 in NAB 19-16, Romero & Gonzalez-Blanco 2019).
Chemical interactions between corrosion products and the buffer do not significantly reduce its function as a hydraulic barrier.	Model-based assessments demonstrate that the extent of corrosion-bentonite interactions is limited compared with the total bentonite thickness (NTB 23-02 Rev. 1, Nagra 2024v).

The provisional design of the HLW disposal canisters, as well as their expected long-term performance, have been described in detail in NTB 24-20 (Nagra 2024d). A low-carbon steel is chosen to minimise the risk of failure from hydrogen embrittlement in the presence of a tensile stress while maintaining an adequate uniform corrosion performance of the canister. The provisional disposal canisters for SF can accommodate either 4 fuel assemblies (FAs) from pressurised water reactors (PWRs) or 12 FAs from boiling water reactors (BWRs). The two SF canister variants (SF-PWR and SF-BWR) share identical designs except for the shape of the inner basket that holds the FAs. Each basket type is designed according to the dimensions of the respective FA type. RP-HLW disposal canisters are currently designed to hold three RP-HLW flasks, stacked on top of each other.

3.2.2 Assessment of long-term performance

The performance assessment of the HLW disposal canisters considers the effects of both corrosion and mechanical degradation as they are expected to happen simultaneously within the repository and could thus interact (NTB 24-20, Nagra 2024d). The processes considered in the performance assessment and prediction of the canister lifetime are:

- Anaerobic corrosion. A constant corrosion rate based on empirical measurements is employed in the estimation of the long-term corrosion behaviour of the canister. Indeed, since the corrosion rate generally continues to decrease with time over extended periods (Hesketh et al. 2023), it can be argued that the use of a corrosion rate determined from an experiment of finite duration is conservative as the long-term rate would be expected to be lower. The long-term anaerobic corrosion rate is defined as 0.7 µm/a, corresponding to the upper bound of the distribution of long-term empirical rates based on comprehensive laboratory and in-situ experiments on steel corrosion under repository-relevant conditions and reviewed by Diomidis et al. (2023, NAB 23-22). Based on this rate, 7 mm of wall loss are expected after 10,000 years of disposal (Fig. 3-3).
- Hydrogen-induced cracking. Hydrogen is generated at the external surface of carbon steel canisters as a product of anaerobic corrosion. Hydrogen will begin to accumulate both within the steel itself and inside the canister as atomic H diffuses through the canister wall and desorbs as H_2 on the inner surface of the canister wall (NTB 09-04, Turnbull 2009). The absorption of hydrogen into the low-strength carbon-steel matrix structure can be responsible for a reduction in tensile ductility and fracture toughness (Xu & Rana 2008, Lam et al. 2009, Xu 2012, Matsunaga et al. 2015), while the susceptibility of carbon steel to hydrogen-induced cracking increases with strength. Hydrogen-induced cracking is included in the assessment of the canister integrity through the specification of a reduced fracture toughness (K_{IH}) due to the absorption of H_2 by the canister material during anaerobic corrosion. The value of K_{IH} for low strength carbon steel parent materials is given by the minimum value of 55 MPa$\sqrt{m}$ for $P_{H2} \sim 11$ MPa. This value is considered conservative primarily because it has been determined at room temperature, and fracture toughness increases with temperature (Turnbull 2009).
- Radiolysis effects. They are implicitly included in the assessment, although the empirical evidence shows no significant effect on the corrosion rate of carbon steel in compacted bentonite for the maximum dose rate of 0.2 Gy/h at the outer surface of the canister.

The corrosion and mechanical processes excluded from consideration in the performance assessment of the HLW disposal canisters and not accounted for in the canister lifetime prediction are:

- Dry air oxidation because the extent of wall loss is insignificant.
- Aqueous corrosion due to the initially trapped O_2 primarily because evidence indicates that the O_2 will be consumed by other processes prior to the wetting of the canister surface. Even for the unrealistic assumption that 100% of the initial O_2 inventory resulted in uniform corrosion, the extent of wall loss would still be insignificant.
- Localised corrosion as it is not expected to occur since the initially trapped O_2 is expected to be consumed prior to wetting of the canister surface. Even if localised corrosion does initiate, evidence suggests that it will evolve into relatively uniform corrosion before the wall thickness has been reduced significantly.
- Stress corrosion cracking because of the absence of a suitable chemical environment in the repository and the absence of the mechanical loading necessary to sustain crack growth.
- Microbial induced corrosion because of the inhibiting effect of compacted bentonite on microbial activity. Microbial activity in the EDZ and undisturbed OPA can produce aggressive metabolic by-products such as sulphide, but the flux of corrosive species to the canister is predicted to be much lower than the corresponding rate of anaerobic corrosion due to the reduction of H_2O (see NTB 16-05, NTB 23-11, NAB 11-05: Leupin et al. 2016, Guillemot et al. 2023, Stroes-Gascoyne 2011).

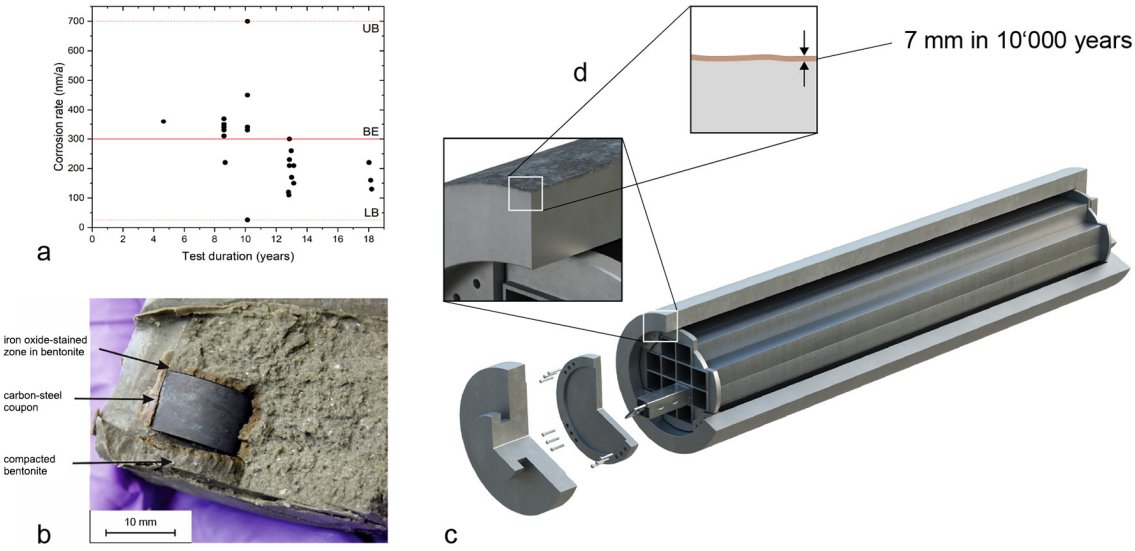

Fig. 3-3: Canister lifetime of at least 1,000 years ensured by appropriate design even under the assumption of unfavourable corrosion rates

(a) laboratory measurements of steel corrosion rates in anaerobic bentonite saturated with artificial OPA porewater as part of Nagra's RD&D programme (NAB 20-10, Diomidis & Reddy 2022). (b) in-situ experiments at the Mont Terri underground research laboratory confirm the low corrosion rates (Hesketh et al. 2023). (c) and (d) SF-BWR canister design (NTB 24-20, Nagra 2024d).

3.2.3 Confidence in predicting disposal canister lifetime

Building confidence in the prediction of canister lifetimes over long timescales is supported by:

- Evidence from in-situ experiments that closely simulate the repository environment. For example, the FE-G experiment at Mont Terri has provided information about the initial aerobic transient period and, in particular, evidence that the initially trapped atmospheric O_2 is consumed within a matter of days or weeks following backfilling (Giroud et al. 2018, King & Briggs 2024). Furthermore, the results from the iron corrosion experiment at Mont Terri (IC-A) (Reddy et al. 2021) have been running for a period of >9 years and directly contribute to the best estimate as well as the upper and lower bounds for the corrosion rates defined by NAB 23-22 (Diomidis et al. 2023).
- Evidence from archaeological analogues dating from periods that may, in some cases, exceed the required lifetimes of the canisters. The evidence from analogue studies is primarily used to build confidence in the long-term predictions by supporting the distribution of anaerobic corrosion rates and the argument that corrosion is generally uniform in nature. As an example, a comparison of the time-dependence of the depth of corrosion from laboratory experiments and iron objects from a 1,500-years-old analogue site in Japan shows an equivalent corrosion rate of 0.3 – 2.0 µm/a after 10,000 years (Yoshikawa et al. 2008).
- The use of complementary models for predicting the rate and extent of different corrosion processes to which the canister could be exposed. The aim is to demonstrate that both the models themselves and the predictions made using the models are robust, for instance in estimating the flux of sulphide and the resulting extent of canister corrosion, or for the prediction of hydrogen induced cracking.
- The demonstration of a sound mechanistic understanding of the corrosion and mechanical degradation processes to which the canisters will be subjected is useful for justifying long-term model predictions and especially supporting the exclusion of various corrosion processes by the development of mechanistically-based reasoned arguments and conceptual or abstracted PA models (King et al. 2024).

3.3 Bentonite buffer / HLW near-field

3.3.1 Claims, arguments and evidence – overview

The HLW near-field represents an efficient transport barrier for dissolved radionuclides (IMS safety function) and provides a chemically and mechanically stable environment for the HLW canisters (CMP safety function). According to the current design, in addition to the HLW itself and the disposal canister, the HLW near-field encompasses the pedestal for the canister, made of bentonite blocks, and granular bentonite, which fills the gap between canister and lining (see Fig. 3-4). In PA, the lining and the EDZ around the HLW emplacement drift are also treated as part of the HLW near-field, representing a separate assessment object (see Tab. 3-3). The reason for this is that the EDZ and the lining primarily affect the safety functions of the HLW near-field and not those of the geological barriers.

An overview of the claims made for this barrier, together with the corresponding lines of argument and evidence, is given in Tab. 3-3. Complementary discussions of arguments and evidence by assessment object are given in Sections 3.3.2 and 3.3.3.

Tab. 3-3: Performance of the bentonite buffer: overview of arguments and evidence for each claim

Argument	Evidence
Bentonite buffer / HLW near-field – claim: Radionuclides will be retained in the bentonite, limiting the release into the host rock over the entire period for assessment.	
The high clay content of the bentonite promotes the retention of the radionuclides by sorption once released by the canister.	Experimental studies have unequivocally shown that compacted bentonite contributes significantly to the retention of radionuclides (NTBs 19-03, 23-08, 23-06: Jenni et al. 2019, Glaus et al. 2024, Miron et al. 2024).
	Wyoming granular bentonite contains a clay content >80% (e.g., Chapter 2.1 in NTB 15-05, Seiphoori 2015).
	Dose calculations demonstrate that a bentonite buffer with a clay content >80% promotes the retention of the radionuclides by sorption once released by the canister (Figure 6-10 of NTB 24-18, Nagra 2024r).
The low hydraulic conductivity of saturated bentonite prevents advective flow.	Experimental studies have shown that an emplacement density of the bentonite buffer >1.45 g/cm^3 can be achieved by compaction, resulting in a hydraulic conductivity of the buffer below 1×10^{-11} m/s (Karnland et al. 2006).
	It has been also demonstrated that in large-scale experiments a degree of compaction of >1.45 g/cm^3 can be achieved (NTB 15-02, Nagra 2019).
Pre-existing or induced discontinuities (e.g., cracks, flow channels along grain boundaries) tend to self-seal when the bentonite is hydrated.	Comprehensive experimental evidence has been reported, demonstrating that an emplacement density of the bentonite buffer >1.45 g/cm^3 is sufficient to reduce efficiently the microporosity of the bentonite after full saturation has been reached (e.g., Seiphoori 2015, Section 3.3 in Leupin et al. 2021, Nagra 2019).
Swelling of the bentonite buffer during hydration results in a microporous environment providing an effective barrier for colloidal transport.	Hydration of bentonite results in a macroscopic swelling that reduces the average pores size. Nanoscale pore size dominate after hydration (Seiphoori 2015).
The buffer should transport corrosion gases without significant reduction of its function as a hydraulic barrier.	Gas generation rates as a result of corrosion of steel canisters are slow enough to allow the gas to diffuse through the bentonite buffer without causing irreversible damage (NAB 23-22, Diomidis et al. 2023, Leupin et al. 2021).
(In a dry state) the bentonite can accommodate elevated temperatures up to 150 °C over extended periods of time without losing its radionuclide retention function.	It has been demonstrated that thermal aging in a temperature range exceeding the range anticipated in the near-field has no impact on the safety relevant properties of the bentonite (Martikainen et al. 2024).

Tab. 3-3: Cont.

Argument	Evidence
Bentonite buffer / HLW near-field – claim: The bentonite buffer provides favourable chemical and mechanical conditions in the HLW near-field, ensuring compatibility with the other engineered and/or geological barriers.	
The emplacement density of the buffer can be designed such that the resulting swelling pressure does not impair the mechanical integrity of the host rock, and that the canister remains centred in the drift.	Large-scale experiments have shown that the bentonite buffer can be emplaced such that the canister movement is limited and the mechanical integrity of the host rock is not affected (Müller et al. 2017).
	Model-based assessments have shown that granular bentonite homogenises upon saturation sufficiently well to ensure evenly distributed beneficial properties (Bosch et al. 2023).
A solid knowledge base has been established to ensure that THMC interactions with other components of the disposal system do not lead to a significant change in, and/or loss of, buffer functions during periods of thermal and chemical disequilibrium.	The reactivity of bentonite under repository-like conditions is experimentally and thermodynamically well constrained and not relevant to safety (NTB 19-03, Jenni et al. 2019 and NTB 23-02 Rev. 1, Nagra 2024v).
	The outcome of the full-scale heater experiment FEBEX showed that the bentonite buffer fulfils its safety relevant properties after 18 years of heating (NTB 17-01, Kober et al. 2021).
Detrimental microbial impacts (e.g., “sulfide attack”) can be avoided effectively by an appropriate bentonite density.	Studies of the microbial reduction of sulphate to sulfide in bentonite indicate that the rate of this process decreases as the saturated density increases. Based on an extensive literature review and results of ongoing studies, a value for a saturated density can be defined in order to minimise the viability of microorganisms in the bentonite (NAB 11-05, Stroes-Gascoyne 2011). Bentonite dry density of 1.45 g/cm^3 is sufficient to avoid effectively detrimental microbial impacts (Masurat et al. 2010).
The buffer conducts heat sufficiently well that the waste form, canister, and buffer do not experience conditions detrimental to the performance of their safety functions.	Sufficient experimental evidence at different scales exists such that uncertainties in the temperature evolution of the near-field are not relevant to safety (Jenni et al. 2019).
	Model-based assessments (NTB 24-22 Rev. 1, Nagra 2024u, Figure 6-11a) and experimental evidence show that temperatures in the expected range do not lead to any significant mineralogical change in the bentonite (NTB 14-12, Leupin et al. 2014 and Nagra 2024v).
	Model-based assessments (NTB 24-23, NAB 24-25: Nagra 2024p, 2024m) show that temperatures do not exceed the palaeotemperature in Opalinus Clay (Figure 4-73 of NTB 24-17, Nagra 2024k).
	Large-scale experiments such as FE show that the temperatures are far below the values that would be detrimental to the canister or waste (Müller et al. 2017).

Tab. 3-3: Cont.

Argument	Evidence
Lining and EDZ – claim: The lining and the EDZ around the HLW emplacement drifts do not represent a significant transport pathway for dissolved radionuclides.	
EDZ fractures in the Opalinus Clay exhibit an excellent self-sealing capacity once the near-field saturates.	Extensive experimental evidence has been gained at Mont Terri (Section 5.3.2 in NTB 14-02 Dossier IV, (Nagra 2014).
	Model-based evidence has been acquired concerning the extent of the EDZ and on EDZ-related permeability enhancement of the rock adjacent to the tunnel wall (NTB 24-02 Dossier IV: Nagra 2014, NAB 18-12: Geomechanica Inc., Toronto 2018 and NAB 18-17: Alcolea 2018).
Repository design prevents significant axial porewater flow along the EDZ and lining.	Model-based evidence exists indicating that the accumulation of corrosion gases in the HLW near-field will not give rise to significant porewater flow along the EDZ and lining (e.g., case TSD 11 in NAB 24-25, (Nagra 2024m).
The choice of the excavation and lining method allows the radial extent of the EDZ to be limited.	Model-based optimisation of tunnel support has been carried out (NAB 23-08 Bd. 8, Nagra 2023c).
Lining and EDZ – claim: The lining and the EDZ around the HLW emplacement drifts do not impair the chemical and mechanical integrity of the other components of the barrier system.	
The HLW near-field was designed such that chemical interactions of the lining with the bentonite do not significantly impair the efficiency of the bentonite buffer as a transport barrier for dissolved radionuclides.	Experimental evidence on chemical interaction between bentonite and cement as well as between cement and OPA have demonstrated that the extent of the chemical interaction is limited to a few mm over 10 years (NAB 22-47: Mäder & Wersin 2023, Bernard et al. 2020, Yokoyama et al. 2021, NAB 22-34: Prasianakis et al. 2022 and NTB 23-02 Rev. 1: Nagra 2024v).
	Reactive transport models have indicated that the extent of chemical interaction between the lining and the bentonite / host rock is limited (NAB 23-33: Kosakowski 2023, Nagra 2024v).
The existence of an EDZ around the HLW emplacement drifts reduces the loads on the lining eventually limiting mechanical loads on the canister (in case of late-time failure of the lining).	Model-based evidence from various sources confirms the favourable impact of stress redistribution on canister loads (Nagra 2023c, 2014, Geomechanica Inc., Toronto 2018).
The evolution of the EDZ around the backfilled HLW drifts associated with the loss of strength of the lining is limited due to the swelling pressure of the bentonite.	Experimental evidence has been gained at tunnel scale, confirming the recompaction of the EDZ in response to radial stresses (Section 5.3.2 in NTB 14-02 Dossier IV, Nagra 2014)
	Model-based assessments confirm the support function of the bentonite in the backfilled HLW drifts (NAB 18-12, Geomechanica Inc., Toronto 2018).

Tab. 3-3: Cont.

Argument	Evidence
Lining and EDZ – claim: The lining and the EDZ around the HLW emplacement drifts do not impair the chemical and mechanical integrity of the other components of the barrier system *(continued)*.	
The accumulation of corrosion gases in the void space of the lining and the EDZ reduces gas pressure build-up in the HLW near-field as a whole.	Model-based assessments have been carried out (NAB 24-24, Nagra 2024w and NTB 24-23, Nagra 2024p), indicating an increased porosity of the EDZ (see also App. B.2.3).

3.3.2 Bentonite buffer

The expected performance of the bentonite buffer has been documented and discussed in e.g., NTB 19-03 (Jenni et al. 2019) and NTB 14-12 (Leupin et al. 2014). The chemical evolution of the HLW near-field and interactions between its components has been described in NTB 23-02 Rev. 1 (Nagra 2024v). According to the authors of the aforementioned studies, there is convincing evidence to suggest that bentonite meets the safety requirements outlined in Leupin et al. (2014). The PA relevant arguments that are derived from these post-closure safety requirements are listed in Tab. 3-3. Dominant phenomena and processes that impact the performance of the bentonite are documented in more detail in the following paragraphs.

Radionuclides released from breached canisters will be retained in the bentonite, limiting the release into the host rock over the entire period for assessment (IMS safety function). Due to its high suction potential, compacted and confined bentonite will saturate rapidly and swell. The swelling process is associated with a complete collapse of the macro-porosity of the bentonite in favour of a nearly impervious network of meso- and micropores, limiting transport processes to molecular diffusion (see Fig. 3-4d; e.g., NTB 15-05, Seiphoori 2015 and Bosch et al. 2023). An extensive review of the hydraulic and swelling parameter has been compiled by Dixon et al. (2023).

Bentonite acts as an efficient barrier to the transport of many radionuclides (IMS safety function). The barrier efficiency is the combined result of the diffusion properties of bentonite (NTB 23-06, Miron et al. 2024) and the radionuclides sorbing in bentonite (NTB 23-08, Glaus et al. 2024).

The bentonite buffer provides favourable environmental conditions, contributing to the longevity of the canisters (CMP safety function). The relatively rapid initial oxic corrosion rate is anticipated to decrease quickly once reducing conditions are established (NAB 23-22, Diomidis et al. 2023). Hydrogen gas from corrosion of the HLW disposal canisters will be produced over tens of thousands of years (see Section 4.4).

Hydrogen from steel corrosion may not completely dissolve and diffuse in aqueous form through the buffer and a gas phase will form around the canisters, which could then migrate through the buffer (Leupin et al. 2021). According to current understanding, however, no significant impact on the long-term integrity of clay barriers is expected after the dissipation of the gas phase (NAB 23-15, NTB 24-23: Nagra 2024g, 2024p).

The high buffering capacity and high cation exchange capacity (CEC) of the bentonite will regulate the porewater composition for an extended period. However, processes buffering the OPA and cementitious porewaters are expected to affect the swelling pressure of the bentonite locally at the interfaces as increased ionic strength in the porewater and increased Ca on the exchanger will decrease swelling pressure.

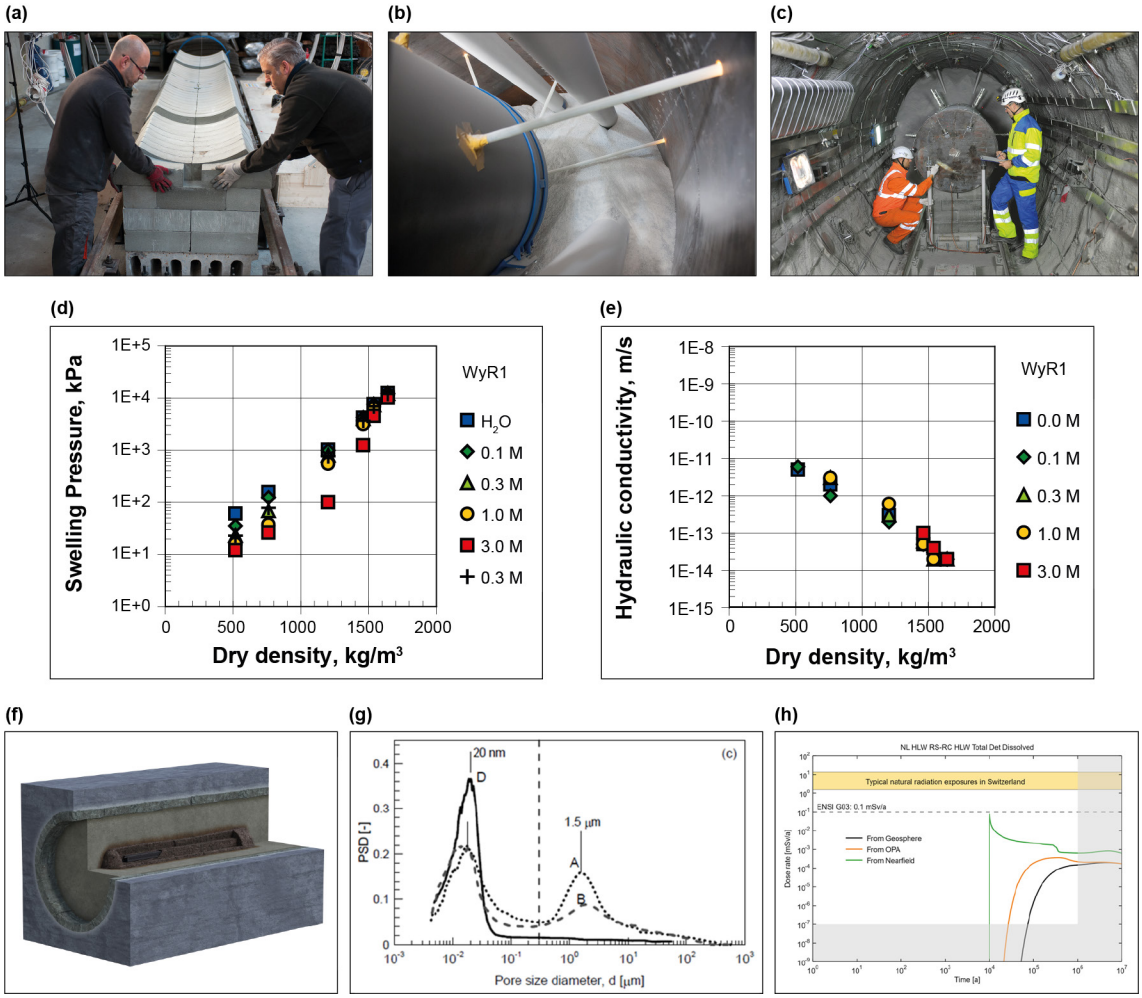

Fig. 3-4: Bentonite buffer / HLW near-field – arguments and evidence

An HLW disposal canister is placed on a pedestal made of bentonite blocks (a, c). The drift is then backfilled with granular bentonite (b). Resaturation of the near-field results in high swelling pressures (3 – 4 MPa for 1,500 g/cm see figure d) and low hydraulic conductivities (10^{-13} – 10^{-14} m/s see figure e). A sound mechanistic understanding of the microstructural evolution of the bentonite has been gained, indicating a tremendous loss of macro-porosity in the saturated state (g). The radionuclide retention capacity of the bentonite is highlighted in SA calculations (h).

In general, the differences between the OPA porewater and bentonite porewater will be relatively small (see Chapter 7 of NTB 23-02 Rev. 1, Nagra 2024v). In the outermost part of the bentonite, chemical interaction with the lining locally affects the porewater composition (NAB 23-33, Kosakowski 2023). Furthermore, there will be interactions with metal corrosion products at the inner surface of the buffer adjacent to the canister. Over time, however, once the lining has degraded, the porewater composition in the buffer will become increasingly similar to that of the Opalinus Clay due to diffusive exchange with the surrounding porewater. The precise interplay between the tunnel lining and the bentonite and the Opalinus Clay has been studied in NAB 23-33 (Kosakowski 2023) and is summarised in NTB 23-02 Rev. 1 (Nagra 2024v).

The variations in bentonite porewater composition have only a slight impact on swelling pressure, which is the primary driving force behind the closure of low-density transport pathways and the homogenisation of the entire buffer porosity. Therefore, the chemical variations mentioned above are of secondary importance.

The chemical interactions and mineral transformations at the buffer/cement interface have been calculated by Kosakowski (2023, NAB 23-33) and are summarised in NTB 23-02 Rev. 1 (Nagra 2024v), taking into account the temperature pulse released from the canister. It could be shown that, for all model variants assessed in Section 6.7.2 in NAB 23-33 (Kosakowski 2023), changes in the chemical composition of montmorillonite bentonite and the illite in the Opalinus Clay are very limited in degree and in spatial extent, especially after some limited reduction of pore space has occurred due to precipitation (NTB 23-02 Rev. 1, Nagra 2024v).

Anaerobic corrosion of the steel disposal canisters begins when mobile oxygen is depleted, and the water activity is high enough. Corrosion rates can be reduced to 1 μm/year or less with the formation of a protective corrosion layer. Fe(II) as a corrosion product is expected to diffuse into the bentonite buffer. Nagra (2024v, NTB 23-02 Rev. 1) has estimated the amount of bentonite that could be converted to Fe-silicates as a result of out-diffusion of Fe(II) from the corroding canister. According to the best estimate, less than ~3% of the bentonite is predicted to be altered during one million years (in a conservative estimate, 17% of the initial mass is altered over a one-million-year period; cf. Section 8.2.3 and Appendix A in NTB 23-02 Rev. 1, Nagra 2024v). Furthermore, there is currently no experimental evidence under realistic conditions that suggests bentonite would not fulfil its long-term requirements due to its interface with corroding steel.

The compacted saturated bentonite buffer, with its high swelling pressure and nanoporous structure, is a hostile environment for microbes; at high enough densities, all microbial activity comes to a halt. Essentially no microbial activity is expected for a well-emplaced bentonite buffer with a dry density of 1,450 kg/m^3 (and above). In the case of poor buffer emplacement, lower density areas could persist within the buffer, and microbial sulphate reduction in the buffer cannot be ruled out, which would lead to the production of sulphide and to increased corrosion of the canisters. This process, however, seems to have a limited impact on the canister lifetime, as shown by Cloet et al. (2017, NTB 17-04).

Buffer post-closure safety performance relies mostly on the hydraulic conductivity and swelling pressure of the bentonite, which are well-known to be dependent mainly on dry density and mont-morillonite content of the bentonite. The buffer will experience considerable temperature variation due to the decay heat of the spent nuclear fuel in the canister. However, this thermal load is transient, and the timescale is in the order of thousands of years. Based on the provisional design, after about 10,000 years only slightly elevated temperatures are expected in the repository section. After about 50,000 years, the temperature will return to the ambient rock temperature of ~45 – 48 °C. Based on experimental results (Martikainen et al. 2024) the initial thermal peak will not impact the safety relevant properties of the bentonite under the anticipated conditions. Even assuming hypothetical conditions of temperatures reaching up to 150 °C, (Martikainen et al. 2024) concluded that the impact on the performance of the buffer remains small.

3.3.3 Lining and EDZ

The lining and the EDZ around the HLW drifts are not assigned any safety functions of their own, but can affect the safety functions of the bentonite buffer. Their relevance to safety is discussed in the following paragraphs.

According to the current provisional design, the HLW emplacement drifts will be excavated with a tunnel boring machine. The rock support will be provided by pre-cast concrete elements (tubbings) and the void space between the lining and the EDZ of the host rock will be filled with cementitious grout (cf. Section 4.5 in NTB 23-02 Rev. 1, Nagra 2024v). The rock support of the emplacement drifts is designed to ensure mechanical stability to the drifts only during the construction and operational phase.

The choice of the excavation and lining method allows the degree of tunnel convergence to be limited (NAB 23-01 Bd. 8, Nagra 2023c) and, as a consequence, the extent of the EDZ will also be limited (NTB 14-02 Dossier IV, Nagra 2014 and NAB 18-12, Geomechanica Inc., Toronto 2018). Fracture mechanics modelling suggests that only a few decimetres of the rock zone around the HLW drift will fail in a tensile mode (see also App. B.2), where a distinct enhancement of rock permeability is expected during the period when unsaturated conditions prevail in the near-field. After resaturation of the EDZ and recovery to static formation pressure, the self-sealing capacity of the Opalinus Clay will cause a distinct reduction in the transmissivity of the EDZ fractures, and the EDZ will eventually approach an effective hydraulic conductivity that is no more than 1 – 2 orders of magnitude above the conductivity of the intact rock (NTB 14-02 Dossier IV, Nagra 2014 and NAB 18-17, Alcolea 2018).

Modelling studies have been carried out aimed at assessing the potential of the EDZ and the lining to act as transport pathways for dissolved radionuclides along the backfilled HLW drifts (NTB 24-23, NAB 24-25: Nagra 2024p, 2024m; Chapters 4 and 6 of the present report). It was demonstrated that the porewater fluxes across the HLW-V1 seals are negligible over the entire period for assessment. Even gas-induced overpressures in the HLW drifts do not give rise to significant liquid fluxes out of the HLW drifts.

Model-based assessment by reactive transport calculations has demonstrated that the chemical interaction between the lining and the bentonite / host rock is limited and only has a minor impact on the adjacent material of both barriers (see Section 3.3.2 of the present report, and, for more details, NAB 23-33, Kosakowski 2023 and Section 6.7.2 in NTB 23-02 Rev. 1, Nagra 2024v). In particular, the carbonation of the grout between the lining and the rock, which occurs within less than 1,000 years, eliminates the chemical gradient between the OPA and the grout and thus halts the progression of the alteration front (Kosakowski 2023, Nagra 2024v).

Experimental studies in URLs have further demonstrated that the extent of chemical interaction, cation exchange and mineral dissolution and reprecipitation is limited to an alteration extent of a few mm within several years, as shown e.g., in the scope of the CI experiment (Yokoyama et al. 2021, Mäder et al. 2017, Bernard et al. 2020) and in the assessment of the interaction carried out within the scope of the FEBEX project (NAB 16-18, Turrero & Cloet 2017) and other field experiment, as summarised in NAB 22-34 (Prasianakis et al. 2022), NTB 23-03 (Kosakowski et al. 2023), NTB 23-02 Rev. 1 (Nagra 2024v) and Wilson et al. (2021). In particular, the production of an interface with reduced porosity reduces the reaction kinetics and progression of alteration fronts (cf. Prasianakis et al. 2022).

3.4 Cementitious L/ILW near-field

3.4.1 Claims, arguments and evidence – overview

The current design of the L/ILW repository section (briefly described in App. A) foresees a cementitious near-field for the disposal of the L/ILW. As the emplacement caverns saturate slowly over time, the different cementitious materials will control the porewater composition in the L/ILW emplacement caverns, contributing to the development of an alkaline near-field. The generation and accumulation of gases caused by corrosion and degradation processes in the L/ILW emplacement caverns will give rise to partially saturated conditions for tens of thousands of years. The alkaline environment and the expected conditions ensure that the L/ILW near-field provides the safety functions:

- Immobilisation, retention and slow release of radionuclides; and
- Compatibility of the components of the repository system.

The main arguments and evidence to support claims related to these safety functions are discussed in the following sections, and key evidence is highlighted in Fig. 3-5. An overview of the claims, arguments and evidence associated with the performance of the cementitious L/ILW near-field is given in Tab. 3-4.

Tab. 3-4: Performance of the cementitious near-field within the L/ILW emplacement caverns: overview of arguments and evidence for each claim

Argument	Evidence
Cement-based near-field of the L/ILW repository – claim: The cement-based components of the L/ILW near-field contribute to the retention and slow release of radionuclides.	
The cement paste contains C-S-H phases which sorb radionuclides.	Thermodynamic calculations indicate that C-S-H is the major cement phase within the cement paste (Appendix A from NTB 23-03, Kosakowski et al. 2023).
	The cement sorption database and the systematically derived sorption values provide a sound foundation for dose calculations (NTB 23-07, Tits & Wieland 2023 and NTB 24-18, Nagra 2024r).
Cement-based near-field of the L/ILW repository – claim: The cement-based components of the L/ILW near-field are compatible with each other.	
The cement-based elements contribute to an alkaline near-field upon contact with water entering the caverns from the Opalinus Clay.	According to the current design, the cement-based elements primarily consist of ordinary Portland cements (OPC) with portlandite and C-S-H as major primary initial mineral phases, which contribute to an alkaline-buffered near-field (cf. Appendix A in NTB 23-03; Kosakowski et al. 2023).
	Thermodynamic calculations indicate that the cement porewaters have an alkaline pH over cement degradation stages I to III (Appendix A from Kosakowski et al. 2023, Tits & Wieland 2023).

Tab. 3-4: Cont.

Argument	Evidence
Cement-based near-field of the L/ILW repository – claim: The cement-based components of the L/ILW near-field are compatible with each other *(continued)*.	
Filling of the disposal containers with a container infill mortar ensures mechanical integrity of the waste packages in the early post-closure phase.	Highly fluid container infill mortar was developed and tested for filling the void space in the disposal containers (Section 3.5.4 in NTB 23-03, Kosakowski et al. 2023).
The backfill mortar is made of single-grain aggregates held together with a limited amount cement paste (Jacobs et al. 1994), such that the aggregates take up the mechanical stress by grain -to-grain contact (NTB 21-02, Nagra 2021c).	By design, the compressive strength of the aggregates is such that they take up the stresses expected under repository conditions (NAB 22-44, Martin et al. 2024).
The gas production rate is limited compared with the gas transport capacity of the rock and repository structures, such that excessive pressure build-up in the repository, which could otherwise affect the properties of the host rock, is avoided.	Experimental data from dedicated laboratory experiments have been reviewed in order to derive representative reference metal corrosion rates under alkaline conditions (NAB 23-22, Diomidis et al. 2023).
	Model-based analyses of pressure build-up in the L/ILW emplacement caverns constructed in a low-permeability host rock indicate that gas production is limited by the availability of water (NTB 24-23, NAB 24-25: Nagra 2024p, 2024m; see also Fig. 4-14b in this report).
The porosity of the cavern backfill mortar provides a gas storage volume and contributes to the release of gas through the sealing elements, such that excessive gas overpressures are avoided in the L/ILW emplacement caverns.	Large-scale experiments on the hydraulic conductivity and gas transport capacity of single grain mortar have been carried out and are reported in NTB 98-03, Mayer et al. 1999).
	Experimental data indicate that the intrinsic porosity of M1 mortar is in the order of 10^{-10} to 10^{-12} m^2 (Section 4.4.6 in NAB 22-44, Martin et al. 2024).
	Experiments demonstrate that the average water fillable porosity is >20 vol.% (Section 4.4.5 in NAB 22-44, Martin et al. 2024).
	Model-based analyses of pressure build-up in the L/ILW emplacement caverns confirm that sufficient pore volume is available to avoid excessive gas overpressure (NTB 24-23, NAB 24-25: Nagra 2024p, 2024m; see also Chapters 5 and 6 in this report).

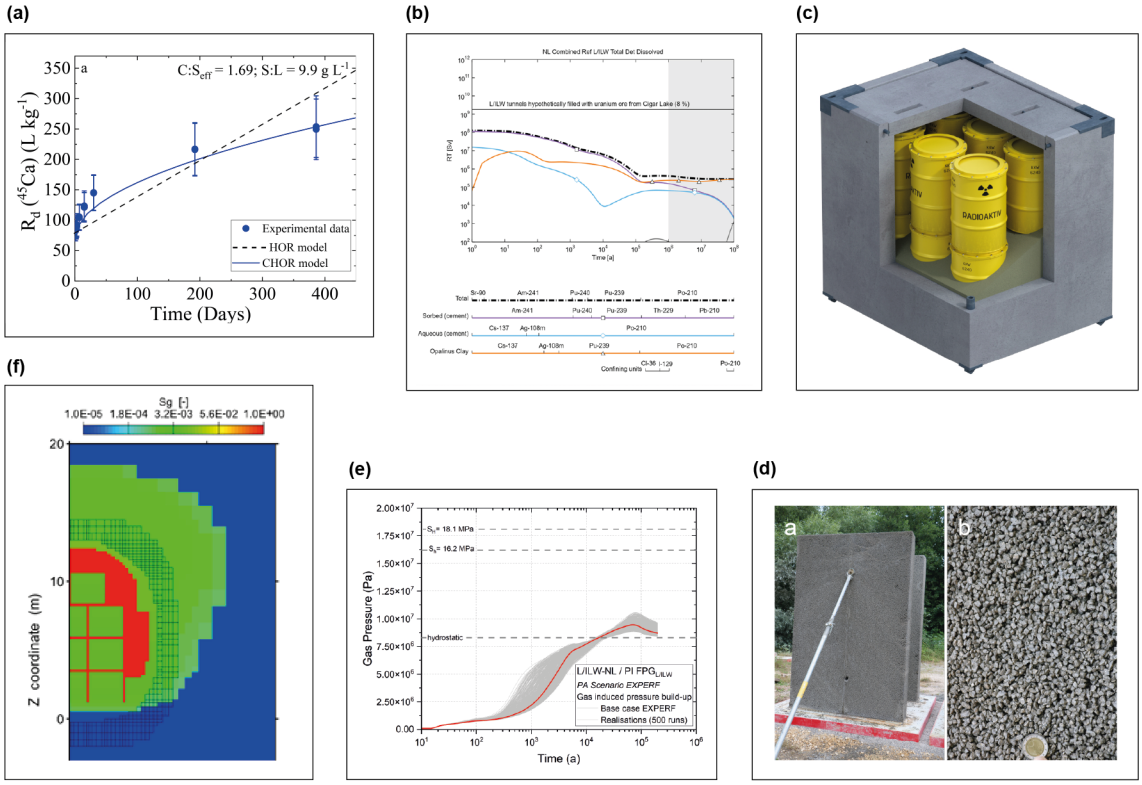

Fig. 3-5: Multiple lines of supporting evidence, confirming the performance of the L/ILW near-field

a) experimental evidence of cement sorption (NTB 23-07, Tits & Wieland 2023); b) retention of radiotoxic elements by the cement in the L/ILW near-field (NTB 24-18, Nagra 2024r); c) illustration of the LC disposal container containing the waste packages for L/ILW, with the void space being filled with the highly flowable, porous container infill mortar; d) emplacement tests of backfill mortar M1; e) TH^2 gas pressure build-up calculations, f) unsaturated gaps between the waste containers representing capillary barriers for ten thousands of years.

3.4.2 Retention of radionuclides in the cement-based near-field

Sorption of radionuclides on the cement paste contributes to the slow release of radionuclides from the L/ILW near-field. Radionuclide retention by sorption on cement minerals (Fig. 3-5a) and cement paste, has been quantified and accounted for in dose calculations (Fig. 3-5b; NTB 24-18, Nagra 2024r). To support these calculations, the cement sorption database, which is founded on decades of experimental research documented in the previous cement sorption databases, has been updated to include the latest published and PSI-inhouse results (NTB 23-07, Tits & Wieland 2023). Cement sorption values have been derived systematically using this database (Appendix D from NTB 23-07, Tits & Wieland 2023).

3.4.3 Contribution of the alkaline near-field to the compatibility of cement-based elements

According to the current provisional design, a large amount of cementitious material (mostly OPC) will be employed for the construction of the L/ILW emplacement caverns as well as for the conditioning of the waste and for the disposal containers. Cementitious material is made by mixing cement and aggregates with water, which causes an exothermic reaction, and the cement starts to harden to cement stone. Cement is a chemically metastable material and will degrade over the assessment period, and by interaction with water, will generate alkaline high-pH conditions in the near-field (see below). Cement will therefore control the chemical conditions in the near-field and, as most components are cement-based, conditions compatible for most materials are established in the long-term (see NTB 23-03, Kosakowski et al. 2023).

However, as Opalinus Clay is a low-permeability rock, water ingress and accumulation in the bottom part of the L/ILW emplacement caverns will occur slowly and takes place over several tens of thousands of years until full saturation of the upper part of the L/ILW emplacement caverns is expected eventually (cf. Section 7.2.4 in NAB 23-21, Martin et al. 2023 and NTB 24-23, Nagra 2024p). The presence of water is a prerequisite for chemical reactions such as those involved in the degradation of cement (NAB 18-05, NAB 20-11, NTB 23-03: Wieland et al. 2018, Kosakowski et al. 2020, 2023). Contact of water with cement-based material within the L/ILW emplacement caverns can lead to external concrete degradation on the top surface of the concrete walls and will lead to the release of Ca-ions and alkali elements by leaching, resulting in a highly alkaline composition of the water present within the cavern (see above). These alkaline conditions (pH > 10.5) contribute to slow steel corrosion (cf. NAB 23-22, Diomidis et al. 2023), resulting in low gas generation rates (H_2 generation by anaerobic corrosion) and thus slow gas pressure build-up in the L/ILW emplacement caverns. To some extent, high-pH conditions also limit the degradation of organic materials by abiotic or biotic processes, which generate CO_2 and CH_4. CO_2 dissolves into the cement porewater, where it interacts with the cement material, locally carbonating it (cf. Section 3.4.3 in NTB 23-03, Kosakowski et al. 2023). These reactions require water and, as water is consumed, e.g., by chemical reactions within waste packages, the chemical reactions come to an halt until new water becomes available for the continuation of the reactions (NAB 20-11, Kosakowski et al. 2020). Scarcity of water will also be a limiting factor in cement degradation and the evolution of the cement-based materials is expected to be variable and heterogeneous in both time and space (cf. Section 4.1.6 in NAB 20-11, Kosakowski et al. 2020). This refers particularly to vertical variations in the degree of cement degradation: disposal containers higher up in the cavern will come into contact with water at a much later stage. Only a continuous water supply will result in new chemical reactions. As a result, alkaline chemical conditions can be maintained for a very long time, particularly within the partial saturated part of the L/ILW emplacement caverns.

3.4.4 Provision of gas storage volume and pathways for gas release by the backfill mortar

Waste packages containing L/ILW are currently foreseen to be packed into disposal containers made of concrete, and backfilled with a flowable container infill mortar, which encases the waste packages with the L/ILW (Fig. 3-5c). This container infill mortar further ensures the mechanical integrity of the waste packages in the early post-closure phase, provides alkaline conditions such that waste packages corrode slowly and further provides connected gas storage porosity, such that the gas initially generated by the degradation of the L/ILW is stored in the waste packages and eventually released into the L/ILW emplacement cavern.

Major gas storage volume in the L/ILW cavern is provided by M1 backfill mortar (Fig. 3-5d), described in Jacobs et al. (1994) and NAB 22-44 (Martin et al. 2024). The mortar consists mainly of siliceous (Jacobs et al. 1994) or alternatively of calcareous aggregates (Martin et al. 2024) with a single aggregate grain fraction (i.e., mono-grain size fraction; e.g., 2/3 mm or 3.5/5.5 mm according to the provisional design). The cement content of the mortar is such that the cement paste, while coating the aggregates and fixing them together, preserves a large amount of spore space for gas storage – in the order of 20 vol.%, measured as water-fillable porosity. The pores themselves are large, up to mm in size, and thus easily drained. The intrinsic permeability of this mortar is high, typically $>10^{-11}$ m^2. The mortar also contributes to the mechanical integrity of the L/ILW emplacement caverns, as the grain-to-grain contact from the aggregates will take up the stresses acting on the tunnel. Emplacement tests at large-scales using various techniques have shown that the mortar can be handled with available construction equipment in such a way that a high porosity and permeability is obtained (Fig. 3-5d). Model calculations indicate that, with the porosity and permeability provided by this backfill mortar, gas overpressures in the L/ILW emplacement caverns do not impair the integrity of the host rock (Fig. 3-5e; NTB 24-23, Nagra 2024p). Furthermore, the unsaturated gaps between the L/ILW container which are filled with porous M1 mortar represent an efficient capillary barrier for ten thousands of years (Fig. 3-5f).

3.5 Closure system and backfill

3.5.1 Claims, arguments and evidence – overview

The closure system of the repository for HLW and L/ILW repository sections will include multiple individual seals, together with the backfill emplaced along the access structures and other connecting underground openings, all of them contributing to the post-closure safety of the repository. Detailed information about closure system is given in NAB 21-12 Rev. 1 (Nagra 2021d) and in NAB 23-21 (Martin et al. 2023). The provisional design for the sealing system of the combined repository, illustrated in Fig. 3-6, foresees three different types of seals and two types of backfill (NAB 21-12 Rev. 1, Nagra 2021d):

- **V1 seals**, which will be placed at the entrances to HLW emplacement drifts and L/ILW emplacement caverns. The design of the V1 seals for the SF/HLW drifts is somewhat different from that of the V1 seals for the L/ILW emplacement caverns because of the requirement for the latter to be more gas permeable. Thus, the notation, HLW-V1 and L/ILW-V1 is adopted.
- **V2 seals**, which will close off the disposal areas for L/ILW and for HLW, as well as the pilot repositories for HLW and L/ILW, after the waste has been emplaced. Like the V1 seals, the notation HLW-V2 and L/ILW-V2 is adopted.
- **V3 seals**, which will be placed in the access and ventilation shafts to seal the repository from the surface environment and protect it from external impacts, including the possibility of future human intrusion. No safety requirements are placed on components within the access shafts above the V3 seals.
- Backfill material will be emplaced in the open tunnels and facilities between these different seals. **VF1** backfill material will be emplaced between the V1 and V2 seals and **VF2** backfill material will be emplaced between the V2 and V3 seals.

The different designs of the three seals reflect the complex requirements for the performance of the closure system in terms of robustness, redundancy and diversity.

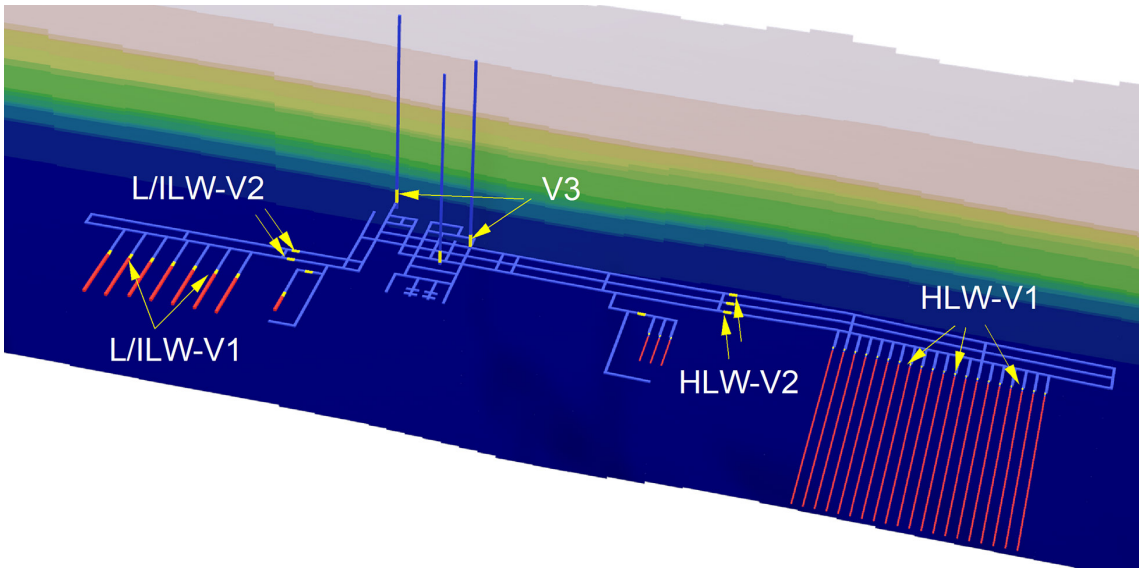

Fig. 3-6: Schematic layout of the underground repository sections for HLW and L/ILW at the Haberstal site

From NAB 24-25 (Nagra 2024m).

The seals V1, V2 and V3 are marked in yellow.

The current design of the closure system contributes to the isolation of radioactive waste from the surface of the earth (ISO safety function) and to the immobilisation, retention and slow release of radionuclides (IMS safety function), and is compatible with the other components of the multi-barrier system (CMP safety function). In PA, the HLW seals, the L/ILW seals, the V3 seals, and the VF1 / VF2 backfill are treated as separate assessment objects. An overview of the claims made for this closure system, together with the corresponding lines of argument and evidence, is given in Tab. 3-5. Complementary discussions of arguments and evidence by assessment object are given in Sections 3.5.2 to 3.5.5.

The current design of the repository foresees that each sealing element consists either of compacted bentonite (for the V1/HLW-V2 and V3 seals) or bentonite mixed with ca. 80 wt.% of sand (for the V1/L/ILW-V2 seals) (NAB 21-12 Rev. 1, Nagra 2021d). The sand provides a grain-supported matrix and, compared with bentonite alone, more readily allows the transport of gases from in the L/ILW emplacement caverns, where the greatest rates of gas production occur.

Abutments next to the sealing elements, as provisional foreseen, will hold the sealing elements in place. No post-closure safety functions are assigned to the abutments other than that they must be compatible with the surrounding materials (cf. NAB 21-12 Rev. 1, Nagra 2021d and NAB 23-21, Martin et al. 2023) and that the abutments are more gas permeable than the sealing elements (cf. Martin et al. 2023). For the safety function of compatibility, the use of low-pH, structural concrete is considered, as it reduces, but does not entirely avoid, the potential for chemical reactions that could lead to precipitation (cf. Section 6.5 in NAB 23-21, Martin et al. 2023 and NAB 21-12 Rev. 1, Nagra 2021d).

The transition layers provide a physical separation between the sealing elements and the abutments, serving to limit chemical interactions between the clay and cement materials. Cohesionless, chemically inert material, e.g., varying sand and gravel layers made of $CaCO_3$, is considered for possible use in these layers (Section 6.3 in NAB 23-21, Martin et al. 2023).

Tab. 3-5: Performance of the closure system: survey of arguments and evidence for each claim

Argument	Evidence
HLW seal – claim: The HLW-V1/V2 seals contribute to a retarded release of dissolved and volatile radionuclides.	
The HLW seals effectively prevent the transport of dissolved radionuclides along the backfilled repository structures.	Extensive experimental evidence of the effectiveness of compacted bentonite as a flow and transport barrier exists (see also Section 3.3).
	Model-based assessment demonstrates that liquid flow through the sealing elements is very slow (Fig. 4-9; see also NAB 24-25, Nagra 2024m).
HLW seal – claim: The HLW-V1/V2 seals ensure the mechanical and chemical integrity of the bentonite buffer.	
The components of the closure system are designed in such a way that they prevent buffer erosion by water ingress and water-induced bentonite mobilisation due to limited ingress of water from the operations tunnels.	By design, the backfill as well as the abutments minimise the potential for buffer erosion by water ingress. The swelling capacity of the bentonite further contributes to filling any unexpected gaps (NTB 15-05, Seiphoori 2015).
The seals are designed in such a way that they prevent patchy saturation of the bentonite buffer.	Model-based assessment shows a radial saturation of the bentonite (Appendix C in Nagra 2024m).
The sealing elements/seals are constructed mostly with materials which are in chemical equilibrium with the surrounding materials.	Model-based assessment indicates that $CaCO_3$-material in the transition layer is in geochemical equilibrium with the bentonite and alkaline fluid emanating from the cement material (NAB 14-16, Kosakowski & Smith 2014).
	Experimental studies as well as geochemical modelling indicate that, for low-pH cement (e.g., for the abutments), the extent of chemical interaction is limited to a few mm/cm in the adjacent clay material and that interfaces between cement-clay materials are not fully clogged (NAB 22-34, Prasianakis et al. 2022, NAB 23-21, Martin et al. 2023, Jenni et al. 2017, Jenni & Mäder 2021).
The HLW-V2 seal prevents interaction between the HLW and L/ILW repository sections.	Model-based assessment indicates an efficient hydraulic separation of the HLW and the L/ILW repository sections (see Section 4.2; NTB 24-23, Nagra 2024p).
L/ILW seal – claim: The L/ILW-V1/V2 seal (sand-bentonite (S/B)-mixture) contributes to a retarded release of radionuclides along the backfilled repository structures.	
The permeability of the seal is so low that transport of dissolved radionuclides across the sealing element predominately occurs by diffusion.	The permeability of fully saturated sand/bentonite mixtures has been characterised extensively (NAB 24-27, Nagra 2024f, NTB 16-07, Manca 2016, Levasseur et al. 2021 and NAB 23-40 Rev. 1, Nagra 2024h).
	Model-based assessments confirm that transport of dissolved radionuclides from the L/ILW emplacement caverns along the backfilled repository structures is insignificant (Sections 6.2 and 6.3 of this report).

Tab. 3-5: Cont.

Argument	Evidence
L/ILW seal – claim: The L/ILW-V1/V2 seals (sand-bentonite (S/B) mixture) contribute to the compatibility of the barrier components.	
The low gas entry pressure of the S/B-mixture ensures efficient gas release (even under the unlikely event of full liquid saturation during the period of gas production) such that damaging gas overpressures do not occur.	Two-phase flow parameters of S/B mixtures have been characterised extensively (NAB 24-27, Nagra 2024f, NTB 16-07, Manca 2016, Levasseur et al. 2021).
	Large-scale experiments under fully saturated conditions confirm a high gas transport capacity of S/B mixtures (NAB 23-40 Rev. 1, Nagra 2024h).
	Model-based assessments, using the current repository layout at the Haberstal site, indicate low gas overpressures in the L/ILW emplacement caverns (NTB 24-23, NAB 24-25: Nagra 2024p, 2024m; Chapters 4 and 6 of this report).
The closure system is designed such that chemical interaction between the Opalinus Clay, clay-based engineered components and cement material is limited.	Model-based assessment has shown that separating the cement-based elements from the S/B mixture by a transition layer, which contains inert material (e.g., sand comprising of $CaCO_3$) limits chemical interaction and pore clogging (NAB 14-16, Kosakowski & Smith 2014, NAB 23-21, Martin et al. 2023).
Backfill material VF1 and VF2 – claim: The VF1&VF2 backfill contributes to retarding the release of radionuclides along the tunnel system.	
The VF1 and VF2 backfill material provide gas storage volume which delays the release of volatile radionuclides through the V3 seal.	Model-based assessments, using the current repository layout at the Haberstal site, indicate insignificant release of ^{14}C through the V3 seal (Nagra 2024p, 2024m; Chapters 4 and 6 of this report).
Backfill material VF1 and VF2 – claim: The backfill VF1&VF2 contributes to the mechanical integrity of the host rock.	
The VF1 and VF2 backfill material provide gas storage volume which contributes to the avoidance of damaging gas overpressure in the repository.	Model-based assessments, using the current repository layout at the Haberstal site, reveal low gas overpressures in the L/ILW emplacement caverns (Nagra 2024p, 2024m; Chapters 4 and 6 of this report).
The VF1 and VF2 backfill material provides mechanical support, limiting the convergence of the access tunnels in the post-closure period.	The intended grain-supported backfill materials provide sufficient compressive strength.

Tab. 3-5: Cont.

Argument	Evidence
V3 shaft seal – claim: The V3 seals contribute to a retarded release of dissolved and volatile radionuclides.	
Backfilling and sealing of the shafts ensure complete isolation of the radioactive waste from the biosphere.	Empirical evidence is available from borehole sealing projects.
The tightness of the V3 shaft ensures efficient retention of volatile and dissolved radionuclides, preventing them from reaching the biosphere.	Model-based assessments, using the current repository layout at the Haberstal site, indicate insignificant release of dissolved / volatile radionuclides from the HLW and the L/ILW repository sections through the V3 seal (NTB 24-23, NAB 24-25: Nagra 2024p, 2024m; Chapters 4 and 6 of this report).

3.5.2 HLW seals

An HLW-V1 seal will be installed at the open end of each HLW emplacement drift immediately after it is backfilled (ENSI Guideline G03, ENSI 2020b). The sealing elements will be constructed with bentonite material, which is emplaced as pellets or granules (NAB 21-12 Rev. 1, Nagra 2021d). The prompt sealing of the HLW emplacement drifts ensures the rapid isolation of the radioactive waste. The HLW-V2 seals serve to close the HLW disposal area and the access to the HLW pilot repository. The functionality of the HLW-V2 seals is to further inhibit interaction between the L/ILW and the HLW repository section. The seals are constructed after all waste has been emplaced and the tunnels are backfilled with VF1.

Accidental flooding of the repository is a hypothetical scenario, but if this were to occur, it has been proven that sufficient time would be available for water retainment measures to be enacted (cf. Chapter 4 in NAB 22-41, Nagra 2022). Erosion of the bentonite by the ingress of water can be excluded; the abutments would be the first mechanical hindrance protecting the bentonite seal from erosion once water has reached the V1 seal after imbibition of the V2 seal and the VF2 and VF1 backfill. Any small gaps formed within the bentonite would be closed by the swelling and self-sealing capacity of the bentonite (Section 2.3.2 in NTB 15-05, Seiphoori 2015).

Cementitious material (such as that used in the abutments) will form a chemical gradient towards the bentonite buffer, which could result in the dissolution of clay minerals. To prevent this, the sealing elements are physically separated from the abutments by transition layers, for which $CaCO_3$ sand is a candidate material (Section 6.5 in NAB 23-21, Martin et al. 2023).

A HLW-V2 seals separate the HLW repository section from the L/ILW repository section, as required by ENSI Guideline G03 (ENSI 2020b). Model-based assessments, using the current provisional repository layout at the Haberstal site, confirm an efficient hydraulic separation of the HLW and the L/ILW repository sections (see Section 4.2).

3.5.3 L/ILW seals

The L/ILW-V1 seals are designed to ensure that gas is readily transported from the L/ILW emplacement caverns into the adjoining tunnels and to the central area at low gas pressure. To this end, the L/ILW-V1 and L/ILW-V2 (Fig. 3-7) sealing elements are composed of sand/ bentonite, with ca. 80 wt.% of sand and 20 wt.% of bentonite according to the current concept (NAB 21-12 Rev. 1, Nagra 2021d). Sand/bentonite mixtures have a low gas entry pressure (Section 3.5 in NTB 16-07, Manca 2016), permitting the release of gas from the L/ILW emplacement cavern to the VF1 backfill and through the L/ILW-V2 seal into the VF2 backfill. This equalises gas pressures within the caverns and backfill and thus prevents the build-up of potentially damaging gas overpressures (NTB 24-23, Nagra 2024p).

Extensive laboratory and in-situ experiments have been carried out since the late 1990s to characterise the S/B material (NAB 24-27, Nagra 2024f) and to demonstrate the assigned safety functions of S/B seals. In NTB 16-07 (Manca 2016) the impact of the microstructure of S/B mixtures on their permeability to water and gas was investigated (Fig. 3-7a, b, c). The in-situ GAST experiment at the Grimsel Test Site (NAB 23-15, Nagra 2024g) demonstrated successfully the construction of S/B seals with the required emplacement densities (Fig. 3-7d) and confirmed the high gas transport capacity of S/B seals at a large-scale (Fig. 3-7f). Several research projects have been launched in recent years to better understand gas invasion processes in fully saturated S/B material at the intermediate scale (Fig. 3-7e).

The impact of pore clogging on the transport and storage of gas has been extensively discussed in NAB 23-21 (Martin et al. 2023). To prevent pore clogging, a transition layer consisting of inert material such as graded $CaCO_3$ sand could be employed (Section 4.1 in NAB 21-12 Rev. 1, Nagra 2021d and Sections 6.4 and 6.5 in NAB 23-21, Martin et al. 2023) to counteract chemical interactions between the cement-based abutments and the sand/bentonite mixture (cf. Section 4.2 in NAB 14-16, Kosakowski & Smith 2014). As demonstrated in a model-based assessment (Kosakowski & Smith 2014) and as summarised in Martin et al. (2023), $CaCO_3$ is a chemically compatible material to both clay and cement, and therefore minimises the effect of chemical interaction. Even if chemical interaction between Opalinus Clay, cement, bentonite or sand/bentonite interfaces were to occur (Section 3.7 in NAB 23-21, Martin et al. 2023 and NAB 22-34, Prasianakis et al. 2022), full pore clogging will not occur, as the interlayer porosity of clays and C-S-H minerals, which permit the release of dissolved gas, will not become fully clogged (Jenni et al. 2017, Jenni & Mäder 2021).

Cation sorption on the clay minerals of the bentonite in the L/ILW-V1 seals also contributes to the retention and slow release of radionuclides from the L/ILW near-field (see NTB 23-06, Miron et al. 2024 for sorption values of cation in bentonite).

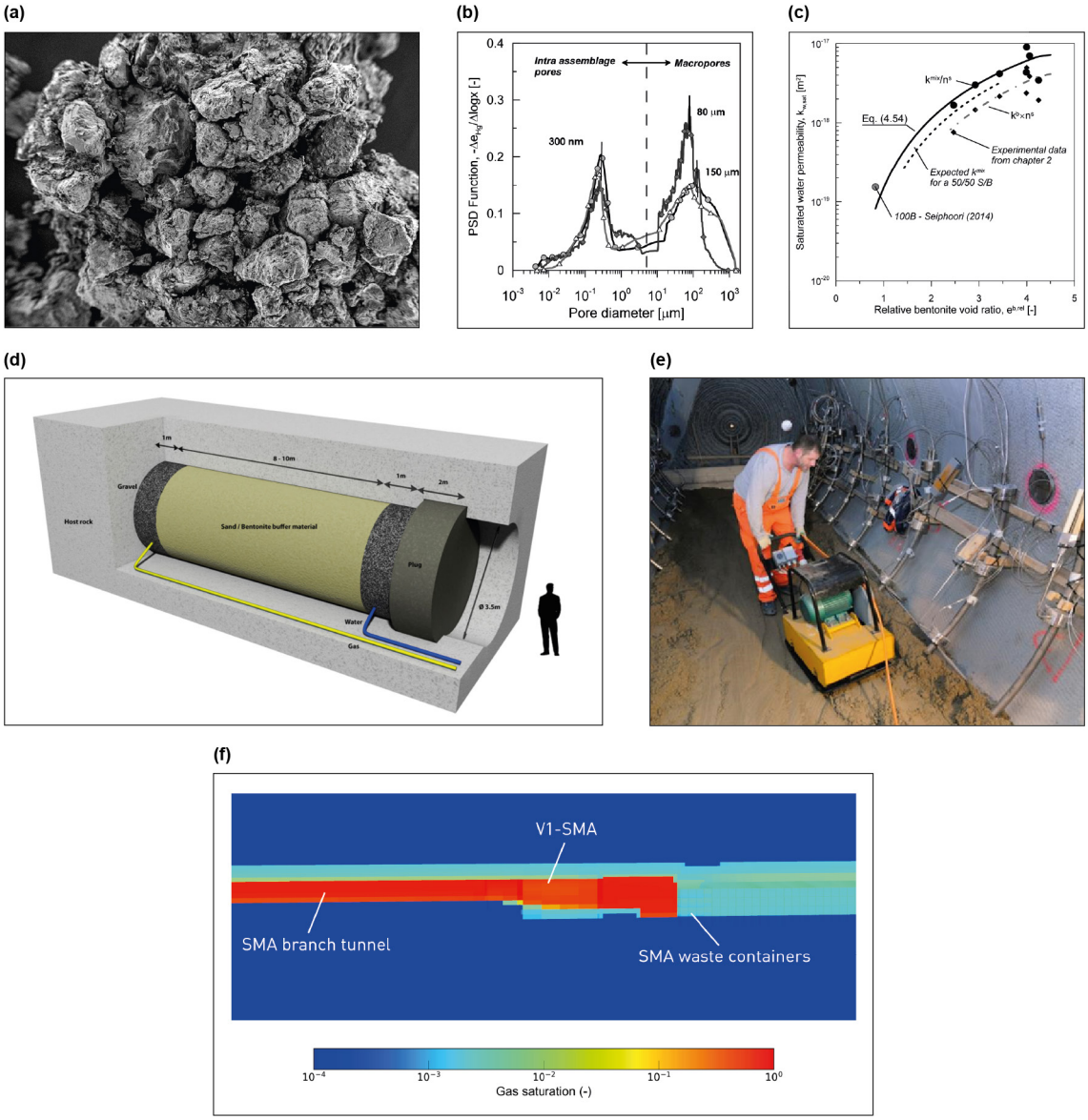

Fig. 3-7: Multiple lines of supporting evidence, confirming the performance of the L/ILW-V1 and V2 seals (S/B mixtures with ca. 80 wt.% of sand and 20 wt.% of bentonite)

(a) + (b) microstructure of the S/B mixture with grain-to-grain contacts, ensuring a significant macroposity even under high compaction; (c) the envisaged low hydraulic conductivity is achieved by compaction of the material to the target porosity; (d) GAST in-situ experiment, confirming the high gas transport capacity of S/B seals and (e) providing experimental evidence of the intended emplacement densities; (f) model-based PAs demonstrate the function of S/B seals as efficient gas transport paths.

3.5.4 VF1 and VF2 backfill material

As noted above, the VF1 and VF2 backfill (Tab. 3-5) contributes to gas transport and storage within the repository, particularly gas released via the L/ILW-V1 seals from the L/ILW emplacement caverns. The VF1 and VF2 backfill is required to maintain gas permeability, at least in the upper part, which is higher than that of the sealing elements. Thus, a lower gas entry pressure, as well as a gas-accessible porosity of around 40%, is envisaged. This implies that the emplacement density of the backfill is lower than that of the sand-bentonite sealing elements.

As discussed in Section 2.4.1 in NTB 16-07 (Manca 2016), gas can flow through larger pores in aggregated multi-structured soils (e.g., silty and clayey soils), depending on the degree of saturation and fluid wettability. Due to the density contrast between gas and water, water will accumulate under gravity in the lower part of the backfill, whereas gas will accumulate above a capillary fringe in the upper part. As indicated in Figures 7-6 and 7-7 in NAB 23-21 (Martin et al. 2023), full saturation of the upper part of the VF1 and VF2 backfill is not expected to occur within the next 100,000 years. Therefore, a continuous gas transport pathway and storage volume is provided in this upper part, which contributes to the limitation of gas pressure in the near-field.

The backfill material will contribute to the mechanical support of the openings. In particular, the grain-to-grain contact of the aggregate-skeleton within the provisionally considered aggregate-clay mixture provides load support, enhancing the macroscopic mechanical stability of the backfill (Kenney et al. 1992). The backfill will therefore take up stresses and limit tunnel convergence, contributing to the integrity of the host rock.

The clay fraction in the backfill material will contribute to the retention of radionuclides along the tunnel system. As stated above, the tunnels will resaturate only very slowly, which will limit the transport of dissolved radionuclides.

3.5.5 V3 shaft seals

The shaft seals (V3) seal the operational, ventilation and construction shafts from the biosphere and contribute to the isolation of radioactive waste. A provisional design for the V3 seals is given in NAB 21-12 Rev. 1 (Nagra 2021d). In this design, the V3 seals are located at the top of the OPA, preventing the ingress of water from the aquifers above and limiting the release of dissolved and gaseous radionuclides from the repository. Once the V3 seals are constructed, the repository is transferred to a passive state.

The design of the V3 seals is based on the following assumptions (NAB 21-12 Rev. 1, Nagra 2021d):

- The geological repository is located roughly in the middle of the OPA host rock. Approximately half the thickness of the OPA is therefore available for the construction of the V3 seals.
- Rock support elements will be dismantled before the seals are constructed to maximise the hydraulic resistance provided by the seals. Only intermittent or linear securing elements will remain in the rock to support any zones of weakness.

The current design assumes compacted bentonite material for the sealing elements. These are expected to saturate rapidly (within about 1,000 years, see NTB 24-23, Nagra 2024p) due to the high suction and the availability of water from more permeable rock formations above the repository. Once saturated, the V3 sealing elements will have a very low intrinsic permeability, which will largely prevent further water flow down the shafts into the unsaturated underground structures of the repository.

In this current design, the sealing elements are interrupted every ten metres by filter layers of fine sand, which will uniformly tend to saturate with water, thus favouring evenly distributed saturation and swelling of the adjacent bentonite material, and the breaking up of any preferential transport pathways (Section 4.3 in NAB 21-12 Rev. 1, Nagra 2021d). Each sealing element is enclosed on either side by abutments.

Because the saturated seal is, in any case, designed to have very low permeability, pore clogging of the V3 seal at the interface between the sealing elements and the overlying concrete abutment, if it were to occur, would have no detrimental impact on post-closure evolution, i.e., on repository performance and safety. As bentonite will be in direct contact with the Opalinus Clay, the compatibility of the material is assured. To prevent interactions between the concrete abutment on top with the bentonite, materials can be separated by a transition layer comprised of fine $CaCO_3$ sand (NAB 21-12 Rev. 1, Nagra 2021d).

The high clay content of the bentonite in combination with the low intrinsic permeability will contribute to the sorption and retention of diffusing radionuclides (NTB 23-06, Miron et al. 2024). According to the current model-based assessment, it will take ca. 30,000 years until gas generated by the waste will be released through the V3 seal (NTB 24-23, Nagra 2024p; see also Fig. 4-12). This corresponds to about five ^{14}C half-lives. Hence, very limited ^{14}C will be released to the biosphere (NTB 14-18, Nagra 2024r and NAB 24-07, Nagra 2024x).

3.6 Geological barrier with the containment-providing rock zone (CRZ)

3.6.1 Claims, arguments and evidence – overview

The geological barrier encompasses three complementary barrier elements (Fig. 3-8), addressed in PA as separate assessment objects, each of them contributing to one or several of the post-closure safety functions of the geological barrier (Tab. 2-2). The Opalinus Clay represents the diffusion-dominated primary transport barrier and provides long-term containment of the waste and ensures a stable geochemical and geomechanical environment. The upper confining units, ranging from the top Opalinus Clay to the base Malm aquifer and the lower confining units, ranging from the base Opalinus Clay to top Keuper aquifer serve as additional transport barriers as part of the CRZ. The regional groundwater flow systems with well-characterised hydro-chemical porewater compositions ensure stable hydrogeological conditions over long time periods. Claim by claim, key arguments and corresponding evidence have been formulated for each barrier element, building confidence in the geological barrier as a pillar of post-closure safety. An overview of the corresponding lines of argument and evidence for each claim is given in Tab. 3-6.

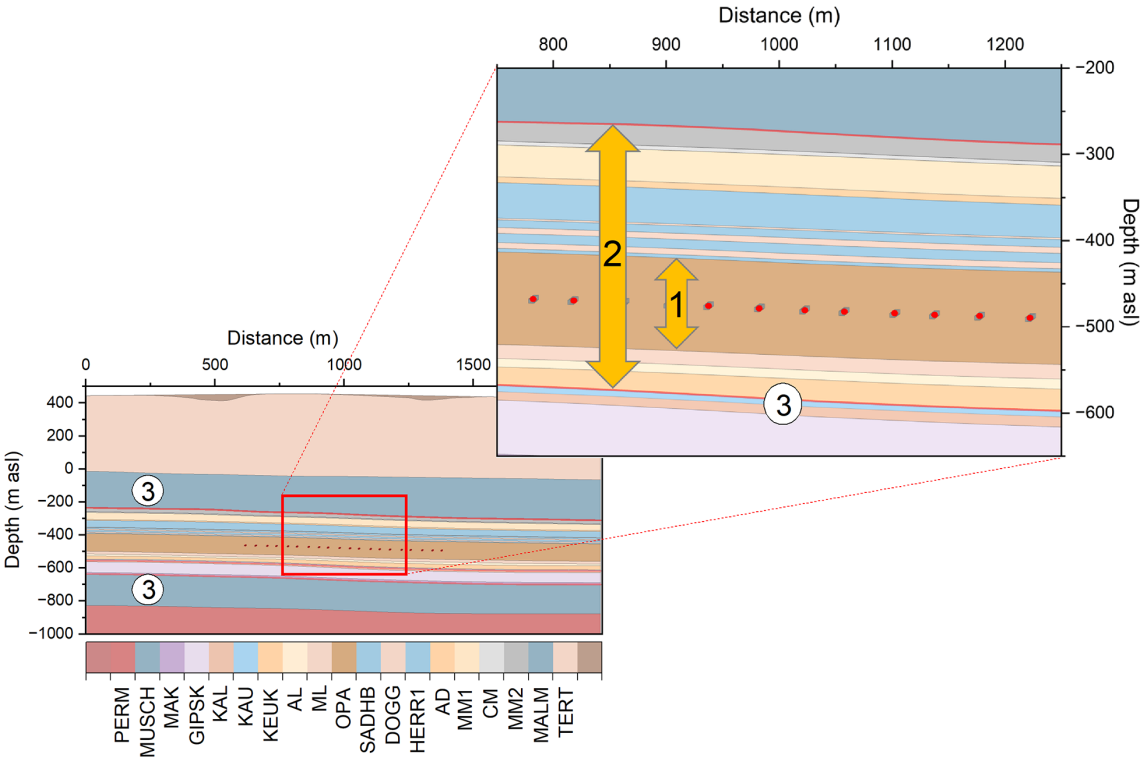

Fig. 3-8: The key elements of the geological barrier in the NL siting region

(1) The Opalinus Clay, representing the host rock sensu stricto; (2) the upper and lower confining units as part of the CRZ; (3) the regional groundwater flow systems in a favourable hydrogeological setting.

Tab. 3-6: Performance of the geological barrier, comprising the host rock and the confining units, embedded in a predictable regional groundwater flow system: survey of arguments and evidence for each claim

Argument	Evidence
Geological barrier / host rock – claim: The host rock at great depth ensures the isolation of radioactive waste from humans and the environment.	
At the repository site, the Opalinus Clay lies at a depth of more than 800 m b.g.l.	Well-established local and regional geological context (NTB 24-17, Nagra 2024k).
Geological barrier / host rock – claim: Radionuclides will be retained in the CRZ over the entire period for assessment.	
The intact Opalinus Clay represents a diffusion-dominated transport barrier with sufficient vertical and lateral extent.	Worldwide databases exist on barrier efficiency of clay-rich cap rocks (Section 5.1 in NTB 24-17, Nagra 2024k).
	Laboratory tests have been carried out on core material and in-situ packer tests in boreholes (NAB 24-10 Rev. 1, Nagra 2024j).
	Site-specific 2-D simulations of tracer flux have been made (NAB 24-25, Nagra 2024m; Sections 6.2 and 6.3 of this report).

Tab. 3-6: Cont.

Argument	Evidence
Geological barrier / host rock – claim: Radionuclides will be retained in the CRZ over the entire period for assessment *(continued)*.	
Flow and transport properties of the Opalinus Clay are well characterised and their spatial variability is low.	Local geological setting embedded in a well-established regional geological context (NTB 24-17, Nagra 2024k).
	An extensive site-specific database exists (Section 5.3 in NAB 24-10 Rev. 1, Nagra 2024j).
	Site-specific 2-D simulations of tracer flux have been made (NAB 24-25, Nagra 2024m; Section 6.3.6 in this report).
Sorption is an additional retardation mechanism, contributing to the efficiency of the host rock as a transport barrier.	Worldwide databases exist on sorption capacity of clay-rich barrier materials (NTB 23-06, Miron et al. 2024).
	Laboratory experiments on core material have been carried out as part of the deep borehole campaign (Miron et al. 2024).
The transmissivity of faults in Opalinus Clay (and clay-rich sequences of the confining units) is limited such that diffusion-dominated transport is maintained in the geological barrier under a wide range of conditions.	Laboratory tests have been carried out on core material and in-situ packer tests in boreholes (Nagra 2024k, 2024j).
	Empirical evidence exists from desk studies in claystone and shale formations worldwide (Nagra 2024k, 2024j).
	Site-specific 2-D simulations of tracer flux have been carried out (Nagra 2024m; Section 6.3.6 in this report).
The self-sealing capacity of the Opalinus Clay ensures re-sealing of activated fractures (both, newly created and existing, re-activated faults).	Worldwide databases exist on the self-sealing capacity of clay-rich barrier materials (Levasseur et al. 2021, Bock et al. 2010).
	Laboratory tests have been made on core material and in-situ packer tests in boreholes (NTB 24-17: Nagra 2024k, Fig. B-3 in NAB 19-06: Seiphoori 2019 and Marschall et al. 2024.
Geological barrier / host rock – claim: The host rock provides a stable geomechanical and geochemical environment which efficiently protects the engineered barriers over the entire period for assessment.	
The Opalinus Clay offers sufficient rock strength to allow construction of the repository structures according to the design requirements (limited EDZ; see also Section 3.3.3).	The engineering design ensures stable waste emplacement rooms for the entire operational time (NAB 23-01 Bd. 8, Nagra 2023c).
	Model-based assessment confirm that the extent of the plastic zone / damage zone around the waste emplacement rooms does not impair the barrier function of the host rock after waste emplacement (NTB 24-02 Dossier IV: Nagra 2014, NAB 18-12: Geomechanica Inc., Toronto 2018, NAB 18-17: Alcolea 2018).

Tab. 3-6: Cont.

Argument	Evidence
Geological barrier / host rock – claim: The host rock provides a stable geomechanical and geochemical environment which efficiently protects the engineered barriers over the entire period for assessment *(continued)*.	
Existing faults in the host rock are not detrimental to the engineered barrier system.	The recent deep borehole campaign revealed a low fault density in the Opalinus Clay at the Haberstal site (NTB 24-17, Nagra 2024k).
	The low transmissivity of faults in the Opalinus Clay (Nagra 2024k) prevents detrimental processes such as buffer erosion, which would require significant localised water flow rates.
Favourable porewater chemistry in terms of pH, eH, pCO_2 ensuring chemical / mechanical long-term stability of the engineered barrier systems of the HLW repository.	Generic studies on the role of porewater chemistry on repository performance (see NAB 14-09: Cloet et al. 2014, NAB 22-47: Mäder & Wersin 2023, NTB 13-03: Hofstetter et al. 2014, NTB 23-02 Rev. 1: Nagra 2024v). Modelling of site-specific porewater composition has been carried out using porewater samples from the deep borehole campaign (see Cloet et al. 2014, Mäder & Wersin 2023, Hofstetter et al. 2014, Nagra 2024v).
Metabolism of microbes is reduced to low levels.	Desk studies and experiments demonstrate a low water activity suppressing, but not completely inhibiting, microbial activity (see NTB 16-05: Leupin et al. 2016, NTB 23-11: Guillemot et al. 2023, NAB 11-05: Stroes-Gascoyne 2011).
	Desk studies and experiments show that there is only a small amount of dissolved organic carbon in the porewater available for microbes, resulting in a low diversity and suppressing, but not completely inhibiting, microbial activity (Courdouan et al. 2007, Bagnoud et al. 2015, Leupin et al. 2016).
	Desk studies have been carried out on the role of porosity in the nm range for undisturbed Opalinus Clay in ensuring limited growth and mobility of microbes (see Leupin et al. 2016).
Geological barrier / confining units – claim: The upper and lower confining units provide an additional transport barrier for dissolved radionuclides.	
The hard beds above the Opalinus Clay do not act as advective transport pathways for dissolved radionuclides.	Packer testing, geophysical logging and laboratory tests on core material have been carried out in the context of the TBO programme and did not find any indication of water conducting features related to the hard beds (NTB 24-17, NAB 24-10 Rev. 1: Nagra 2024k, 2024j).
	2-D transport simulations have demonstrated that hard beds do not significantly impair the barrier performance of the CRZ (NAB 24-25, Nagra 2024m; Section 6.3.6 in this report).

Tab. 3-6: Cont.

Argument	Evidence
Geological barrier / confining units – claim: The upper and lower confining units provide an additional transport barrier for dissolved radionuclides*(continued)*.	
The «Herrenwis Unit» does not act as an advective transport pathway for dissolved radionuclides.	Based on the results of the deep borehole campaign, it is concluded that the «Herrenwis Unit» is an isolated carbonate platform embedded in clay-mineral-rich rocks. Hydraulic conductivities are low for the lithofacies that have been tested (NTB 24-17, NAB 24-10 Rev. 1: Nagra 2024k, 2024j).
	2-D transport simulations have demonstrated that the «Herrenwis Unit» does not significantly impair the barrier performance of the CRZ (NAB 24-25, Nagra 2024m; Section 6.3.6 in this report).
The Keuper aquifer in the vicinity of the site consists of spatially limited and partly isolated local water conducting features, often with stagnant conditions.	In the NL siting region, groundwater samples from the Keuper aquifer could be retrieved from two deep boreholes out of four. The groundwater flow rates are low, with inferred mean residence times of at least several 100,000 years (Nagra 2024k).
Steeply dipping faults through the repository structures do not act as advective transport pathways for dissolved / volatile radionuclides.	Diffusion-dominated transport in the host rock and confining units is evidenced by the profiles of natural tracers despite the presence of faults in the confining units (Nagra 2024k).
	2-D transport simulations have demonstrated that a vertical fault does not reduce the barrier performance of the CRZ significantly (Nagra 2024m; Section 6.3.6 in this report).
Geological barrier / regional groundwater flow systems – Claim: Favourable groundwater flow conditions at regional scale contribute to retarded release of radionuclides into the regional aquifer systems.	
Hydraulic gradients between the regional aquifer systems are moderate, which ensures diffusion-dominated transport of radionuclides from the repository through the CRZ into the aquifers.	The database on static formation pressure was extended in the deep borehole campaign, confirming modest vertical gradients between the regional aquifers (Nagra 2024k, 2024j).
	Regional hydrogeological modelling confirms modest vertical and horizontal hydraulic gradients in the regional aquifer systems (Nagra 2024k)
	Model-based PA calculations confirm diffusion-dominated transport of dissolved radionuclides in the CRZ (Nagra 2024m; Section 6.3.6 in this report).
Stagnant porewaters in the regional aquifer systems contribute to the retarded release of radionuclides.	Groundwater samples from the Malm and Keuper aquifers indicate long residence times of natural tracers (Nagra 2024k).
	At NL, the Global Meteoric Water Line indicates a particularly large component of old porewater and lower influence by meteoric components (Nagra 2024k).

3.6.2 Host rock (Opalinus Clay)

The primary component of the geological barrier is the Opalinus Clay, representing the host rock sensu-stricto. The great burial depth ensures the isolation of radioactive waste from humans and the environment (ISO safety function). Radionuclides will be retained in the host rock and released slowly over the entire period for assessment (IMS safety function). Last, but not least, the host rock provides a stable mechanical and geochemical environment which protects efficiently the engineered barriers (CMP safety function). The supporting arguments and multiple lines of evidence with the corresponding references are presented in Tab. 3-6.

The exceptional performance of the Opalinus Clay as a transport barrier for dissolved and volatile radionuclides is due to its uniform mineralogical composition with a typical clay mineral content of more than 40% (Fig. 3-9a). Clay aggregates form the main constituents of the solid skeleton of the rock matrix at the microscopic scale, while porosity is dominated by a poorly connected network of micro- and mesopores. (Fig. 3-9b). Extensive experimental evidence has been collected in previous site investigation programmes, revealing a very low hydraulic conductivity of intact Opalinus Clay in a range between 10^{-12} and 10^{-14} m/s (Fig. 3-9c). The material retains its low permeability even in a partially or completely de-structured state. Typical examples are rock zones with significant tectonic overprint and in an extreme case, the fault gouge of fractured Opalinus Clay (Fig. 3-9d). Multiple laboratory experiments and in-situ tests have been carried out to demonstrate the self-sealing capacity of the Opalinus Clay, when fractured by repository-induced effects or by processes in the context of geological long-term evolution (Fig. 3-9e).

A comprehensive synopsis of many lines of evidence in support of the radionuclide retention capacity of the Opalinus Clay is given in the geosynthesis report (Section 5.8 from NTB 24-17, Nagra 2024k). The corresponding databases are reported in (NAB 24-10 Rev. 1, Nagra 2024j).

Further arguments and multiple lines of evidence on the role of the Opalinus Clay for the mechanical and geochemical protection of the engineered barriers are detailed in the reference reports, which are listed in Tab. 3-6. An in-depth discussion in the context of this report is omitted.

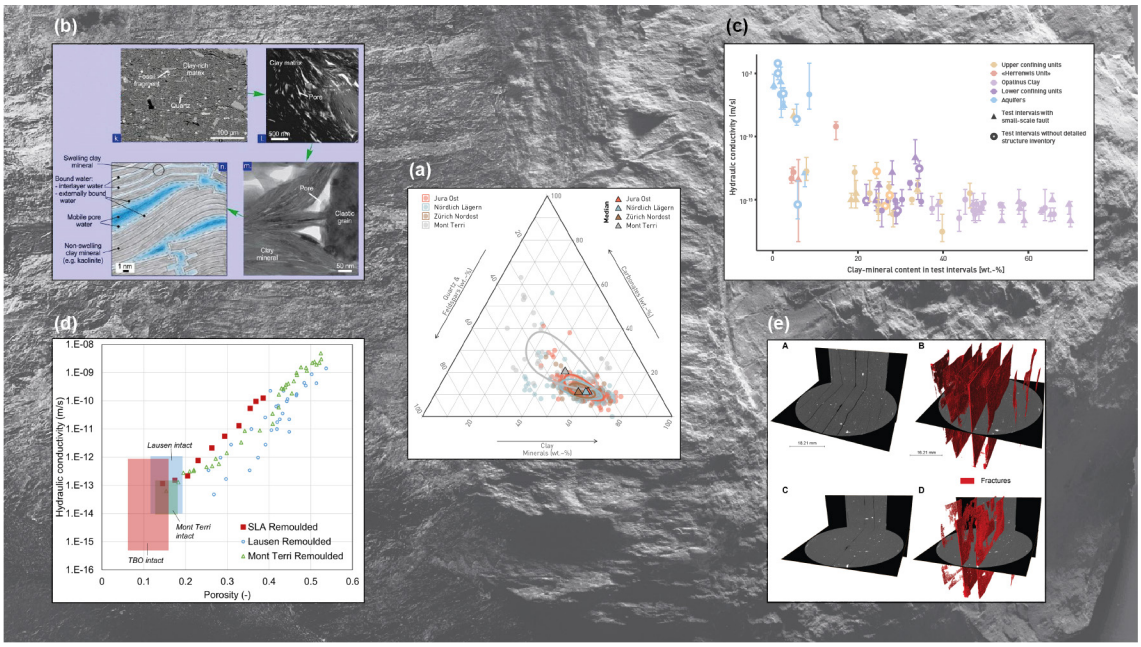

Fig. 3-9: Multiple lines of supporting evidence, confirming the exceptional performance of the Opalinus Clay as a transport barrier for dissolved and volatile radionuclides

From NTB 24-17 (Nagra 2024k) and NAB 24-10 Rev. 1 (Nagra 2024j).

(a) Mineralogical composition, (b) microfabric, (c) low hydraulic conductivities of the intact rock, (d) low conductivities of destructured and recompacted rock, (e) extensive experimental evidence on the effectiveness of self-sealing of fractured Opalinus Clay.

3.6.3 Upper and lower confining units as part of the CRZ

The upper and lower confining units, as part of the CRZ, serve as additional effective transport barriers (IMS safety function). The supporting arguments and the corresponding evidence, along with references, are presented in Tab. 3-6.

At the proposed site, the Dogger Group above Opalinus Clay refers to the clay-mineral-rich «Brauner Dogger» studied in detail during Stage 2 of the Sectoral Plan. With the recently drilled deep investigation boreholes, the hydrogeological dataset was substantially extended, notably by hydraulic packer testing, geophysical logging, core testing and by the investigations of natural tracers in the porewater. The hydraulic conductivities from the boreholes within the siting region are very low (Fig. 3-10a) and the profiles of the natural tracers in the porewater show no excursions (Fig. 3-10b).

The units directly above and below the Opalinus Clay include so-called “hard beds” which were controversially discussed in earlier project phases. Despite intensive testing, none of the deep boreholes provided evidence that these hard beds allow for larger-scale groundwater flow. Especially at the proposed site, the rock directly above the Opalinus Clay is characterised by its high clay-mineral content, assuring substantial self-sealing behaviour. PA modelling confirmed that the hard beds do not represent a distinct release pathway for dissolved radionuclides (Fig. 3-10c; see also Section 6.3.6).

The 40-m-thick, clay-mineral-poor «Herrenwis Unit» in the east of the siting region is regarded as part of the low-permeability upper confining units, as the observed hydraulic conductivities are low, and the unit is embedded in clay-mineral-rich units. Furthermore, the observed low hydraulic heads indicate that the unit is hydraulically isolated from the regional flow systems (Fig. 3-10d).

In the Zürich Nordost and Jura Ost siting regions, a continuous Keuper aquifer beneath the Opalinus Clay seems to be present across the region (formed by the stratigraphic units, called Seebi Member and likely Gansingen Member, respectively). In the Nördlich Lägern siting region, the enhanced hydraulic conductivities are limited to locally occurring sandstone channels of the so-called Ergolz Member, stratigraphically beneath the Seebi and Gansingen Members (Fig. 3-10e). The fragmentation of the water-conducting features in the Keuper formation of the NL siting region suggests that the lower confining units extend to the Muschelkalk aquifer, thus contributing substantially to the barrier function of the CRZ.

A comprehensive synopsis of many lines of evidence in support of the radionuclide retention capacity of the upper and lower confining units is given in the geosynthesis report (NTB 24-17, Nagra 2024k. The corresponding databases are reported in NAB 24-10 Rev. 1 (Nagra 2024j).

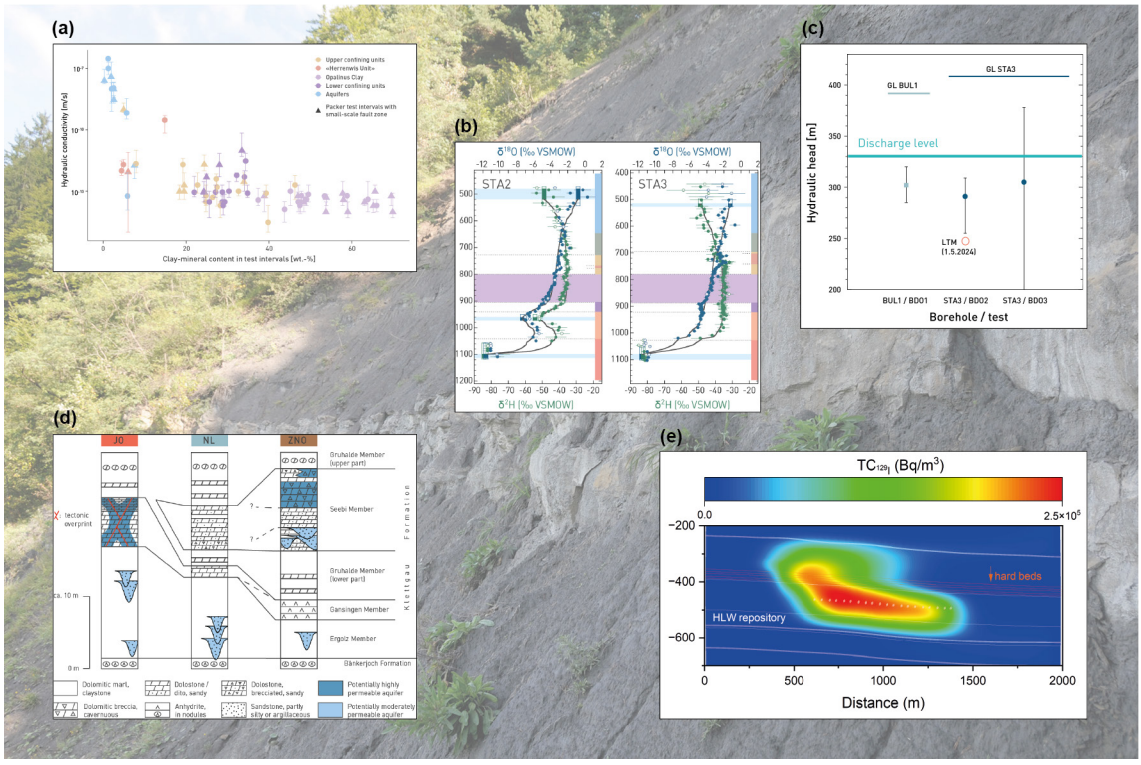

Fig. 3-10: Performance of the upper and lower confining units as an additional transport barrier for dissolved radionuclides in the NL siting region

Multiple lines of supporting evidence: (a) low hydraulic conductivities of the clay-rich sequences of the confining units; (b) measured and simulated profiles of stable water isotopes, indicating a diffusion-dominated regime in the confining units, (c) anomaleous hydraulic heads in the «Herrenwis Unit», (d), fragmented water-conducting features in the Keuper unit beneath the Opalinus Clay, (e) PA modelling of the role of the hard beds as a release path for dissolved radionuclides (from NTB 24-17, Nagra 2024k and NAB 24-10 Rev. 1, Nagra 2024j; Section 6.3.6 of this report).

3.6.4 Regional groundwater flow systems

The deep geological repository at the Haberstal site is embedded in a favourable hydrogeological setting. The regional aquifer systems represent the hydraulic boundaries of the CRZ and thus contribute to the performance of the geological barrier in terms of retention and slow release of radionuclides (IMS safety function). The supporting arguments and corresponding evidence are discussed briefly in the following paragraphs, and an overview of the key references is given in Tab. 3-6.

Geomorphology at the regional scale and a certain fragmentation of the deep groundwater flow by regional fault systems suggest that there are only minor head differences between the regional aquifer systems above and beneath the host rock. Experimental evidence has been gained in the site investigation programme for the deep borehole campaign, indicating hydraulic heads close to hydrostatic conditions in the Malm, Keuper and Muschelkalk aquifers of the NL siting region (Fig. 3-11a). Marked artesian heads <1 MPa above hydrostatic were only observed in the Benken borehole in the ZNO siting region. The small vertical pressure differences between the regional aquifers limit the vertical porewater flow through the backfilled repository structures and thus relativise the importance of advection as a transport mechanism for dissolved radionuclides (Fig. 3-11b). Several PA-Scenarios were analysed with a pressure difference of 1 MPa between the Keuper und Malm aquifers, indicating only a minor impact of advection on the barrier performance of the CRZ (see also Section 6.3.6).

Regional scale groundwater models were used to estimate lateral hydraulic gradients and to delineate the recharge and discharge areas of the regional aquifer systems (Fig. 3-11c). In the NL siting region, the recharge of the Malm aquifer mainly takes place through the thick Molasse units in the area north of the Jura Main Thrust (altitude 400 – 450 m a.s.l.) and discharge is expected in the Kaiserstuhl – Hohentengen region in the Rhine Valley north of the NL siting region (altitude around 350 m a.s.l.). The corresponding horizontal hydraulic gradient is in the order of 1%. The potential recharge areas of the Keuper aquifer are located along the Wutach valley north of the NL siting regions (altitude 650 – 700 m a.s.l.). The Keuper aquifer is discharging in the lower Aare Valley (altitude around 370 m a.s.l.). The horizontal hydraulic gradient is also in the order of 1%.

The database related to the hydrogeochemistry of groundwater in the deep aquifers (including natural tracers) was substantially expanded in the context of the deep borehole campaign, confirming the general picture of their palaeohydrogeological evolution in the siting regions. Groundwater from the Malm aquifer in NL reveals a uniform composition of stable water isotopes, showing a substantial shift to the right of the Global Meteoric Water Line. In the plots of $\delta^{18}O$ vs. $\delta^{2}H$ representing data from the STA2-1 and STA3-1 boreholes (Fig. 3-11d), the shift away from the Global Meteoric Water Line points to a particularly large component of old porewater and lower influence by meteoric components compared to the other siting regions. Further independent evidence for the hydraulic separation of the aquifer systems above and below the CRZ are gained from the chloride concentrations and ^{81}Kr model ages, indicating a highly distinct, aquifer-specific evolution of the deep groundwaters (Fig. 3-11e).

An in-depth discussion of palaeohydrogeology of the NL siting region is found in Nagra (2024k, NTB 24-17), providing extensive empirical and experimental evidence from the deep borehole programme, together with model-based interpretations of the acquired hydrochemical data. The geological synthesis confirms that the favourable hydrogeological conditions contribute to the retarded release of radionuclides into the regional aquifer systems.

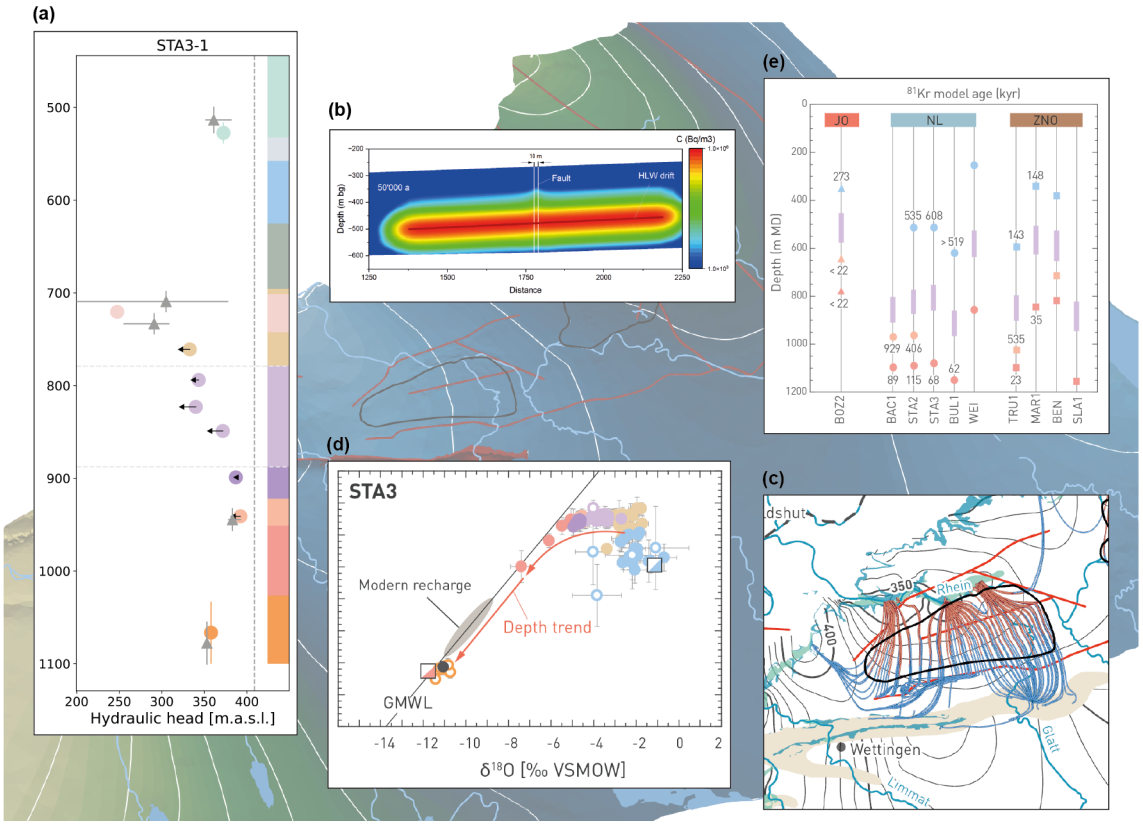

Fig. 3-11: Contributions of the regional aquifer system to the performance of the geosphere as an effective transport barrier for dissolved radionuclides in the NL siting region

Multiple lines of supporting evidence: (a) long-term monitoring in deep investigation boreholes reveals hydrostatic heads in the aquifers close to hydrostatic conditions; (b) PA modelling indicating only a minor impact of vertical hydraulic gradients on the barrier performance of the CRZ; (c) regional-scale groundwater models confirm that lateral hydraulic gradients are moderate; (d) stable water isotopes exhibit a substantial shift to the right of the Global Meteoric Water Line, indicating stagnant porewater in the Malm and Keuper aquifers; (e) measured groundwater ages provide further evidence for long residence times of groundwater in the aquifer systems (from NTB 24-17, Nagra 2024k and NAB 24-10 Rev. 1, Nagra 2024j; Section 6.3.6 of this report).

3.7 Deep underground location

3.7.1 Claims, arguments and evidence – overview

The deep underground location of the repository at the Haberstal site in a setting that is not prone to disruptive geological events and processes ensures that the radioactive waste can be safely enclosed for a very long time and will not have to be retrieved. Careful selection of the prospect disposal zone at a depth of more than 800 m b.g.l. contributes to the post-closure safety functions of isolation of radioactive waste from humans and the environment (ISO safety function), immobilisation, retention and slow release of radionuclides (IMS safety function) and long-term stability of the repository system with regard to long-term geological and climatic evolution (STB safety function).

The main arguments and evidence to support the claims related to the above-mentioned safety functions are discussed in the following sections, encompassing the assessment issues neotectonics (Section 3.7.2) and erosion and glaciation (Section 3.7.3). Key evidence is highlighted in Fig. 3-12. An overview of the claims, arguments and evidence associated with the deep underground location is given in Tab. 3-7.

Tab. 3-7: Contribution of the deep underground location to the performance of the geological barrier: survey of arguments and evidence for each claim

Argument	Evidence
Deep underground location / neotectonics – claim: Neotectonic events will not compromise the radionuclide retention capacity of the engineered and geological barriers of the repository.	
The location of the repository site in a tectonically quiet zone of Switzerland ensures that radionuclides will be retained in the CRZ over the entire period for assessment.	Geodetic surveys (Precise levelling, GNSS) and tectono-geomorphological investigations confirm that recent tectonic deformation rates in Northern Switzerland are small. Future deformation is expected to result in the reactivation of existing faults, primarily the regional fault zones (NTB 24-17, Nagra 2024k). Reactivated or new faults in the prospect repository zone are expected to be sequented and short in length and offset.
	Due to the location of the repository site in one of the seismically quietest zones of Switzerland and due to the placement of the repository zone in an area devoid seismically mappable fault, it is very unlikely that a major earthquake will occur within the period for assessment in the repository area (NAB 24-28, Nagra 2024i).
	PA calculations confirm the sufficient barrier performance of the repository system even in the extremely unlikely case that a vertical fault plane cuts through the repository area (see Section 6.3.6).

Tab. 3-7: Cont.

Argument	Evidence
Deep underground location / erosion and glaciation – claim: The deep underground location of the repository structures ensures the isolation of the radioactive waste from humans and the environment.	
Isolation of the radioactive waste is ensured by placement of the repository at a depth of more than 800 m b.g.l. in a geologically stable siting region.	Nagra's Quaternary investigation programme (refined timing of past fluvial incision during the Early Pleistocene; depth / timing of glacial overdeepenings in Northern Switzerland) extends existing databases, substantiating the knowledge about the isolation capacity of the geological barrier (NTB 24-17, Nagra 2024k).
	Model-supported quantitative estimation of future erosion with a hybrid-probabilistic approach confirms large safety margins (Nagra 2024k).
Deep underground location / erosion and glaciation – claim: The long-term geological stability of the site (wrt. erosion and glaciation) ensures that radionuclides will be retained in the CRZ over the entire period for assessment.	
The flow and transport properties of the host rock remain stable over the period for assessment with regards to erosion and glaciation.	A systematic review of the impact of mechanical unloading of the host rock on its efficiency as a transport barrier revealed subordinate changes in diffusion properties and only minor increases of hydraulic conductivity, provided that the remaining overburden is >200 m (Section 6.5.2 in Nagra 2024k).
	PA calculations confirm that the loss of overburden at the repository site does not affect significantly the barrier performance of the host rock within the period for assessment (see Section 6.3.6).
Deep underground location / erosion and glaciation – claim: The long-term geological stability of the site (wrt erosion and glaciation) ensures the mechanical integrity of the geological barrier to protect the engineered barriers over the entire period for assessment.	
The thick Malm units (and to a lesser extent the «Herrenwis Unit») protect the host rock due to their reduced erodibility.	Desk studies indicate reduced glacial erosion within more erosion-resistant rocks (e.g., Finger Lakes/USA; Nagra 2024k).
	Dedicated measurements of unconfined compressive strength and abrasion mill erosion rates confirm the capacity of the competent layers above the Opalinus Clay to slow down erosion processes (Nagra 2024k).
	Model-supported quantitative estimation of future erosion with a hybrid-probabilistic approach confirms large safety margins (Nagra 2024k).

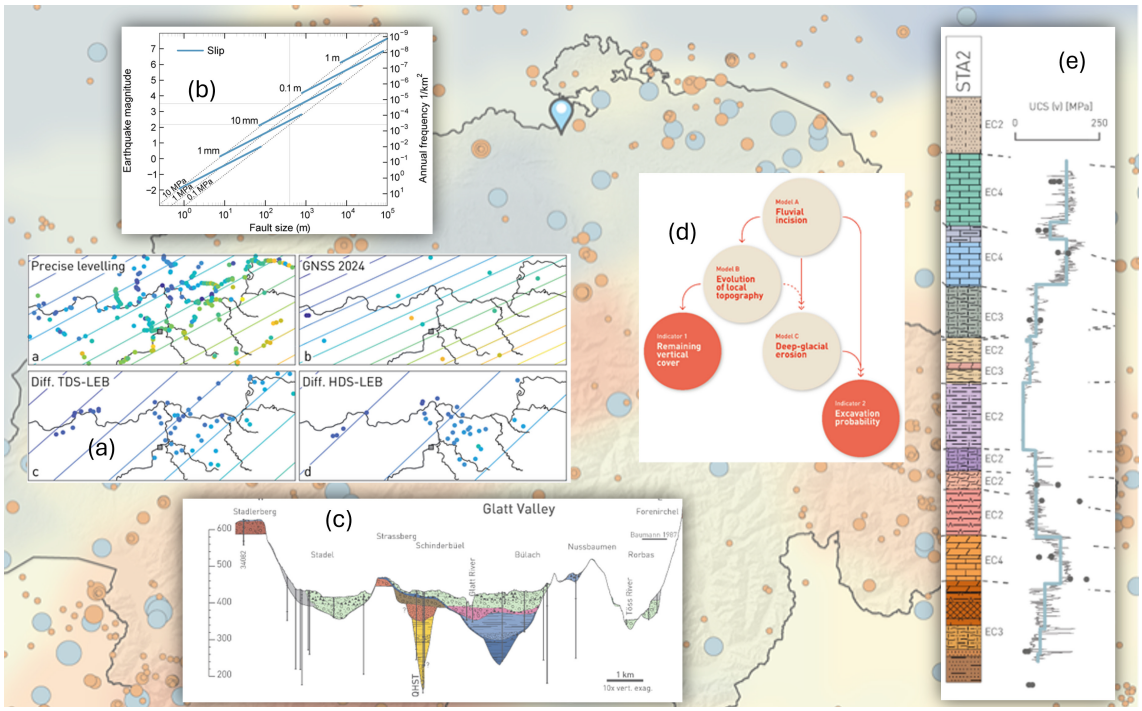

Fig. 3-12: The deep underground location of the repository at the Haberstal site provides long-term stability of the multi-barrier system regarding the long-term geological and climatic evolution (NTB 24-17, Nagra 2024k)

Multiple lines of supporting evidence: (a) geodetic surveys confirm that recent tectonic deformation rates in Northern Switzerland are small; (b) regional studies of earthquake occurrence in Switzerland and empirical correlations between earthquake magnitude and displacement from earthquakes worldwide; (c) integrated interpretation of high resolution 2-D seismic, borehole and outcrop data from the Glatt Valley with the overdeepened Strassberg and Bülach Troughs; (d) quantitative estimation of future erosion with a hybrid-probabilistic approach; (e) measurements of unconfined compressive strength and abrasion mill erosion rates as quantitative indicators of bedrock erodibility in the formations above the host rock.

3.7.2 Impacts of neotectonics on repository performance

The location of the repository site in a tectonically quiet zone of Switzerland and due to the placement of the repository zone in an area devoid seismically mappable fault ensures that neotectonic events will not compromise the radionuclide retention capacity of the engineered and geological barriers of the repository (IMS safety function). New evidence has been gained from precise levelling and permanent GNSS stations (Fig. 3-12a), which confirms that recent tectonic deformation rates in Northern Switzerland are small. This trend is anticipated to continue. Future deformation is expected to result in the reactivation of existing faults, primarily the regional fault zones. The site selection procedure foresees that any faults known from the seismic surveys are avoided (NAB 24-23 Rev. 1, Nagra 2024q). If new faults were to develop in the host rock in the future, they are expected to be segmented and small in length and offset.

Regional studies of seismic hazard show that the prospect repository zone at the Haberstal site is one of the seismically quietest zones in Switzerland (NAB 24-28, Nagra 2024i). In the context of worldwide seismicity studies, empirical scaling relationships have been developed which can be used to infer the probability of an earthquake cutting through the repository area (Fig. 3-12b). The

likelihood of such an event is extremely low, as discussed in Section 6.3.7. Even if such an extremely unlikely case were to occur, PA calculations confirm sufficient barrier performance of the repository system (see Sections 6.3.6 and 6.3.7).

3.7.3 Impacts of erosion and glaciation on repository performance

The deep underground location of the repository structures at a depth of more than 800 m b.g.l. ensures the isolation of the radioactive waste from humans and the environment (ISO safety function). Extended databases from recent field investigations provide confidence in the isolation capacity of the geological barrier (refined timing of past fluvial incision during the Pleistocene; depth / timing of glacial overdeepenings in Northern Switzerland). Examples are 2-D seismic campaigns across glacial troughs and drilling through the filling of selected and representative glacial overdeepenings as part of Nagra's Quaternary investigation programme. In the NL siting region (Fig. 3-12c), glacial overdeepenings did not exceed 185 m below the local erosion base (Figure 6-48 in NTB 24-17, Nagra 2024k). Knowledge of the timing of glacial overdeepenings and on the filling history was substantially refined by dating the sediments from the drill cores. Several newly determined ages reveal that part of the overdeepening formation occurred earlier than previously suggested, i.e. it is older than the Beringen glacial at MIS 6 dating from ~191 – 123 ka. For the older part of the filling a minimum age of 610 ± 120 ka was postulated applying the ^{4}He/U-Th dating method on porewaters (Section 6.4.1.4 of NTB 24-17, Nagra 2024k).

The assessment of future erosion was done in a robust, structured hybrid-probabilistic approach, based on available field data, laboratory tests, parameter estimation using expert elicitation and numerical modelling, to evaluate the behaviour of the erosional system in Northern Switzerland for different future scenarios (Fig. 3-12d). Glacial and non-glacial excavation probabilities of the repository within the next one million years can be considered extremely unlikely in the provisional disposal areas in all the siting regions but are about an order of magnitude lower in NL. The NL site is best protected against future erosion due to the greatest emplacement depth and other factors enhancing resilience to the main erosive processes. Within the period for assessment, it can be concluded that the isolation capacity of the geosphere in NL is unlikely to be impaired by deep erosion into the bedrock caused by future fluvial incision and deep glacial erosion.

The long-term geological stability of the site towards erosion and glaciation ensures that radionuclides will be retained in the CRZ over the entire period for assessment (IMS safety function). In this context a systematic review was subjected to the question, how the future geodynamic evolution, changing climate and morphological changes due to erosion might alter the hydrogeological and hydrogeochemical conditions (states, properties) and might ultimately affect barrier efficiency (NTB 24-17, Nagra 2024k). Of particular interest was the impact of mechanical unloading of the host rock, revealing minor changes in diffusion properties and only minor increases of hydraulic conductivity, provided that the remaining overburden is >200 m (Section 6.5 in NTB 24-17, Nagra 2024k). Complementary PA calculations confirm that the loss of overburden at the repository site does not significantly affect the barrier performance of the host rock (see Section 6.3.7). It can be concluded for the repository project at the Haberstal site that the flow and transport properties of the host rock remain stable over the period for assessment.

Last, but not the least, the long-term geological stability of the prospect repository site towards erosion and glaciation ensures the mechanical integrity of the geological barrier to protect the engineered barriers over the entire period for assessment (CMP safety function). Desk studies suggest that glacial overdeepenings tend to widen rather within the more easily erodible rocks (like the Northern Swiss Molasse assemblage) than to extend into the harder limestone units (Section 6.4.1.4 in NTB 24-17, Nagra 2024k). This is consistent with desk studies, indicating reduced glacial erosion within more erosion-resistant rocks (e.g., Finger Lakes/USA). Dedicated measurements of unconfined compressive strength and abrasion mill erosion rates were initiated

as part of the Quaternary investigation programme as quantitative indicators of bedrock erodibility in the formations above the host rock (Fig. 3-12e). The measurements confirm the capacity of the competent layers above the Opalinus Clay to slow down erosion processes.

3.8 Performance assessment by component – concluding remarks

Chapter 3 documents the arguments and evidence contributing to the systematic evaluation of repository performance at the component level. The arguments substantiate claims that relate to how the seven pillars of safety contribute to the different safety functions.

The systematic book-keeping of claims, arguments and evidence was motivated by the need for *logical, transparent assessment workflows within an auditable framework* as requested in OECD/NEA (2002). For each pillar of safety, multiple lines of argument and evidence were developed to confirm their performance with respect to their assigned safety functions. The arguments comprised empirical knowledge, project specific databases from site investigations, dedicated experiments, and a safety-oriented repository layout, based on model-supported designs. Consistency of different lines of argument and wide-ranging evidence from independent data sources provides confidence in the general safety concept, as requested in OECD/NEA (2004).

For the sake of traceability, the compilation in Chapter 3 focusses on the key arguments and evidence for the claims made for each pillar of safety to convey a clear ranking of the safety relevance of the collected evidence. In order to meet the requirement for completeness of arguments and evidence, technical documents are referenced for in-depth reading.

4 Performance of the total system

4.1 Overview

The construction and operation of the repository will cause thermal, hydraulic, geomechanical and geochemical disequilibrium in the repository near-field over an extended period of time. These perturbations of the physico-chemical state conditions are the drivers for thermal, hydraulic, mechanical and chemical (TH^2M-C)[7] interactions between the individual repository components. Changing chemical conditions can also trigger microbiological activity. Performance assessment addresses the impact of THM-C interactions on the overall performance of the repository system ("total system performance") in an auditable framework ("*Claims, Arguments and Evidence*") using model-based assessment tools and quantitative performance indicators whenever possible.

The main drivers for TH^2M-C interactions at the total system level are phenomena and processes that occur along the backfilled and sealed underground structures. Model-based analyses of the interactions between the different barrier components require large model set-ups (Fig. 4-1), including complex couplings between the phenomena and processes involved. Performance indicators are temperature, pore pressure and gas saturation in the repository near-field. The indicators are used to evaluate the performance of the multi-barrier system and to obtain an insight into the interactions between the repository components. In this context, Section 4.2 addresses the decoupling of the L/ILW and HLW repository sections as required from a regulatory perspective. Section 4.3 is dedicated to thermal interactions. Section 4.4 addresses gas-induced interactions and transport of volatile radionuclides along the backfilled underground structures. A comprehensive description of the modelling tools, material properties and simulation cases applied in this assessment is given in NAB 24-25 (Nagra 2024m) and in NTB 24-23 (Nagra 2024p).

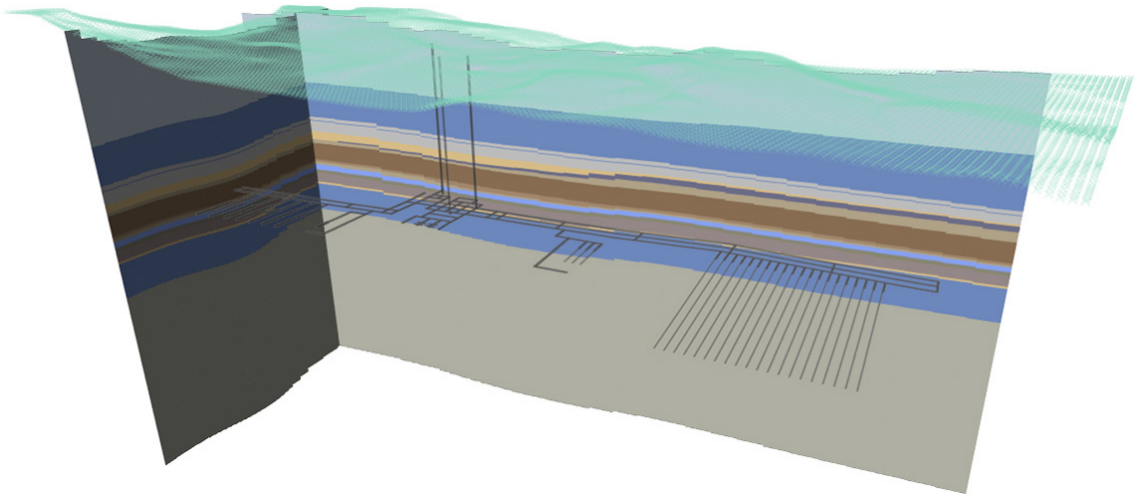

Fig. 4-1: Illustration of the 3-D repository model

From NTB 24-23 (Nagra 2024p).

The figure shows stratigraphic units or formations from Permocarbon to Tertiary and the main repository structures, including waste emplacement rooms, sealing sections and the rest of the tunnels, galleries, and shafts.

[7] The acronym TH^2M-C emphases the fact that two-phase flow conditions (H^2) prevail in the vicinity of the backfilled repository structures for an extended time period.

4.2 Interactions between HLW and L/ILW repository sections

4.2.1 Spatial separation of disposal areas for HLW and L/ILW

Nagra's *Entsorgungsprogramm* 2021 (NTB 21-01, Nagra 2021a) addresses regulatory safety requirements associated with possible interactions between different types of waste in a deep geological repository. Quantitative estimates are provided of the minimum distance between the HLW and L/ILW repository sections required to avoid detrimental interactions. The quantitative estimates, which are based on comprehensive numerical analyses, are documented in NAB 20-31 (Nagra 2021b) for a generic repository project. In addition, site-specific assessments are reported in NAB 24-25 (Nagra 2024m) and NTB 24-23 (Nagra 2024p), addressing a wide range of safety-relevant TH^2M-C interactions between the HLW and L/ILW repository sections of a combined repository for HLW and L/ILW at the proposed site.

Claims, arguments and evidence related to regulatory requirements addressing the safety-relevant TH^2M-C interactions between the HLW and the L/ILW repository sections of the combined repository are summarised in Tab. 4-1. Arguments and evidence are detailed in Section 4.2.2.

Tab. 4-1: Claims, arguments and evidence related to safety-relevant TH^2M-C interactions between the HLW and the L/ILW repository sections of the combined repository

Argument	Evidence
Claim: HLW and L/ILW repository sections are separated from each other, effectively preventing any detrimental TH^2M-C interactions between the two repository sections.	
The layout of the combined repository with a large separation distance ensures that thermal perturbations originating in the HLW repository section will not impair the performance of the L/ILW repository section (incl. thermo-mechanical effects).	Model-based evidence compiled in a generic study (NAB 20-31, Nagra 2021b) and in site-specific assessments (NAB 24-25, NTB 24-23: Nagra 2024m, 2024p; Section 4.2.2 in this report).
The design of the staggered closure system ensures an effective hydraulic decoupling of the HLW and L/ILW repository sections, when gas pressure builds up in the waste emplacement rooms (HLW and L/ILW).	
The design of the staggered closure system ensures volatile ^{14}C from the L/ILW repository section does not invade the HLW repository section.	

4.2.2 Arguments and evidence related to regulatory requirements

In accordance with the regulatory requirements, the current layout of the combined repository foresees that the HLW and L/ILW repository sections are separated from each other, effectively preventing any detrimental TH^2M-C interactions. As illustrated in Fig. 4-1, the distance between the centres of the HLW and the L/ILW repository sections is ≈ 2 km and even the V2 seals of the two repository sections are more than 1 km apart. This is significantly more than the required minimum distance of ≈ 200 m, which was derived from model-based assessments with a generic repository configuration (NAB 20-31, Nagra 2021b).

Fig. 4-2 presents contour plots of temperature distribution at repository level at different times between 100 and 100,000 years, calculated for the base case according to NTB 24-23 (Nagra 2024p). A marked local increase of temperature in the HLW repository area is observed after 500 and 1,000 years. However, the temperature disturbance caused by the heat emission from the HLW canisters never reaches the L/ILW repository, indicating that the two repository areas are thermally decoupled (see also NAB 24-25, Nagra 2024m). Complementary probabilistic assessments with thermal source terms representing the upper limit of heat output and unfavourable thermal properties of the host rock exhibit similar results, which confirm an efficient thermal separation of the two repository areas.

The hydraulic separation of the repository areas is apparent in the contour plots of pore pressure distribution and gas saturation at repository level (Fig. 4-3 and Fig. 4-4). During the first 10,000 years, resaturation of the repository structures is the dominating process, the pressure in both repository areas remains below hydrostatic and the repository structures remain unsaturated. Significant gas-induced overpressures develop after 20,000 years in the main HLW repository area and in the HLW pilot repository; the corresponding HLW-V1 seals effectively prevent pressure dissipation into the HLW access tunnels. In the L/ILW repository, the gas overpressures are less pronounced, but still noticeable. The gas generated in the L/ILW emplacement caverns accumulates in the central area due to the high gas permeability of the sand – bentonite seals. The HLW-V2 seals effectively prevent any gas flow towards the HLW repository section (see also Nagra 2024m). Complementary simulations with higher gas generation rates show a similar picture (see Nagra 2024m and 2024p for further details), confirming that the HLW-V2 seals ensure an efficient hydraulic separation between the HLW and the L/ILW repository sections.

Mechanical interactions could be caused by thermal disturbances in the vicinity of the HLW repository, giving rise to thermal stresses and thermal expansion of the host rock. Calculations of thermal heave above the HLW repository section highlight the limited lateral range of impact.

The potential heat- and gas-induced heave is estimated following Senger et al. (2014, NAB 14-11). Rock grains are assumed to be solid and maintain their volumes, such that any heave is caused by changes in the porosity of the host rock. In TOUGH, heat- and gas-induced porosity changes are proportional to the changes in temperature dT and pressure dP, written:

$$d\phi = \phi_0\left(C_p dP + \zeta_p dT\right) \tag{4-1}$$

where $d\phi$ is the total porosity change, ϕ_0 is the initial porosity, C_p is the pore compressibility, and ζ_p is the thermal pore expansivity.

The potential heave dz at any spatial coordinate of the model is calculated by vertically integrating the porosity change according to:

$$dz(x,y,z) = \int_{z_0}^{z} d\phi(x,y,h)dh \tag{4-2}$$

with z_0 chosen such that $d\phi(x, y, z_0) = 0$. As this approach assumes that the overlying and underlying units are incompressible, z_0 can be chosen as the bottom of the host rock unit. In addition, it is assumed that rock deformation only occurs in the vertical direction (i.e., no lateral displacement, no bending effect of overlying layers, elastic caverns and tunnels); thus, the calculated potential heave can be considered as an upper bound estimation compared to that of a fully coupled THM calculation. The contour plots in Fig. 4-5 present the calculated heave at the top of the Opalinus Clay at different times between 500 and 100,000 years. The impacts are restricted to the footprint area of the HLW repository section, while the L/ILW repository section remains unaffected. Note that the calculated heave at 100,000 years is dominated by the gas pressure build-up associated with anaerobic corrosion of the waste canisters in the HLW repository section.

Deterministic and probabilistic assessment of the failure potential (see Section 2.5.4) show a similar picture. The highest failure potential, about 0.5, is observed shortly after HLW emplacement in the immediate vicinity of the HLW repository section (see Fig. 4-6), whereas the L/ILW repository remains unaffected.

Mechanical interactions associated with gas-induced overpressures are even less important. Probabilistic assessments of the failure potential associated with gas-induced overpressures are discussed in Section 6.3.

In summary, the PA simulations at the scale of the entire repository provide clear evidence that the HLW and L/ILW repository sections are separated from each other, effectively preventing any detrimental TH^2M-C interactions (Claim in Tab. 4-1).

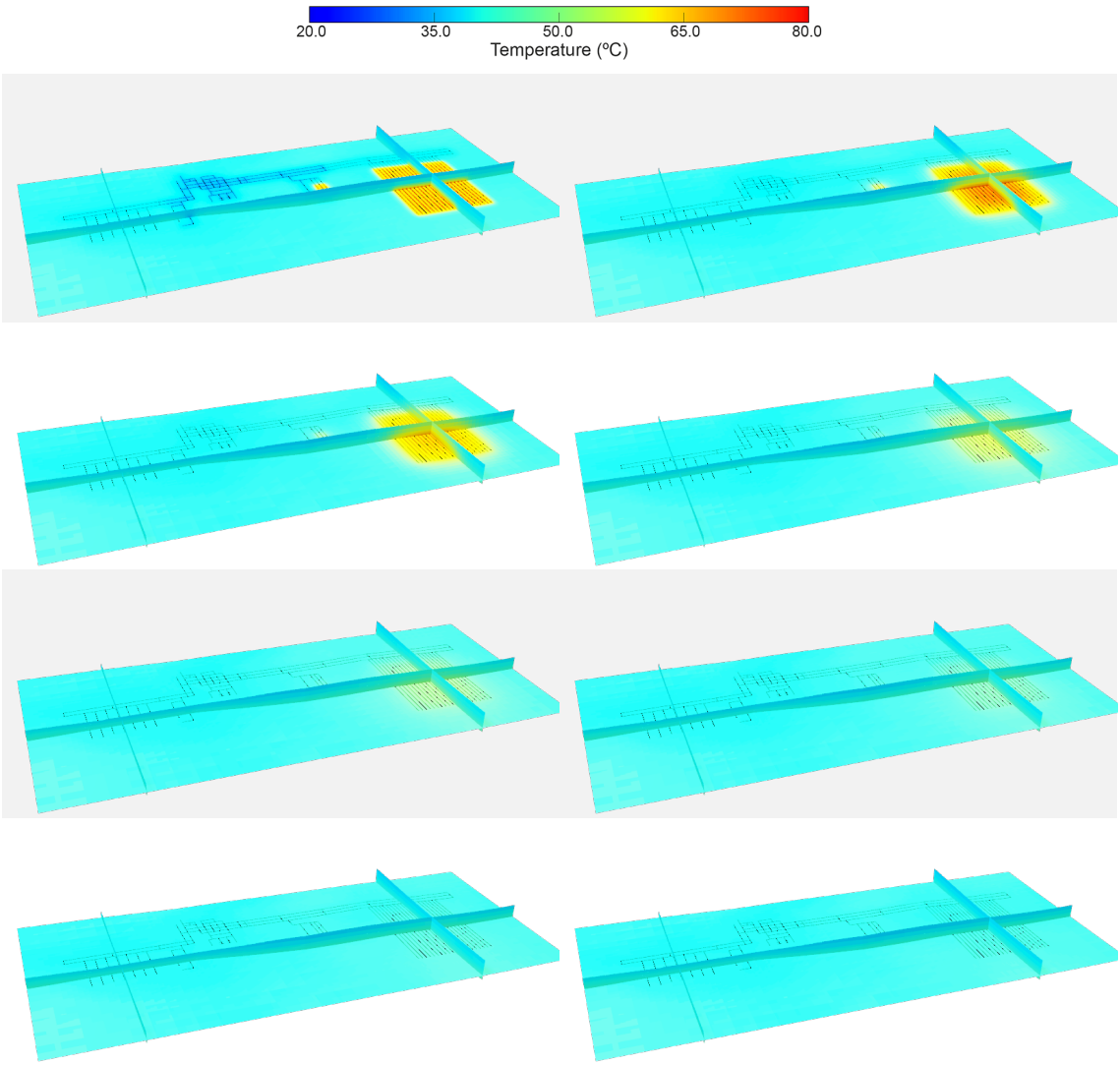

Fig. 4-2: Spatial distribution of temperature in the repository near-field after 100, 500, 1,000, 5,000, 10,000, 20,000, 50,000 and 100,000 years

Referring to the base case in NTB 24-23 (Nagra 2024p).

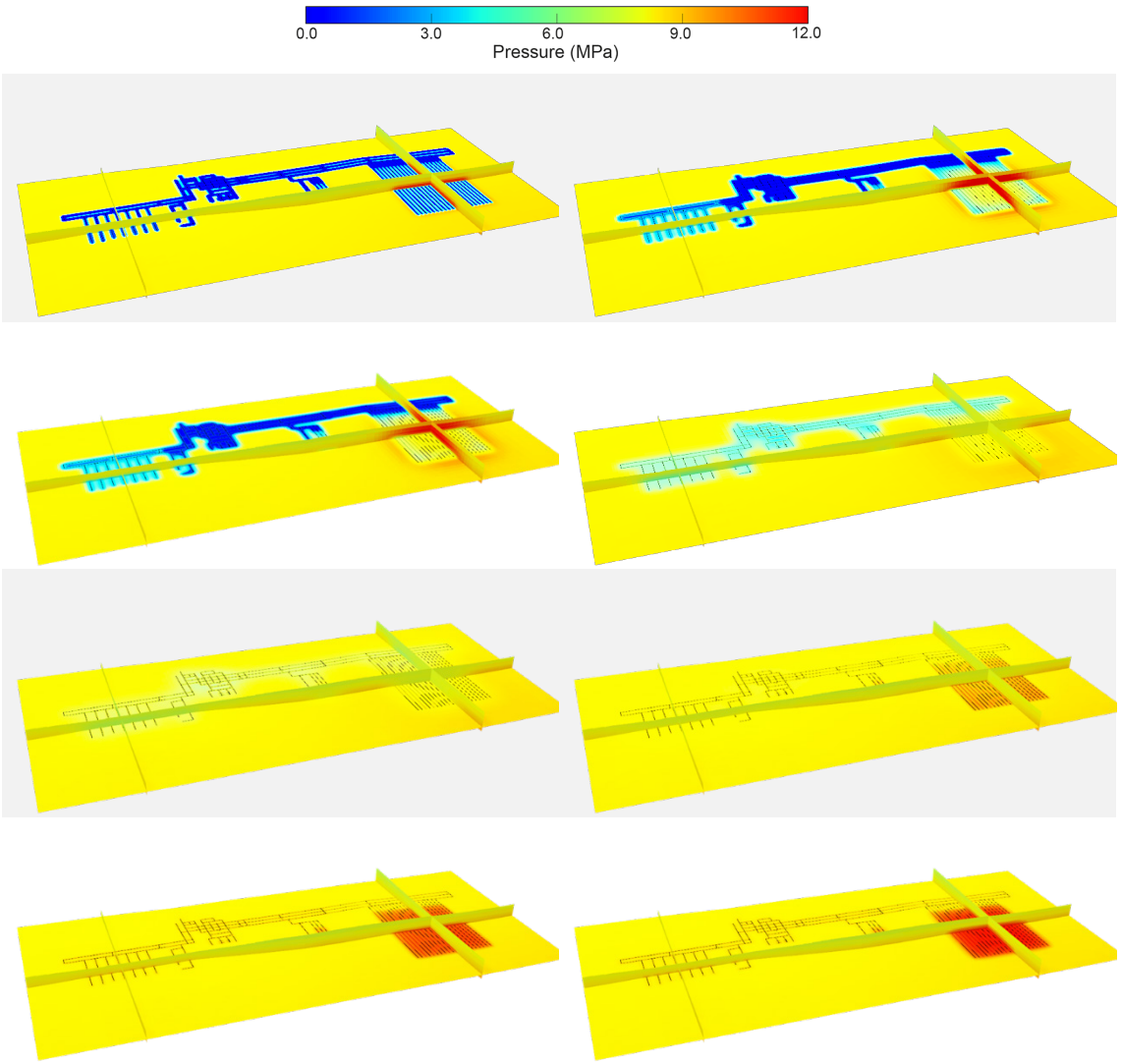

Fig. 4-3: Spatial distribution of pressure in the repository near-field after 100, 500, 1,000, 5,000, 10,000, 20,000, 50,000 and 100,000 years

Referring to the base case in NTB 24-23 (Nagra 2024p).

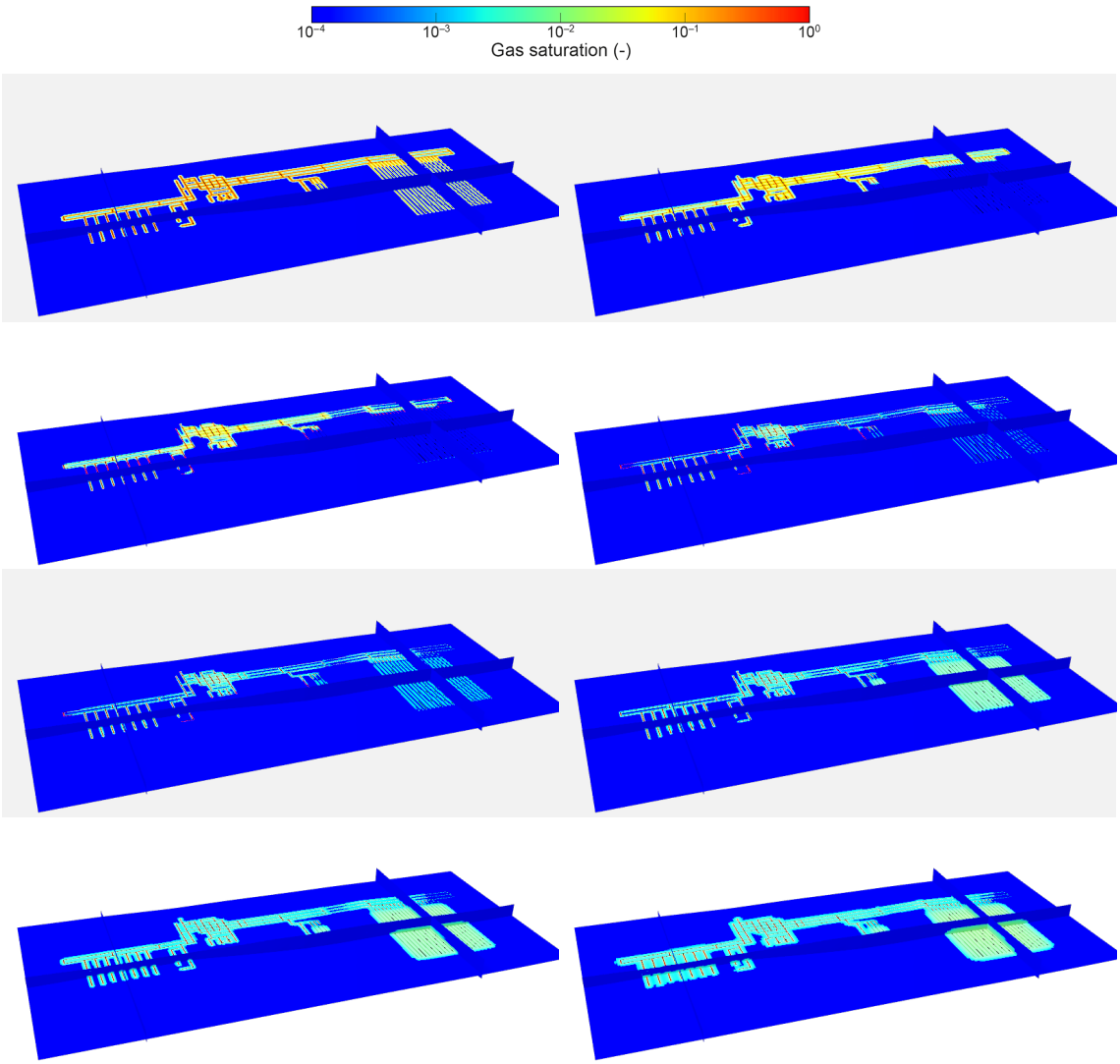

Fig. 4-4: Spatial distribution of gas saturation in the repository near-field after 100, 500, 1,000, 5,000, 10,000, 20,000, 50,000 and 100,000 years

Referring to the base case in NTB 24-23 (Nagra 2024p).

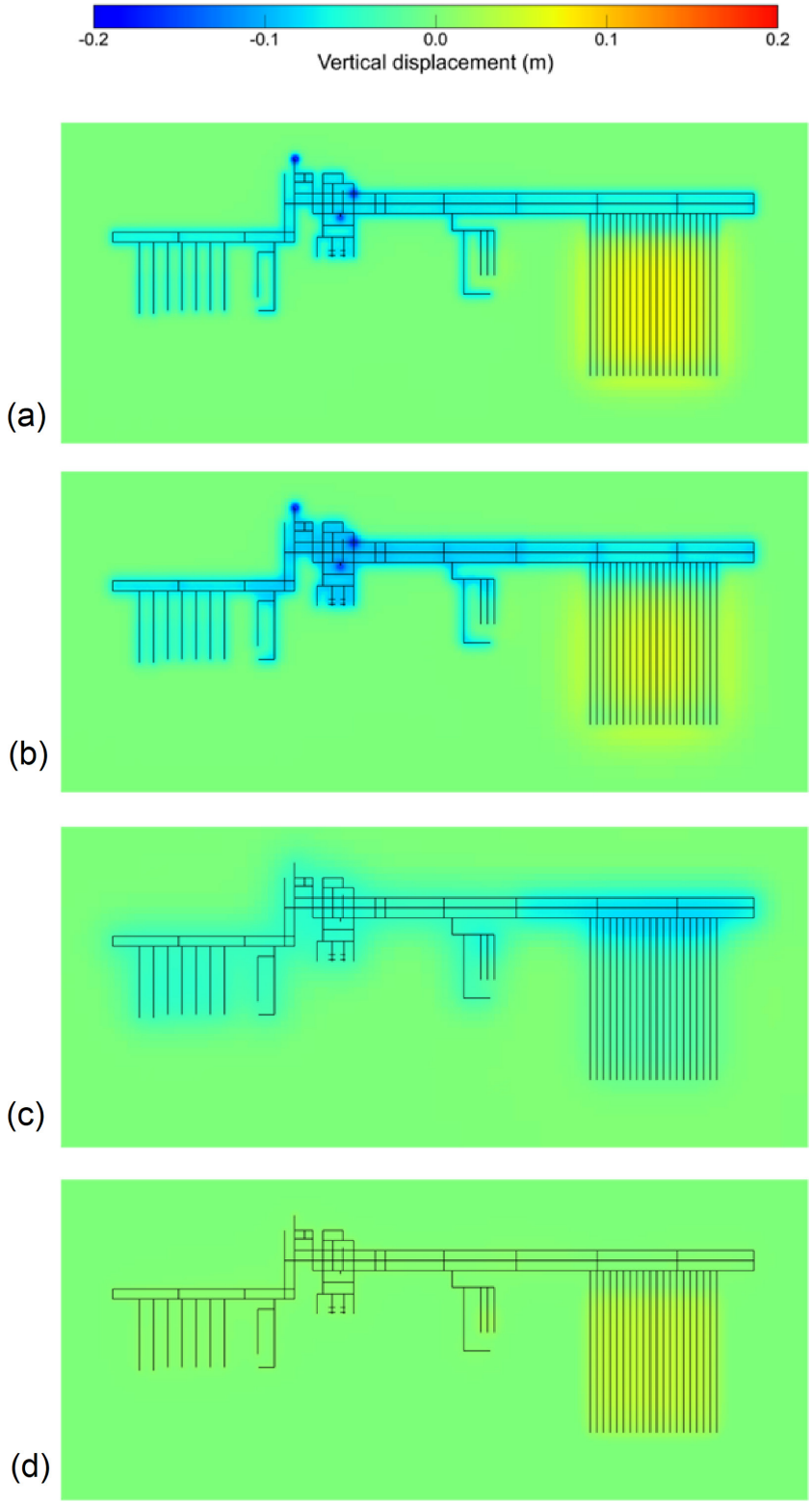

Fig. 4-5: 2-D spatial distribution of heave at the top of the Opalinus Clay caused by thermal- and gas-related disturbances in the vicinity of the HLW repository section

Heave after 500, 1,000, 10,000, and 100,000 years.

Referring to the base case in NTB 24-23 (Nagra 2024p).

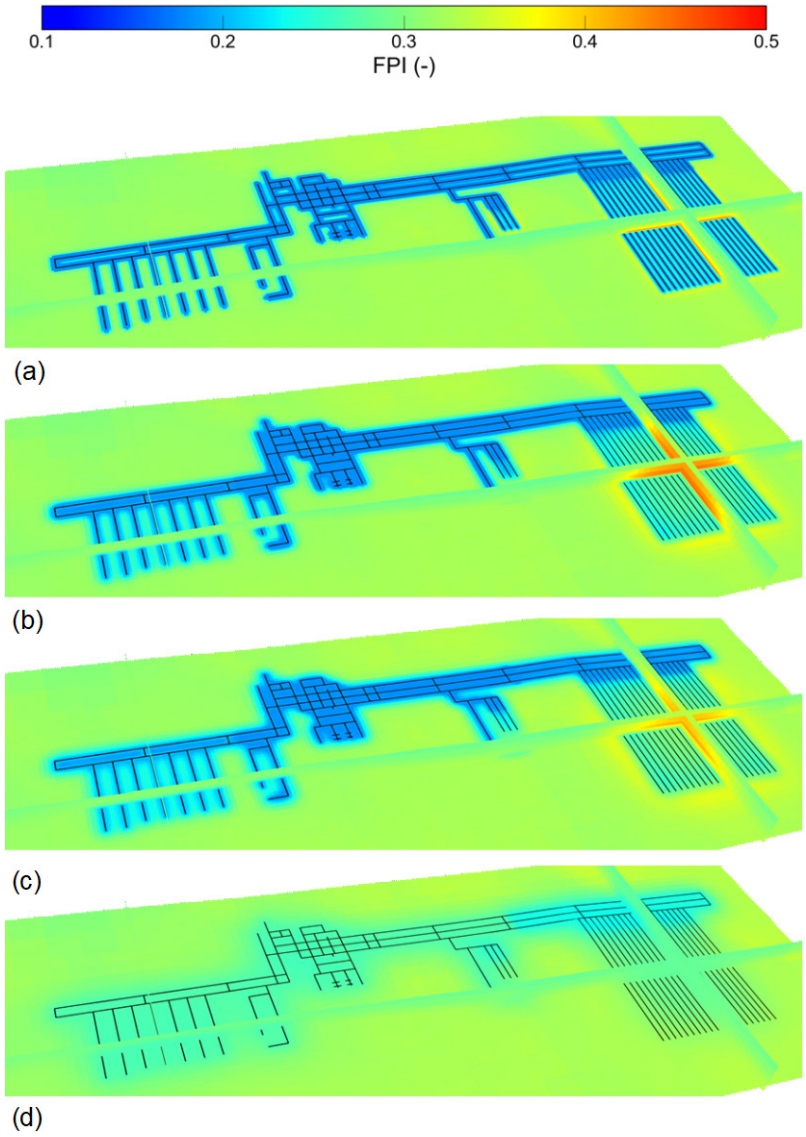

Fig. 4-6: Calculated Failure Potential (FPH_{HLW}) associated with thermally induced pore pressure increase in the host rock around the HLW drifts after 100, 500, 1,000 and 10,000 years

Referring to the base case in NTB 24-23 (Nagra 2024p).

4.3 Thermal interactions

4.3.1 Claims, arguments and evidence related to thermal interactions

The decay heat emitted by the HLW canisters causes elevated temperatures in the HLW near-field for thousands of years, which could potentially impair the safety functions of the bentonite buffer, the host rock and the HLW-V1 seals. In addition, the thermal disturbances to the HLW near-field could enhance radionuclide release in the event of premature breaching of the HLW canisters. As part of the provisional repository design and implementation workflow (see Fig. 2-1), the necessary design measures have been taken to avoid any detrimental impacts of thermal interactions on the safety functions of individual components and on the multi-barrier system as a whole. The evaluation of the safety-related impacts in the framework of performance assessment mainly draws on model-based evidence, addressing a wide range of parametric and conceptual uncertainties. Confidence in the validity of the $TH^2(M)$-models that are applied is gained by model benchmarking (see Section 5.3.2) and by back-analyses of in-situ experiments (Section 5.6).

Claims, arguments and evidence related to the impact of thermal interactions are summarised in Tab. 4-2. For each claim, arguments and evidence are detailed in Sections 4.3.2 and 4.3.3.

Tab. 4-2: Claims, arguments and evidence related to safety-relevant thermal interactions between the components of the multi-barrier system of the HLW repository

Argument	Evidence
Claim: Thermal impacts do not impair the stable geochemical and geomechanical environment.	
By design, the heat emission of the HLW canisters will not impair the safety functions of the bentonite buffer.	Model-based evidence compiled in a generic study (NAB 20-31, Nagra 2021b) and site-specific assessments (NAB 24-25, NTB 24-23, NTB 24-22 Rev. 1: Nagra 2024m, 2024p, 2024u). See also Section 4.3.2 in this report.
By design, the heat emission of the HLW canisters will not impair the safety functions of the host rock.	
By design, the heat emission of the HLW canisters will not impair the safety functions of the V1 seal.	
Claim: Thermal impacts do not enhance radionuclide release along the backfilled and sealed HLW structures.	
Even in the unlikely case of premature canister failure, the loss of radionuclide retention capacity of the bentonite buffer associated with thermal disequilibrium is insignificant.	Model-based evidence compiled in a generic study (Nagra 2021b) and site-specific assessments (Nagra 2024m, 2024p, 2024u). See also Section 4.3.3 in this report.
Thermally induced displacement of porewater along the backfilled repository structures is insignificant.	

4.3.2 Impacts on the mechanical and chemical integrity of the multi-barrier system

The assessment of thermal impacts on the mechanical and chemical integrity of the multi-barrier system can be limited to the HLW repository section only; the L/ILW repository section is not affected, as demonstrated in Section 4.2.2. Model-based assessment workflows for the evaluation of thermal effects have been developed and tested during previous stages of the Sectoral Plan (e.g., NAB 14-11, Senger et al. 2014 and NABs 16-07 & 16-08, Papafotiou & Senger 2016a, 2016b). The selection of the site for a repository for both HLW and L/ILW in NL (Haberstal site) required minor adjustments of the HLW repository design, resulting in a slightly larger diameter for the HLW emplacement drifts, and of the lining and a greater thickness of the bentonite buffer. Descriptions of the updated HLW near-field design from the perspective of post-closure safety are reported in Nagra (2024m, NAB 24-25) and Nagra (2024p, NTB 24-23) together with comprehensive assessments of repository-induced effects on barrier performance. The main findings are summarised in the following paragraphs.

Fig. 4-7 presents the evolution of temperature, gas saturation and pore pressure in the vicinity of the HLW emplacement drifts for the base case of the so-called PA-Scenario of expected repository performance *EXPERF*, which is defined in Section 6.2 (see also Nagra 2024m). In the period immediately after waste emplacement, temperatures up to 125 °C are expected in the bentonite buffer next to the HLW canisters. Note that, even during the initial phase, more than 70% of the bentonite buffer does not experience temperatures above 100 °C. In this temperature range, the favourable radionuclide retention behaviour of the bentonite associated with its high sorption capacity, its low hydraulic conductivity and its high swelling pressure remains unaffected; irreversible thermo-mechanical effects are also not expected in this temperature range. The temperature of the bentonite decreases rapidly with increasing water saturation, reaching values between 60 and 80 °C after 100 years. After 10,000 years, the temperature disturbance has spread out over the entire Opalinus Clay, with slightly elevated temperatures in the HLW near-field, typically 10 to 30 °C above the initial undisturbed temperature at repository depth.

The transients of gas saturation $S_g = 1 - S_w$ indicate that the bentonite saturates within two to three hundred years, which is a longer period for saturation than observed for previous HLW near-field designs. The reason is the larger tunnel diameter and the associated greater thickness of unsaturated bentonite surrounding the canisters. The small gas saturation after 1,000 years is indicative of the accumulation of hydrogen generated by anaerobic corrosion processes at the canister surfaces. An interesting aspect in this context is the fact that the bentonite is at no time fully water saturated, which means that the hydrogen generated at canister surfaces invades a partially saturated bentonite at pressures below the gas entry pressure of the saturated bentonite. Consequently, the mechanical effects of hydrogen invasion on the fabric of the bentonite are only moderate, because the invading hydrogen occupies mainly the pore space of the macropores, which were formerly filled with air. The creation of new pathways, which could affect the safety function of the bentonite buffer as a hydraulic barrier and as a barrier to the transport of dissolved radionuclides, is not very plausible under such conditions, when a residual gas saturation remains in the bentonite.

The development of pore pressure in the HLW near-field is controlled by two processes, namely by the flow of porewater from the host rock towards the unsaturated HLW tunnel due to the capillary suction of the bentonite and by the propagation of the thermal pulse and associated pressure build-up in the host rock. The thermal effects are mainly observed in the fully saturated host rock (Fig. 4-7, right column), where the thermal expansion of the porewater (relative to the expansivity of the of the host rock) in response to the heat pulse causes overpressures in the porous rock matrix at the front of the propagating temperature perturbation. The dissipation of the thermally induced overpressures is controlled by the low hydraulic conductivity of the Opalinus Clay. As shown in Fig. 4-7, the extent of the zones of high porewater overpressure is driven by

the temperature front initially propagating in radial direction from the HLW drifts and, at later times, propagating upwards and downwards towards the confining units. The most distinct overpressures are observed around 20 m above and below the HLW repository section centre plane. From a geomechanical point of view, it is the overpressure zone above the repository which needs to be considered. This is because the lithostatic stress in the overpressure zone above the repository is around 0.5 MPa lower than at the repository level, resulting in a lower effective stress when thermally induced porewater overpressures develop. Consequently, the failure potential of the overpressure zone above the repository is always higher than that below the repository. For the base case presented in Fig. 4-7, the maximum porewater pressure at a vertical distance of 20 m above the central HLW drift (point P6) is around 12.5 MPa (corresponding to an overpressure of 4.1 MPa above hydrostatic), resulting in a moderate failure potential FPH < 0.4 (see Section 2.5.4 and App. C.3 for the definition of the failure potential). Probabilistic assessment of the failure potential confirms these results; the mechanical integrity of the host rock remains unaffected even assuming the upper bound of the thermal source term and unfavourable thermo-hydraulic properties of the host rock (PA-Scenario *UBHEAT*, see Section 6.3).

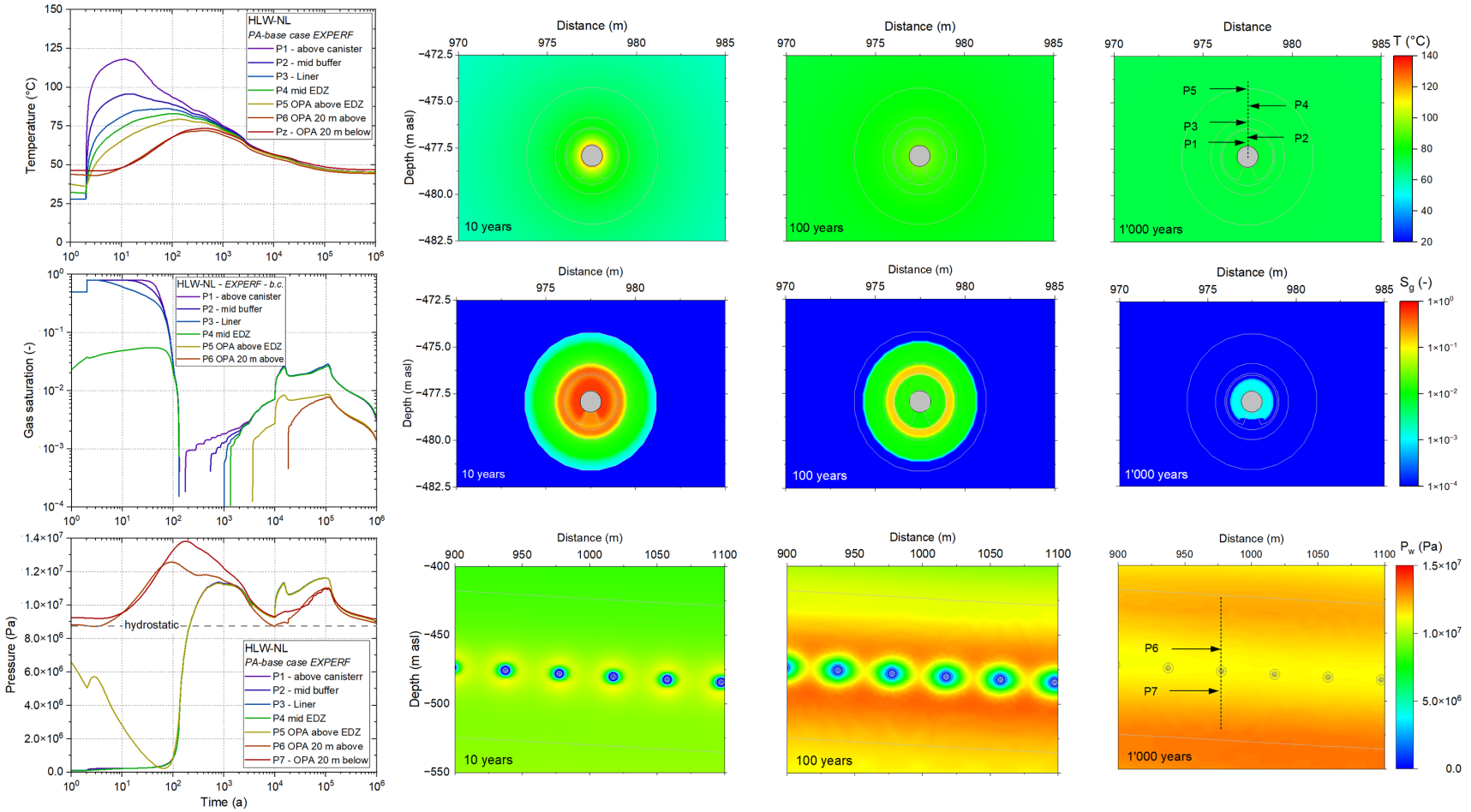

Fig. 4-7: Development of temperature, gas pressure and saturation in the HLW near-field, derived for the base case of the PA-Scenario EXPERF See Section 6.2. (left) Time histories and (right) contour plots after 10, 100 and 1,000 years.

By design the distance of the HLW-V1 seals from the heat emitting canisters is sufficiently large to avoid any detrimental heat effects. The maximum temperature in the centre of the HLW-V1 seals always remains below 65 °C (Fig. 4-8). It is evident that such moderate increases in temperature will not give rise to any significant loss of the mechanical and chemical integrity of the closure system. In particular, the high swelling capacity and low hydraulic conductivity of the bentonite sealing elements will remain at the design values.

It can be concluded from the PA simulations at the scale of the entire repository system that thermal impacts do not impair the stable geochemical and geomechanical environment (Claim in Tab. 4-2).

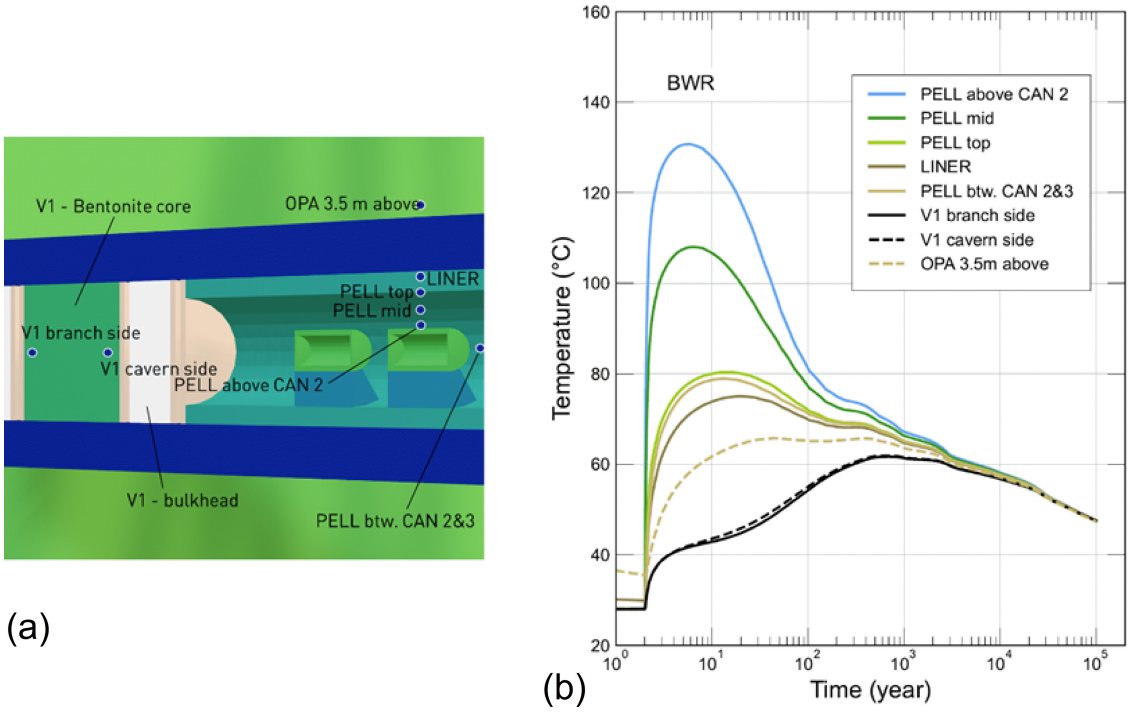

Fig. 4-8: Development of temperature in the vicinity of a HLW-V1 seal

Referring to base case in NTB 24-23 (Nagra 2024p).

(a) Sketch of the components of the HLW-V1 seal, with bentonite sealing element, transition layers and concrete bulkheads, and (b) transients of temperature at different observation points.

4.3.3 Impacts of heat on radionuclide release along the backfilled repository structures

The HLW canisters are designed such that they provide full containment of SF and RP-HLW during the non-isothermal early post-closure phase (see Section 3.2). By design, the expected lifetime of the canisters is ≥ 10,000 years. Only in the unlikely case of premature canister breaching could thermal disturbances to the HLW near-field enhance radionuclide release and transport. There are two effects to be considered in the case of premature canister failure: (i) early release of the radionuclides from the canister into the bentonite and propagation of the diffusion front under the action of the thermal gradient, and (ii) advective transport of radionuclides dissolved in the bentonite porewater under the action of thermally induced porewater overpressures. Both effects were evaluated with the PA model portfolio (NAB 24-25, Nagra 2024m).

When a canister breaches, porewater penetrates the canister and eventually contacts the waste forms. Radionuclides from the waste are dissolved in the inflowing porewater and released by diffusion into the bentonite buffer. During the non-isothermal early post-closure phase, the bentonite in contact with the canister is characterised by a low water saturation which prevents the release of dissolved radionuclides. A significant release of dissolved radionuclides can take place only when the water saturation of the bentonite reaches values close to $S_w = 1$. Probabilistic simulations carried out as part of the PA-Scenario WPFAIL (see Section 6.3) indicate that, even for the hypothetical case of an instantaneous failure of the canister at the time of repository closure, the early radionuclide release is of low significance. The loss of barrier function of the HLW repository associated with premature failure of the canister is marginal (see Fig. 6-10).

The other effect, namely the thermally induced displacement of porewater, is also of minor importance, contributing insignificantly to advective transport of dissolved radionuclides along the backfilled repository structures. Water displacement from the HLW-V1 seals into the adjacent branch tunnels is very low (in the order of 0.01 m^3/year) and stops after ~20,000 years (Fig. 4-9), as discussed in greater detail in Nagra (2024m). Radionuclide transport along the backfilled HLW emplacement drifts towards the HLW-V1 seals would also only happen in the extremely unlikely case of premature canister failure. It can be concluded from the PA simulations, both at repository and at component scale, that the thermally induced release of radionuclides by advective transport along the backfilled structures of the HLW repository is negligible (Claim 2 in Tab. 4-2).

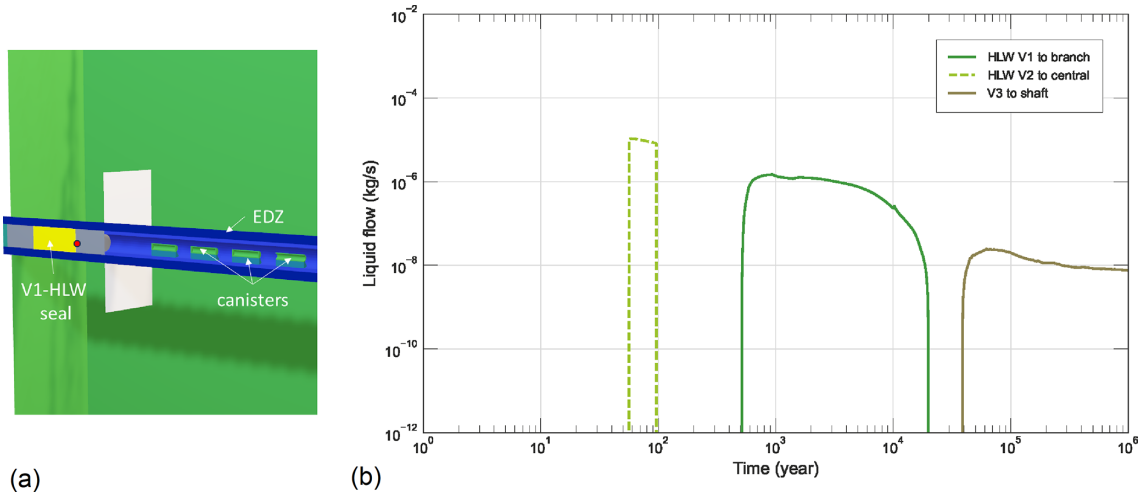

Fig. 4-9: Transients of liquid flow rate through the sealing sections HLW-V1 and HLW-V2

Referring to base case in NAB 24-25 (Nagra 2024m).

(a) Sketch of the components of the HLW-V1 seal (bentonite sealing element, transition layers and concrete bulkheads), the EDZ and the HLW canisters, and (b) transients of liquid flow across the sealing sections.

4.4 Gas-induced interactions

4.4.1 Claims, arguments and evidence related to gas-induced interactions

The anaerobic corrosion of the HLW canisters gives rise to hydrogen accumulation and gas pressure build-up in the HLW near-field for more than 100,000 years (see Fig. 4-3). Gas-induced overpressures could impair the mechanical integrity of the bentonite buffer, the host rock and the HLW-V1 seals. In addition, the accumulated gas in the HLW near-field could enhance the release of radionuclides dissolved in the liquid phase along the backfilled repository structures. Similar impacts on the safety functions of the barrier components of the L/ILW repository section could occur due to the accumulation of waste-generated gasses from corrosion of metals and degradation of organic materials in the L/ILW emplacement caverns.

The provisional repository design and implementation workflow (see Fig. 2-1) foresees a suite of design measures both for the HLW and the L/ILW repository sections to avoid any detrimental impacts of gas-induced interactions on the safety functions of individual components and on the entire multi-barrier system. As in the case of thermal impacts, the evaluation of potential gas-related impacts in the framework of performance assessment is mainly based on numerical modelling, which allows parametric and conceptual uncertainties to be assessed in a quantitative manner. Model benchmarks (see Section 5.3.2) and back-analyses of in-situ experiments (Section 5.6) play a similar role for building confidence in the validity of the TH^2(-M)-models that are applied, as in the case of thermal impacts.

Claims, arguments and evidence related to the impact of gas-induced interactions are summarised in Tab. 4-3. Arguments and evidence are detailed for the HLW repository section in Sections 4.4.2 and 4.4.3 and for the L/ILW repository section in Sections 4.4.4 and 4.4.5.

Tab. 4-3: Claims, arguments and evidence related to safety-relevant gas-induced interactions between the components of the multi-barrier system of the repository

Argument	Evidence
Claim: Gas-related impacts do not impair the stable geochemical and geomechanical environment of the HLW repository section.	
The design of the HLW near-field (drift diameter, emplacement density of bentonite buffer) has been chosen such that gas overpressures in the HLW drifts remain moderate, even assuming upper bounding values for gas generation rates.	Model-based evidence collected in site-specific assessments (NAB 24-25, NTB 24-23: Nagra 2024m, 2024p). See also Section 4.4.2 in this report.
Favourable effects, such as hydrogen diffusion, water consumption associated with anaerobic corrosion and microbial activities, limit gas pressure build-up in the HLW repository section.	
The EDZ around the HLW drifts and the drift lining represent preferential gas release paths, which will be activated before the intact host rock fails.	
Claim: Gas-related impacts do not enhance radionuclide release along the backfilled and sealed HLW structures.	
Gas release from the HLW drifts across the HLW-V1 and HLW-V2 seals is low and does not carry a significant quantity of volatile radionuclides.	Model-based evidence collected in site-specific assessments (Nagra 2024m, 2024p). See also Section 4.4.3 in this report.
Gas-induced displacement of porewater along the backfilled repository structures is insignificant.	
Claim: Gas-related impacts do not impair the stable geochemical and geomechanical environment of the L/ILW repository section.	
The concept of the closure system as a design measure aimed at reducing the build-up of gas overpressures in the L/ILW repository without compromising the radionuclide retention capacity of the engineered barrier system.	Model-based evidence collected in site-specific assessments (Nagra 2024m, 2024p). See also Section 4.4.4 in this report.

Tab. 4-3: Cont.

Argument	Evidence
Claim: Gas-related impacts do not enhance radionuclide release along the backfilled and sealed L/ILW structures.	
Gas-induced displacement of porewater along the backfilled repository structures is insignificant.	Model-based evidence collected in site-specific assessments (NAB 24-25, NTB 24-23: Nagra 2024m, 2024p). See also Section 4.4.5 in this report.
Unsaturated conditions in the backfilled L/ILW emplacement caverns retard the release of dissolved radionuclides from the waste containers.	Model-based evidence collected in site-specific assessments (Nagra 2024m, 2024p). See also Section 4.4.5 in this report.

4.4.2 Gas-induced impacts on barrier integrity – HLW repository

The current HLW near-field layout includes several design measures to avoid any detrimental impacts of gas-induced interactions on the geochemical and geomechanical integrity of individual components and on the multi-barrier system as a whole. In particular, a slightly enlarged diameter of the HLW drifts and a greater thickness of the bentonite buffer provide more gas storage volume. Contrary to previous design variants (e.g., NTB 16-01, Nagra 2016), there are no intermediate seals foreseen along the HLW drifts, which means that the gas accumulates along the EDZ at more or less uniform pressure.

The hydrogen gas generated in the HLW tunnel by anaerobic corrosion of the steel canisters is expected to accumulate in the pore space of the bentonite buffer, in the EDZ and along the interface between the concrete lining and the EDZ. Gas invasion from the locus of gas generation at the canister surfaces into the bentonite buffer occurs at a gas pressure significantly below the gas entry pressure of the saturated bentonite. As noted previously, this is because the bentonite buffer is not yet fully saturated at the onset of gas generation. Rather, it still contains a residual gas phase of undissolved air in its macropores (see Fig. 4-7). The prevailing gas transport mechanism in the partially saturated bentonite is therefore two-phase flow, rather than dilatancy-controlled gas flow. Thus, the mechanical integrity of the bentonite buffer remains largely unaffected, because gas flow takes places predominantly in the partially saturated macropores of the bentonite buffer.

Model-based assessment workflows for the evaluation of gas-induced effects have been developed and tested as part of previous stages of the Sectoral Plan (e.g., NAB 24-10, Papafotiou & Senger 2014b and NAB 16-08, Papafotiou & Senger 2016b). As noted in Section 4.3.2, the selection of the site for the repository in NL required adjustments to be made to the HLW repository design (slightly larger diameter of the HLW emplacement tunnels, greater thickness of the lining and the bentonite buffer). Furthermore, the gas-related source terms have been revised, drawing on new experimental evidence derived in the framework of Nagra's long-term corrosion studies. Descriptions of the updated HLW near-field design and the gas-related source terms from the perspective of post-closure safety are reported in Nagra (2024p, NTB 24-23) and Nagra (2024m, NAB 24-25), together with comprehensive assessments of repository-induced effects on barrier performance. The main findings are summarised in the following paragraphs.

The transients of pressure simulated in the HLW repository section with the 3-D repository model are shown in Fig. 4-10 (base case TS00 in NAB 24-25, Nagra 2024m). The pressure drop at the beginning of the ventilation phase corresponds to the decrease from the initially hydrostatic to atmospheric pressure in the repository tunnels. In the early post-closure phase of the HLW repository section of the repository, pressures first increase in the host rock surrounding the emplacement drifts due to the differential thermal expansion in the low-permeable rock, as described in Section 4.3.1. At the selected location 30 m above the centre of the repository, pressure reaches ~13 MPa after 200 years. The thermally induced pressures in the emplacement drifts only reach hydrostatic values after ~2,000 years, owing to the depressurisation and partial saturation of the near-field at the time of emplacement. Pressures then continue to increase due to gas accumulation in the HLW emplacement drifts, reaching ~10.5 MPa shortly after canister breaching, assumed to occur at 10,000 years. Due to additional corrosion of the canister from the inside (not in contact with bentonite), pressure continues to increase and reaches a maximum of ~11.8 MPa when the canister is corroded entirely after ~115,000 years. Unlike the thermally induced pressures, which reach their maximum values in the rock surrounding the tunnels, gas-induced pressures are higher at the gas source and dissipate in the rock away from the tunnels. After the corrosion of the steel canisters is complete, pressures decrease steeply due to the decrease in the gas generation rate.

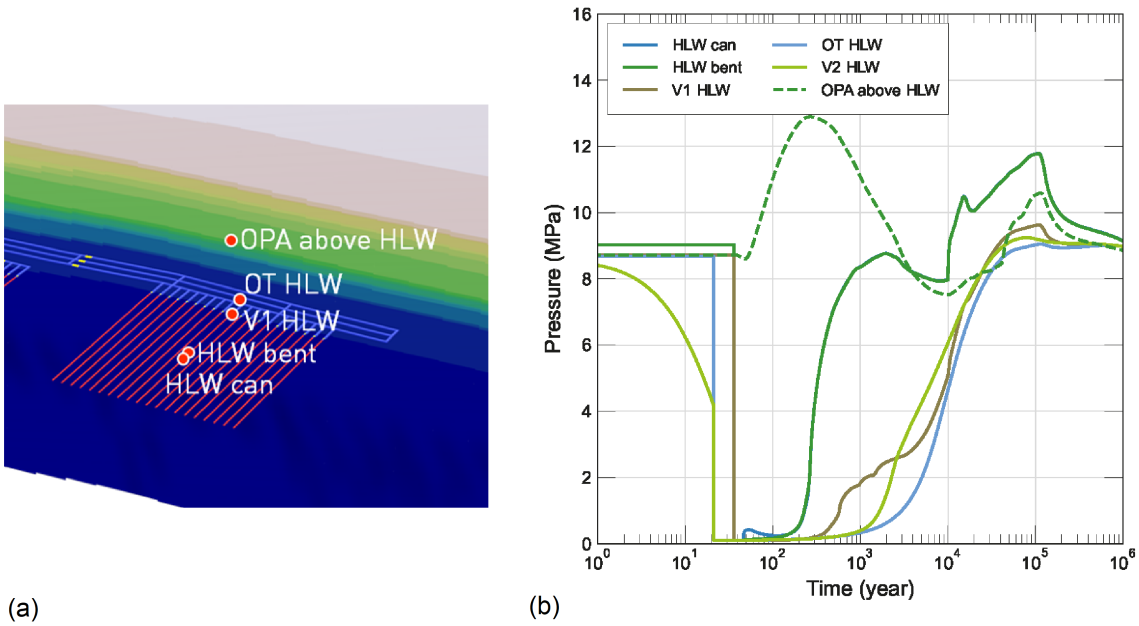

Fig. 4-10: Simulation of pore pressure evolution in the vicinity of the HLW repository section calculated with the 3-D repository model

Referring to the base case TS00 in NAB 24-25 (Nagra 2024m).

(a) observation points and (b) transients of pressure in the HLW repository section.

From a geomechanical point of view, the gas-induced overpressures at repository level cause a reduction in the effective stress in the surrounding rock and an increase in failure potential. For the base case presented in Fig. 4-10, the maximum pore-water pressure of around 11.8 MPa calculated at repository level corresponds to moderate failure potential of FPG < 0.35 (see Section 2.5 and App. A for the definition of the failure potential). Probabilistic assessment of the failure potential confirms the results; the mechanical integrity of the host rock remains unaffected even assuming an upper bound for the gas source term and unfavourable thermo-hydraulic properties for the host rock (PA-Scenario UBGAS, see Section 6.3).

There are further favourable effects that were not considered in the simulations of gas-induced pressure build-up presented above. First, the conservative assumption was made that diffusion of dissolved hydrogen does not significantly affect the build-up of gas pressure in the HLW drifts. Second, the role of water consumption associated with the chemical process of anaerobic corrosion was not accounted for. A further phenomenon that could reduce the build-up of gas overpressures is microbial activity, associated with hydrogen consumption in the backfilled tunnels.

The diffusion coefficient of hydrogen dissolved in pure water is 4 – 5 times higher than the diffusion coefficient of other species such as iodine or sodium. It is therefore to be expected that diffusion of dissolved hydrogen in the fully water-saturated host rock could be an additional transport process, reducing gas pressure build-up in the HLW drifts. While this transport process was not accounted for in the base case simulation TS00 shown in Fig. 4-10, an additional case (TSD19) is reported in Nagra (2024m, NAB 24-25), which accounts for diffusion of dissolved hydrogen. A clear effect is observed, in that the peak pressure after 115,000 years is reduced by around 1 MPa compared with the base-case simulation (TS00). This effect is also seen in the 2-D base case simulation of the PA-Scenario EXPERF, described in Section 6.2. Fig. 4-11a compares the base case without hydrogen diffusion (red line) and the corresponding with diffusion (blue line). A significant reduction in the peak pressure by more than 1 MPa is observed, confirming that hydrogen diffusion is a transport mechanism that reduces the build-up of gas-induced overpressures in the HLW near-field.

The role of water consumption due to anaerobic corrosion was the subject of previous investigations on gas pressure build-up, still referring to a former HLW near-field design (Senger et al. 2008). The former analyses revealed that a significant reduction of gas pressure build-up in the HLW near-field can be expected when the host rock exhibits a very low hydraulic conductivity of $\leq 1 \times 10^{-14}$ m/s. Recent PA simulations using the latest layout of the HLW repository confirm the previous results. Fig. 4-11b compares the base case in the PA-Scenario EXPERF without water consumption (red line) and with the corresponding case with water consumption (blue line). A significant reduction of the peak pressure by more than 1 MPa is observed.

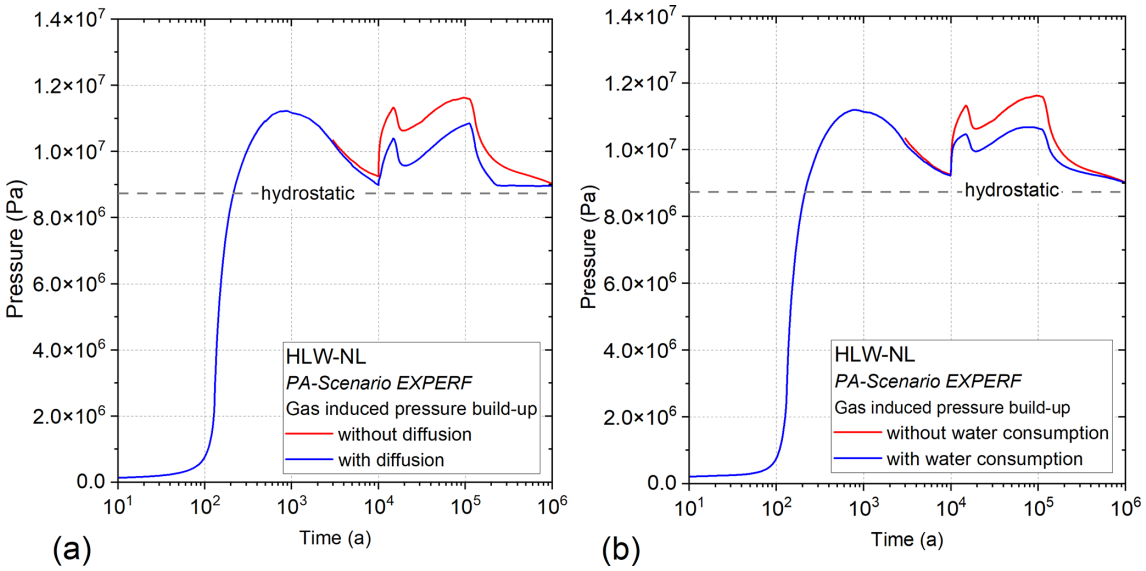

Fig. 4-11: Transients of pressure build-up in the HLW drifts, considering favourable phenomena

Base case simulation of the EXPERF scenario, see Section 6.2 and NAB 24-25 (Nagra 2024m).

(a) The role of diffusion of dissolved hydrogen, and (b) impact of water consumption in the case of a low-permeability host rock.

The simulations presented above provide clear evidence that diffusion of dissolved hydrogen and water consumption due to anaerobic corrosion are processes that contribute significantly to the reduction of gas-induced pressure build-up in the HLW near-field. For the sake of conservatism, these favourable processes were not implemented in the PA-Scenarios of expected barrier performance and deviations thereof (Chapter 6). While the hydrogen diffusion coefficient in pure water is a well-established parameter derived from the Stokes-Einstein law, measuring the effective diffusion coefficient of hydrogen in clay materials proves to be a major challenge (e.g., Jacops & Kolditz 2024). The experimental database on the effective diffusion coefficient of hydrogen in Opalinus Clay is still incomplete and exhibits significant uncertainties. Likewise, the mechanism of water consumption due to anaerobic steel corrosion is undisputed in principle. However, the phenomena and processes associated with the special environmental conditions of canister corrosion in the non-isothermal HLW near-field are still a topic of ongoing research.

Microbial activity represents another mechanism that could reduce the build-up of gas pressure in the HLW repository section. Basic concepts of microbial gas consumption were discussed in Leupin et al. (2016) and scoping calculations on the effectiveness of this mechanism were carried out with a generic repository model. The scoping calculations confirm that microbial activity has the potential to reduce the build-up of gas overpressures in the backfilled repository structures. However, after closure of the repository, the predictability of microbial processes in the repository is limited, depending strongly on the evolution of the TH^2-C conditions in the HLW near-field. Microbial gas consumption was not considered in the present PA calculations.

In summary, 2-D and 3-D PA simulations provide comprehensive evidence conforming that gas-related impacts do not impair the stable geochemical and geomechanical environment of the HLW repository (Claim 1 in Tab. 4-2).

4.4.3 Gas-induced impacts on radionuclide release – HLW repository section

The partially resealed EDZ around the HLW drifts together with the tunnel lining represents a potential gas storage volume. It starts to form a preferential gas release path along the drift axis when a pressure gradient develops across the HLW-V1 seal (Fig. 4-12a). Normal stress on the EDZ fractures is reduced with increasing gas pressure and fracture transmissivity increases steadily, long before the intact host rock fails. In the PA models, the EDZ is characterised by a slightly enhanced permeability (typically 1 order of magnitude higher than the intact host rock) and a reduced gas entry pressure. Simulation results for the base case TS00, described in Nagra (2024m, NAB 24-25), are presented in the following paragraphs.

Liquid flow rates through the HLW sealing sections are shown in Fig. 4-9. The short period of water flow from the HLW drifts to the branch tunnels is caused by the thermal effects, as described in Section 4.3.3, whereas gas-induced displacement of porewater is not observed. Therefore, the claim that gas-related impacts do not enhance the release of dissolved radionuclides along the backfilled and sealed HLW structures can be confirmed.

Flow rates of gas released through the HLW sealing sections are shown in Fig. 4-12b. These are compared with the corresponding gas generation rates in the HLW repository section. In general, gas flow through the HLW seals changes direction as it is controlled by pressures developing across each seal. Note that Fig. 4-12b only shows the gas flow in one direction, as defined in the legend. Because of the log-scale, the change in flow direction is indicated by no flow. Initially, the change in flow direction is the result of the depressurisation of the operation galleries during ventilation, followed by the thermal pulse in the HLW emplacement drifts, which may displace water and gas (see Section 4.3). Later, gas flow across the sealing sections is controlled by the gas pressure build-up in the emplacement drifts and in the repository central area (near the shaft and the V3 seal). After canister breaching (10,000 years) and until ~250,000 years, gas flow from the HLW-V1 seals to the adjacent branch tunnels is ~3 – 4 orders of magnitude below the gas generation rate in the HLW emplacement drifts. Between ~25,000 years and 600,000 years, there is no gas flow from the HLW-V2 seals in the direction of the central area, indicating that HLW-generated gas remains within the HLW repository section during that time.

Volatile radionuclides (predominantly ^{14}C) from the canisters after they breach will mix with the hydrogen in the accumulated gas phase that forms due to the anaerobic corrosion processes at the canister surfaces and, over time, invades the bentonite buffer and the EDZ around the HLW drifts. The hydrogen may act as a carrier gas for the volatile radionuclides when a pressure gradient develops across the HLW-V1 seal. The low gas release rates along the HLW-V1 seals (Fig. 4-12), which are 3 – 4 orders of magnitude lower than the gas generation rates, ensure, that the backfilled repository structures do not constitute a significant lateral transport path for volatile radionuclides.

It can be concluded from the PA simulations at repository scale that the gas-induced release of dissolved and volatile radionuclides by advective flow along the backfilled structures of the HLW repository is negligible (Claim 2 in Tab. 4-3).

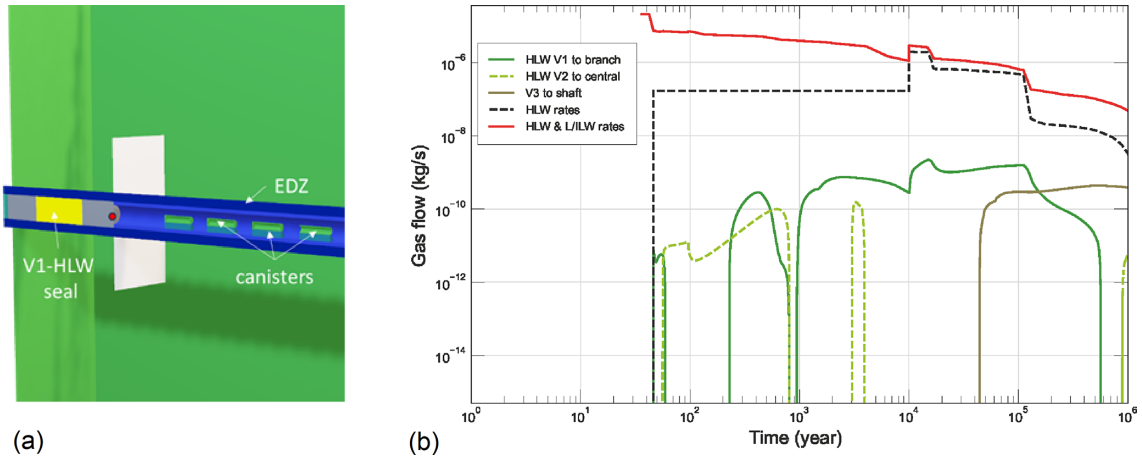

Fig. 4-12: Transients of gas flow rate through the sealing sections HLW-V1 and HLW-V2

Referring to base case TS00 in NAB 24-25 (Nagra 2024m).

(a) Sketch of an HLW drift with control point of calculated gas/liquid flux at the seal HLW-V1 (seal HLW-V2 not presented here), (b) gas generation rate in the HLW repository and gas flow rates through the cross-sections at the control points HLW-V1 and HLW-V2.

4.4.4 Gas-induced impacts on barrier integrity – L/ILW repository

The concept of designing the closure system in such a way as to reduce the build-up of gas over-pressures in the L/ILW repository without compromising the radionuclide retention capacity (safety function IMS) of the engineered barrier system was introduced in Nagra (2008, NTB 08-07). A technical solution was developed that includes high porosity backfill materials in the L/ILW emplacement caverns in combination with gas permeable L/ILW-V1 and L/ILW-V2 seals. The sealing sections are made of sand/bentonite mixtures with a low bentonite content. They are characterised by a low permeability for water and a relatively high permeability for gas due to the (micro)structure of the sand/bentonite. The gases produced by corrosion and degradation in the L/ILW emplacement caverns accumulate in the high porosity cementitious mortar of the cavern backfill. When gas pressures increase, a gas path develops through the gas permeable seals into the backfilled access and operations tunnels and the central area. The gas storage volume provided by these structures causes a delayed and reduced pressure build-up in the L/ILW emplacement caverns.

Model-based assessments of the performance of the closure system with respect to gas-pressure build-up were carried out for previous L/ILW repository configurations (NTB 08-07, NAB 13-92, NAB 16-07: Nagra 2008, Papafotiou & Senger 2014a, 2016a), demonstrating its general effectiveness. Since then, the gas-related source terms for metal corrosion in cementitious environments have been revised, drawing on new experimental evidence derived in the framework of Nagra's long-term corrosion studies. For the current repository design with extended access structures and a larger central area, the gas pressure build-up in the L/ILW repository is substantially reduced. Comprehensive evidence from model-based assessments is provided in NTB 24-23 (Nagra 2024p) and NAB 24-25 (Nagra 2024m). The main findings are summarised in the following paragraphs.

The transients of pressure simulated in the L/ILW repository section with the 3-D repository model (base case TS00 in Nagra 2024m) are shown in Fig. 4-13. As described above, pressure drops in the repository tunnels at the beginning of the ventilation phase from the hydrostatic to atmospheric pressure. During the early post-closure phase of the L/ILW repository section,

pressures increase faster in the emplacement caverns than in the operations tunnels due to the gas generation from the corrosion and degradation processes. This pressure gradient results in axial gas transport from the emplacement caverns to the adjacent tunnels through the L/ILW-V1 and L/ILW-V2 seals, which is a key feature of the L/ILW repository section. After ~5,000 years, pressures equilibrate across the L/ILW structures while remaining below hydrostatic. From that time until the end of the simulation, all tunnels in the L/ILW repository section have approximately the same pressure at any given time, indicating that there is effective hydraulic connection across the tunnels with sufficient gas transport capacity to distribute the gas in the available pore volume (NTB 24-23, Nagra 2024p). Hydrostatic pressure is reached in the L/ILW repository section after ~20,000 years. Pressures then continue to increase until ~70,000 years, reaching a peak value of ~9.3 MPa before eventually decreasing again towards hydrostatic pressures as gas generation gradually declines. Pressures in the emplacement caverns, operations tunnels and sealing sections of the L/ILW repository section and in the central area of the repository all evolve in a similar manner. On the other hand, the fast restoration of hydrostatic pressure in the shaft above the V3 seal is indicative of the hydraulic separation of the shaft from the repository provided by the V3 seal (Nagra 2024p).

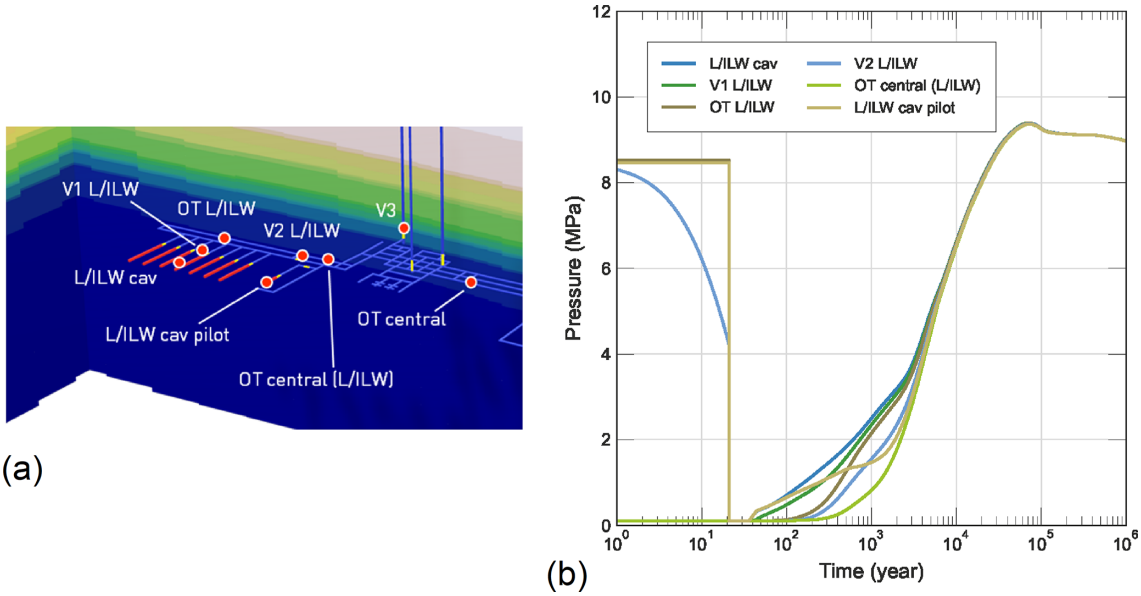

Fig. 4-13: Simulation of pore pressure evolution in the L/ILW repository section and other adjacent repository structures with the 3-D repository model

Referring to the base case TS00 in NAB 24-25 (Nagra 2024m).

From a geomechanical point of view, the gas-induced overpressures in the L/ILW emplacement caverns lead to a reduction in effective stress in the surrounding rock and an increase in failure potential. For the base case, as presented in Fig. 4-13, the maximum porewater pressure in the cavern near-field of around 9.3 MPa corresponds to a moderate failure potential FPG < 0.31 (see Section 2.5 and App. A for the definition of the failure potential). Probabilistic assessment of the failure potential confirms the results; the mechanical integrity of the host rock remains unaffected even assuming an upper bound gas source term and unfavourable hydro-mechanical properties of the host rock (PA-Scenario PESSGAS, see Section 6.3).

As with the HLW repository, there are further favourable effects which were not considered in the simulations of gas-induced pressure build-up, namely (i) the diffusion of dissolved hydrogen, (ii) water consumption associated with the chemical process of anaerobic corrosion and (iii) microbial activity leading to methane and hydrogen consumption by bacteria.

Although the diffusion of hydrogen dissolved in the porewater was not addressed in the base case simulation TS00 shown in Fig. 4-13, an additional case (TSD19) is reported in NAB 24-25 (Nagra 2024m), which accounts for hydrogen diffusion. A distinct reduction of gas pressure is observed, with the peak pressure after 70,000 years reduced by more than1 MPa. This effect is also seen in the 2-D base case simulation of the PA-Scenario EXPERF, described in Section 6.2. Fig. 4-14a compares the base case without hydrogen diffusion (blue line) and the corresponding case with diffusion (red line). As noted above, a significant reduction in the peak pressure by more than 1 MPa is observed, confirming that hydrogen diffusion is a transport mechanism, which reduces the build-up of gas-induced overpressures in the L/ILW repository section.

PA simulations using the current layout of the L/ILW repository section reveal only a marginal effect of water consumption due to anaerobic corrosion on gas pressure build-up in the cavern. Fig. 4-14b shows a comparison of the base case in the PA-Scenario EXPERF without water consumption (blue line) and in the corresponding case with water consumption (red line).

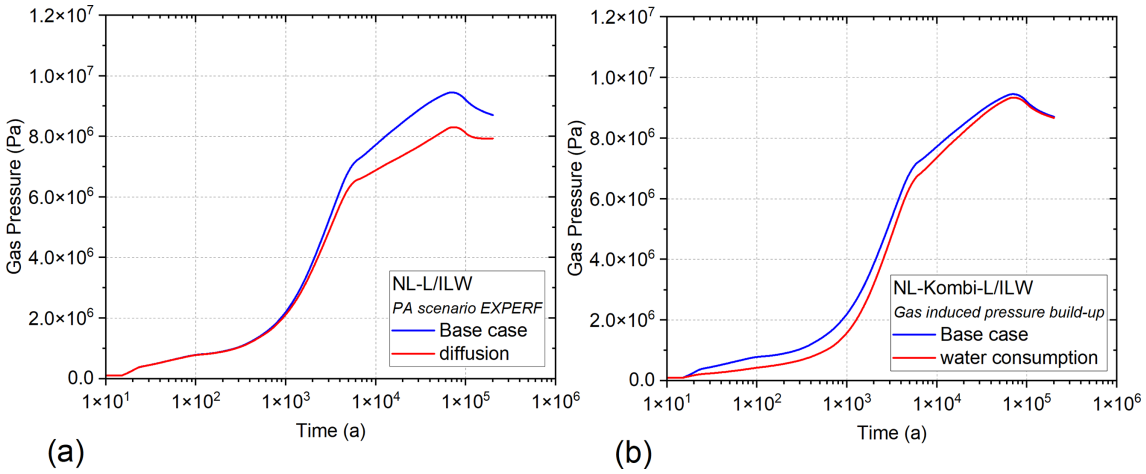

Fig. 4-14: Transients of pressure build-up in the L/ILW emplacement caverns in the base case and in cases considering favourable phenomena

(a) The role of diffusion of dissolved hydrogen, (b) impact of water consumption in the case of a low-permeability host rock.

The simulations presented above provide clear evidence that diffusion of dissolved hydrogen and, to a lesser extent, water consumption due to anaerobic corrosion are processes that contribute to the reduction of gas-induced pressure build-up in the L/ILW near-field. The reasons for not considering these favourable processes in the probabilistic PA-Scenarios in Chapter 6 are the same as for the HLW repository (see last paragraphs in Section 4.4.2).

Scoping calculations addressing the effectiveness of microbial methane consumption for a generic L/ILW repository model are presented in NTB 16-05 (Leupin et al. 2016). The calculations confirm that microbial activity has the potential to reduce the build-up of gas overpressures in the backfilled structures of the L/ILW repository section. However, after closure of the repository, the predictability of microbial processes in the repository is limited, since these processes depend strongly on the evolution of the H^2-C conditions in the L/ILW near-field. Microbial gas consumption was not taken into account in the present PA calculations.

The PA simulations at repository scale together with the results from the probabilistic assessments of gas overpressures in the L/ILW near-field indicate large safety margins, confirming that gas-related impacts do not impair the stable geochemical and geomechanical environment of the L/ILW repository section (Claim 3 in Tab. 4-3).

4.4.5 Gas-induced impacts on radionuclide release – L/ILW repository section

The low hydraulic conductivity of the Opalinus Clay ensures that the L/ILW emplacement caverns remain partially saturated for hundreds of thousands of years. This is shown in the spatial distributions of gas saturations simulated with the 3-D model of a L/ILW emplacement cavern reported in NTB 24-23 (Nagra 2024p), shown in Fig. 4-15. In the early post-closure phase (Fig. 4-15a), water gravitates to the lower part of the cavern while gas accumulates in the mortar surrounding the waste containers in the middle and upper part of the cavern. Low-saturation conditions around the waste containers are enhanced and persist with the accumulation of waste-generated gas for at least 100,000 years (Fig. 4-15d). Notably, this holds for all stacks of containers along the cavern axis (Fig. 4-15e). The low water saturation of the emplacement caverns has a large impact on the release of dissolved radionuclides from waste packages for L/ILW into the cementitious cavern backfill, because the effective diffusion coefficient of the cementitious barrier materials of the L/ILW near-field decreases by orders of magnitude with decreasing water saturation (see Levasseur et al. 2021, 2023). This can be explained simply by the rearrangement of the porewater in the microscopic pore space of the materials. With decreasing water saturation, the porewater remains preferentially in the meso- and micropores of the pore space, whereas the macropores are occupied by the gas phase, leading to a significant enhancement of the tortuosity of the water-filled pore space. The enhancement of tortuosity leads to a reduction of the effective diffusion coefficient. As a consequence, soluble radionuclides of the L/ILW inventory are retained efficiently in the waste forms as long as water saturation remains low. According to the functional relationship between phase saturation and tortuosity given by Millington & Quirk (1961), a decrease in water saturation by a factor of 2 reduces the effective diffusion coefficient by an order of magnitude.

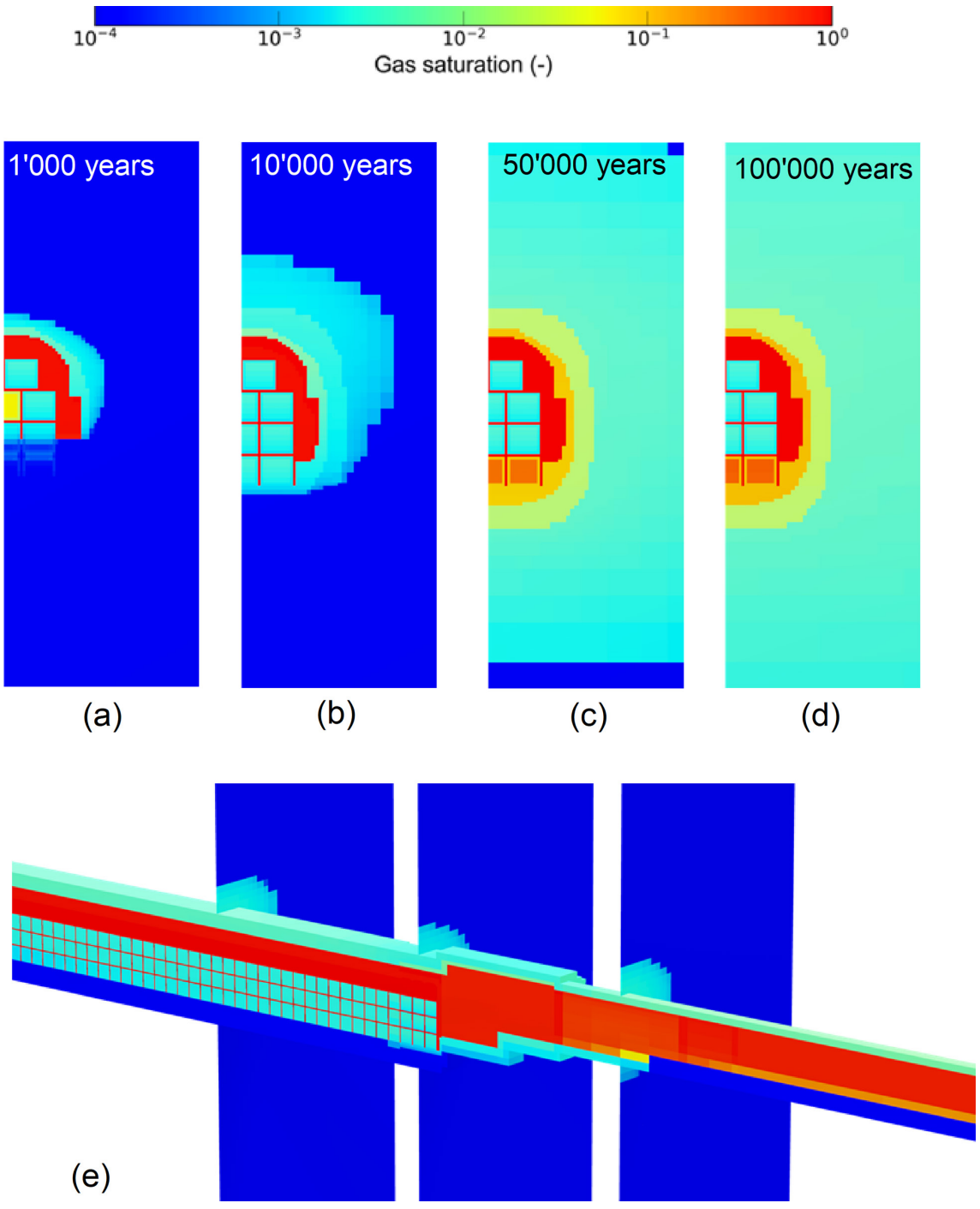

Fig. 4-15: Snapshots of gas saturation in the L/ILW emplacement cavern calculated with the 3-D cavern model: perpendicular to the cavern axis after (a) 1,000, (b) 10,000, (c) 50,000, and (d) 100,000 years, and (e) through the centre of the cavern parallel to the cavern axis after 10,000 years

Referring to the base case in NTB 24-23 (Nagra 2024p).

Fig. 4-16 displays snapshots of L/ILW-generated gas saturation S_g in the L/ILW repository section after 1,000, 10,000, 20,000 and 100,000 years (termed "partial gas saturation", which is the product of gas saturation times mass fraction of H_2 generated by L/ILW). The transients of gas saturation S_g calculated in the L/ILW repository section and in the central area simulated with the 3-D repository model (base case TS00 in NAB 24-25, Nagra 2024m) are shown in Fig. 4-17 and the liquid/ gas fluxes through the sealing sections are presented in Fig. 4-18. In the operations tunnels of the L/ILW repository section, gas saturations increase continuously after backfilling until the end of the simulation due to gas migrating from the L/ILW emplacement caverns and accumulating at the roof of the tunnels (Fig. 4-17b). The same effect with increasing gas saturation during the post-closure phase is observed in the central area of the repository (Fig. 4-17c). Overall, a continuous gas path is maintained along the emplacement caverns, the operations galleries, the L/ILW-V1 and L/ILW-V2 sealing sections and the central area of the repository during the simulated time of 1 million years. On the other hand, the lower part of the V3 seal of the access shaft, composed of compacted bentonite, becomes fully water saturated after ~5,000 years due to porewater inflow from the surrounding formation (Fig. 4-17). After ~20,000 years, a gas phase develops once more in the V3 seal with gas saturations in the order of 1 – 2% due to upward gas migration from the central area.

Flow rates of liquid and gas released through the L/ILW sealing sections are shown in Fig. 4-18. With the backfilling of the L/ILW emplacement caverns (t = 36 years), water is displaced into the ventilated branch tunnels through the L/ILW-V1 seals. After backfilling of the operations tunnel and emplacement of the adjacent L/ILW-V2 seal (t = 56 years), water is displaced into the adjacent ventilated central area until it is also backfilled (t = 96 years). After backfilling of the central area and closure of the repository, water displacement from the L/ILW disposal area towards the operations tunnels and central area continues until ~70,000 years. The maximum liquid flow rate is observed through the L/ILW-V2 seal after ~5,000 years, corresponding to less than 0.2 m^3 per year.

The simulations at repository scale confirm that the water saturation in the L/ILW emplacement caverns remains below 0.7 for more than 100,000 years, until most of the L/ILW radionuclide inventory has decayed, indicating that most of the dissolvable radionuclides are retained efficiently in the cementitious waste forms. The low liquid fluxes of less than 0.2 m^3 per year through L/ILW-V2 seal (Fig. 4-18b) carry a total volume of porewater of 1,780 m^3 from the L/ILW repository section into the central area. Radionuclides which are not retained by sorption but are dissolved in the displaced porewater will be dispersed into the backfilled structures of the central area and eventually migrate into the host rock by diffusion.

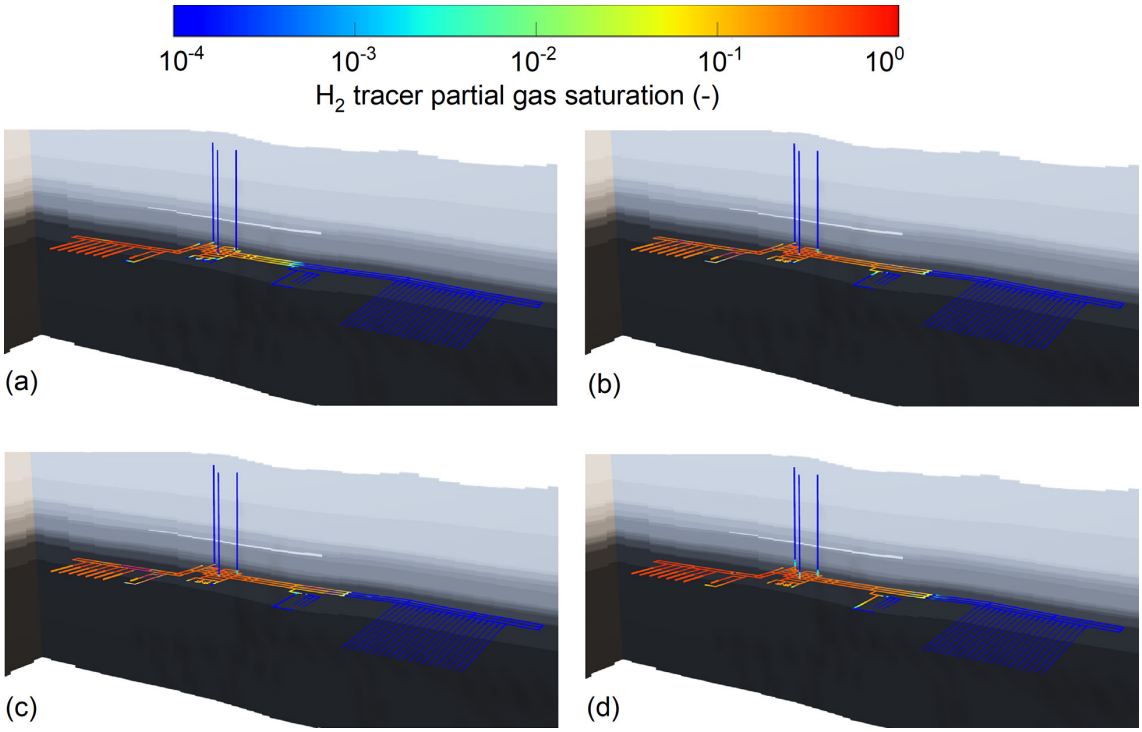

Fig. 4-16: Snapshots of partial gas saturation in the L/ILW repository section calculated with the 3-D repository model

Referring to the base case TS00 in NAB 24-25 Nagra (2024m).

(a – d) After 1,000, 10,000, 20,000 and 100,000 years. Note that the hydrogen from the HLW repository section is specified as a separate gas species to better identify the original of the produced gases.

Direct evidence for the radionuclide retention capacity (IMS safety function) of the L/ILW near-field for dissolved radionuclides is provided by probabilistic release calculations of the dose relevant radionuclide ^{36}Cl (Chapter 6). The performance indicator $TF_{Cl36,V3}$ evaluates the transport of radionuclides along the backfilled repository structures through the V3 seal (definitions in Section 2.5). The Monte Carlo simulations of the probabilistic PA-Scenario *EXPERF* (see Section 6.2) account for the unsaturated conditions in the L/ILW emplacement caverns. The simulation results reveal for the indicator $TF_{Cl36,V3}$ that essentially no dissolved radionuclides will cross the V3 seal within the period for assessment. Several PA-Scenarios were formulated to address deviations from expected behaviour, such as early resaturation of the L/ILW emplacement caverns in the presence of undetected faults (PA-Scenario FLTLILW in Section 6.3). Even these unfavourable scenarios revealed an excellent performance of the L/ILW repository section as a transport barrier for dissolved radionuclides. The calculated tracer fluxes along the backfilled underground structures, expressed in terms of performance indicator $TF_{Cl36,V3}$, confirmed that dissolved radionuclides from the L/ILW cavern will not cross the V3 seal within the period of consideration. In conclusion, repository scale PA modelling confirms the claim that gas-related impacts do not enhance the release of dissolved radionuclides along the backfilled and sealed L/ILW structures (Claim 4 in Tab. 4-3).

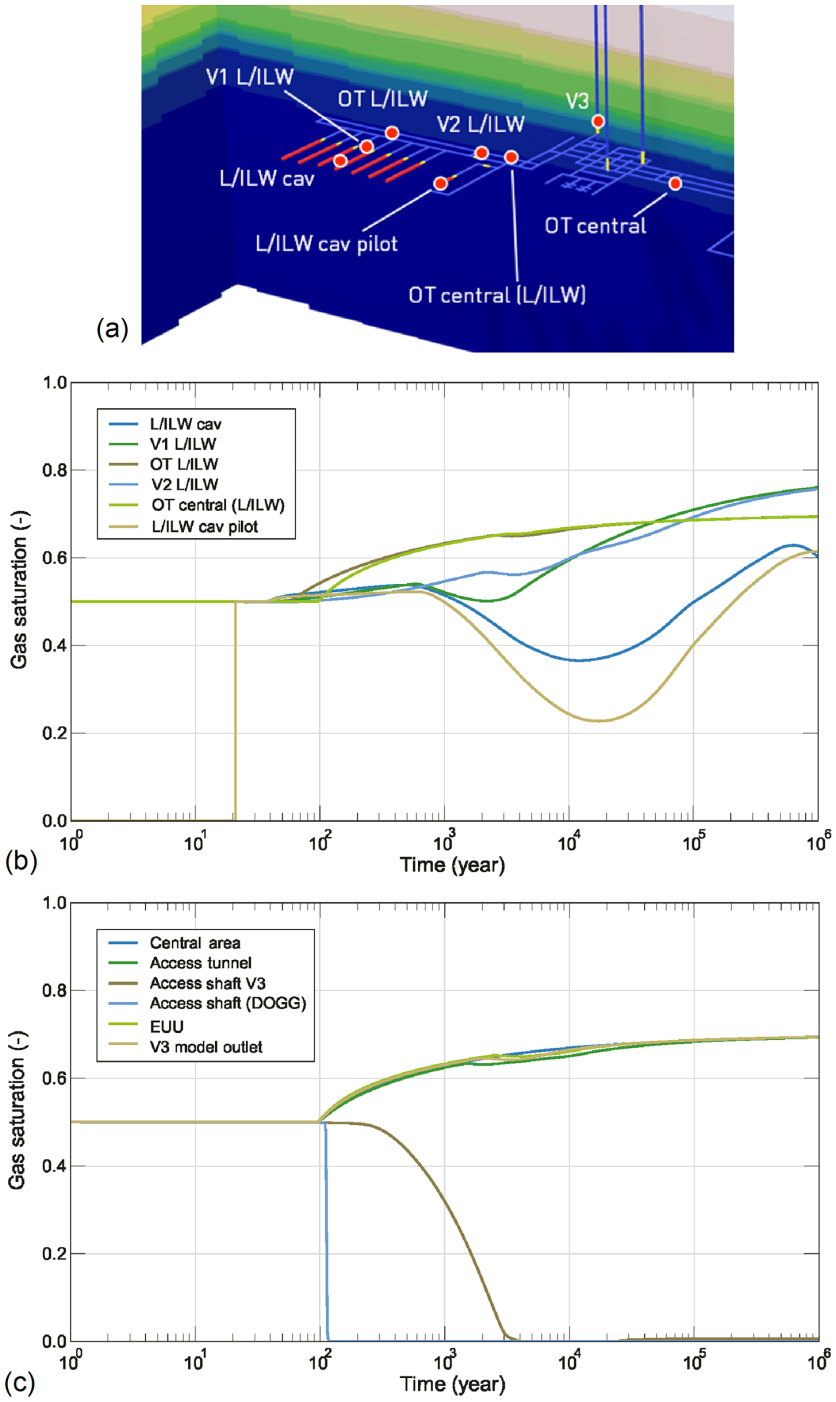

Fig. 4-17: Simulation of transients of gas saturation within and around the L/ILW repository section with the 3-D repository model

Referring to the base case TS00 in NAB 24-25 Nagra (2024m).

(a) Sketch of the L/ILW repository with control points of calculated gas saturation and gas/liquid flux, (b) transients of gas saturation in the L/ILW section, (c) transients of gas saturation in the central area.

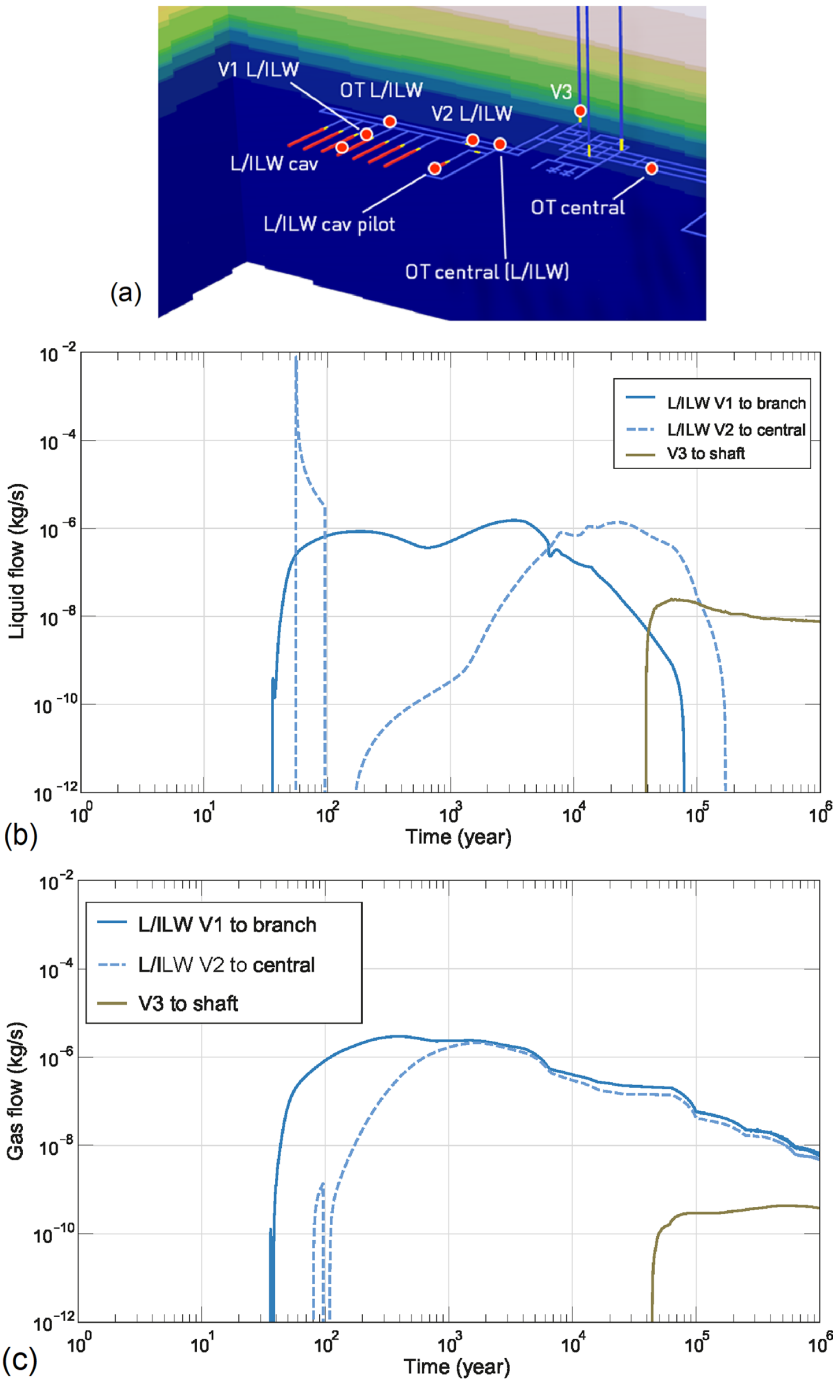

Fig. 4-18: Transients of gas flow rate at selected control points with and around the L/ILW repository section

Referring to base case TS00 in NAB 24-25 Nagra (2024m).

(a) Sketch of the L/ILW repository section with control points of calculated gas/liquid flux, (b) transients of liquid flow, (c) transients of gas flow.

Transport of volatile radionuclides (predominantly ^{14}C) in the L/ILW repository section needs to be considered separately. The closure system is designed such that the waste-generated gases in the L/ILW emplacement caverns are released through the gas permeable seals into the backfilled structures of access tunnels and the central area (see also Fig. 4-16). Hydrogen originating from corrosion of metallic waste represents the dominant species of the gas phase. ^{14}C originating from degradation of organic waste, in the form of CO_2 or CH_4, represents a minor component. The hydrogen can act as a carrier gas transporting ^{14}C out of the repository system when a pressure gradient develops across the V3 seal. According to Fig. 4-18c, the gas breakthrough via the V3 seal into the upper confining units is observed only after more than 30,000 years. The gas released through the V3 seal represents only a small fraction of the amount of gas generated in the L/ILW repository section. Fig. 4-19a shows the normalised amount of gas released through the V3 seal into the upper confining units (i.e., the ratio of released amount of gas divided by the total amount of gas produced in the L/ILW emplacement caverns), indicating that only 0.05% of the generated gas is released into the upper confining units after 100,000 years, while the rest remains in the backfilled repository structures. The transients of total activity of the volatile ^{14}C in the L/ILW repository are presented in Fig. 4-19b (blue line: ^{14}C production rate in [Bq/year], red line: total activity of ^{14}C in [Bq]). The total activity of the volatile ^{14}C released through the V3 seal (green line in Fig. 4-19b) is many orders of magnitude lower, indicating that the backfilled repository structures do not constitute a significant transport path for volatile radionuclides (Claim 4, Tab. 4-3).

The probabilistic PA-Scenarios FLTLILW and V3PERM described in Section 6.3 postulate a fast resaturation of the L/ILW emplacement caverns. Even for such unfavourable conditions, transport along the backfilled structures of the L/ILW repository does not represent a significant release path for volatile radionuclides from the L/ILW repository.

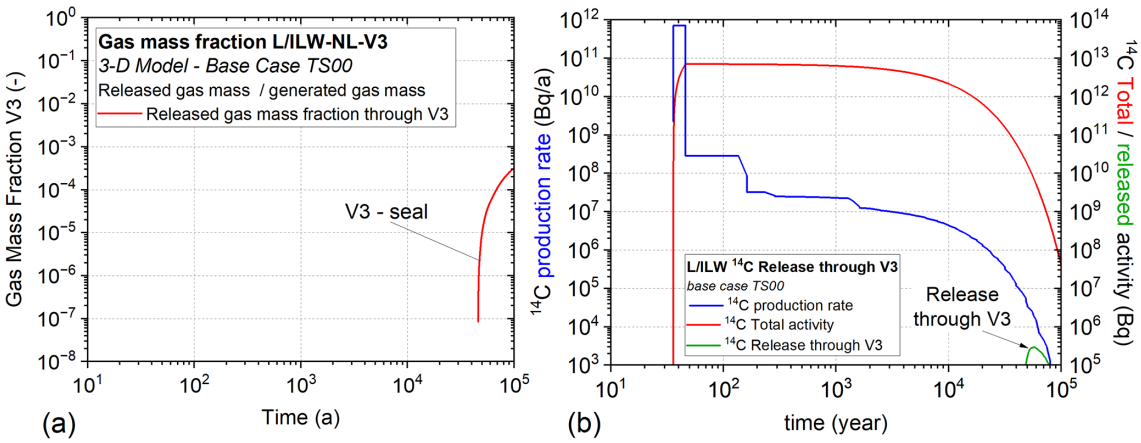

Fig. 4-19: Transients of gas mass fraction and ^{14}C activity released from the L/ILW repository section through the V3 seal

Referring to the base case TS00 in NAB 24-25 Nagra (2024m).

(a) Gas mass fraction released through the V3 seal normalised to the total mass of gas produced in the L/ILW repository section, (b) transients of ^{14}C production rate in [Bq/year] (blue line) and total activity of ^{14}C in [Bq] (red line) according to NTB 24-23 (Nagra 2024p) and calculated activity of the ^{14}C released through the V3 seal into the upper confining units (green line).

4.5 Performance assessment of the total system – concluding remarks

The performance assessment at the system level emphasises the TH^{2}M-C interactions between the individual repository components. It concentrates predominantly on phenomena and processes that occur along the backfilled and sealed underground structures. Following the general PA workflow, claims are formulated for all types of interaction, each related to one or several safety functions. Numerical modelling is the main tool for verifying the barrier performance of the repository at the system level. Chapter 4 documents the arguments and evidence contributing to the systematic evaluation of repository performance at the system level in terms of the assigned safety functions.

Repository-scale modelling of TH^{2}M processes[8] reveals that the HLW and L/ILW sections of the repository are hydraulically and thermally decoupled from each other. The separation distance of around 2 km and the efficient sealing systems ensures that thermal perturbations in the HLW repository section will not impair the safety functions of the L/ILW repository. The HLW-V2 seals provide an efficient hydraulic separation of the two repository sections. This allows the re-saturation and gas accumulation processes in the two repository sections to be analysed independently from each other. Mechanical interactions, such as thermally induced heave above the HLW drifts, are limited to the immediate HLW footprint area.

The thermal- and gas-induced perturbations in the HLW repository section occur at different times, which means that detrimental superposition of the thermal- and gas-related impacts on the safety functions of the engineered and geological barriers can be excluded. Neither the thermal- nor the gas-related disturbances lead to an increased pore-water flow along the sealed and backfilled repository structures, which could otherwise give rise to increased radionuclide release. Likewise, the impact of thermal- and gas-induced perturbations on the mechanical and chemical integrity of the engineered and geological barriers of the HLW repository is modest.

The layout of the repository provides large gas storage volumes, which are crucial for reducing the gas pressure build-up in the L/ILW repository section. The L/ILW-V1-V1 and L/ILW-V2 seals, which are designed to be gas permeable, while still limiting water flows and hence retaining dissolved radionuclides, ensure that gas is distributed in the repository underground structures, including the central area, up to the HLW-V2 and V3 seals. The resulting moderate gas over-pressures in the repository structures of up to 2 – 3 MPa are not expected to impair the mechanical integrity of the engineered and geological barriers of the L/ILW repository section. Volatile radio-nuclides (mainly ^{14}C) are safely contained until they finally disappear due to radioactive decay. At the same time, the unsaturated conditions in the L/ILW emplacement caverns, with moderate gas overpressures, ensure that the release of dissolved radionuclides from the waste packages into the host rock is strongly retarded for very long times, because the mortar backfill around the waste containers represents a capillary barrier for dissolved radionuclides (see Fig. 4-15). So-called “mixing tank conditions” in a fully saturated environment, as used in NTB 24-18 (Nagra 2024r), are based on conservative assumptions with respect to the radionuclide release from the L/ILW near-field.

[8] In clay-rich host rocks, chemical interactions are of little relevance at the scale of the repository system as a whole, because transport of dissolved substances in the repository near-field are diffusion-dominated. This means that chemical interactions are localised processes which occur predominantly at the interfaces between two barrier components. Chemical interactions are discussed at the component level in Chapter 3.

5 Model abstractions and uncertainty quantification in PA

Traceable handling of uncertainty is an indispensable element in the confidence building process contributing to the assessment of post-closure performance and safety of deep geological repositories (NTB 24-19, Nagra 2024t). It is common practice to categorise uncertainty as *scenario uncertainty*, *model uncertainty* (also termed *conceptual uncertainty*) and data uncertainty (also termed *parameter uncertainty*). Thacker et al. (2004) define uncertainty as a potential deficiency in the description of the exact state of a physical system or numerical model that is due to inherent variability (*irreducible uncertainty*) or lack of knowledge (*reducible uncertainty*). When the uncertainties in the parameters describing the state of a physical system or the input parameters to a numerical model give rise to uncertainties in the system response, the effect is termed *propagation of uncertainty*. The systematic characterisation of all input parameter and model uncertainties and the analysis of their effects on the (computed) model response is called *uncertainty quantification*, which aims to bracket the confidence bounds in the expected system response. Section 5.1 is dedicated to the quantification of uncertainties in the performance assessment.

By its nature, a model is an abstraction of a real system, produced by eliminating unnecessary details. Consequently, any type of model abstraction (in other words "conceptualisation") introduces inaccuracy and additional uncertainty, which involves a reduction of the degrees of freedom of the real system. In performance assessment and safety assessment workflows, the "elimination of unnecessary detail" is a required and desirable feature as it can lead to a better understanding of the system behaviour. At the same time, it must be proven that the "elimination of unnecessary detail" does not impair the intended use of a model as a tool for an unbiased assessment of repository safety. This calls for a traceable analysis of uncertainty propagation during the model abstraction procedure. Sources of conceptual uncertainty are associated with the following abstractions:

- Geometric abstractions (Section 5.2) – simplified representation of geometry;
- Process abstractions (Section 5.3) – simplified formulation of phenomena and processes;
- Homogenisation / scaling of parameters (Section 5.4) – spatial and temporal averaging of effective material properties;
- Simplified formulation of boundary conditions, initial conditions and source terms (Section 5.5).

Note that the adequacy of the representation of the real system in a model is subjective and depends on the intended use of the model. Nevertheless, the suitability of a model for its intended purpose can be judged by a well-planned and executed code and calculation verification and model validation (V&V) programme formulated in terms of qualitative and quantitative performance measures. Nagra's efforts in code benchmarking and model validation are summarised in Section 5.6. It concludes the considerations on model abstraction and uncertainty quantification.

5.1 Uncertainty quantification in PA

Uncertainty quantification in PA is embedded in the general safety assessment uncertainty management framework (NTB 24-19, Nagra 2024t). Tracking of uncertainty propagation along the model abstraction chain is a complex process, which starts with the model-supported interpretation of uncertain field observations, site characterisation data and laboratory experiments. Using the modelling framework, the uncertainty ranges of the associated model outputs can be traced back to the uncertain input parameters in a quantitative manner. At the other end of the abstraction chain, focus is on the performance of the entire repository system, or a component

thereof, with respect to predefined targets. For this, simplified model geometries, simplified formulations of phenomena and processes, homogenised model components and simplified boundary / initial conditions are specified and feed into the PA/SA models as uncertain inputs for estimating the uncertainty ranges of the corresponding performance indicators. As illustrated in Fig. 5-1, the process of uncertainty quantification can be decomposed into two key steps:

- *Identification and quantification of uncertainties associated with model abstractions:* conceptual uncertainties associated with the model abstraction process are identified and quantified in numerical benchmarks as part of a model validation procedure to ensure readiness of the simplified PA models for quantitative evaluations. Examples of such model validation are given in Sections 5.2 to 5.5.
- *Probabilistic PA – quantification of confidence ranges:* Parametric uncertainty of PA model inputs is used to calculate the confidence ranges of the PA model outputs. The probabilistic PA workflow is applied in Chapter 6 to evaluate in a quantitative manner the expected barrier performance of the repository system and deviations thereof (see also Fig. 6-4).

The assessment workflows are embedded in a long-term code verification and model validation process in the framework of Nagra's RD&D Programme (see Section 5.6), forming a solid basis for the process of uncertainty quantification.

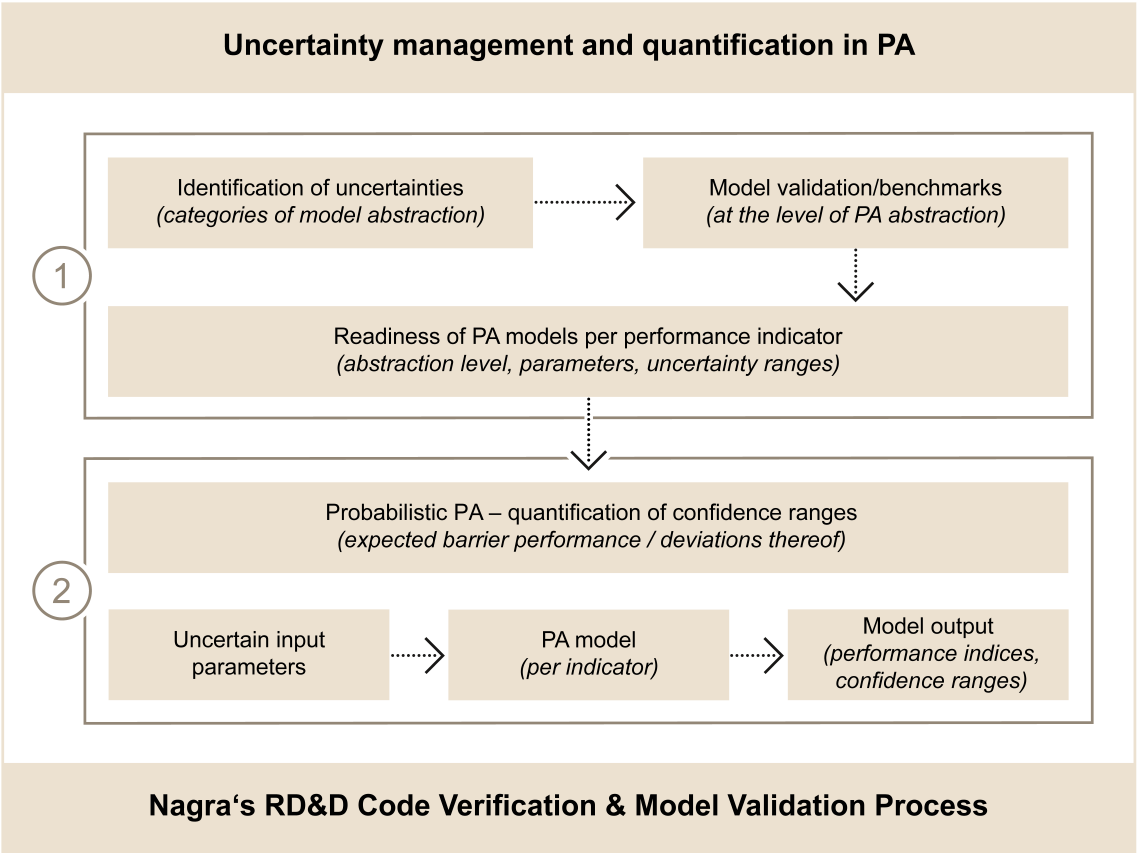

Fig. 5-1: Uncertainty quantification in PA: a two-step procedure embedded in a long-term code verification and model validation process in the framework of Nagra's RD&D Programme

5.2 Geometric abstractions

Like most realistic systems, a geological repository cannot be represented in all its geometric detail by the corresponding PA model. Sensible reductions of geometric complexity are made by the "elimination of unnecessary detail". At the same time, it must be proven that the simplified PA model is still able to simulate the required performance indicators without unacceptable bias. Evidence is provided by a traceable analysis of uncertainty propagation along the model abstraction chain, as shown in the subsequent examples. A comprehensive discussion of uncertainty propagation associated with geometric abstraction is given in NAB 24-25 (Nagra 2024m).

5.2.1 Reduction of dimensionality

The transport of dissolved radionuclides released from the HLW emplacement drifts through the CRZ and into the Keuper and Malm aquifers is a 3-D process driven by diffusion and advection. Modelling of the complex transport paths with high spatial resolution requires a detailed representation of the repository structures and of the geological layers in a 3-D framework. From a computational point of view, such complex 3-D model set-ups are inappropriate for probabilistic analyses as used to assess uncertainty and robustness. However, a limited number of deterministic transport simulations can be carried out with a detailed 3-D repository model. The results are then used for benchmarking the accuracy of simplified 2-D and 1-D approaches, which are preferred for probabilistic assessments of barrier performance due to their lower computational demands.

Fig. 5-2 displays different levels of abstraction for an HLW repository (or the HLW section of a combined repository) in terms of dimensionality. The 3-D model (Fig. 5-2a) is a cube with a footprint of 2,200 m by 2,200 m enclosing 20 HLW emplacement drifts, each 850 m long, spaced every 40 metres and located in the middle of the host rock. The geological model is implemented as a layer stack of lithostratigraphic units with variable thicknesses, ranging from base Mesozoic to ground surface. The corresponding 2-D model set-up (Fig. 5-2b) covers a vertical cross-section through the centre of the HLW repository, perpendicular to the emplacement drifts. The model domain is 2,000 metres wide, again extending from base Mesozoic to ground surface, and enclosing all 20 emplacement drifts. A fine numerical discretisation is applied in the vicinity of the drifts. The 1-D model (Fig. 5-2c) is displayed as a vertical stack of 1-m thick, 800-m wide, and 850-m long elements with a 680,000 m^2 cross-sectional area (equal to the areal footprint of the repository).

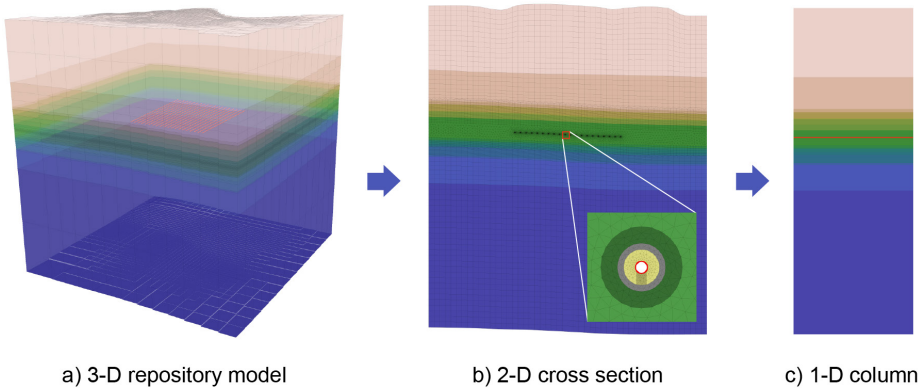

Fig. 5-2: HLW repository displayed at different levels of geometric abstraction

(a) 3-D representation of the HLW repository section with 20 HLW emplacement drifts in red, (b) 2-D cross-section through the centre of the HLW repository section with 20 emplacement drifts, and (c) 1-D representations of the HLW repository section in red.

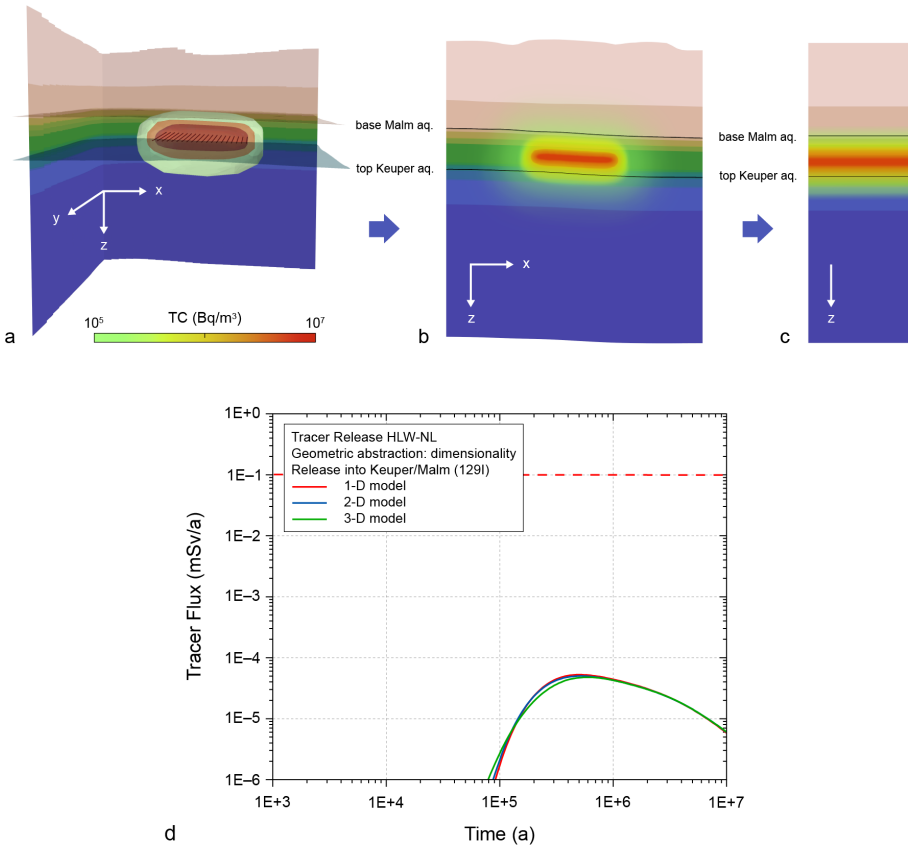

Fig. 5-3: Contour plots of tracer concentrations after 1,000,000 years and transients of tracer flux into the Keuper and Malm aquifers

(a) 3-D model, (b) 2-D model, (c) 1-D model and (d) corresponding transients of tracer release from the emplacement drifts into the Keuper and Malm aquifers (calculated dose, corresponding to ^{129}I releases to the surface environment assuming the present-day climate).

To assess the sensitivity of simulated diffusive tracer transport to the level of abstraction, an initial activity of 4.4×10^{12} Bq of ^{129}I tracer (corresponding to a mass of 68 kg, representing 10% of the total inventory; see App. C.1) is instantly released from the emplacement drifts and allowed to diffuse for 10 million years. Fig. 5-3a – c shows the contours of the diffused tracer concentration calculated using the 3-D, 2-D, and 1-D model set-ups. The transients of the sum of the tracer fluxes into the Keuper and Malm aquifers are shown in Fig. 5-3d.

The contour plots of tracer concentration and the tracer flux for the 3 levels of abstraction considered are similar both in terms of magnitude and timing. Only the 3-D model deviates slightly, in that the first arrival happens earlier and the peak flux is reached later. This discrepancy can be explained, at least partly, by the coarser mesh used to discretise the 3-D model, which yields less accurate results compared with the finerduscretisations used in the 1-D and 2-D models. More detailed analyses of the origin of the deviations were omitted because the computational efforts for mesh refinement of the 3-D model increase disproportionally.

5.2.2 Simplified model geometries

Geometric simplifications are always made in any approximation of the real repository structures. Depending on the intended purpose, model conceptualisations represent structures using simple shapes and assuming perfect implementation of these shapes. For the purposes of safety-related performance assessments on the scale of the entire repository, it is possible to reduce the level of detail in which the repository layout and structures are implemented in model geometries, as shown in the example in Fig. 5-4a. The main components of the repository, such as waste emplacement rooms and access tunnels, are approximated in 3-D using elements with rectangular cross-sections by scaling volumes and cross-sectional areas of the respective components. Such geometries are used for deterministic assessments of the entire system, aimed at investigating TH^2M interactions between the repository components (see Chapter 4).

The impact of the abstraction inherent in this approach can be assessed by comparing with models also implemented in 3-D, but at the scale of individual components, allowing the introduction of a greater level of detail (Fig. 5-4b). The comparison is carried out in terms of key metrics related to indicators used in the performance assessment and aims to confirm that the abstracted representation at the repository scale captures the essence of component-scale effects in a representative and conservative manner. These more detailed models are further used for deterministic in-depth assessments of TH^2M couplings on the level of components (see NAB 24-25, Nagra 2024m).

In the next step, so-called 2.5-D geometries are implemented at selected locations, combining repository components and their respective volumes with cross-sections through the geological environment (Fig. 5-4c; see NAB 24-25, Nagra 2024m for further details). These geometries are used for probabilistic assessments to address parametric uncertainty (see Chapter 6). The appropriate implementation is achieved through benchmarking and validation with the 3-D models.

Benchmarking of the three types of models, with further model refinement, if necessary, aims to (i) reduce the deviations in modelling results and (ii) quantify the uncertainties associated with the different levels of geometric abstraction. Reduction in any deviations between the outputs of the three model types can be achieved by adjusting the lengths or cross-sections of the different repository components, or by modifications to the effective properties assigned to the backfill materials (see also Section 5.4.1). An example of such a benchmarking process is shown in Fig. 5-5, which shows transients of gas saturation and gas pressure build-up in the L/ILW emplacement caverns, derived using the models shown in Fig. 5-4a and c. Fig. 5-5a illustrates that the 3-D model of the entire repository (L/ILW section, central area, HLW section), with its coarse representation of the underground structures, does not adequately represent gas saturation in the L/ILW emplacement caverns. The transients of gas saturations for a 2.5-D model of the seven caverns and a 2.5-D model of a half cavern match almost perfectly. The consistency of

these latter results with those observed in the analysis of the hydraulic evolution of the L/ILW emplacement cavern (NTB 24-23, Nagra 2024p) provides confidence in the ability of the two models to simulate the evolution of the unsaturated L/ILW cavern near-field with the accuracy that is necessary, for example, to investigate corrosion and precipitation effects.

The evolution of gas pressure in the L/ILW emplacement caverns was introduced in Section 2.5.4 as an important performance indicator, required for the probabilistic assessments as part of the workflow for performance screening. Fig. 5-5b shows the development of gas pressure in the L/ILW emplacement caverns for each of the three models, following a comprehensive calibration process in which total pore volumes of the individual repository components and of the entire repository are matched to the specifications given in the engineering reports (NAB 23-01 Bd. 1 – 9, Nagra 2023a). Details of the calibration process, including the scaling of porosities and lengths and cross-section areas of the individual repository components, are given in NAB 24-25 (Nagra 2024m). The transients in Fig. 5-5b compare well in all three models, especially in the high-pressure range, which is of particular relevance in PA. In the example presented in the figure, the peak pressures differ by less than 0.1 MPa, indicating that all three models are suitable for PA-related simulations of gas pressure build-up in the L/ILW repository section, since there are no significant differences in accuracy. From the perspective of computational efforts, the 2.5-D model of a half cavern is the preferred set-up to carry out the probabilistic simulations, which are presented in Chapter 6.

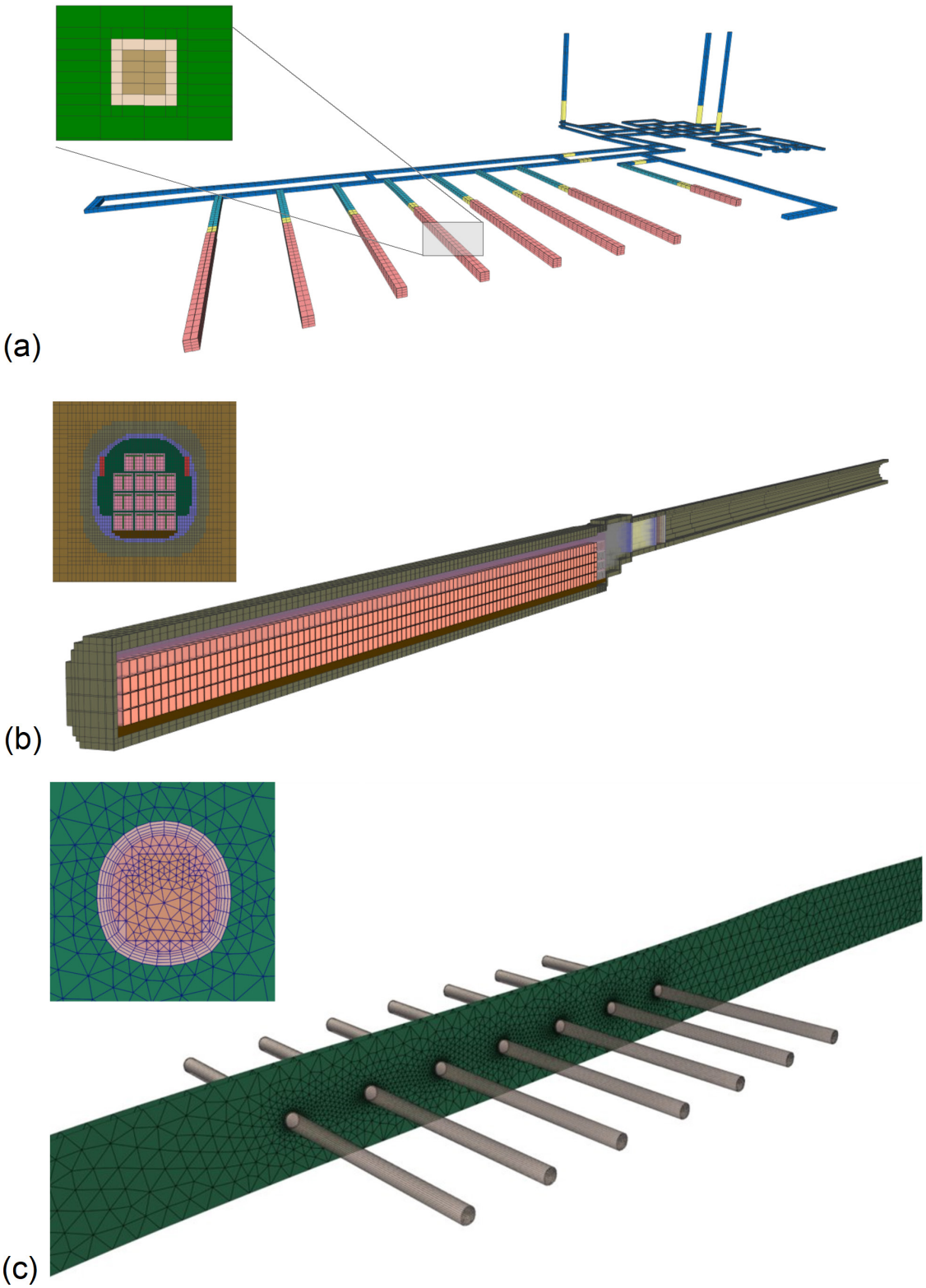

Fig. 5-4: Examples of simplified geometric representations of the L/ILW repository section as part of the entire repository

(a) 3-D representation of the entire repository, including the L/ILW and HLW repository sections; (b) 3-D representation of a single L/ILW emplacement cavern; (c) 2.5-D representation of an L/ILW repository section.

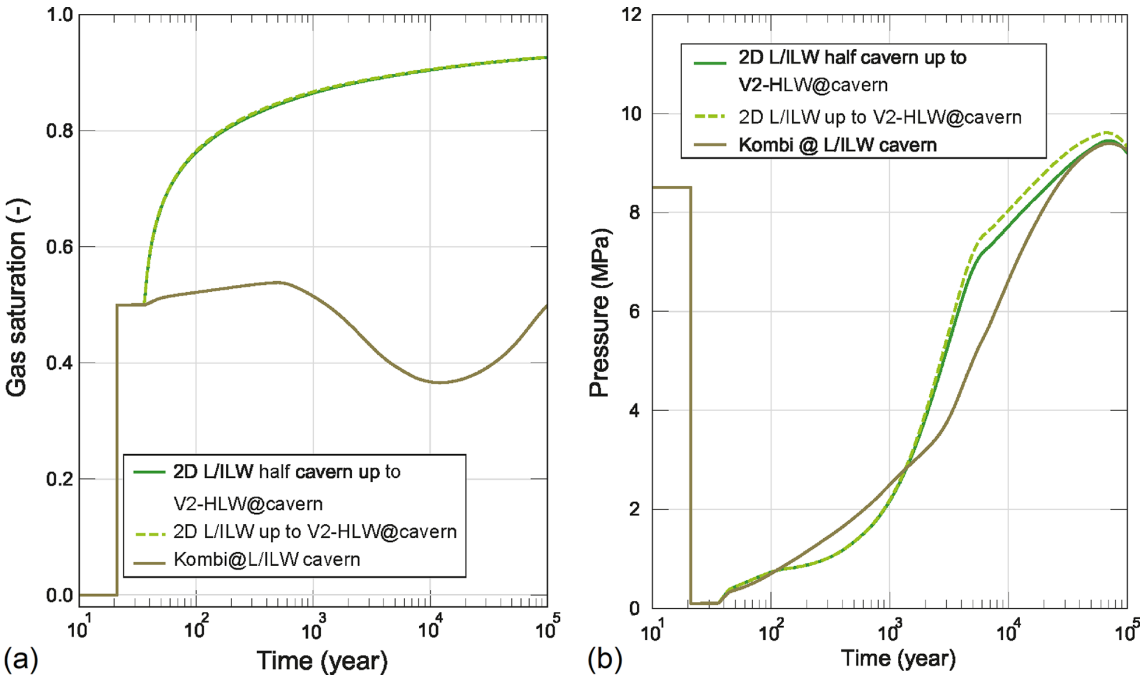

Fig. 5-5: Comparison of modelling results derived from the three models of the L/ILW repository at different abstraction levels

(a) transients of gas saturation; (b) transients of gas pressure.

The observation point is in the roof of the central L/ILW emplacement cavern (see Fig. 5-4).

5.3 Simplified representation of phenomena and processes

Modelling of physical phenomena is most useful when it is based on a description of the underlying processes rather than purely on correlations of observed data, as it offers the possibility to assess how the system will react when subjected to different initial and boundary conditions that are beyond the range of data used in the correlation (Pinder & Gray 2008). Modelling adopted in the performance assessment is therefore based on fundamental principles of continuum mechanics, namely the conservation of mass, the conservation of momentum, and the conservation of energy. However, modelling realistic systems based on purely physical expressions is unfeasible. NAB 24-25 (Nagra 2024m) gives a comprehensive synopsis of the principles that govern the systems of interest and the associated assumptions and simplifications adopted in the performance assessment. The following paragraphs provide some specific examples of process abstraction, which are relevant for performance assessment.

5.3.1 Two-phase flow in deformable porous media

Flow and transport problems in porous media can be expressed as mathematical formulations of conservation laws. However, these equations alone are not sufficient to describe the system behaviour. Even the assumption of a rigid, i.e., non-deformable control volume that is available to fluids introduces material-specific parameters like porosity and specific heat capacity. Moreover, the laws for mass advection, mass diffusion, and heat conduction introduce material-dependent parameters, namely hydraulic conductivity, diffusion coefficient, and thermal conductivity. Even with such material parameters, the number of unknown state variables that arise is greater than the number of conservation equations, so the equations must be complemented by correla-

tions, or constitutive relationships, that describe some system dynamics in terms of other variables (e.g., dependency of viscosity on temperature). The need for constitutive relationships complicates efforts to model real systems, especially in porous media where constitutive relationships may be scale- and time- dependent.

In the case of multiple immiscible fluids and species present in the system (termed TH^2 systems), conservation laws are formulated in a similar way for each phase and each species. Two additional state variables are introduced when two immiscible fluids are present in a porous medium: fluid saturation, defined as the fraction of the pore space occupied by the fluid, and capillary pressure, defined with the Laplace equation as the difference between non-wetting (e.g., gas) and wetting (e.g., liquid) fluid pressure. An additional constitutive relationship is formulated between capillary pressure and fluid saturation, introducing the so-called entry pressure, also known as capillary threshold pressure, a shape parameter, residual saturations and further empirical coefficients. In gas-water problems, the capillary threshold pressure in practice represents the difference between gas and water pressure required to displace porewater from the medium when it is initially fully water-saturated. In theory, the capillary strength corresponds to the capillary pressure of the largest pore radius that the gas pressure needs to overcome for the gas to enter the water-filled pores, whereas the shape parameter is a proxy for the pore size distribution and variability of the pore network. Moreover, Darcy's law is extended by the so-called relative permeabilities for each fluid, expressed as constitutive functions of fluid saturation, to account for the fact that the presence of the other fluid decreases the space available for flow.

In summary, in visco-capillary flow systems, fluid transport is controlled by the interaction of viscous, capillary and gravity/buoyancy forces, phase partitioning ("solubility") and diffusion of species, and the connectivity and variability of the pore network. The integral form of the mass and energy conservation equations expressing this problem, complemented by the extended Darcy's law and the constitutive relationships (e.g., relative permeability - saturation relationships, capillary pressure - saturation relationship) required to close the system of equations, can then be discretised and solved by means of numerical modelling.

A further degree of complexity is added when the porous medium is deformable rather than rigid (resulting in a TH^2M system). Material-specific stress-strain relationships must be specified to account for (potentially irreversible) deformations in response to changes of total stress and pore pressure and the momentum equations must be extended to account for the effect of pore pressure on the stress state of the solid skeleton of the porous medium ("effective stress formulations"). Due to the irreversibility of the deformation processes, constitutive relationships are no longer time invariant material properties but depend on the hydro-mechanical state of the porous medium. Back-analyses of combined water and gas injection experiments with Opalinus Clay samples in an oedometric cell are reported in NAB 24-27 (Nagra 2024f). The experiments confirm that gas invasion in fully saturated Opalinus Clay involves an expansion of the test specimen in response to gas pressure build-up, and a contraction of the sample, when gas pressure decreases. The back-analyses with a numerical two-phase flow simulator (iTOUGH2) confirm that the deformation behaviour of the test specimen can be reproduced comparatively well with extended constitutive relationships.

Comprehensive code verification and model validation exercises have been carried out in the framework of the European Joint Programme on Radioactive Waste Management – Work Package EURAD-GAS (2020-2024), aimed at building confidence in TH^2M modelling of gas transport processes in deformable media. The results are reported in Wendling et al. (2024) and Marschall et al. (2024), encompassing benchmark exercises on gas transport in engineered and geological clay barriers. Modelling activities covered a wide range of spatial scales, from the analysis of small-scale laboratory experiments on gas transport in clay-rich barrier materials to gas release calculations at the scale of the entire repository system. Notably, broad agreement was

reached among the participating modelling teams to use classical two-phase flow modelling frameworks with extended constitutive models to address the deformation of the solid skeleton by complementary stress-strain relationships.

5.3.2 TH²M-to-TH² abstraction

The evolution of the near-field around an HLW emplacement drift depends on complex coupled thermal-hydrological-mechanical processes. TH²M numerical codes have been developed and validated in the past for the simulation of the coupled non-isothermal two-phase flow and hydro-mechanical phenomena associated with repository-induced effects in the near-field of an HLW repository. The TH²M codes are based on formulations of physical conservation laws and constitutive laws described in Section 5.3.1. However, it is most practical to perform the computationally expensive performance assessment calculations using a simpler conceptual model that only explicitly accounts for thermal-hydrological processes (termed TH² if separate gas and liquid phases are considered). This simplification requires a TH²M-to-TH² abstraction and model validation step.

The numerical implementation of TH²M-processes using simplified TH² models must be validated specifically for the intended purpose, which includes a traceable quantification of the uncertainties associated with the abstraction process. Process-related uncertainty quantification is carried out in the context of numerical benchmarks, demonstrating that TH²M processes can approximately be represented by determining effective TH² parameters. These effective parameters are estimated by the inversion of data reflecting TH²M processes using a TH² model. An example describing the validation workflow for simplified representation of the TH²M evolution of the HLW near-field in a 2-D TH² numerical model is given in App. D.

5.3.3 TH²C abstractions

Modelling the geochemical evolution of the multi-barrier system at the repository scale using fully coupled TH²C models is neither computationally feasible nor scientifically warranted. Multiple types of empirical and experimental evidence have been used in the past to demonstrate that repository-induced chemical and biological processes, such as the propagation of redox fronts, alkaline plumes or chemical alteration of interfaces between barrier components, are limited to the immediate vicinity of the repository structures. In performance assessment, TH²C models and simplifications thereof are mainly needed to evaluate hydro-chemical interactions at the component scale.

A common approach adopted in geochemical models is to use abstracted representations of the two-phase flow transport problem, postulating that chemical reactions predominantly depend on the availability of water. Hydraulics are therewith approximated, e.g., assuming stationary conditions or using proxy state variables, mainly fluid saturation and/or flows, in the form of boundary conditions or source terms.

Accordingly, the essence of geochemical effects in the TH² consideration is captured in a simplified manner. The abstraction follows two main assumptions:

- Chemical reactions that result in changes in the chemical composition of fluids can be approximated as species source and sink terms that are variable in time and space.
- Chemical reactions that result in mineral precipitation / dissolution can be approximated as porosity and permeability changes that are variable in space and time.

In turn, variants of source / sink terms and porosity are assigned to specified sections of the repository in performance assessment modelling, e.g., in the waste emplacement rooms. These feed directly into the mass conservation formulations adopted for the TH^2 problem. The TH^2 model outcomes feed back into the geochemical analyses to check assumptions and inform variants related to the hydraulic evolution of repository components.

The geochemical evolution of individual components of the multi-barrier system has been the subject of previous PA modelling activities. This includes studies on water consumption associated with steel corrosion in the HLW near-field (Senger et al. 2008), salt enrichment in the backfilled L/ILW emplacement caverns (Senger & Papafotiou 2013), and consumption of repository-produced gases caused by chemical reactions and microbial activity (NTB 16-05, Leupin et al. 2016 and NTB 16-03, Diomidis et al. 2016). Three examples of TH^2C process abstractions related to the safety case are discussed in App. D.2.

5.4 Homogenisation / scaling of parameters

The effect of parametric uncertainties must be taken into account when effective material properties are assigned to the model components. The causes of parametric uncertainties are diverse and include reducible uncertainties originating from a lack of knowledge of the fabric of the modelled material, as well as simply the inaccurate representation of the model shape due to computational constraints (e.g., implementation of the waste containers in the L/ILW emplacement cavern; Section 5.4.1). In addition, irreducible uncertainties may arise due to the inherent variability / randomness of the modelled material properties (Section 5.4.2). Homogenisation or scaling processes are required to average adequately the material properties such that the modelled phenomena and processes remain unbiased. Evidence must be provided to demonstrate the validity of the modelling results obtained using homogenised parameter assignments. For this, numerical benchmarks are carried out, aimed at quantifying the deviations between the modelling results calculated using heterogeneous and homogenised parameters.

5.4.1 Parametric uncertainties associated with the inaccuracy of the model form

Geometric model abstractions are inherently to the simplified representation of the individual components of the multi-barrier system, which is tailored to the phenomena and processes under consideration. In Section 5.2.2, three examples were discussed that represent the L/ILW repository structures at different levels of detail depending on the intended use of the models. Benchmarking of the three models was aimed at identifying and then minimising the deviations in the model results. It was stated that the minimisation of deviations between the outputs of the three models can be achieved (i) by adjusting the lengths or cross-sections of the different repository components, or (ii) by modification to the effective properties of the backfill materials. The following example is dedicated to the assignment of modified effective properties to the backfill materials.

Fig. 5-6 shows three 2-D representations of an L/ILW emplacement cavern, developed for different purposes. Fig. 5-6a shows a detailed model set-up that takes into account the lining, backfill mortar and the different containers and materials inside them (LC, Dorodur, waste packages). This model set-tup has been formerly used for the simulation of salt enrichment during the resaturation of the backfilled L/ILW emplacement caverns (NAB 13-72, Senger & Papafotiou 2013). The coarser grid in Fig. 5-6b has been used to simulate resaturation processes in the L/ILW emplacement cavern and to model the release of dissolved species from the waste containers into the L/ILW near-field. All materials in the containers are lumped into a single material with properties similar to those of concrete. The gaps between the containers are still discretised and treated as a high-porosity material to maintain the effect of gas pathways. The porosity of the

mortar backfill is scaled accordingly to correct for volume differences introduced by the coarser mesh. The simplest grid (Fig. 5-6c) was established for the simulation of gas pressure build-up in the L/ILW near-field. This model set-up is implemented in the repository model with a single material representing the waste containers and surrounding backfill mortar. Volumetric averaging is used for porosity, and geometric averages for permeability and capillary strength. In all three cases, the EDZ surrounding the repository structures is also homogenised and represented in a stylised fashion.

An efficient way to fit the outputs of the three models in terms of gas saturation and gas pressure evolution is the assignment of model-specific effective parameters to the backfill materials ("property scaling"). A more detailed discussion of property scaling is given in NAB 24-25 (Nagra 2024m).

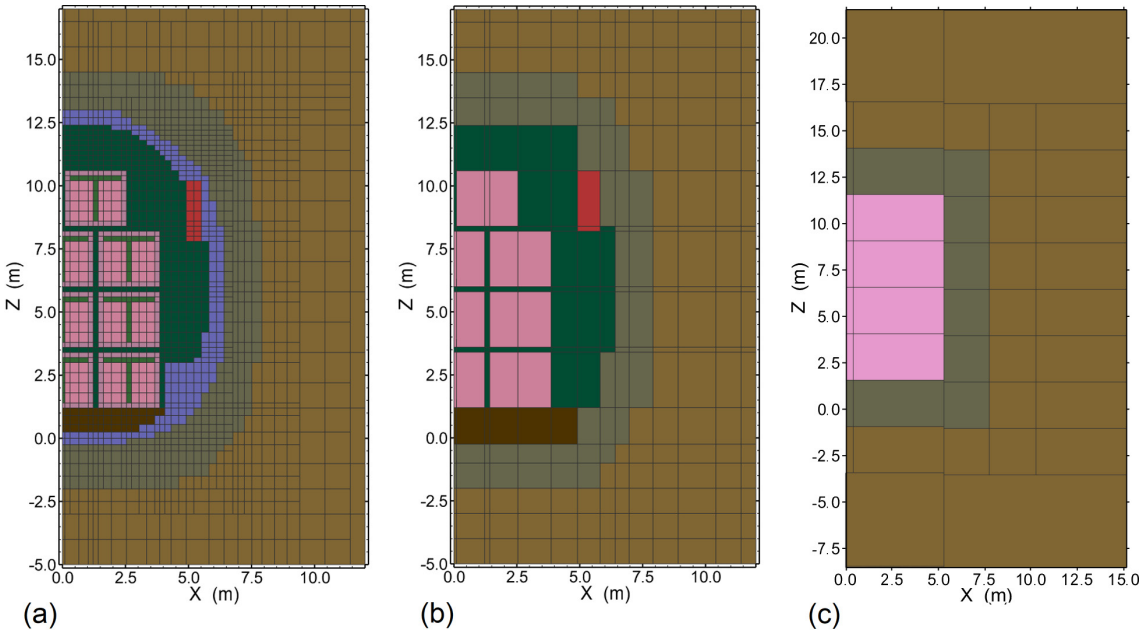

Fig. 5-6: 2-D representations of an L/ILW emplacment cavern for different purposes
Consistent modelling outputs are achieved by property scaling.

5.4.2 Inherent variability of the modelled material properties

An example is shown in the following paragraphs that illustrates the role of facies variability of the Opalinus Clay on its performance as a transport barrier.

As stated in Section 5.2.3 of NTB 24-17 (Nagra 2024k), the Opalinus Clay is the most clay-mineral-rich unit in all three siting regions considered in SGT Stage 3, with no systematic differences in the mineralogical composition between the siting regions. The lateral and vertical lithological variability is generally small compared with other Mesozoic formations. A recent subfacies classification of the Opalinus Clay has been reported in Section 4.2.6 of NTB 24-17 (Nagra 2024k), which was also applied to represent the host rock in the NL siting region. It comprises six subunits, with two dominant facies classified as homogenous claystone (SF1) and finely laminated claystone (SF2), complemented by four auxiliary facies, called lenticular claystone (SF3), thin-bedded limestone (SF3), siderite rich limestone (SF4) and limestone hardground (SF6).

Inspired by this subfacies classification scheme, a generic stochastic model was developed for the Opalinus Clay in the NL siting region to investigate the role of facies variability on the performance of the host rock as a transport barrier for dissolved radionuclides. A stochastic realisation of the facies model FPi(x,z) is shown in Fig. 5-7a, which presents a vertical cross-section through the centre of the HLW repository section.

Each of the facies exhibits characteristic lithological and mineralogical features. In the generic calculations presented in the following paragraphs, each facies is characterised by a specific probability density function of clay mineral content $PDF_{cc}(FPi)$, such that the calculated bulk clay mineral content of all facies is consistent with the observed values. The stochastic facies distribution FPi(x,z), together with the probability density functions of clay mineral content for each facies, allow the simulation of random distributions of clay mineral content cc(x,z). In a next step, the known empirical correlations between clay mineral content and effective diffusion coefficient (see NTB 23-08, Glaus et al. 2024) are used to derive the corresponding random fields D_{eff} (x,z) in the Opalinus Clay formation. Fig. 5-7b shows a single realisation of the D_{eff} (x,z) distribution in the Opalinus Clay formation as used for the probabilistic PA calculations. It is worth noting that the spread of the D_{eff}-values in the Opalinus Clay is (x,z) is modest, typically in the range 2 – 3 × 10^{-12} m^2/s (arithmetic mean: 2.6 × 10^{-12} m^2/s; geometric mean: 2.4 × 10^{-12} m^2/s; harmonic mean: 2.3 × 10^{-12} m^2/s). The homogeneous D_{eff}-values of the other rock units represent the reference values according to Tab. A-6.

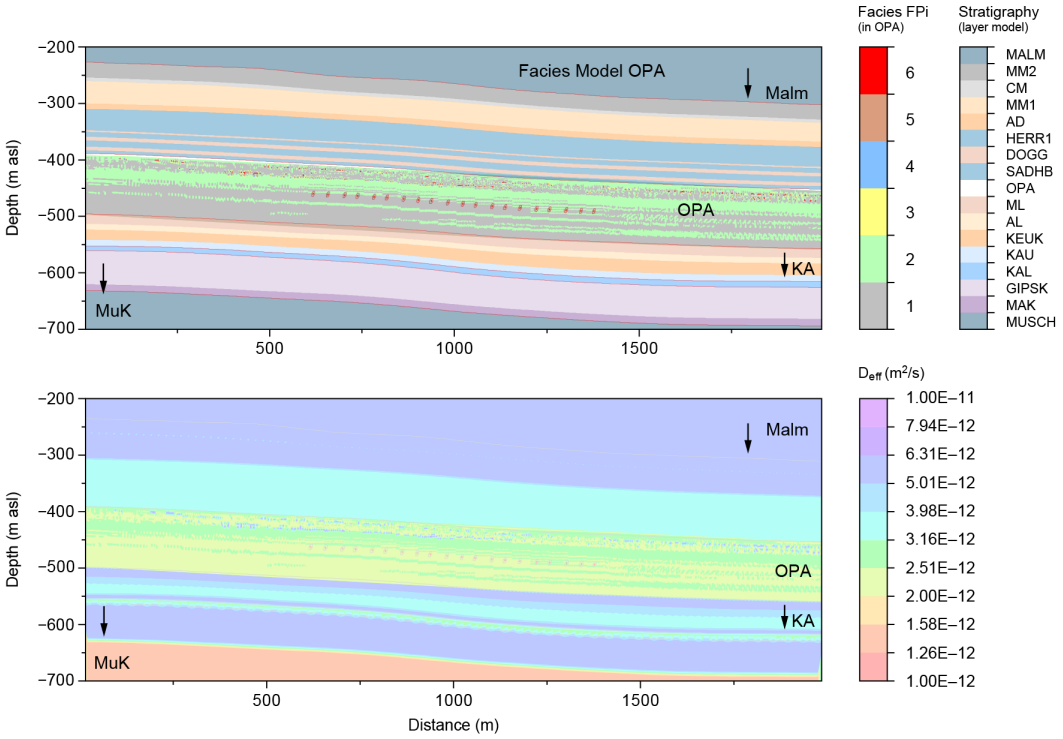

Fig. 5-7: Generic stochastic facies model of the Opalinus Clay in the NL siting region embedded in the layer stack between Muschelkalk and Malm aquifer

Vertical cross-sections through the centre of the HLW repository section (the 20 HLW drifts are marked in red): (a) single realisation of the spatial distribution of the facies FP1 – FP6 in the Opalinus Clay; (b) single realisation of the random distribution of D_{eff}(x,z) in the Opalinus Clay. Note that the homogeneous D_{eff}-values of the other rock units represent the best estimates according to Tab. A-6.

Probabilistic transport simulations were carried out with the 2-D model set-up shown Fig. 5-7b. For this, a total of 100 realisations of the D_{eff} (x,z) distribution in the Opalinus Clay were generated. A non-sorbing tracer, representing the dose-relevant radionuclide ^{129}I, was released from the HLW emplacement drifts into the CRZ, finally reaching the regional aquifer systems. The tracer flux $TF_{CRZ,I\text{-}129}$ defined in App. A.1 was used as the performance indicator that evaluates the efficiency of the Opalinus Clay to retain the ^{129}I.

100 Monte Carlo simulations were conducted with the stochastic D_{eff} (x,z) distributions and the sum of the tracer fluxes at the top and base of the Opalinus Clay was calculated. The results were compared with the corresponding tracer fluxes derived for a homogeneous representation of the Opalinus Clay with a constant effective diffusion coefficient, representing the geometric mean of the stochastic D_{eff} distributions. Fig. 5-8 presents the results of the probabilistic simulations, indicating that the 100 simulations with stochastic property distributions are practically indistinguishable from the simulations with the homogeneous Opalinus Clay. This is because the spread of effective diffusion coefficients in the 6 facies of the Opalinus Clay is quite modest, in the range $2 - 3 \times 10^{-12}$ m^2/s. The simulation with homogeneous host rock properties (geometric mean of $D_{eff} = 2.4 \times 10^{-12}$ m^2/s) represents the barrier efficiency of the host rock without significant loss of accuracy.

It is worth mentioning that the impact of the spatial variability of transport properties has been investigated not only for the Opalinus Clay, but also for the «Herrenwis Unit» (see Section 6.3.6). In the case of the «Herrenwis Unit», facies variability was expressed in terms of stochastic permeability distributions k(x,y). Similar conclusions were drawn, confirming that homogenisation of hydraulic conductivity does not introduce significant additional uncertainty.

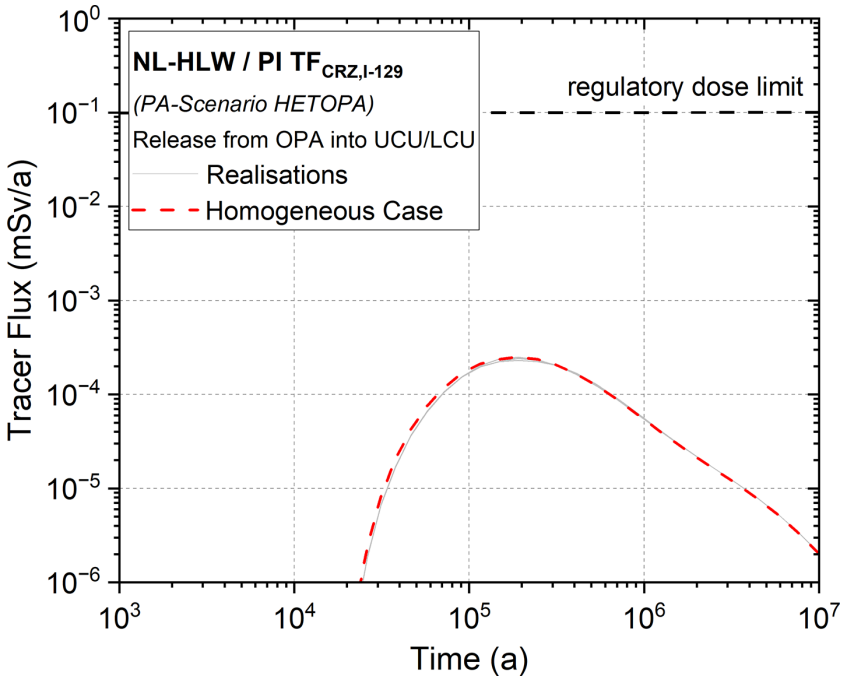

Fig. 5-8: Tracer flux released from the Opalinus Clay into the upper and lower confining units

Diffusion-dominated transport is assumed.

Probabilistic simulations with 100 stochastic property distributions of D_{eff}(x,z) are practically indistinguishable from the simulation with the homogeneous Opalinus Clay (red dotted line).

5.5 Simplified formulation of boundary conditions, initial conditions and source terms

Inherently, numerical models are based on simplified representations of boundary conditions, initial conditions and source terms. Well-established approaches have been developed to show the validity of boundary and initial conditions and to quantify the associated uncertainties for a given model application. Benchmarking with analytical solutions and enlargement of the model domain are typical methods for checking the validity of boundary conditions.

Likewise, representing the source terms in a simplified manner is unavoidable. Examples are the releases of radionuclides from the HLW canisters and the L/ILW containers, which are often expressed in terms of an average rate of mass release per canister or rate of mass release per tunnel meter. Gas generation rates for L/ILW are derived from corrosion rates and waste degradation rates of the different gas sources, which are lumped together to form a time dependent gas generation rate per L/ILW emplacement cavern.

The abstracted gas source terms for the simulation of gas pressure build-up in the HLW repository section exhibit a distinctive shape. As described in NTB 24-23 (Nagra 2024p), it is assumed that the HLW canisters corrode initially with a constant corrosion rate, corresponding to a constant gas generation rate. The corrosion rate increases for a short time by more than a factor 10 when the canisters breach and porewater ingress gives rise to additional corrosion processes inside the canisters. Over time, gas generation decreases and eventually stops when all steel is corroded. In the formulation of the stylised gas source term for HLW, it is assumed that all canisters fail at the same time after 10,000 years, which leads to the distinctive shape of the gas generation curve as shown in Fig. 5-9a (red line). Numerical benchmarks are required to make sure that such stylised source terms are appropriate for model-based PA; a general workflow for the quantification of the associated uncertainties is presented in the following paragraphs.

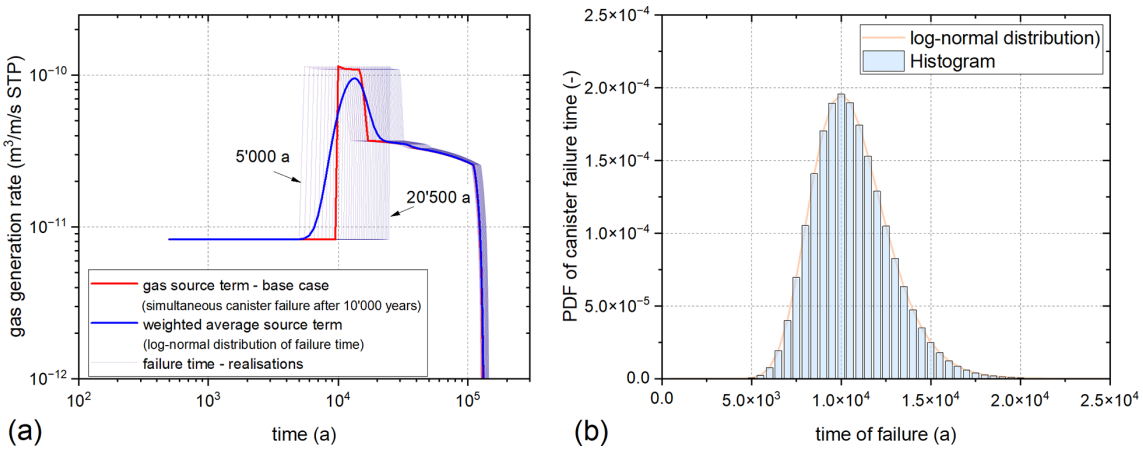

Fig. 5-9: HLW gas source term: stylised gas source term (red line) and average gas source term, assuming log-normal distribution of canister failure times (blue line)

(a) The stylised gas source term is based on the assumption that all canisters become breached at the same time after 10,000 years. Alternatively, the average gas generation rate can be derived for log-normal distribution of canister failure times. (b) Probability density function representing a hypothetical log-normal distribution of canister failure times.

The assumption that all canisters breach at the same time after 10,000 years is purely hypothetical – it is more likely that the time of failure of the HLW canisters will follow a certain probability density distribution. Fig. 5-9b displays a generic example of a log-normal distribution of canister failure times (modal value $MV_{t@f}$ = 10,000 years; $Var_{t@f}$ = 0.2 OoM). For each sample of the probability density function, the stylised gas source term (red line in Fig. 5-9a) was modified to represent the gas generation rates of the sample of HLW canisters that breach at the same time (colour-coded lines). The sampled gas generation rates were multiplied by the probability of canister failure and cumulated to represent the gas generation rate of the entirety of failed canisters (blue line in Fig. 5-9a). The cumulated gas generation rate obtained in this way is smoother than the stylised source term and the maximum rate is slightly lower.

The impact of the source term on the gas pressure build-up in the HLW emplacement drifts is evaluated by numerical simulations. Fig. 5-10 shows a comparison between the stylised source term and the averaged gas generation rates, assuming a log-normal distribution of failure times of the canisters. Peak pressures are slightly higher for the stylised source term, but the shape of gas pressure transients is very similar. It can be concluded that, for this application, the stylised source term is a conservative approximation of the more realistic gas generation rates which account for distributed failure times.

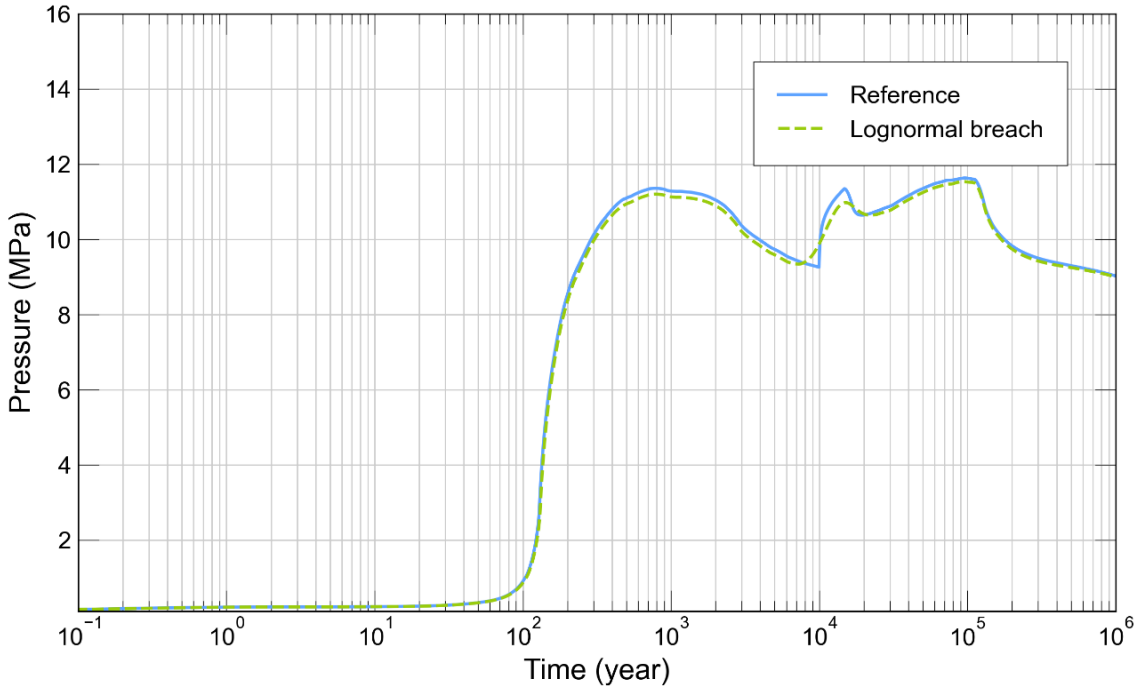

Fig. 5-10: Comparison of the impact of gas source terms on gas pressure build-up in the HLW emplacement drift

Stylised gas source term (blue line) and gas source term based on a generic example of a log-normal distribution of canister failure times (green dotted line).

5.6 Verification of codes and validation of models

Extensive benchmark exercises were carried out to validate the modelling tools which are used in the context of safety assessment (NTB 24-18, Nagra 2024r). An example of code comparisons between the TOUGH- and the PICNIC-code is reported in NAB 24-25 (Nagra 2024m). Calculation verifications and model calibrations were carried out in NAB 20-31 (Nagra 2021b), aimed at benchmarking the so-called macro-element approach with full 3-D models of two-phase flow at repository scale.

Code and calculation verification and model validation (V&V) exercises, aimed at the justification of model abstractions and uncertainty quantifications, are embedded in Nagra's long-term RD&D strategy. Development of benchmark workflows for code verification and model validation on international modelling platforms, as well as continuously surveying the state-of-the-art of coupled process modelling, are key elements in the RD&D programme, intended to ensure the readiness of the existing TH^2M-C model portfolio for safety assessment.

Recent modelling activities with international modelling teams are associated with Nagra's FE Task Force (NAB 19-40: Alcolea et al. 2021, Buchwald et al. 2025, Wojnarowicz et al. 2024), EURAD-HITEC, EURAD-GAS (Jacops & Kolditz 2024, Marschall et al. 2024, Wendling et al. 2024) and with EBS-Task Force (NAB 19-16: Romero & Gonzalez-Blanco 2019, NAB 19-27: Madaschi & Laloui 2019).

6 Performance screening

Safety scenarios describe the possible paths for the evolution of the disposal system and its environment under the effects of an assumed geological scenario and other assumed features, events and processes (NTB 24-19, Nagra 2024t). The development of safety scenarios as input for the analysis of radiological consequences requires a traceable and transparent simplification of the evolution of the real repository system from the perspective of post-closure safety. Features, events and processes (FEPs) that are deemed not applicable or of low probability are eliminated in the safety scenarios. Furthermore, the large number of evolutionary paths of the repository system must be converted into a manageable number of safety scenarios. It is the role of PA to screen the possible paths of repository performance and to identify, bundle and formulate the safety relevant paths in a format, that can be subjected to the next step in the safety assessment workflow (Fig. 2-7), namely scenario development as input for radiological consequence analysis.

The possible paths of repository performance are assessed in the performance screening workflow (Section 6.1) in a probabilistic framework with an indicator-based modelling approach. The results of quantitative assessment are classified in terms of expected performance of the multi-barrier systems (Section 6.2) and deviations thereof (Section 6.3). Deviations from expected performance are reviewed with emphasis on the likelihood of their occurrence and on their relevance for safety (Section 6.4). The likelihood of the PA-Scenarios that are assessed is determined using qualitative arguments, encompassing the consistency with independent evidence and compliance with design requirements. Their safety relevance is evaluated in a quantitative manner in the context of the model-supported scenario assessment by comparison of the safety relevant performance indicators. The PA-Scenario of expected performance (*EXPERF*) together with the safety relevant deviations from expected performance form the main input for the development of safety scenario addressed in the analysis of radiological consequences (Section 6.4).

6.1 Performance screening - evaluation workflow

The iterative process of repository development presented in Section 2.1 (see also lower part in Fig. 2-1) ends with the elaboration of a provisional design and implementation plan for the repository. By design, the multi-barrier system of this repository is expected to provide all the required post-closure safety functions over the entire period for assessment, both at the component and the total system scale. Accordingly, its evolution under the action of the expected source terms and expected initial and boundary conditions corresponds to the PA-Scenario called "*Expected Performance – EXPERF*". It encompasses all paths of repository evolution, which are related to the intended safety functions of all barrier components. The PA-Scenario "EXPERF" consists of a base case (all parameters describing the repository system take a set of reference parameter values derived from the assessment basis; see Section 2.4.1) and multiple realisations, delineating the confidence range of system evolution in the base case. The confidence limits are determined by parametric uncertainty of input parameters associated with the initial state as defined in the assessment basis. Fig. 6-1 illustrates generically the relevant paths of repository evolution in the PA framework, comprising the paths related to expected performance and deviations thereof. In the schematical sketch the *state of the barrier system* can be considered as any of the performance indicators introduced in Section 2.5.4 (see also App. C).

Deviations from expected performance can occur if one or several barrier components do not perform according to their assigned safety functions. In such cases, the inherent redundancy of the multi-barrier system foresees that the properly functioning barrier components ensure an adequate overall performance of the repository system.

The schematic drawing in Fig. 6-1 illustrates the repository evolution during the entire period for assessment. The initial state[9] of the repository is well-constrained by a solid assessment basis (see Section 2.4.1). This well-constrained initial state is characterised by a narrow opening of the funnel-shaped *"event horizon"*, dividing the space of state of the multi-barrier system in domains of possible and hypothetical states. Throughout the *period for assessment*, the state of the repository system evolves with time under the impact of internal and external events and processes (*"prevailing regimes"* in Fig. 6-1), encompassing repository-induced effects and the impacts of geological long-term evolution. The evolution of the repository system is accompanied by a loss of determinism of the associated state variables. At the end of the assessment period the evolution of the repository system associated with a given PA-Scenario and the corresponding performance indicator can be inferred within an uncertainty range, expressed in the sketch in terms of *probability density functions*. For a given PA-Scenario, the uncertainty range of system evolution at the end of the assessment period is primarily determined by parametric uncertainty of input parameters associated with the initial state.

Deviations from expected performance arise over time if a barrier component does not perform according to its assigned safety functions. Furthermore, detrimental impacts associated with an unfavourable evolution of internal and / or external perturbations may impair the performance of the entire repository system. From the perspective of uncertainty management, deviations from expected performance are associated with conceptual uncertainties rather than parametric uncertainties. The paths of repository evolution related to deviations from expected performance can be grouped for each barrier component to form PA-Scenarios, with the naming convention PA-Scenario *XY*.

Each PA-Scenario addresses a well-defined assessment aspect, expressed in terms of performance indicators / indices, performance targets and evaluation scales, as introduced in Sections 2.4.4 and 2.5.4. Fig. 6-2 presents schematically the evaluation workflow together with results of the evaluation procedure in tabular form. Barrier performance is evaluated with quantitative PA models by comparing each PA-Scenario having a specified deviation from expected performance (PA-Scenario *XY*) with the performance of the repository system as designed (PA-Scenario *EXPERF*). A comprehensive evaluation matrix is established which comprises a survey of the assessment aspects addressed, the corresponding performance indices (PIx_j) and the associated performance scores (based on evaluation scales) that quantify the deviation from the expected performance. The table provides insight into the contribution of each barrier component to the overall performance of the multi-barrier system.

[9] The initial state of the repository is assumed to correspond to the repository as designed – i.e., uncertainties associated with possible manufacturing defects and implementation errors, or failure of QA/QC are not considered here. In PA, such deviations from the repository as designed are classified as hypothetical.

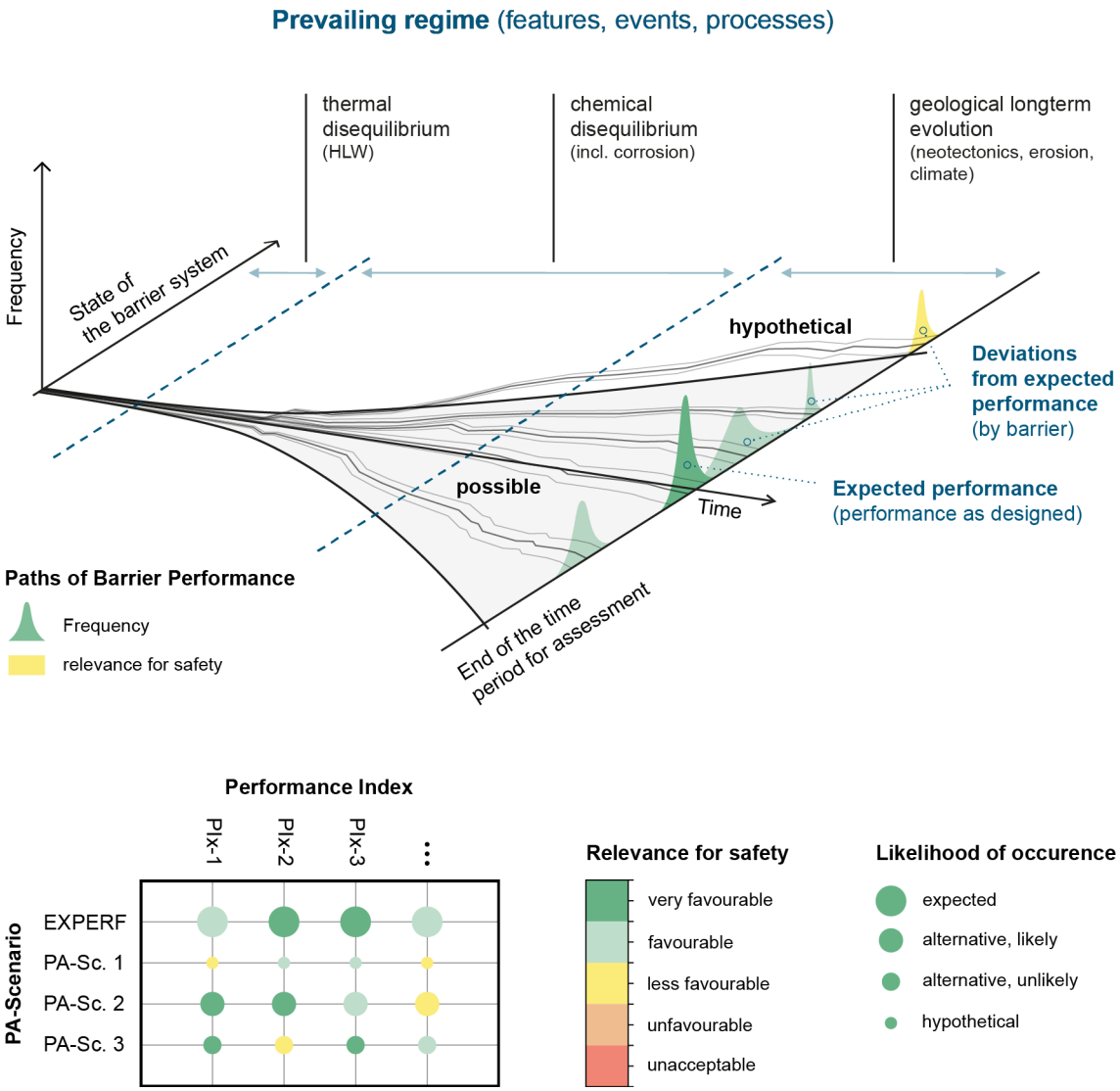

Fig. 6-1: Funnel-shaped "event horizon", dividing the space of state of the multi-barrier system in domains of possible and hypothetical states

Illustration of the relevant paths of repository evolution in the PA framework, encompassing expected performance and deviations thereof.

Note that the specification of deviations from expected performance can include hypothetical scenarios aimed at delimiting the maximum effect of a single barrier component on the performance of the total system (see Fig. 6-1, hypothetical paths of repository performance outside the funnel-shaped event horizon).

The general workflow of performance screening encompasses three steps as displayed graphically in Fig. 6-2 and described in greater detail in the following paragraphs:

1. The expected performance of the repository system as-designed is characterised quantitatively by a manageable number of calculated performance indicators of special safety relevance (Section 6.2).
2. Deviations from expected performance – by barrier component and by interaction – are modelled taking into account parametric and conceptual uncertainties and scenario uncertainties associated with repository evolution (Section 6.3). Reduced performance of a barrier component is quantified by comparison of the corresponding performance indices with those of the repository implemented according to design and evolving as expected.
3. Screening of performance by barrier provides insight into the contribution of each barrier to total system performance. Deviations from expected performance are evaluated with respect to their likelihood of their occurrence and safety relevance. This allows safety relevant deviations from expected performance to be assigned to various categories of safety scenarios (Section 6.3).

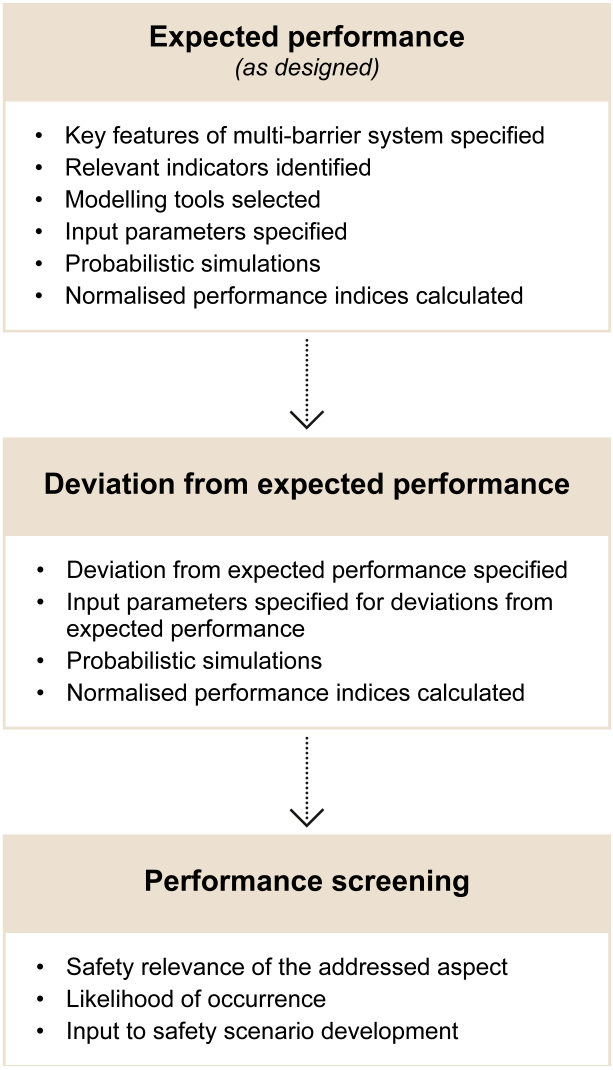

Fig. 6-2: Performance screening – general workflow encompassing a careful evaluation of the expected performance of the multi-barrier system and deviations thereof as input to safety scenario development

6.2 Expected barrier performance

6.2.1 PA-Scenario of expected performance (*EXPERF*) – key features

The current repository design and implementation plan, which has been elaborated for the general licence application complies by design with the assigned functionality of the multi-barrier repository system. Its expected performance is deduced from a well-constrained assessment basis (Section 2.4.1), complemented by numerical PA simulations of repository evolution under the action of representative source terms and representative initial and boundary conditions. The entire set of paths of repository evolution in which the safety functions of the barrier components are provided as intended forms the so-called *PA-Scenario of expected barrier performance* (PA-Scenario *EXPERF*). The following specifications and assignments are required to formulate this PA-Scenario:

- The assessment aspects, performance indicators and performance targets must be specified to evaluate the safety functions of the repository components that are addressed.
- A model configuration is specified representing the geometry of the barrier components that are addressed in sufficient detail for the intended purpose.
- A conceptual framework of the phenomena and processes of concern is formulated, which allows the evaluation of the assessment aspects in sufficient detail.
- The assignment of properties to the barrier components assumed as-designed conditions.
- Assignment of initial and boundary conditions and source terms is based on the expected conditions.

The following key features of the as-designed HLW and the L/ILW repository are implemented in the PA models of the EXPERF scenario:

- All elements of the multi-barrier system perform according to design requirements (e.g., failure of the HLW canister after 10,000 years).
- For the HLW repository section, the source term for the simulation of the release of a non-sorbing tracer in the liquid phase has been specified to represent the dose-relevant radionuclide ^{129}I. It is assumed that 10% of the total inventory of ^{129}I is released into the surrounding porewater immediately after breaching of the HLW canisters. Further details concerning the HLW source term, including a comparison with the corresponding source term in NTB 24-18 (Nagra 2024r), are given in App. A.1.3 and App. C.1.
- For the L/ILW repository, the source term for the transport simulations in the liquid phase has been specified to represent the dose-relevant radionuclide ^{36}Cl. It is conservatively assumed that the total inventory of ^{36}Cl is released instantaneously after closure of the L/ILW repository (see App. A.1.3 and App. C.1 for further details).
- For the L/ILW repository, another source term has been specified to represent the release of volatile radionuclides (focus on ^{14}C). It is conservatively assumed that the total L/ILW inventory of ^{14}C is released instantaneously after closure of the L/ILW repository (see App. A.1.3 and App. C.1 for further details).
- Thermal (HLW only) and gas-related source terms correspond to the “representative average” values specified in the gas synthesis report (NTB 24-23, Nagra 2024p). Graphical representations of the gas-related and thermal source terms are given in App. A.1.1 and A.1.2.

The model representation of the lithostratigraphic units of the CRZ and their mineralogical composition is largely consistent with the geological setting described in the geosynthesis report (Sections 4.2 and 5.2 in NTB 24-17, Nagra 2024k). Minor adjustments to the layer sequence, particularly the combination of thin lithostratigraphic units, were, however, implemented to improve the numerical performance of the transport simulations (see App. A.3).

Hydrogeological and geomechanical conditions in the underground correspond to present-day conditions as described in the geosynthesis report (Sections 5.6 and 5.5 in NTB 24-17, Nagra 2024k) and NAB 24-10 Rev. 1 (Nagra 2024j).

Diffusion is the dominant radionuclide transport mechanism in the CRZ. Advective transport along steeply dipping faults does not represent a relevant vertical release pathway. Sedimentary features such as hard beds in the upper and lower confining units do not act as lateral release paths.

Expected flow and transport properties of the geological layer stack and their uncertainty ranges are well constrained according to the geological databases given in NAB 24-10 Rev. 1 (Nagra 2024j). Summary tables of the relevant parameters are given in App. A.3.

The model set-ups used in the PA screening workflow are described in greater detail in NAB 24-25 (Nagra 2024m). A brief overview is given in the following paragraphs.

6.2.2 Model set-up

All model-based analyses that are part of the PA screening workflow are carried out with models developed with the TH-code family TOUGH3 (Jung et al. 2018). Modelling of solute transport under single-phase conditions is performed with EOS 1 Equation-of-State module for water and tracer, whereas two-phase modelling is performed using the EOS 5 module. Parametric uncertainty in the input parameters is assessed in a probabilistic framework with Monte Carlo simulations. This calls for model set-ups of moderate size (typically 2-D models or so-called 2.5-D models) and simplified representations of the complex TH^2M processes in the repository near-field to limit computational efforts. The results of much more time-consuming 3-D simulations at the scale of the entire repository, which were discussed in Chapter 5, confirm that the HLW and the L/ILW repository sections are hydraulically and mechanically decoupled from each other. This means that the two parts of the combined repository can be analysed independently. Accordingly, separate model set-ups are used for calculating the performance indicators for the HLW and the L/ILW repository sections.

A 2-D mesh representing a vertical cross-section through the centre of the HLW repository section perpendicular to the axis of the HLW emplacement drifts is the common model set-up for the simulation of pore pressure evolution in response to repository-induced effects and for modelling transport of a dissolved tracer from the emplacement drifts to the regional aquifer systems (Fig. 6-3a). A so-called 2.5-D model of the HLW repository section is required for special applications, such as transport simulations through a vertical fault that intersects the HLW repository perpendicular to the axes of the HLW emplacement drifts (see Section 6.3.3; PA-Scenario *FLTHLWN*).

The simulation of unsaturated conditions in the L/ILW repository section generally requires 2.5-D models to account for interactions between the L/ILW emplacement caverns and the other repository structures. Two different configurations were used, one of them representing the seven caverns in a vertical cross-section through the centre of the repository (Fig. 6-3b), whereas the other model was implemented as a single half-cavern model with symmetry conditions (Neumann boundary conditions) at the lateral boundaries. The single cavern model was used for all those scenarios, that were particularly time consuming.

An overview of the four model set-ups used for the probabilistic assessments is given in Tab. 6-1. The models are part of the PA model portfolio described in NAB 24-25 (Nagra 2024m). The models run fast enough to allow the hundreds of simulations needed to delineate the uncertainty ranges of the evaluated performance indicators to be carried out and are also accurate enough to provide unbiased modelling results. To demonstrate their accuracy, a rigorous benchmarking of the simplified models with the full 3-D models has been carried out using the base case parameter sets, as well as selected extreme parameter variants. More detailed descriptions of the PA model portfolio and of the benchmark process are given in NAB 24-25 (Nagra 2024m).

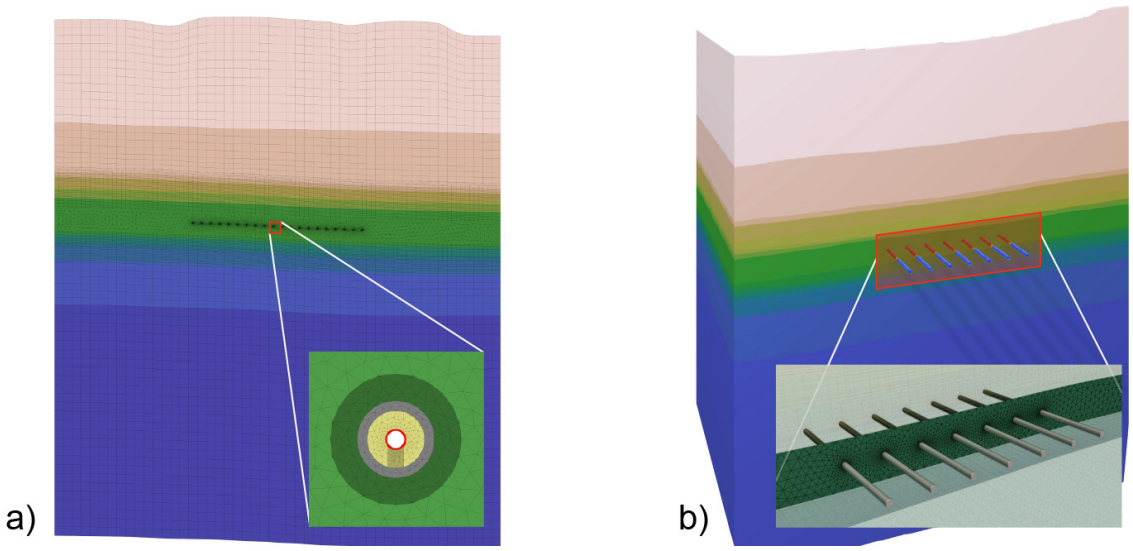

Fig. 6-3: PA models for indicator-based assessment of the multi-barrier repository system

(a) 2-D model, representing a vertical cross-section through the centre of the HLW repository section (b) 2.5-D model of the L/ILW near-field addressing flow and transport pathways through the CRZ and along the backfilled underground structures.

Tab. 6-1: PA model set-ups used for the probabilistic simulations in the context of performance screening

Model ID	Geometry	TOUGH-EOS Module
HLW		
2-D-HLWx20	2-D model set-up, vertical cross-section through the centre of the repository section, 20 HLW emplacement drifts	EOS 1
		EOS 5
2.5-D-HLWx20	2.5-D model set-up, 20 HLW emplacement drifts; fault perpendicular to the drifts represented as separate slices	EOS 5
L/ILW		
2.5-D-LILWx7	2.5-D model set-up, 7 L/ILW emplacement caverns; seals and access tunnels are represented as separate slices	EOS 5
2.5-D-LILWx1	2.5-D model set-up, 1 L/ILW half-cavern; lateral Neumann boundary conditions; seals and access tunnels are represented as separate slices	EOS 5

Input parameter values for the probabilistic modelling workflows were derived from the geological database in terms of probability density functions (App. E). Probability density functions of hydraulic conductivity and effective diffusion coefficient for all hydrogeological units were required for modelling tracer release from both the HLW and L/ILW repository section. Probability density functions of hydraulic conductivity, pore compressibility, thermal conductivity and other TH^2-parameters of the host rock formation and of the relevant EBS components were needed for the assessment of the repository-induced effects in the HLW and L/ILW repository sections. A complete survey of the input parameters for the probabilistic modelling workflows and the corresponding probability density functions is given in NAB 24-25 (Nagra 2024m). The key parameters are summarised in tabular form in App. A.3.

6.2.3 Performance indicators and probabilistic assessments

The following performance indicators and the corresponding normalised, dimensionless performance indices (in parenthesis) defined in Section 2.5.4 and Tab. 2-4 are used for performance screening:

- Tracer flux $TF_{CRZ, I\text{-}129}$ representing the dose-relevant, non-sorbing radionuclide ^{129}I, which is dissolved in the porewater and released from the HLW near-field into the host rock and transported to the regional aquifer systems overlying and underlying the CRZ (normalised tracer flux - $NTF_{CRZ, I\text{-}129}$);
- Temperature T_B in the bentonite at a distance of 0.05 m above an HLW canister (normalised bentonite temperature – NBT);
- Pore pressure $P_{HLW,heat}$ in the host rock at a distance of 20 m above an HLW canister (Failure Potential associated with thermal impacts in the HLW repository – FPH);
- Pore pressure $P_{HLW,gas}$ in the host rock at a distance of 20 m above an HLW canister (Failure potential associated with gaseous impacts in the HLW repository – FPG_{HLW});
- Tracer flux $TF_{CRZ,Cl\text{-}36}$ representing the dose relevant, non-sorbing radionuclide ^{36}Cl, dissolved in the porewater and released from the L/ILW near-field into the host rock and transported to the regional aquifer systems overlying and underlying the CRZ ($NTF_{CRZ, Cl\text{-}36}$);
- Tracer flux $TF_{CRZ,C\text{-}14}$ representing the dose relevant, volatile radionuclide ^{14}C, released from the L/ILW emplacement caverns through the CRZ into the host rock and transported to the regional aquifer systems overlying and underlying the CRZ ($NTF_{CRZ, C\text{-}14}$);
- Tracer flux $TF_{V3,C\text{-}14}$ of the volatile tracer ^{14}C released from a container into the L/ILW emplacement cavern backfill and transported through the repository structures and released through the V3 seals ($NTF_{V3,C\text{-}14}$);
- Gas pressure $P_{L/ILW}$ at a point inside an L/ILW emplacement cavern (Failure potential associated with gaseous impacts in the L/ILW repository – $FPG_{L/ILW}$).

Note that tracer flux $TF_{V3,Cl\text{-}36}$ representing the transport and release of ^{36}Cl along the backfilled repository structures through the V3 repository seals is not shown here because, for all PA-Scenarios investigated, the release of the ^{36}Cl through the V3 seals remained below the limit of significance.

Fluxes of dissolved and volatile species are the performance indicators for the assessment of the IMS safety function as specified in Section 2.2.2. Temperature and pore pressures represent the primary performance indicators for the assessment of barrier integrity (CMP safety function).

Monte Carlo simulations are carried out for each performance indicator with a typical number of runs per simulation and per indicator of 100 to 1,000 to account for the impact of parametric uncertainty of the input parameters on the simulated outputs. Flow and transport parameters, two-phase flow parameters and thermal parameters for the entire layer stack represented in the 2-D assessment models of the HLW repository section and 2.5-D models of the L/ILW repository section (Fig. 6-3) are derived from the geological databases, as described in Section 6.2.2.

The probabilistic workflow is illustrated in Fig. 6-4. The figure illustrates the derivation of the performance indicator T_B by Monte Carlo simulations of temperature distribution in the HLW near-field. In a first step, representative thermal and hydraulic input parameters and their uncertainty ranges are extracted from the existing geoscientific data sources (NABs 24-10 Rev. 1, 24.24, 24-27: Nagra 2024j, 2024w, 2024f). For each uncertain input parameter, a representative parameter value and 100 to 1,000 Latin Hypercube samples are provided, forming the base case and the probabilistic realisations for the Monte Carlo simulations. The TH simulations of the

HLW near-field are carried out with the 2-D vertical cross-section through the centre of the HLW repository section (Fig. 6-3a). Temperature transients in the bentonite are extracted at the control point T_B, 5 cm above the canister. The maximum temperature $T_{B,max}$ is determined for each Monte Carlo simulation and normalised by dividing it by the performance target T_{max} = 150 °C, forming the dimensionless performance index NBT. In this context, the performance target T_{max} = 150 °C represents the maximum temperature the dry bentonite can sustain without irreversible geochemical alterations (see also App. C.2). A histogram with the probability density function (PDF) and the cumulative density function (CDF) of the normalised performance index NBT is derived and used to calculate the performance margins and the corresponding evaluation scales. Further details concerning the probabilistic workflow are found in App. C.2 and NAB 24-25 (Nagra 2024m).

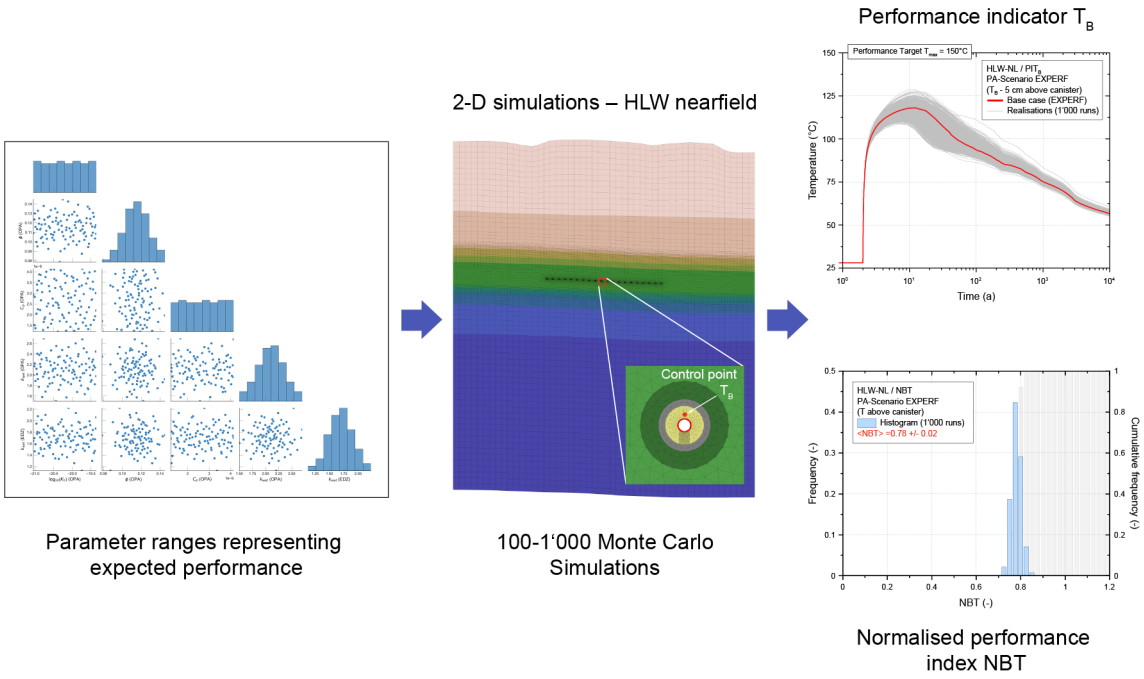

Fig. 6-4: Probabilistic workflow for the simulation of the evolution of temperature in the HLW near-field

Left: Scatter-plot matrix of the 100 Latin Hypercube samples with distributions of thermal and hydraulic input parameters; Middle: close-up of the 2-D model through the centre of the HLW repository section with the control point representing the performance indicator T_B in the bentonite buffer; Right: transients of performance indicator T_B showing the reference case and 1,000 probabilistic realisations, representing the confidence range of the performance indicator (see NAB 24-25, Nagra 2024m for further details).

6.2.4 PA-Scenario of expected performance – indicator-based assessments

The PA-Scenario of expected barrier performance (*EXPERF*) includes all paths of repository evolution that conform with the intended safety functions of the barrier components under consideration (see Section 6.2.1). Only four performance indicators for the HLW repository section and four for the L/ILW repository section are required in the performance screening process to evaluate the role of the different barrier components and their contribution to the overall perfor-

mance of the repository system. The results of performance assessment for the expected performance of the HLW and the L/ILW repository sections are discussed in the following paragraphs.

HLW repository

The $TF_{CRZ,I\text{-}129}$ indicator evaluates the efficiency of the CRZ in retaining the dose-relevant radionuclide ^{129}I (see also App. C.2). Assuming that all barrier components perform according to expectations, the tracer flux from the CRZ into the regional Keuper and Malm aquifers, based on an instantaneous release $IRF_{I\text{-}129}$ (10% of total initial activity of ^{129}I) from the HLW repository section is calculated over a timescale, which exceeds by a factor of 10 the period for assessment (1 million years). The probabilistic simulations of tracer flux based on a sample set of 1,000 simulations show that the maximum release into the regional aquifer systems is reached after around 0.3 – 1 million years (Fig. 6-5a). The corresponding performance indices are calculated for each simulation by normalising the peak dose for each tracer breakthrough curve by dividing it by the regulatory dose limit of 0.1 mSv/a (note that the biosphere dose conversion factor corresponding to the present day climate is used to convert the activity release rate of ^{129}I into a dose rate; further details in App. C.2). The histogram of expected performance based on the 1,000 samples is displayed in Fig. 6-6a, indicating a maximal release of about 7×10^{-5} mSv/a, which is 3.1 orders of magnitude (OoM) below the regulatory dose limit. In the histogram, the spread of maximal release is narrow with a width of 0.05 OoM.

The temperature T_B is the indicator used to characterise the long-term chemical and mechanical integrity of the bentonite (corresponding to the CMP safety function). The temperature of the bentonite at a distance of 5 cm above a canister must not exceed 150 °C in order to maintain its barrier capacity (further details in App. C.2). Probabilistic simulations of temperature distribution in the HLW near-field are carried out with a TH^2 model and the 2-D mesh (Fig. 6-3a). The modelling results, based on a sample set of 1,000 simulations, show that the maximum temperature is reached after around 10 years and that the peak temperatures are below 125 °C (Fig. 6-5b). The corresponding performance indices are calculated for each simulation by normalising each temperature curve by dividing by the performance target of 150 °C. The histogram of expected performance based on 100 samples is displayed in Fig. 6-6b. The median of normalised peak temperature is 0.78 and the 95^{th} and 99^{th} percentiles of the frequency distribution are 0.82 and 0.84, indicating a narrow frequency distribution with a favourable safety margin.

The pore pressure $P_{HLW,heat}$ at a distance of 20 m above an HLW canister is the indicator for the mechanical integrity of the CRZ in response to thermal loads (corresponding to safety function CMP). Probabilistic simulations of pore pressure transients in the host rock based on a sample set of 1,000 simulations indicate peak pressures up to 15.9 MPa (Fig. 6-5c). The magnitudes of the principal components of minimum and maximum horizonal stress S_h and S_H at the control point (20 m above the HLW canister in the centre of the repository) are 16.8 and 18.8 MPa, feeding into the estimation of the normalised performance indicator FPH, or heat-induced failure potential FPH, which represents the potential for shear failure (further details in App. C.3). FPH is derived using the Mohr-Coulomb shear failure criterion for a given in-situ stress state, considering an enhanced total stress due to thermal expansion of the rock matrix according to Eq. (C-1). The histogram of expected performance based on a sample size of 1,000 simulations is shown in Fig. 6-6c. The median of the FPH is 0.37, and the 95^{th} and 99^{th} percentiles of the frequency distribution are 0.47 and 0.55, indicating large safety margins.

The pore pressure $P_{HLW,gas}$ in the backfilled HLW tunnels is the indicator for the mechanical integrity of the CRZ in response to gas-induced loads (corresponding to CMP safety function). Probabilistic simulations of pore pressure transients based on a sample size of 1,000 simulations indicate peak pressures up to 14.0 MPa, with a first peak after 10,000 years and a second peak after 100,000 years (Fig. 6-5d). The origin of the first peak is related to the breaching of the

canisters (additional corrosion inside the canister), whereas the second peak is linked to the end of canister corrosion (distinct drop of gas generation rate after 80,000 years). The magnitudes of the principal components of minimum and maximum horizonal stress S_h and S_H at the control point (at the top of the EDZ above the HLW drift in the center of the repository) are 17.2 and 19.2 MPa, respectively, and the vertical stress is 21.9 MPa. Principal stresses are needed for the estimation of the gas induced failure potential FPG_{HLW}, derived with the help of using the Mohr-Coulomb shear failure criterion for a given in-situ stress state (further details in App. C.3). FPG_{HLW} is the normalised performance index, representing the potential for shear failure due to gas overpressures. The histogram of expected performance based on a sample size of 100 is shown in Fig. 6-6d. The median of the FPG_{HLW} is 0.35, and the 95th and 99th percentiles of the frequency distribution are 0.45 and 0.46, again indicating large safety margins.

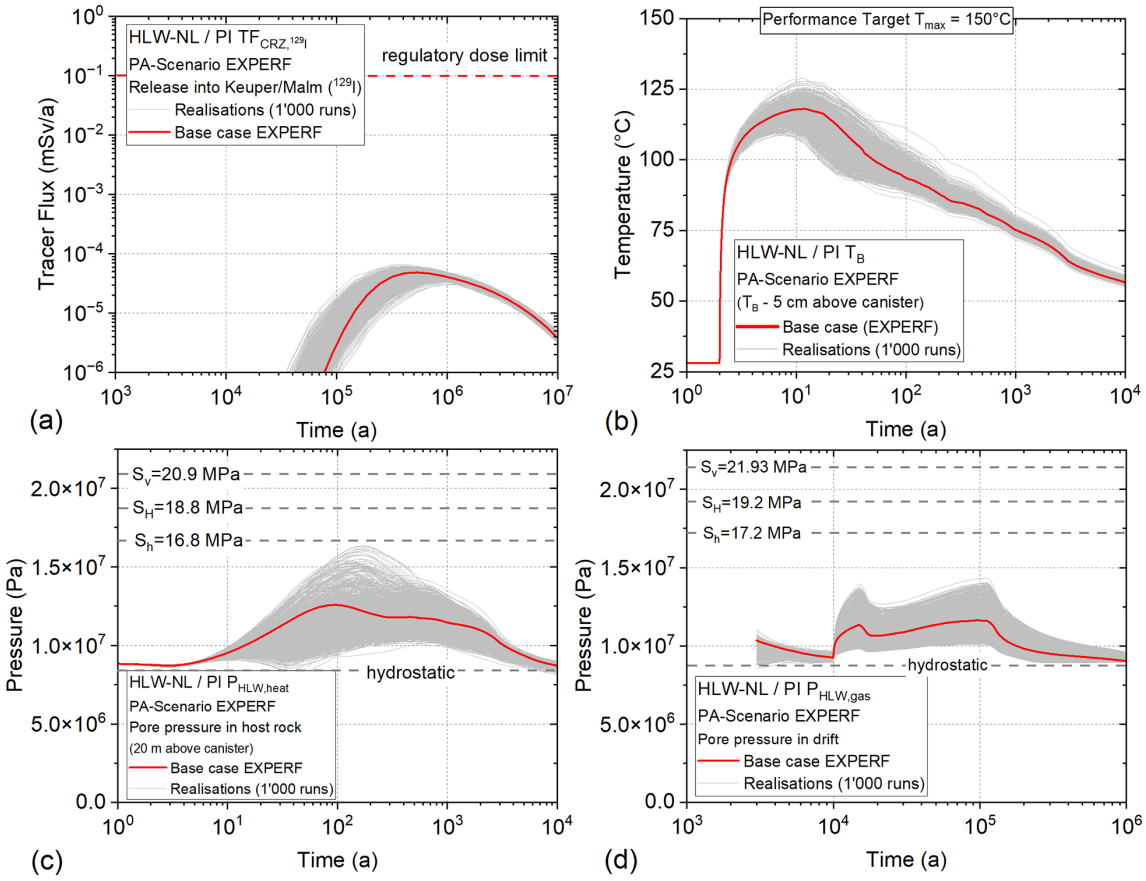

Fig. 6-5: Expected barrier performance for HLW – performance indicators and uncertainty ranges

(a) Tracer release from the CRZ into the regional aquifer systems; (b) temperature evolution in the bentonite 5 cm above the canister; (c) thermally induced pore pressures at a distance of 20 m above repository level; (d) gas-induced pore pressures above an HLW emplacement drift (interface host rock / EDZ).

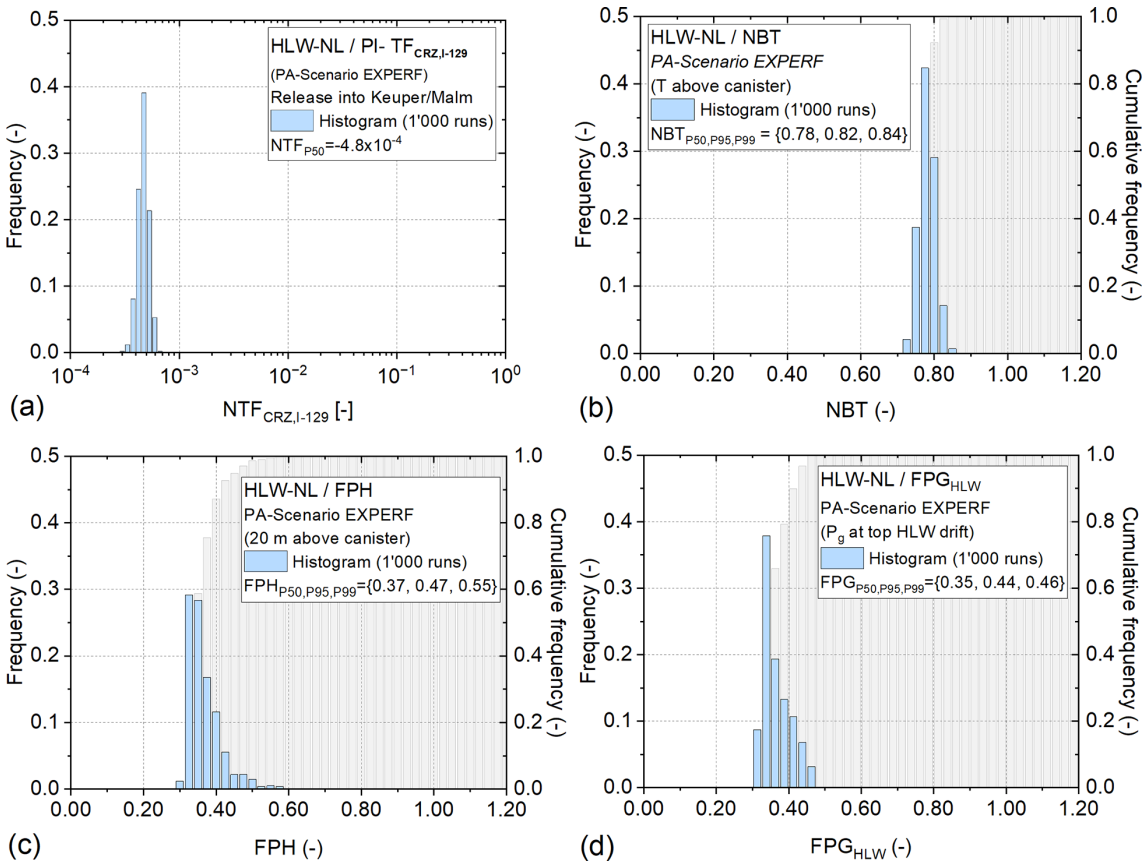

Fig. 6-6: Expected barrier performance for HLW – normalised performance indices and safety margins

(a) Normalised tracer flux NTF; (b) normalised bentonite temperature NBT; (c) failure potential of the host rock due to thermally induced overpressures (FPH); (d) failure potential of the host rock due to gas-induced overpressures (FPG_{HLW}).

L/ILW repository

The $TF_{CRZ,Cl\text{-}36}$ indicator evaluates the efficiency of the CRZ in retaining the dose-relevant radionuclide ^{36}Cl (half-life time 3.013×10^5 years), dissolved in the porewater of the L/ILW near-field. It is assumed that all barrier components perform according to expectations and the entire inventory of ^{36}Cl is released instantaneously into the porewater of the L/ILW near-field (see App. C.1 for a detailed description of the performance indicator). The unsaturated initial conditions and the gas production in the L/ILW emplacement caverns are explicitly considered in the simulations, because they have a significant impact on the release of the ^{36}Cl from the waste matrix into the L/ILW near-field (arguments are presented in Section 4.4.5). The tracer flux $TF_{CRZ,Cl36}$ into the regional Keuper and Malm aquifers is calculated over a timescale of more than 3 times the half-life of ^{36}Cl. The probabilistic simulations of tracer flux with a sample set of 100 simulations in total show that the tracer flux into the regional aquifer systems remains below 10^{-7} mSv/year during the entire period for assessment (Fig. 6-7a). The corresponding performance indices NTF are more than 6 orders of magnitude below the regulatory dose limit (Fig. 6-8a).

The indicators $TF_{CRZ,C14}$ and $TF_{V3,C14}$ evaluate the efficiency of the CRZ and the backfilled and sealed underground structures, respectively, in retaining the dose-relevant radionuclide ^{14}C (half-life time 5,700 years) in the gas phase in the L/ILW near-field. It is assumed that all barrier components perform according to expectations. Furthermore, the conservative assumptions are made that the entire inventory of ^{14}C (mainly methane and carbon dioxide) is released instantaneously into the gas filled pore space of the L/ILW emplacement caverns and dissolution of the corresponding species in the porewater does not take place. The unsaturated initial conditions and the gas production in the L/ILW emplacement caverns are explicitly accounted for in the PA calculations. The tracer flux $TF_{CRZ,C14}$ into the regional Keuper and Malm aquifers and $TF_{V3,C14}$ released through the V3 seals is calculated over a period of 100,000 years, which is more than 17 times the half-life of ^{14}C.

The probabilistic simulations of tracer flux $TF_{CRZ,C14}$ with a sample set of 100 simulations in total reveal that no ^{14}C is released into the regional aquifer systems (Fig. 6-7b). The corresponding performance index $NTF_{CRZ,C14}$ is below the limit of significance (Fig. 6-8b). The tracer flux $TF_{V3,C14}$ along the backfilled repository structures and its release through the V3 seals indicate maximum dose rate in the order of 10^{-10} to 10^{-8} mSv/year after 30,000 – 50,000 years (Fig. 6-7c). The calculated dose is more than 7 OoM below the regulatory dose limit as expressed by the corresponding performance index $NTF_{V3,C14}$ (Fig. 6-8c).

The gas-induced overpressure $P_{gas,L/ILW}$ is an indicator for the mechanical integrity of the CRZ around the L/ILW emplacement caverns in response to gas-induced loads. The pore pressure at the interface between the undisturbed host rock and the EDZ above the backfilled L/ILW emplacement cavern in the centre of the repository is extracted from the TH^2-modelling results. The magnitudes of the principal components of minimum and maximum horizonal stress, S_h and S_H, at the control point (i.e., interface host rock / EDZ above the backfilled L/ILW emplacement cavern) are 16.2 and 18.1 MPa, respectively, and the vertical stress is 20.2 MPa. Principal stresses are needed for the estimation of the gas-induced failure potential $FPG_{L/ILW}$. $FPG_{L/ILW}$ is the performance index representing the potential for shear failure (further details in App. C.3). Probabilistic simulations of pore-pressure transients with a sample size of 100 simulations in total indicate peak pressures up to 10.5 MPa (Fig. 6-7d). The histogram of expected performance based on a sample size of 100 is shown in Fig. 6-8d. The median of the $FPG_{L/ILW}$ is 0.31 and the 95th and 99th percentiles of the frequency distribution are 0.33 and 0.34, respectively, once again indicating large safety margins.

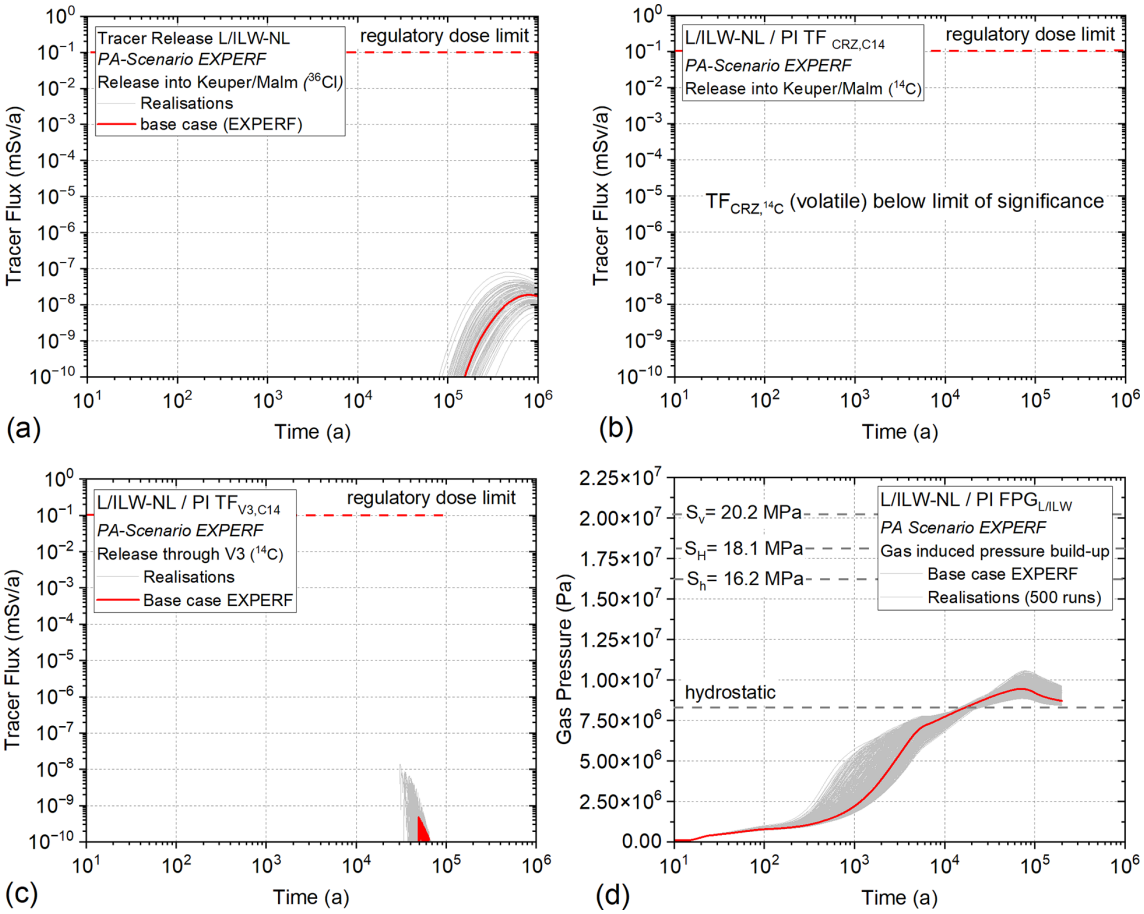

Fig. 6-7: Expected barrier performance for L/ILW: performance indicators and uncertainty ranges

(a) Tracer release from the CRZ into the regional aquifer systems, (b) gas fluxes through the CRZ, (c) gas fluxes through the V3 seals, (d) gas-induced effects on porewater pressure above the L/ILW emplacement caverns.

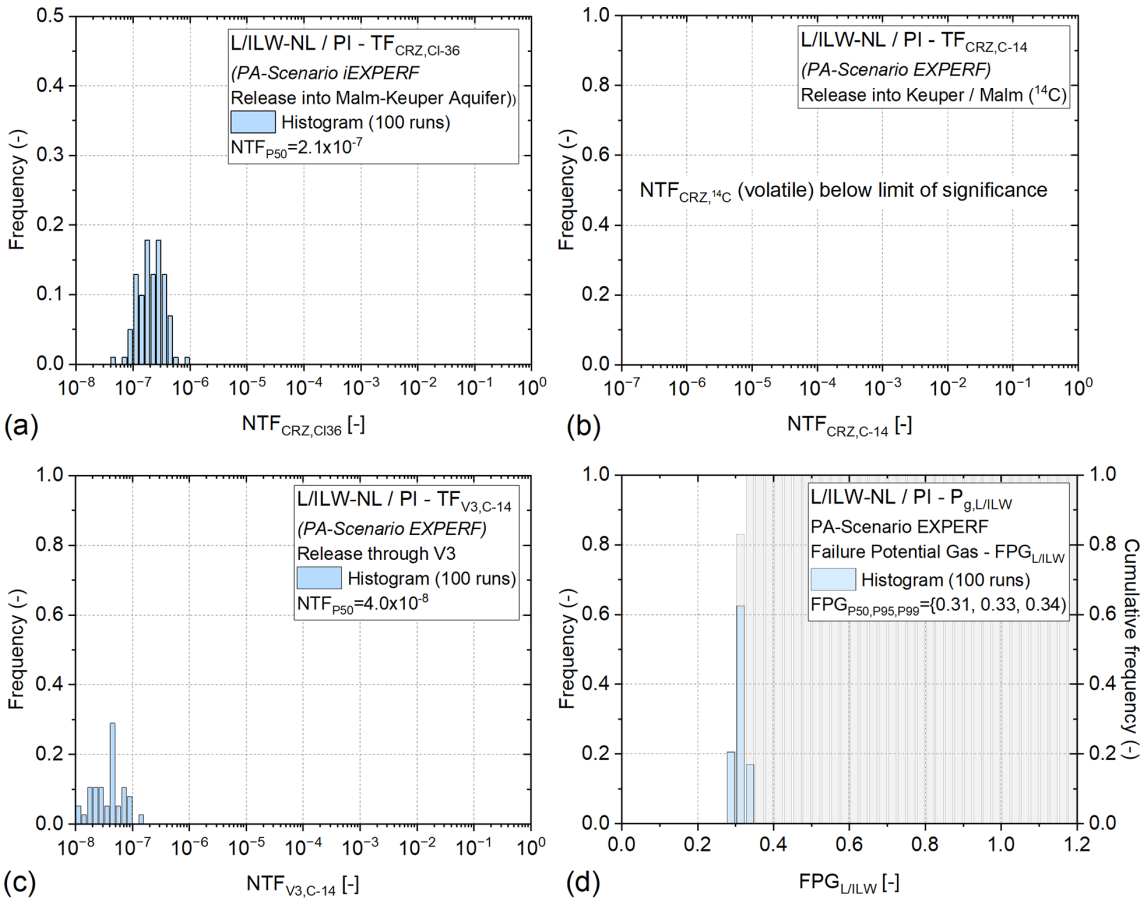

Fig. 6-8: Expected barrier performance for L/ILW: performance indicators and uncertainty ranges

(a) Normalised tracer flux ($NTF_{CRZ,Cl-36}$) of dissolved ^{36}Cl into the Keuper and Malm aquifers; (b) normalised tracer flux ($NTF_{CRZ,C-14}$) of volatile ^{14}C into the Keuper and Malm aquifers; (c) normalised tracer flux ($NTF_{V3,C-14}$) of volatile ^{14}C through the V3 repository seals; (d) failure potential of the host rock ($FPG_{L/ILW}$) due to gas-induced overpressures.

Expected repository performance - conclusions

The PA-Scenario of expected barrier performance (*EXPERF*) complies with the assigned functionality of the multi-barrier repository system as designed. The indicator-based probabilistic assessments of the HLW and the L/ILW repository sections highlight the large safety margins of the multi-barrier system in terms of radionuclide retention capacity and resilience to repository-induced effects. The robustness of the repository system has been confirmed in the context of a Monte-Carlo based perturbation analysis for a wide range of uncertainty in input parameters.

6.3 Deviations from expected performance

Deviations from expected performance occur over time if a barrier component fails to perform its assigned safety functions or if detrimental impacts (e.g., repository-induces effects, effects of geological long-term evolution) impair the performance of the entire repository system. According to the design principles of redundancy and diversity, the reduced performance of a single barrier component will not give rise to the failure of the entire multi-barrier system. The motivation for the quantitative assessment of deviations from expected performance lies in the estimation of the resulting effect on the global safety margins of the barrier system. The impacts are addressed by barrier with respect to the eight performance indicators defined in Section 6.2.3. For this, conceivable and hypothetical PA-Scenarios are formulated, each assuming a reduced performance of a barrier component compared with its expected performance. The likelihood of occurrence of the deviations is discussed and the relevance to safety is evaluated. PA-Scenarios are specified to evaluate the impact of reduced performance of individual components on the safety margins of the entire multi-barrier system. The results of the assessments are discussed in the following paragraphs. Tab. 6-2 presents a compilation of the PA-Scenarios addressed, and the indicators and model set-ups that are used.

Tab. 6-2: PA-Scenarios, performance indicators and assessment models used to evaluate deviations from expected performance

PA-Scenario	**Performance indicator**	**Assessment model / ID** (see NAB 24-25, Nagra 2024m)
HLW matrix		
PA-Sc01 (IRMAX): Instant release of entire activity (^{129}I)	$TF_{CRZ,I\text{-}129}$	2-D-HLWx20 (EOS 1)
HLW canister		
PA-Sc02 (WPFAIL): Canister failure at time of repository closure (non-isothermal phase)	$TF_{CRZ,I\text{-}129}$	2-D-HLWx20 (EOS 1)
PA-Sc03 (UBHEAT): Upper bound heat source	$P_{HLW,heat}$, T_B	2-D-HLWx20 (EOS 5)
PA-Sc04 (UBGAS): Upper bound gas source term	$P_{HLW,gas}$	
Closure system		
PA-Sc05 (V3PERM): Permeable V3 seals (early saturation of V2 seals, impact on ^{14}C)	$TF_{CRZ,L/ILW}$	2.5-D-LILWx1 (EOS 5)
	$TF_{CRZ,volat}$	
	$TF_{V3,volat}$	
	$P_{gas,L/ILW}$	
L/ILW matrix		
PA-Sc06 (ZEROGAS) Zero gas generation	$TF_{CRZ,Cl\text{-}36}$	2.5-D-LILWx1 (EOS 5)
PA-Sc07 (PESSGAS): Pessimistic gas generation	$P_{gas,L/ILW}$	

Tab. 6-2: Cont.

PA-Scenario	**Performance indicator**	**Assessment model / ID** (see NAB 24-25, Nagra 2024m)
Containment-providing rock zone (CRZ)		
PA-Sc08 (UPFLOW): Upflow with artesian pressure in Keuper aquifer	$TF_{CRZ,I-129}$	2-D-HLWx20 (EOS 5)
PA-Sc09 (DWNFLOW): Downflow with artesian pressure in Malm		
PA-Sc10 (HARDBED): Hard beds of the upper confining units as release pathways		
PA-Sc11 (HERWIS): «Herrenwis Unit» as release pathway		
PA-Sc12 (MKALK): Release into Muschelkalk		
PA-Sc13 (HETOPA): Heterogeneous Opalinus Clay		
PA-Scenario	Performance indicator	Assessment model / ID (see Nagra 2024m)
Undetected Fault HLW FLTHLW		
PA-Sc14 (FLTHLWP): Undetected fault parallel to the HLW drifts	$TF_{CRZ,I-129}$	2-D-HLWx20 (EOS 5)
PA-Sc15 (FLTHLWN): Undetected fault normal to the HLW drifts		2.5-D-HLWx20 (EOS 1)
PA-Sc16 (FLTLILW): Undetected fault L/ILW	$TF_{CRZ,Cl-36}$ $P_{gas,L/ILW}$	2.5-D-LILWx1 (EOS 5)
PA-Sc17 Thermally- and gas-induced faults HLW (RIEHLW)	$TF_{CRZ,I-129}$	2-D-HLWx20 (EOS 5)
PA-Sc18 Gas-induced fault L/ILW RIELILW	$TF_{CRZ,Cl-36}$	2.5-D-LILWx1 (EOS 5)
Geological Longterm Evolution		
PA-Sc19 (SEISHLW): Earthquake HLW		-
PA-Sc20 (SEISLILW): Earthquake L/ILW		-
PA-Sc21 (LOSSOB): Loss of overburden – permeability increase	$TF_{CRZ,I-129}$	2-D-HLWx20
PA-Sc22 (LOSSFLT) Loss of overburden – fault activation		-

6.3.1 High-level waste

Immobilistation, retention and retarded release of radionuclides is the primary safety function of the SF and RP-HLW matrices (IMS safety function). After canister failure, when water contacts the spent fuel cladding and pellets, a few percent of the total radionuclide inventory is released relatively rapidly ("Instantaneous Release Fraction" – IRF). The IRF is, however, small. According to NTB 24-18 (Nagra 2024r), the IRF of ^{129}I does not comprise more than 6.5% of the entire ^{129}I inventory (see Fig. C-2a), and the rest of the ^{129}I inventory is continuously released as the so-called "congruent release" fraction. The probabilistic simulations with the performance indicator $TF_{CRZ,I\text{-}129}$ described in App. C.1 are based on an IRF of ^{129}I of 10% of the total inventory to account in a simplified manner for the additional early release, which can be assigned to the congruent release.

While the simulations of tracer flux $TF_{CRZ,I\text{-}129}$ in the PA-Scenario of expected performance *EXPERF* are based on an IRF of ^{129}I of 10% (Fig. 6-5a), the PA-Scenario *IRMAX* assumes the instantaneous release of the entire ^{129}I inventory (i.e., assuming an IRF of ^{129}I of 100%). This can be seen as a hypothetical deviation in performance of the HLW matrix, presuming instantaneous dissolution of the UO_2 pellets after canister failure and porewater ingress. The assessment of such a hypothetical case with complete and instantaneous release gives an insight into the role of the waste matrix as a primary safety barrier and tests the robustness of the entire multi-barrier system. In reality, the waste matrix is expected to be highly stable under expected conditions upon contact with water. Furthermore, the canister interior is expected to saturate only slowly after canister breaching; the accumulation of corrosion gases inside the canister will keep gas pressure in the HLW near-field above hydrostatic for several hundred thousands of years as seen in Fig. 6-5d. The accumulated gas in the corroded canister represents a capillary barrier, which contributes to the retention of dissolved radionuclides in the HLW near-field.

Fig. 6-9a presents the performance indicator $TF_{CRZ,I\text{-}129}$ for the hypothetical PA-Scenario *IRMAX* (instant release of 100% of total ^{129}I inventory). The typical shape of a breakthrough in response to a pulse-like release is observed, with the peak of tracer flux reaching the Malm and Keuper regional aquifers after less than 1 million years. However, the dose rate at peak is by a factor of 10 higher than in the *EXPERF* scenario (Fig. 6-4a). In the histogram, representing the normalised tracer flux at peak (i.e., performance index $NTF_{CRZ,I\text{-}129}$ in Fig. 6-9b), the flux maximum remains 3.3 orders of magnitude (OoM) below the regulatory dose limit for the *EXPERF* scenario, whereas a reduced but nonetheless still large safety margin of ≈ 2.3 OoM is observed for the hypothetical *IRMAX* scenario. It can be concluded that the immobilisation of radionuclides in the HLW matrix contributes significantly to the overall performance of the multi-barrier system of the HLW repository.

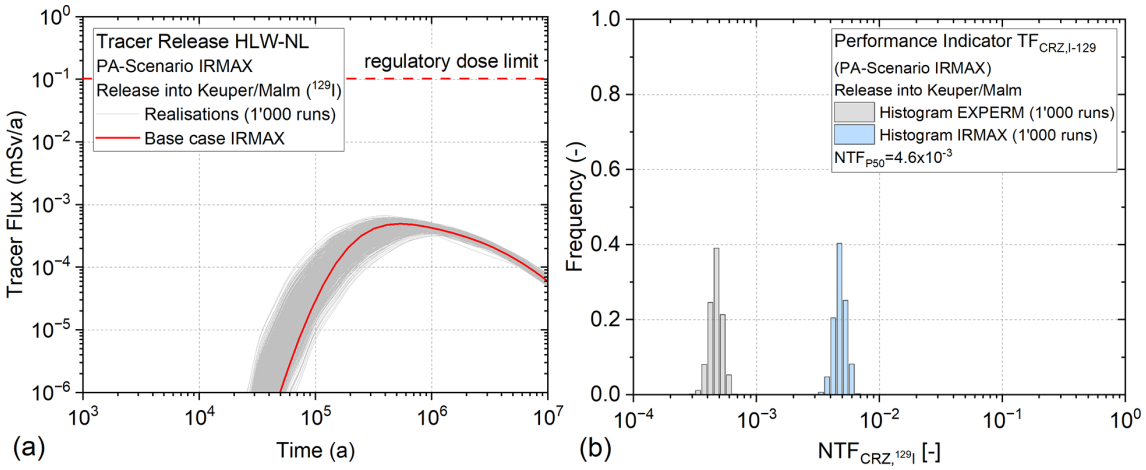

Fig. 6-9: Deviations from expected barrier performance of the HLW canister – PA-Scenario *IRMAX*

(a) Probabilistic simulations of tracer flux $TF_{CRZ,I129}$; (b) histograms of the normalised performance index $NTF_{CRZ,I-129}$ representing the PA-Scenarios *EXPERF* and *IRMAX*.

6.3.2 HLW canister

The HLW canisters are designed such that they provide full containment of the waste and its associated radionuclides for a period extending well beyond the early non-isothermal post-closure phase. The assessment of expected performance of the HLW canisters (Section 6.2.4) is based on an assumed canister lifetime of 10,000 years and on the expected source terms for heat emission from the waste (see App. A.1.2) and for gas release associated with anaerobic canister corrosion (App. A.1.1).

Deviations from expected canister performance occur if the canister is exposed to unexpected THM-C conditions, such as high and heterogeneous buffer swelling pressures, high canister temperatures or unfavourable chemical conditions. Safety relevant impacts of such deviations are the early onset of radionuclide release due to early canister breaching during the non-isothermal post-closure phase and the loss of compatibility with the other barrier components due to enhanced heat emission and gas generation. Three PA-Scenarios are dedicated to the evaluation of deviations in canister performance (Tab. 6-2), as discussed in the following paragraphs.

WPFAIL is a hypothetical PA-Scenario which examines the impact of early canister failure on the performance of the CRZ as a transport barrier (IMS safety function). Probabilistic simulations of tracer flux are carried out assuming the onset of tracer release immediately after canister emplacement in a period characterised by a strong thermal disequilibrium in the HLW near-field. The simulations account for temperature-dependent diffusion coefficients and thermally induced overpressures around the HLW drifts, which might lead to porewater movement and to advective transport of dissolved radionuclides. Other effects that could give rise to an increased release from the waste matrix (temperature-dependent solubility, chemical effects) are not accounted here. Fig. 6-10a displays the performance indicator $TF_{CRZ,I-129}$ evaluated in this scenario In the histograms representing the normalised tracer flux at peak $NTF_{CRZ,I-129}$ (Fig. 6-10b), the maximum of flux is 3.3 orders of magnitude (OoM) below the regulatory dose limit in the *EXPERF* scenario, whereas a slightly reduced safety margin of ≈ 3.2 OoM is observed for the hypothetical scenario *WPFAIL*. This illustrates how, in the case of premature failure of the canister, the CRZ would still represent an efficient transport barrier for dissolved radionuclides.

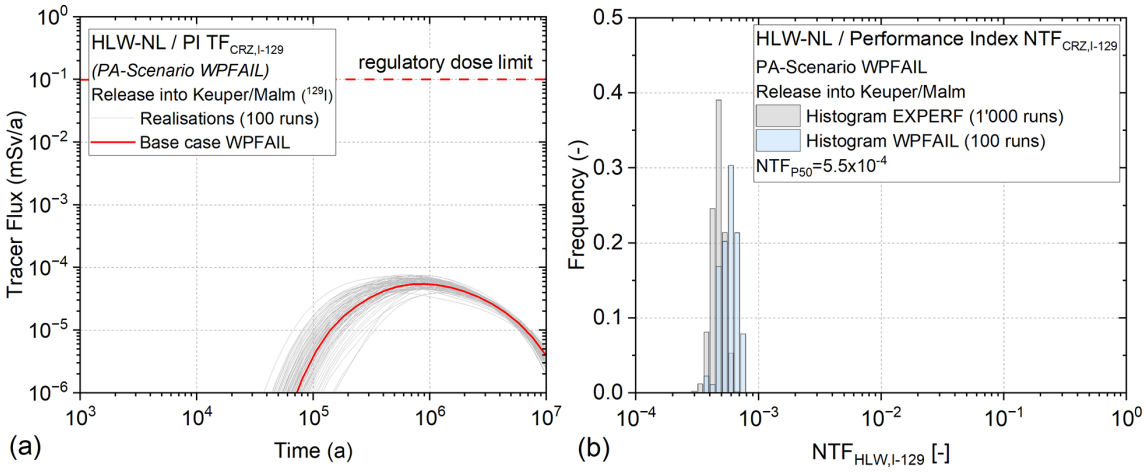

Fig. 6-10: Deviations from expected barrier performance of the HLW canister – PA-Scenario *WPFAIL*

(a) Probabilistic simulations of tracer flux $TF_{CRZ,HLW}$; (b) histograms of the performance index $NTF_{CRZ,HLW}$ evaluated for the PA-Scenarios *EXPERF* and *WPFAIL*.

The PA-Scenario *UBHEAT* addresses unexpectedly high thermal loads (i.e., upper bound heat source term, see App. A.1.2) associated with an unfavorable clustering of the canisters with high heat output in the HLW repository section. The *UBHEAT* scenario is a hypothetical scenario; it can be avoided by careful canister placement, which ensures that the MOX canisters with the highest thermal output are spread evenly across the HLW emplacement drifts. The performance indicators considered in this scenario are the temperature T_B in the bentonite at a distance of 5 cm above an HLW canister and the pore pressure $P_{HLW,heat}$ in the host rock 20 m above a canister (further details in App. C).

The upper bound heat source term does not affect significantly the temperature evolution in the bentonite buffer. Evidence for this is provided by a set of 100 Monte Carlo simulations, showing maximum temperatures well below 125 °C (Fig. 6-11a); the corresponding performance index NBT (Fig. 6-11b) does not differ from that deduced for the *EXPERF* scenario. In contrast, a distinct effect of the increased thermal load is observed in the pore pressure $P_{HLW,heat}$ (Fig. 6-11c) and in the corresponding performance index FPH (Fig. 6-11d), which represents the thermally-induced failure potential of the host rock (App. C.3). The maximum pore pressure in the host rock above the canister reaches values of up to 17.5 MPa, which exceeds the magnitude of local minimum stress S_h = 16.8 MPa. The performance index FPH for thermally induced shear failure remains below 1 (95^{th} percentile FPH_{P95} = 0.56) but the histogram exhibits a longer tail in comparison with the *EXPERF* scenario. Based on the limited number of Monte Carlo simulations, it cannot be excluded that the performance target would be exceeded if a greater number of simulations have been carried out. However, the likelihood of occurrence can be classified as hypothetical, because careful canister placement based on rigorous quality assurance procedures will prevent clustering of the MOX canisters across the HLW emplacement tunnels. The relevance for safety of thermally induced failure of the host rock can be bracketed with the PA-Scenario *HLWRIE* (Tab. 6-2, Section 6.3.6).

In the *UBGAS* scenario, it is assumed that the prevailing chemical conditions in the bentonite buffer give rise to enhanced corrosion processes. Enhanced corrosion is linked to the upper bound gas source term, which is specified in the gas synthesis report (NTB 24-23, Nagra 2024p). It should be noted that the experimental databases derived from Nagra's dedicated laboratory programme on steel corrosion (see also Section 3.2.1) do not support such high gas generation rates.

Another limiting factor is the low ingress of porewater from the low-permeability host rock, which restricts the process of anaerobic corrosion and thus makes the *UBGAS* scenario unlikely (see also Section 4.4.2 / impact of water consumption).

The performance indicator considered in this scenario is the pore pressure $P_{HLW,gas}$ in host rock above the HLW drift (see App. C.3.2). A marked effect of the enhanced gas generation rates is observed in the calculated pore pressure $P_{HLW,gas}$ (Fig. 6-11e) and in the corresponding performance index FPG (Fig. 6-11f). The maximum pore pressure in the host rock above the canister reaches values of up to 18.3 MPa, which is significantly above the magnitude of local minimum stress (17.2 MPa). The performance index FPG for shear failure is significantly higher than in the *EXPERF* scenario with an extended tailing, which reaches the performance limit ($FPG_{P95} = 0.80$). For the expected in-situ stress conditions, it cannot be excluded that the performance target of 1 would be exceeded with an increased number of Monte Carlo simulations. For this reason, the relevance for safety of the gas-induced failure of the host rock has been additionally checked with the PA-Scenario *HLWRIE* (Tab. 6-2), focusing on the loss of radionuclide retention capacity of the CRZ due to thermally- or gas-induced fracturing (results discussed in Section 6.3.6). The *UBGAS* scenario can be classified as a scenario with low likelihood of occurrence and low impact on radiological safety of the HLW repository (model-based evidence provided in Section 6.3.6). Under unfavourable stress conditions and assuming unexpectedly low rock strength, it is conceivable that thermally- or gas-induced rock failure could occur. Gas induced fractures would propagate preferentially along the re-sealed EDZ around the emplacement drift, representing a zone with reduced rock strength (see also Levasseur et al. 2023). Fracture propagation would come to a halt when gas is released to the gas storage volumes between the seals HLW-V1 and -V2.

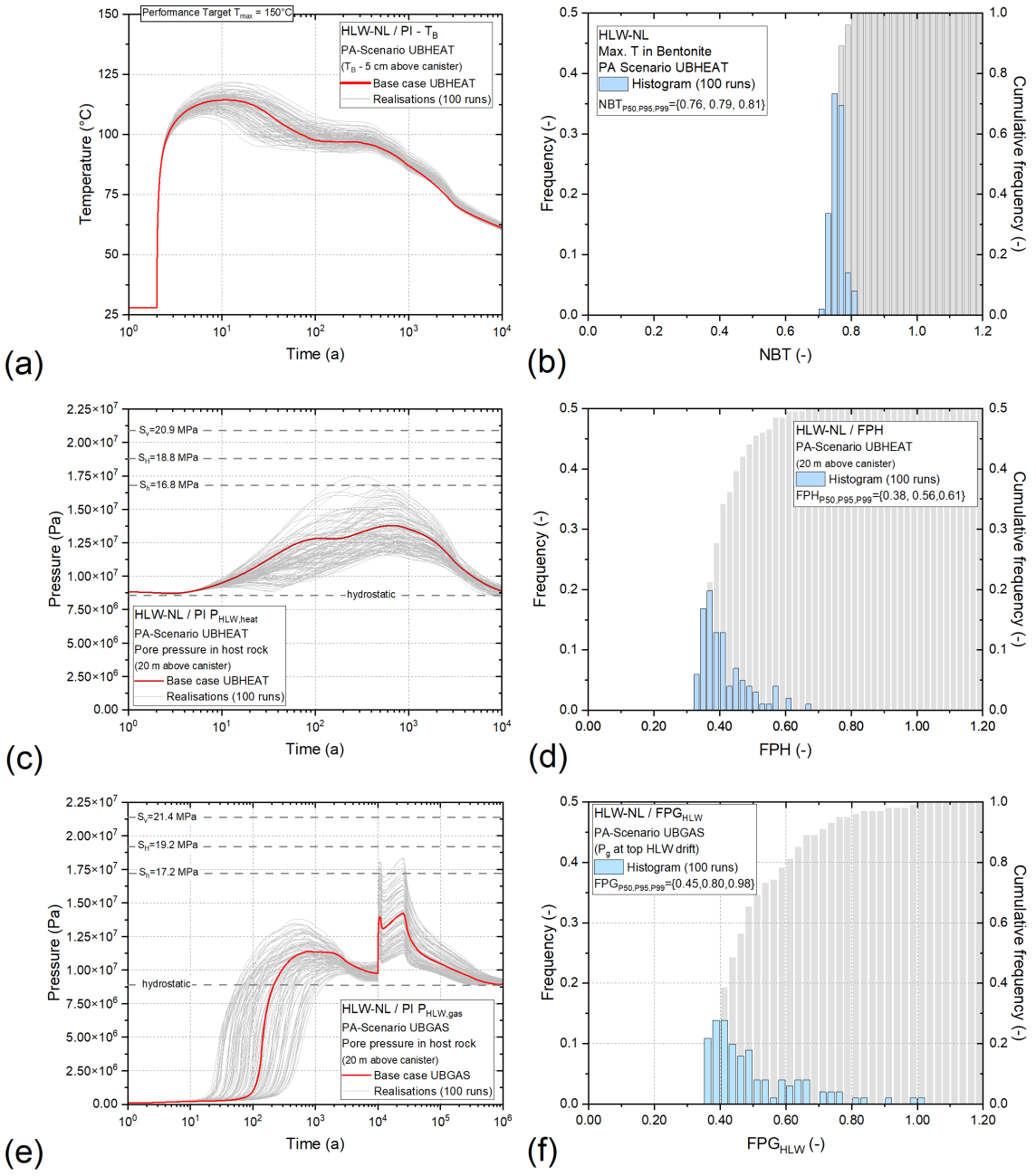

Fig. 6-11: Deviations from expected barrier performance of the HLW canister in PA-Scenarios *UBHEAT* and *UBGAS*

(a+b) impact of pessimistic upper-bound heat production rates on temperature evolution in the bentonite buffer (T_B and NBT); (c+d) on pore pressure in the host rock 20 m above the HLW canister ($P_{HLW,heat}$ and FPH); (e+f) impact of pessimistic gas-generation rates on pore-pressure evolution in an HLW emplacement drift ($P_{HLW,Gas}$ and FPG_{HLW}).

6.3.3 Bentonite buffer, liner and EDZ

Radionuclides will be retained in the bentonite buffer around the HLW canisters by sorption and slow diffusive transport, limiting their release into the host rock over the entire repository lifetime (IMS safety function). Furthermore, the bentonite buffer ensures favourable environmental conditions, contributing to the longevity of canister and liner and supporting the ongoing self-sealing processes in the EDZ (CMP safety function). Arguments and evidence in support of the expected performance of the bentonite buffer are given in Section 3.3. Possible deviations from the expected performance of the buffer as a transport barrier are mainly associated with (i) the maximum temperature of the bentonite experienced in the early post emplacement time and (ii) a possible change of the prevailing hydro-chemical conditions in the HLW near-field, affecting the radionuclide specific sorption capacity of the bentonite. The impact of temperature was evaluated quantitatively, indicating that the bulk of the bentonite buffer will not experience temperatures >125 °C, ensuring a sufficient safety margin with respect to the performance target (performance index NBT, equal to T_B divided by 150 °C, <1; see Fig. 6-11a).

Possible impacts of the hydro-chemical conditions in the HLW near-field on the radionuclide specific sorption capacity of the bentonite are addressed with dedicated hydrochemical near-field models as part of the radiological consequence analysis (NTB 24-23, Nagra 2024p).

The role of the bentonite buffer as a radial flow and transport barrier for non-sorbing radionuclides (e.g., ^{129}I) is of limited significance due to its limited thickness compared with the surrounding host rock. Therefore, a quantitative assessment of the bentonite buffer in the context of PA is omitted.

The role of the liner and the EDZ as a preferential axial transport path for dissolved radionuclides and gas has been addressed in Sections 4.3.3 and 4.4.3. Deterministic simulations of porewater flow and gas flow along the EDZ of the HLW tunnels reveal insignificant fluxes of porewater and gas (Fig. 4-9b, Fig. 4-12b). Probabilistic assessments of axial porewater flow and gas transport along EDZ and the liner are omitted.

6.3.4 Closure system

HLW sealing system

The HLW sealing system (HLW-V1 drift seals, the HLW-V2 repository seals and the V3 shaft seals), as part of the overall repository closure system, prevents the release of dissolved and volatile radionuclides along the backfilled repository structures, thus contributing to the IMS safety function. The backfill material emplaced between the bentonite sealing sections contributes to the CMP safety function, acting as a storage volume for corrosion gases in case of release through the sealing sections. When the closure system performs according to design (addressed with the *EXPERF* scenario), porewater flow and transport of radionuclides along the backfilled underground structures is negligible, as was shown in Chapter 4. The rapid saturation of the bentonite seals ensures the efficient retention of dissolved radionuclides. The backfill between the seals HLW-V1 and HLW-V2 seals remains unsaturated over a time period of more than 100,000 years (Fig. 4-4), and represents a large gas storage volume that efficiently reduces the gas-induced overpressures in the repository structures (see also NTB 24-23, Nagra 2024p).

Reduced performance of the HLW sealing system will not increase radionuclide transport along the underground structures. This is because diffusion-dominated transport in any case prevails in the bentonite buffer around the canisters. Furthermore, gas-driven displacement of porewater along the liner and in the EDZ around the HLW emplacement drifts remains insignificant, even if the performance of the HLW sealing system is assumed to be degraded. The deterministic simulations described in Chapter 4 confirm that the fluxes of porewater and gas from the emplacement drifts through the HLW-V1 seals into the access tunnels remain insignificant over the entire period for assessment (Fig. 4-9b, Fig. 4-12b). Probabilistic assessments of axial porewater flow and gas transport through the HLW-V1 seals are thus omitted due to their low relevance.

L/ILW sealing system

By design, the L/ILW sealing system (L/ILW-V1 cavern seals, the L/ILW-V2 repository seals and the V3 shaft seals), also a part of the overall closure system, ensures retarded release of dissolved and volatile radionuclides along the backfilled repository structures (contributing to the IMS safety function) and prevents the build-up of excessive gas pressures in the L/ILW emplacement caverns (contributing to the CMP safety function). The sealing sections of the L/ILW-V1 and L/ILW-V2 are composed of a sand/bentonite mixture with an elevated permeability to gas compared with the bentonite sealing sections of the V3 seals and HLW sealing system, but still with a low permeability to water. By contrast, the bentonite V3 shaft sealing sections are both gas- and water-tight.

The PA-Scenario *EXPERF* demonstrates excellent functioning of the L/ILW sealing system with large safety margins, expressed by the performance indicators $TF_{CRZ,Cl\text{-}36}$, $TF_{CRZ,C\text{-}14t}$, $TF_{V3,C\text{-}14}$ and $P_{L/ILW,gas}$ (Fig. 6-7). Deviations from expected performance were examined in the PA-Scenario *V3PERM*, aimed at evaluating the impact of a permeable V3 shaft seal on the performance of the L/ILW repository section. Probabilistic simulations were conducted for this PA-Scenario with an assumed permeability of the V3 seal following a log-uniform distribution between 10^{-20} and 10^{-16} m^2, and a capillary strength (P_o parameter in van Genuchten's capillary pressure – saturation relationship) of between 0.22 and 21 MPa; all other input parameter values remained the same as in the base case simulation of the *EXPERF* scenario. The transients of tracer flux of the volatile radionuclide ^{14}C through the V3 seal and the gas pressure evolution in the L/ILW emplacement caverns are presented in Fig. 6-12. The simulations show that a V3 seal with an elevated permeability of around 10^{-16} m^2 would be favourable with respect to the gas pressure build-up, with modest gas-induced overpressures of less than 1.5 MPa (Fig. 6-12b). On the other hand, the tracer flux of the volatile radionuclide ^{14}C through the V3 seal increases significantly with increasing permeability of the seal, with a distinct loss of safety margins (though these are still around two orders of magnitude below the regulatory guideline). It can be concluded that the shaft seal permeability is a sensitive parameter for the release of volatile ^{14}C. Only permeabilities that are greater than 10^{-16} m^2 could result in an unfavourable functioning of the L/ILW sealing system as a transport barrier for volatile radionuclides. The likelihood of occurrence of the *V3PERM* scenario can be classified as hypothetical, because careful construction of the shaft seals based on rigorous quality assurance procedures will ensure that the bentonite sealing sections will be placed according to the specifications.

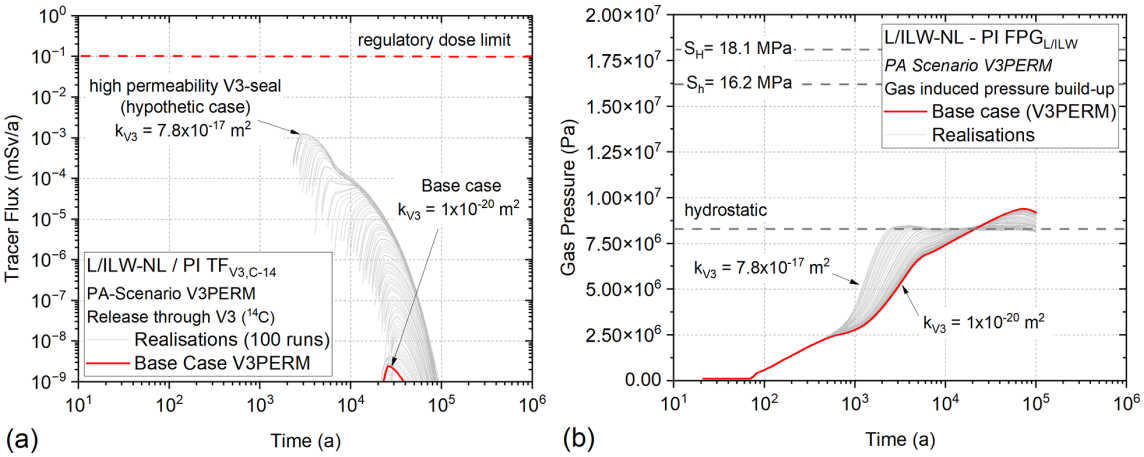

Fig. 6-12: Deviations from expected barrier performance of the V3 shaft seal on the performance of the L/ILW repository (*V3PERM*)

(a) Transients of tracer flux $TF_{V3,C14}$ and (b) transients of $P_{LILW,gas}$. The Monte Carlo simulations represent 100 runs with permeabilities of the V3 seal between 1×10^{-20} to 1×10^{-16} m^2, while all other parameters are identical with the base case.

6.3.5 L/ILW near-field

The fixation and confinement of the L/ILW in a cement-based near-field establishes favourable chemical conditions within the L/ILW emplacement caverns, (i) ensuring the immobilisation and retarded release of radionuclides (IMS safety function) and (ii) reducing the gas generation rates due to metal corrosion and degradation of organic substances (CMP safety function). The expected performance of the L/ILW repository is expressed through the four L/ILW performance indicators, confirming very favourable radionuclide retention conditions for volatile and dissolved radionuclides and moderate gas overpressures in the emplacement caverns, which do not impair the mechanical integrity of the multi-barrier system (Fig. 6-7). Two PA-Scenarios, *ZEROGAS* and *PESSGAS*, were analysed to evaluate deviations from expected performance associated with the L/ILW near-field. *ZEROGAS* explores the evolution of the L/ILW repository in case of insignificant gas generation rates, whereas *PESSGAS* is dedicated to the effect of high gas generation rates.

The *ZEROGAS* scenario with insignificant gas generation in the L/ILW repository was addressed in NTB 24-17 (Nagra 2024p) by a deterministic simulation case, indicating saturation of the L/ILW emplacement caverns after less than 10,000 years and recovery to hydrostatic pore pressure conditions after more than 50,000 years. Complementary probabilistic simulations with a simplified 2.5-D model geometry (NAB 24-25, Nagra 2024m) explore the effect of parametric uncertainties on the resaturation of the L/ILW emplacement caverns and the associated release of dissolved radionuclides (represented by the performance indicator $TF_{CRZ,Cl-36}$). The performance indicators $TF_{CRZ,C-14}$, $TF_{V3,C-14}$, and P_{gas} are not relevant for the *ZEROGAS* scenario, because their safety margins are at least as large as those of the *EXPERF* scenario. The transients of performance indicator $TF_{CRZ,Cl-36}$ are shown in Fig. 6-13a, confirming that the CRZ of the L/ILW repository represents an efficient transport barrier for dissolved radionuclides. The peak tracer flux is approximately 7 OoM below the regulatory dose limit as expressed by the normalised tracer flux $NTF_{CRZ,Cl-36}$ in Fig. 6-13b. The barrier efficiency of the CRZ in the *ZEROGAS* scenario is marginally lower than in the *EXPERF* scenario, which is explained by a more rapid saturation

of the L/ILW emplacement caverns. The *ZEROGAS* scenario can be classified as a hypothetical scenario and its safety relevance is low, because of the very favourable barrier function of the CRZ.

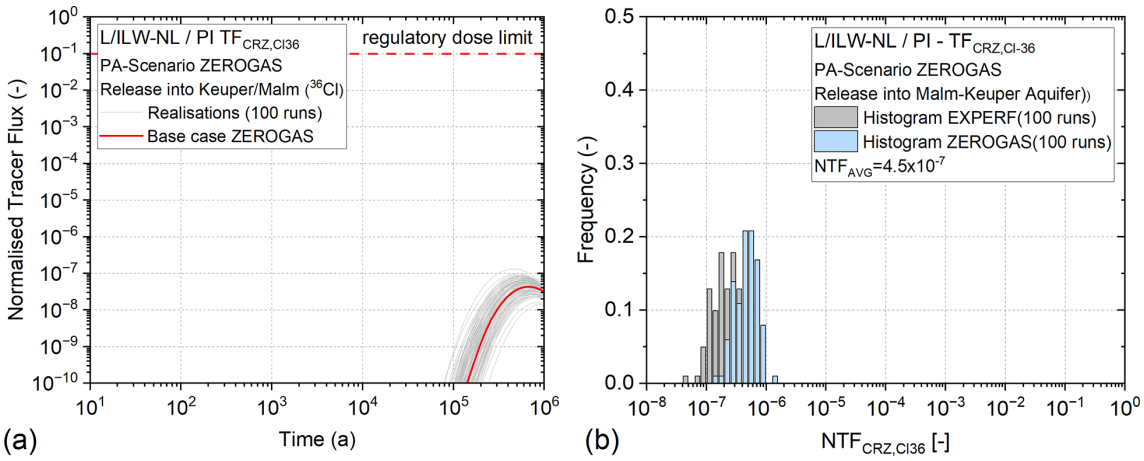

Fig. 6-13: Deviations from expected gas generation rates on the performance of the L/ILW repository section (PA-Scenario *ZEROGAS*)

(a) Transients of tracer flux $TF_{CRZ,Cl\text{-}36}$ and histogram of performance index $NTF_{CRZ,Cl\text{-}36}$; (b) comparison of the histograms of performance index $NTF_{CRZ,Cl\text{-}36}$ of the scenarios *ZEROGAS* and *EXPERF*.

In the scenario *PESSGAS*, it is assumed that the prevailing chemical conditions in the L/ILW emplacement caverns give rise to increased rates of the gas-producing corrosion and degradation processes. Elevated corrosion and degradation rates are linked to the upper bound gas source term for L/ILW (App. A.1.1), which was specified in the gas synthesis report (NTB 24-23, Nagra 2024p). It should be noted that the experimental databases derived from Nagra's dedicated laboratory programme on steel corrosion (NAB 23-22, Diomidis et al. 2023) do not support such high gas generation rates.

Upper bound gas generation rates in the L/ILW repository section were analysed with a deterministic simulation using the 3-D repository model (*Case 3* in NTB 24-23, Nagra 2024p). The deterministic *Case 3* revealed a build-up of maximum gas pressures of less than 10 MPa. The probabilistic simulations as part of the PA-Scenario *PESSGAS* were carried out with a simplified 2.5-D model geometry (NAB 24-25, Nagra 2024m). The aim was to explore the effect of the upper bound gas generation rates on the performance indicators $TF_{CRZ,Cl\text{-}36}$ and $P_{gas,L/ILW}$ by perturbation of the input parameters of the TH^2 model (Fig. 6-14). The comparison of the *PESSGAS* scenario with the scenario of expected performance *EXPERF* indicates only marginal differences in barrier performance. The tracer flux $TF_{CRZ,Cl\text{-}36}$ is practically indistinguishable from that of the *EXPERF* scenario. The pressure evolution P_{gas} shows an earlier peak after 10,000 – 20,000 years with magnitudes between 9 and 11 MPa and a low failure potential ($FPG_{P95} = 0.35$). The *PESSGAS* scenario can be classified as a scenario of low likelihood of occurrence and insignificant impact on radiological safety of the L/ILW repository section.

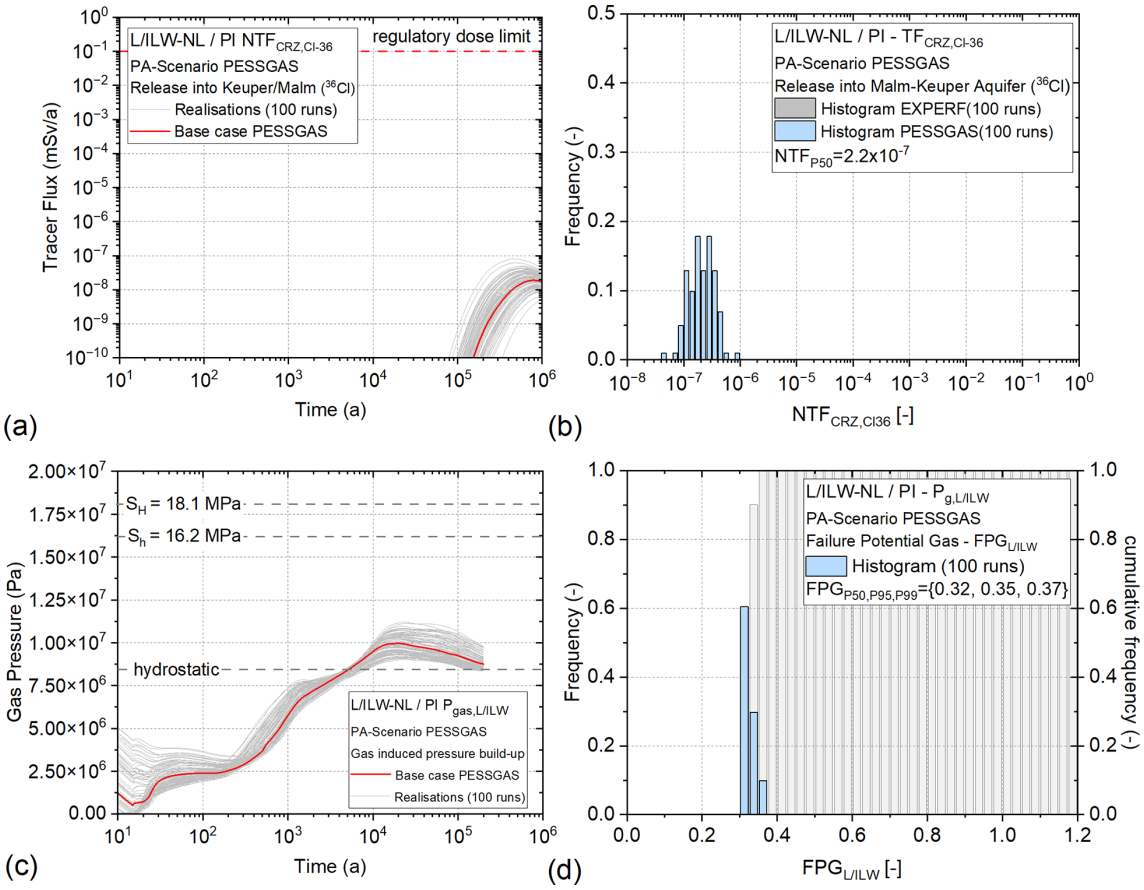

Fig. 6-14: Deviations from expected gas generation rates on the performance of the L/ILW repository section (*PESSGAS*)

(a) Transients of tracer flux $TF_{CRZ,Cl\text{-}36}$ and (b) histogram of performance index $NTF_{CRZ,Cl\text{-}36}$; (c) transients of $P_{LILW,gas}$ and (d) histogram of performance index $FPG_{L/ILW}$.

6.3.6 Containment-providing rock zone (CRZ)

The CRZ represents the main transport barrier for radionuclides for both the HLW and the L/ILW repository sections (IMS safety function). Diffusion-dominated transport is ensured by low hydraulic conductivities of the host rock and the confining units. Based on careful site characterisation carried out in support of the SGT siting processes, there is no evidence for the existence of major fault systems with increased transmissivity in the proposed repository area. Moreover, the high clay content of the host rock gives rise to an efficient self-sealing of any undetected minor tectonic features in the repository near-field. These favourable features of the CRZ form a cornerstone of the safety-oriented repository design, expressed by an expected performance of the repository with large safety margins (Fig. 6-5 to Fig. 6-8).

Several possible deviations from the expected performance of the CRZ are conceivable. Six PA-Scenarios were specified for the HLW repository section to evaluate possible deviations from diffusion-dominated transport in the CRZ ("*UPFLOW*", "*DWNFLOW*", "*HRDBED*", "*HERWIS*", "*MKALK*" and "*HETOPA*"). Five further PA-Scenarios address the effect of undetected faults and repository-induced faults on the barrier performance of the CRZ for both the HLW and the L/ILW repository sections ("*FLTHLWP*", "*FLTHLWN*", "*FLTLILW*", "*RIEHLW*" and "*RIELILW*").

Upward / downward porewater flow

Upwardly directed porewater flow through the CRZ would be expected if the Keuper aquifer below the repository footprint exhibits artesian conditions with a hydraulic head higher than the heads in the lithostratigraphic layer stack above. Artesian conditions were observed in the Benken borehole of the siting region ZNO, but not in NL. In Benken, overpressures <1 MPa above hydrostatic conditions were first measured by packer testing and later confirmed by long-term hydraulic monitoring. Inspired by the observations in the Benken borehole, the PA-Scenario *UPFLOW* assumes a head difference of 1 MPa between Keuper and Malm aquifers (Fig. 6-15a). Furthermore, a comparatively high hydraulic conductivity of 1×10^{-5} m/s is assigned to the Keuper aquifer, representing the upper bound of the observed conductivity values.

Downwardly directed porewater flow is less plausible from a hydrogeological perspective, because it would require artesian conditions in the aquifer systems above and / or sub-hydrostatic conditions below the host rock. Such formation pressures have not been observed in any of the siting regions[10]. Furthermore, the Malm and Keuper aquifers share the same recharge and discharges areas, so that distinct head differences with downwards directed porewater flow are unlikely. The PA-Scenario *DWNFLOW* assumes the unlikely hydrogeological setting with sub-hydrostatic conditions in the Keuper Aquifer (1 MPa below hydrostatic) and hydrostatic conditions in the Muschelkalk and Malm aquifers (Fig. 6-15b).

The PA-Scenarios *UPFLOW* and *DWNFLOW* contribute to the evaluation of the CRZ as a transport barrier for dissolved radionuclides in case of a superimposed vertical advective transport component. The probabilistic analyses were carried out only for the HLW repository section using the performance indicator $TF_{CRZ,I\text{-}129}$ (Fig. 6-15c+d). Hydraulic conductivities and effective diffusion coefficients were assigned to each hydrogeological unit according to the probability density functions given in NAB 24-25 (Nagra 2024m; see also App. A.3). A moderate effect of advective transport on the barrier performance of the CRZ is observed for both scenarios, indicating a loss of safety margins of less than 0.5 OoM when compared with the *EXPERF* scenario; this is seen in the histograms of the NTF performance index (Fig. 6-15e+f). It can be concluded that transport of dissolved radionuclides in the CRZ remains diffusion-dominated, even if distinct pore pressure differences between the regional aquifer systems are assumed. Such pore pressure differences have not been observed in the siting region. Furthermore, the natural tracer profiles observed in the TBO programme (Section 4.6 in NTB 24-17, Nagra 2024k) do not indicate significant deviations from diffusion-dominated transport in the CRZ. *UPFLOW* and *DWNFLOW* can be classified as alternative scenarios, where the *UPFLOW* scenario may be more likely to occur than the *DWNFLOW* scenario. Both scenarios have a low relevance for safety, because the impact on the function of the CRZ as a transport barrier for dissolved radionuclides is small.

[10] Note: indications of modest sub-hydrostatic heads have been observed in the Muschelkalk aquifer. However, the vertical head gradients are too small to create a significant downward directed porewater flow through the repository plane.

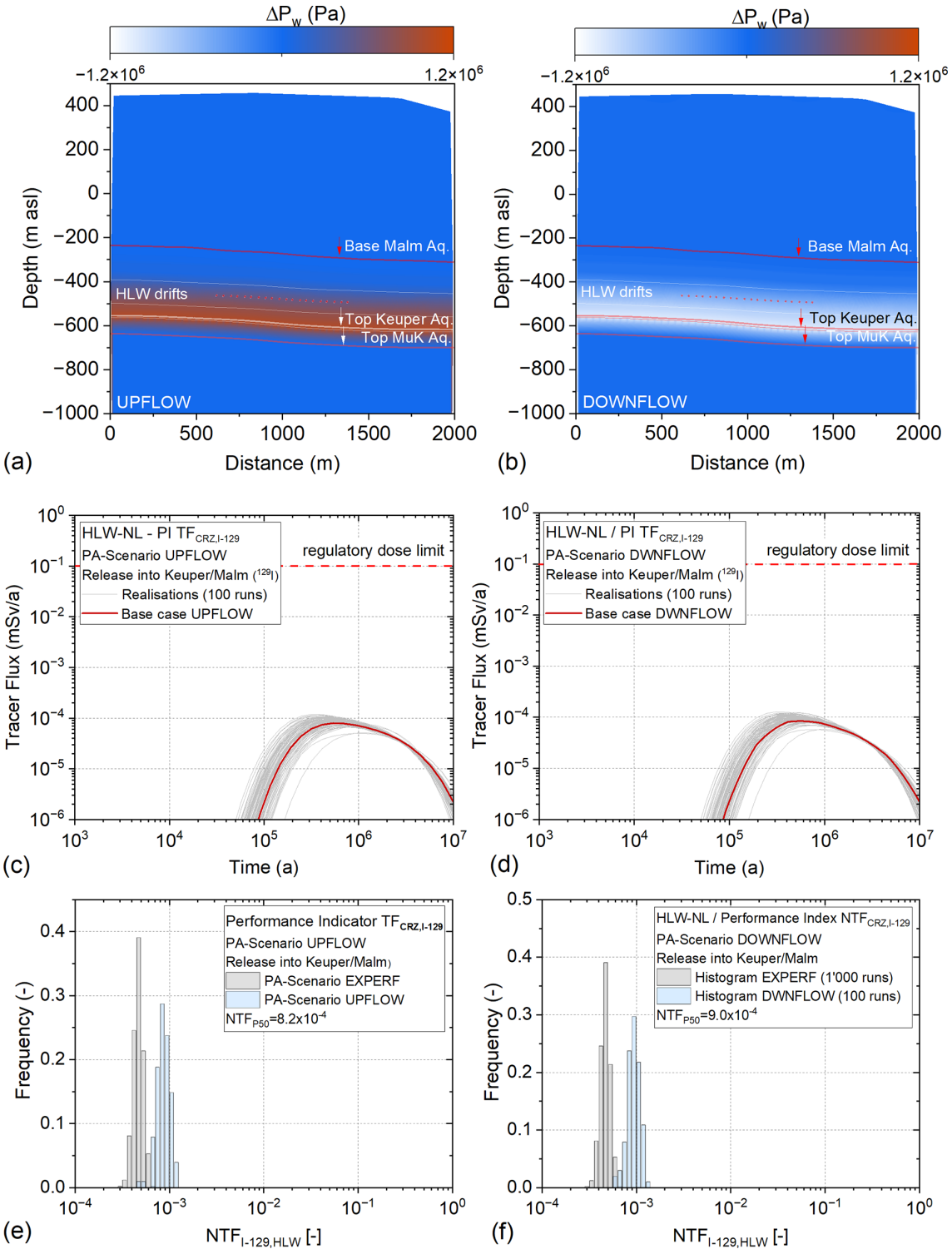

Fig. 6-15: Deviations from expected barrier performance – PA-Scenarios *UPFLOW* and *DWNFLOW* for the assessment of the CRZ of the HLW repository section

Hydraulic head distribution in (a) the *UPFLOW* and (b) the *DWNFLOW* scenarios (deviations from hydrostatic conditions, base case); (c + d) transients of tracer flux $TF_{CRZ,I\text{-}129}$ and histogram of performance index $NTF_{CRZ,I\text{-}129}$ for the *UPFLOW* scenario; (e+f) transients of tracer flux $TF_{CRZ,I\text{-}129}$ and histogram of performance index $NTF_{CRZ,I\text{-}129}$ for the *DWNFLOW* scenario.

Hard beds in the upper confining units and heterogeneous «Herrenwis Unit»

The role of the hard beds in the upper confining units as potential lateral release paths was discussed intensively in SGT Stage 2. In the context of the deep borehole site investigation programme of SGT Stage 3, considerable effort was dedicated to the hydraulic characterisation of the hard beds in the three siting regions. The existing hydrogeological database was confirmed, indicating very limited porewater circulation in the hard beds of the upper confining units. Furthermore, the parametric uncertainties of the relevant flow and transport properties were reduced for all siting regions and especially for NL. The site selection process required that the repositories for HLW and L/ILW must be placed with a minimum lateral distance of 200 m from any major fault systems that could act as potential release paths towards the regional aquifer systems.

The «Herrenwis Unit» occurs in the eastern part of NL as a roughly 40 m thick isolated carbonate platform that is embedded into clay-mineral-richer units above and below (Section 4.5.3.7 in NTB 24-17, Nagra 2024k). It is interpreted as a paleo-reef, exhibiting a substantial variability of mineralogical composition, which could be associated with enhanced matrix permeability. However, the hydraulic conductivities from the in-situ testing in the BUL1 and STA3 boreholes are very low ($<10^{-11}$ m/s). Moreover, sub-hydrostatic hydraulic heads were observed, which are explained in Sections 4.5.3.7, 5.6.5 and 7.2 of NTB 24-17 (Nagra 2024k) by the fact that the «Herrenwis Unit» constitutes a lens of stiff rock embedded in low-permeability clay rocks. This is a strong argument in support of the hydraulically isolated nature of the «Herrenwis Unit», and against its role as a potential release path for radionuclides.

Two PA-Scenarios *HARDBED* and *HERWIS* were specified to investigate the role of the hard beds and the «Herrenwis Unit» in the upper confining units as possible release paths for dissolved radionuclides. The scenario *HARDBED* considers three hard beds in the Sandy-Argillaceous Dogger (SAD) unit above the host rock, each of them characterised by an elevated hydraulic conductivity, but still in the parameter range specified in NAB 24-10 Rev. 1 (Nagra 2024j) (Fig. 6-16a). As a further unfavourable assumption, it is assumed that there is a high lateral hydraulic gradient of 0.1 m/m. A hypothetical vertical fault 200 m from the HLW repository section is assumed to provide a potential release path towards the regional aquifer systems. Fig. 6-16b shows a snapshot of tracer concentration after 1 million years, assuming that the tracer is released instantaneously from the HLW emplacement drifts into the CRZ. The simulation represents the base case of scenario HARDBED, which means that the hydraulic conductivities and effective diffusion coefficients of the layer stack correspond to the reference values as specified in NAB 24-25 (Nagra 2024m). The tracer plume exhibits a peculiar shape, with a uniform diffusive tracer front propagating from the HLW drifts downwards to the Keuper aquifer and a somewhat deformed front propagating upwards towards the Malm aquifer. The shape of the tracer front towards the Malm aquifer can be explained by the effect of lateral porewater flow through the hard beds, which exhibit a higher horizontal permeability than the Opalinus Clay, carrying the tracer towards the assumed fault and reducing the diffusive flux towards the Malm aquifer.

The probabilistic assessment of the *HARDBED* scenario is based on a set of 100 Monte Carlo simulations. The performance indicator $TF_{CRZ,I\text{-}129}$ (Fig. 6-16c) is used to infer the total tracer flux into the regional aquifer systems, including the release via the steeply dipping fault. The corresponding histogram of the performance index $NTF_{CRZ,I\text{-}129}$ is presented in Fig. 6-16d. The simulations show that tracer flux increases by around 0.5 OoM with respect to PA-Scenario of expected evolution. The barrier performance of the CRZ is still favourable, meaning that the expected dose remains around 3 OoM below the regulatory dose limit. Keeping in mind that the assumed high lateral porewater flow in the hard beds is not supported by the observed hydrogeological evidence, such as natural tracer profiles in the deep investigation boreholes in the NL siting region, the *HARDBED* scenario can be classified as having a low probability of occurrence.

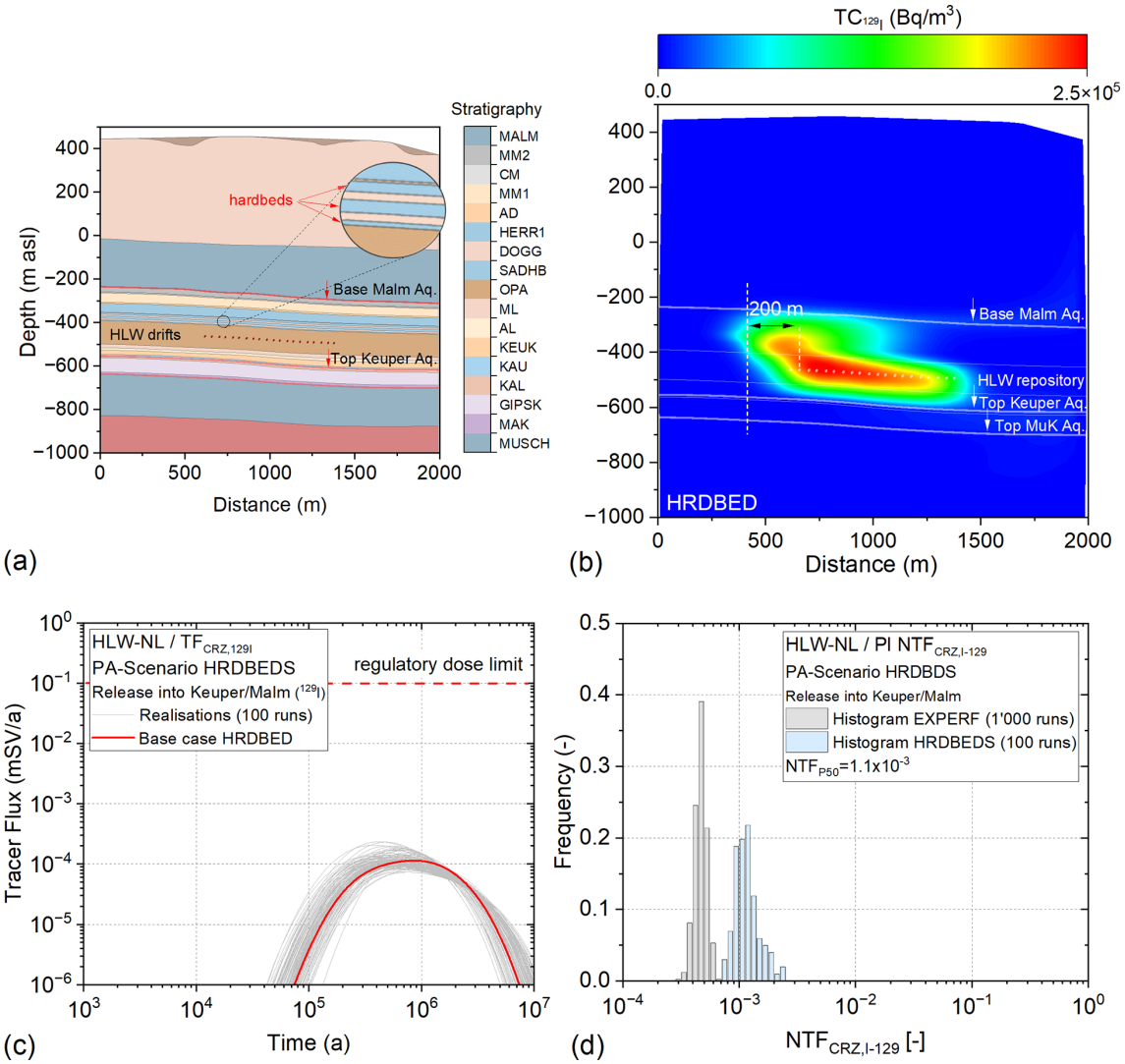

Fig. 6-16: Deviations from expected barrier performance – PA-Scenario *HARDBED* for the assessment of the CRZ of the HLW repository section

(a) Representation of the hard beds in the upper confining units, implemented in the *HARDBED* scenario; (b) snapshot of tracer concentration in the CRZ after 1 million years; (c) transients of tracer flux $TF_{CRZ,I\text{-}129}$ and (d) histogram of performance index $NTF_{CRZ,I\text{-}129}$.

The scenario *HERWIS* is a hypothetical scenario which considers the «Herrenwis Unit» as a heterogeneous carbonate formation with high permeability features. A generic facies model was developed, comprising high permeability subfacies embedded in the heterogeneous carbonate formation sequence. All other sequences of the Mesozoic layer stack are assumed homogeneous, which means that the hydraulic conductivities and effective diffusions coefficients correspond to the reference values specified in NAB 24-25 (Nagra 2024m). The hydraulic conductivity distribution of the base case of the *HERWIS* scenario is presented in Fig. 6-17a. Similarly to the *HARDBED* scenario, it is assumed that a high lateral hydraulic gradient of 0.1 m/m is present in the «Herrenwis Unit». A hypothetical vertical fault 200 m from the HLW repository section is again assumed to provide a potential release path towards the regional aquifer systems.

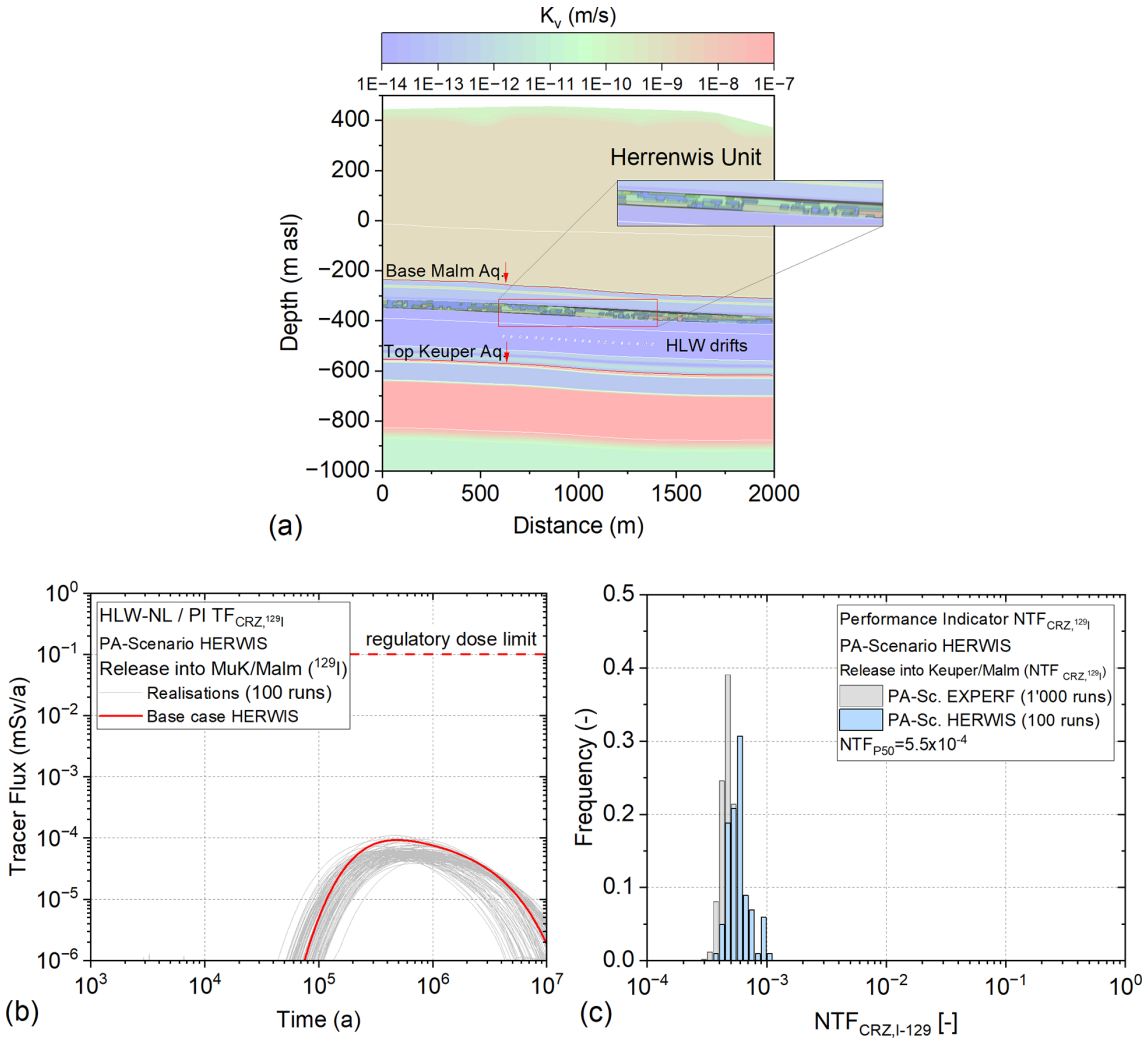

Fig. 6-17: Deviations from expected barrier performance – PA-Scenario *HERWIS* for the assessment of the CRZ of the HLW repository section

(a) Stochastic model of permeability distribution implemented in the *HERWIS* scenario; (b) transients of tracer flux $TF_{CRZ,I\text{-}129}$ and (c) histogram of performance index $NTF_{CRZ,I\text{-}129}$.

The tracer fluxes $TF_{CRZ,I\text{-}129}$ into the regional aquifer systems evaluated in the Monte Carlo simulations of the *HERWIS* scenario (including the tracer flux across the virtual fault) are shown in Fig. 6-17b, showing a behaviour very similar to that observed in the HARDBED scenario. The corresponding histogram of the performance index $NTF_{CRZ,HLW}$ is presented in Fig. 6-17c. The simulations show that tracer fluxes increase by less than 0.5 OoM with respect to the *EXPERF* scenario. The barrier performance of the CRZ is still very favourable, meaning that the expected ^{129}I dose remains more than 3 OoM below the regulatory dose limit. Recalling the fact that geological evidence does not support the existence of high permeability features in the «Herrenwis Unit» in direct hydraulic contact with the Malm aquifer, nor significant lateral groundwater flow in the upper confining units, the *HERWIS* scenario can be classified as hypothetical with low relevance to safety.

Release to the Muschelkalk aquifer

At the scale of the regional groundwater flow, the Keuper aquifer consists of spatially limited and partly isolated local groundwater flow systems with often stagnant conditions. The isolated and local nature is linked to the local lithofacies of the potential transmissive layers (Section 4.5.3.10 in NTB 24-17, Nagra 2024k). In the NL siting region, groundwater samples from the Keuper aquifer could be retrieved from two TBO boreholes (STA2 and BAC1) in the western part of the siting region. The Keuper groundwaters in the NL region represent a hydro-geochemically more evolved state than those from the ZNO siting region. This is likely caused by the fact, that, in the NL siting region, the Seebi Member is thinner and of different lithofacies, and that Keuper groundwater samples in NL were retrieved from individual sandstone channels of the Ergolz Member, likely not representing a well-connected regional aquifer (see Section 4.5 in NTB 24-17, Nagra 2024k) for a detailed hydrogeological interpretation).

The isolated and local character of the water conducting features in the Keuper aquifer of the siting region NL motivates the assessment of the favourable PA-Scenario *MKALK*, in which the entire Keuper formation is part of the lower confining units and the Muschelkalk represents the lower regional aquifer system (Fig. 6-18a). It is assumed that flow and transport properties of the layer stack are the same as in the scenario of expected performance (Section 6.2) and the Bänkerjoch Formation ("Gipskeuper") at the base of the Keuper can be seen as a supplementary aquitard. Diffusion is the dominant transport mechanism.

The *MKALK* scenario encompasses a set of 100 Monte Carlo simulations to evaluate the effect of the extended transport barrier in the lower confining units in terms of the performance indicator $TF_{CRZ,HLW}$ (Fig. 6-18b). The histograms of normalised tracer flux (performance index $NTF_{CRZ,I129}$) derived from 100 Monte Carlo simulations indicate a significant improvement of barrier performance with a gain of 0.4 OoM (Fig. 6-18c). The *MKALK* scenario is supported by the observed hydrogeological evidence, especially by the profiles of natural tracers in the BUL1 and STA3 TBOs, leading to its classification as a likely alternative scenario.

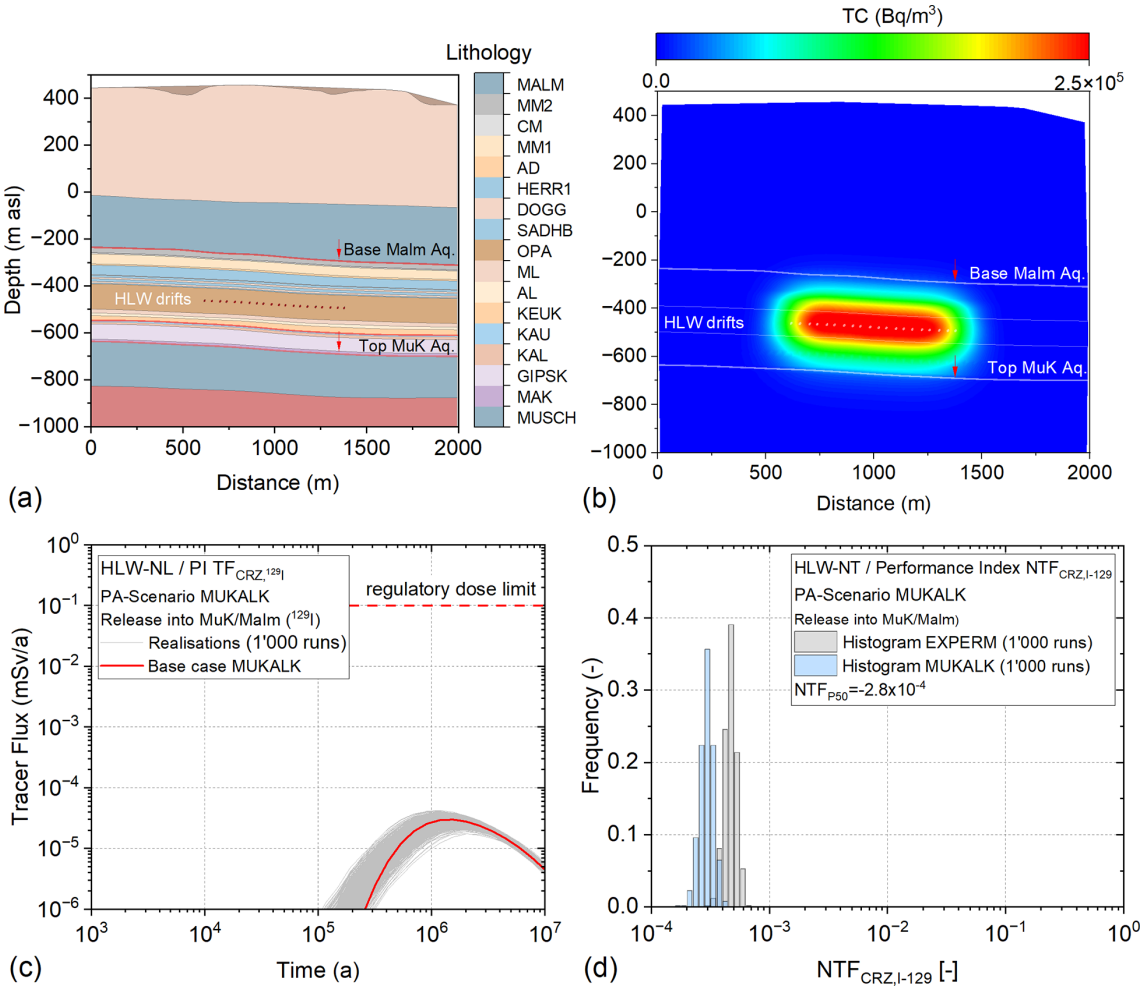

Fig. 6-18: Deviations from expected barrier performance – PA-Scenario *MKALK* for the assessment of the CRZ of the HLW repository section

(a) Representation of an extended CRZ in the lower confining units, implemented in the *MKALK* scenario; (b) snapshot of tracer concentration in the CRZ after 1 million years, (c) transients of tracer flux $TF_{CRZ,I\text{-}129}$ and (d) histogram of performance index $NTF_{CRZ,I\text{-}129}$.

Heterogeneous Opalinus Clay

The Opalinus Clay is known to be the most clay-mineral-rich unit within the area of interest in Northern Switzerland, with no systematic differences in the mineralogical composition between the siting regions investigated in SGT Stage 3 (Section 5.2.3 in NTB 24-17, Nagra 2024k). Furthermore, the lateral and vertical lithological variability is generally small compared with other Mesozoic formations. Despite these favourable characteristics of the Opalinus Clay, the Sectoral Plan requires explicit evidence that spatial variability of the transport properties does not impair the overall barrier performance of the host rock and the CRZ (criterion 3.1 in BFE 2008).

The *HETOPA* scenario addresses the regulatory requirement associated with the spatial variability of transport properties in the host rock. The effect of a heterogeneous distribution of effective diffusion coefficients in the Opalinus Clay on the overall barrier performance of the CRZ was analysed with the stochastic facies model described in Section 5.4.2. The probabilistic 2-D model was based on 100 realisations of the effective diffision coefficinet distribution in the Opalinus

Clay, as given in Fig. 5-7b. All other hydrogeological units were modelled as homogeneous, with the base case input parameters as specified for the *EXPERF* scenario. Hydraulic conditions were assumed hydrostatic, implying that diffusion is the dominant transport process.

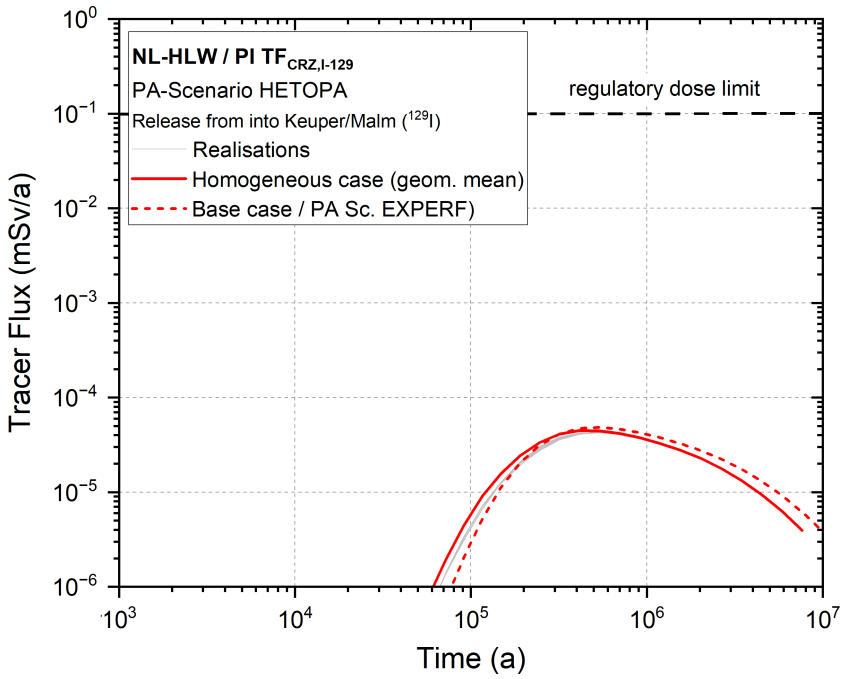

Fig. 6-19: Deviations from expected barrier performance – PA-Scenario *HETOPA* for the evaluation of the CRZ of the HLW repository section

Transients of tracer flux $TF_{CRZ,I-129}$ (gray lines: 100 Monte Carlo simulations, based on stochastic realisations of the $_{effective}$ diffusion coefficient (D_{eff}) distribution in the Opalinus Clay; bold red line: homogeneous Opalinus Clay with $D_{eff} = 2.4 \times 10^{-12}$ m^2/s, representing the geometric mean of the D_{eff} distribution; dashed red line: $D_{eff} = 2.7 \times 10^{-12}$ m^2/s, representing the base case in the *EXPERF* scenario).

Fig. 6-19 shows transients of the performance indicator $TF_{CRZ,I-129}$, representing the release of dissolved ^{129}I into the Malm and Keuper aquifers. The gray lines show the results of the 100 Monte Carlo simulations, based on stochastic realisations of the effective diffusion coefficient ($D_{eff,}$ (x,z)) distribution in the Opalinus Clay, whereas the bold and the dashed red line refer to the deterministic cases of a homogeneous Opalinus Clay with two different D_{eff} values (bold red line: $D_{eff} = 2.4 \times 10^{-12}$ m^2/s, representing the geometric mean of the D_{eff}(x,z) distribution; dashed red line: $D_{eff} = 2.7 \times 10^{-12}$ m^2/s, representing the base case in the *EXPERF* scenario). The probabilistic simulations are characterised by an exceptionally low spread and the transients are bracketed by the deterministic results. It can be concluded that the spatial variability of D_{eff} in the Opalinus Clay formation does not affect significantly the overall performance of the CRZ as a transport barrier.

Steeply dipping faults through the HLW repository section

According to the current design and implementation plan, the HLW emplacement drifts will be placed at a minimum lateral distance of 200 m from all fault systems detected during the seismic surveys. Undetected minor tectonic features within and around the HLW repository section, if they exist at all, exhibit very low transmissivities due to the self-sealing capacity of the host rock. Experimental and empirical evidence for this self-sealing capacity is given in Section 5.7 of NTB 24-17 (Nagra 2024k). Direct evidence for the low transmissivity of faults in the Opalinus Clay has been derived during the TBO campaign, where hydraulic testing of fractures (faults, joints) was a primary test target in all boreholes. The histogram of the interval transmissivities shows generally low values of approximately 10^{-12} m^2/s ± one order of magnitude (Fig. 6-20).

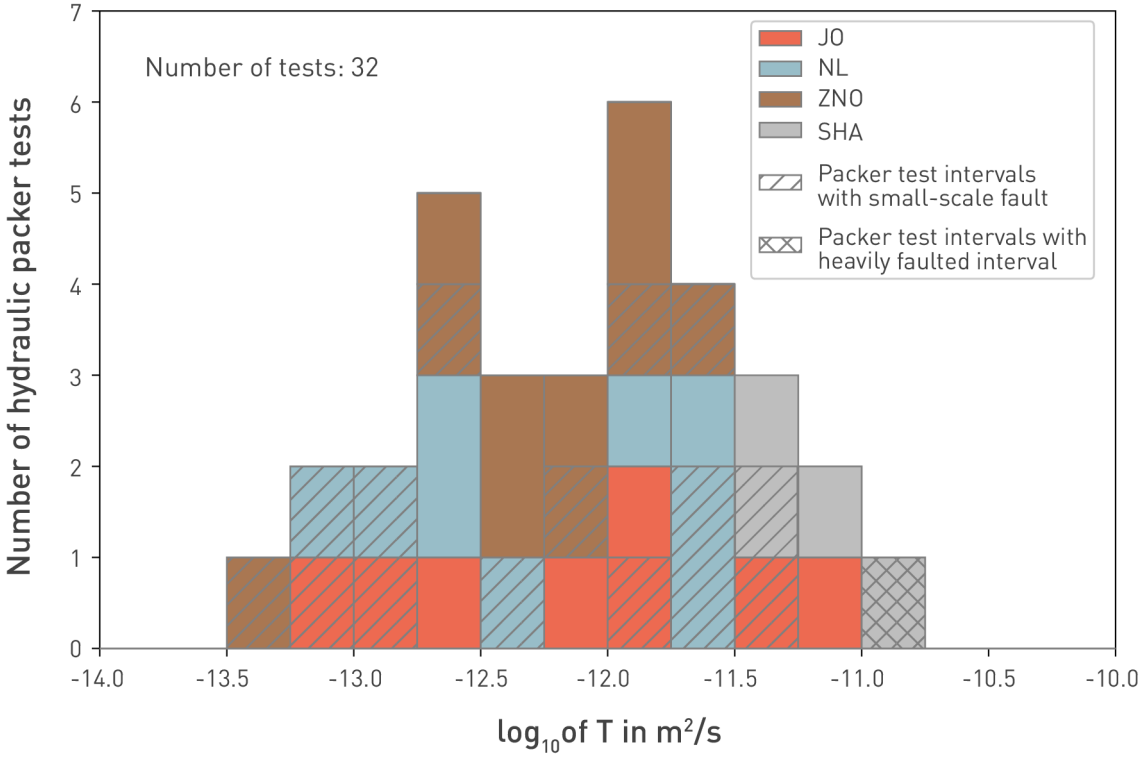

Fig. 6-20: Distribution of the logarithm of the best estimate of the in-situ test transmissivities in the Opalinus Clay

Figure 5-40 from NTB 24-17 (Nagra 2024k).

Tests performed in the BOZ2, BOZ1, RIN, BAC1, STA2, STA3, RHE1, BEN and TRU1 boreholes of the JO, NL and ZNO siting regions as well as the earlier tests carried out in the Schafisheim borehole (SHA).

For HLW, the effect of undetected vertical faults on the barrier performance of the CRZ has been assessed with two PA-Scenarios, namely *FLTHLWP* (Fig. 6-21a), assuming the presence of a fault parallel to the HLW emplacement drifts and *FLTHLWN* (Fig. 6-21b), representing a fault which intersects the 20 HLW drifts in the centre of the HLW repository section. It was assumed that the transmissivity of the fault does not exceed 10^{-10} m^2/s, which is an upper bound of fault transmissivity in clay-rich formations (clay mineral content >40%) with a significant self-sealing capacity (see Fig. 6-20; further evidence in NTB 24-17, Nagra 2024k). Furthermore, a vertical hydraulic gradient is applied between Keuper aquifer and Malm, driven by artesian conditions in the Keuper aquifer (1 MPa above hydrostatic), giving rise to significant advective flow along the fault.

The model configurations for the assessment of the two scenarios *FLTHLWP* and *FLTHLWN* are illustrated in Fig. 6-21a and b. Note that a 2-D model with a discrete fault 1 m in thickness was used for the scenario *FLTHLWP*, whereas a 2.5-D model with the same fault thickness was implemented for the scenario *FLTHLWN*. Further details of the model set-ups are given in Nagra (2024m, NAB 24-25). 100 Monte Carlo simulations were executed to evaluate the effect of porewater flow along the vertical faults parallel and perpendicular to the HLW drift axes. The PDFs of hydraulic conductivity and effective diffusion coefficient of all hydrogeological units formed the input parameters for the probabilistic simulations (see NAB 24-25, Nagra 2024m for further details). Furthermore, a PDF of fault transmissvity was specified as a uniform distribution in the range 10^{-10} $m^2/s \geq T_f \geq 10^{-13}$ m^2/s.

The Monte Carlo simulations of the *FLTHLWP* scenario show characteristic tracer fluxes indicative of diffusion-dominated transport (Fig. 6-21c). More specifically, the vertical porewater flow through the transmissive fault causes an enhanced diffusive transport of the tracer from the nearest HLW emplacement drifts towards the fault, from where it is carried by advection towards the Malm aquifer. Only the nearest drifts contribute to the increased lateral tracer flux to the fault, whereas the more distant drifts remain more-or-less unaffected. In addition to the 100 Monte Carlo simulations, two deterministic cases are presented in Fig. 6-21c. The base case with an impermeable fault (dashed red line) is identical to the base case of the *EXPERF* scenario; the base case of the *FLTHLWP* scenario (bold red line) represents the upper bound of the fault transmissivities with a fault transmissivity of 10^{-10} m^2/s. The corresponding histogram with the performance index of $NTF_{CRZ,I\text{-}129}$ (Fig. 6-21e) shows a moderate reduction in the barrier performance of the CRZ by ≈ 0.5 OoM for the scenario *FLTHLWP*. Complementary simulations with hypothetical fault transmissivities ≥ 10^{-10} m^2/s indicate that a significant loss of barrier performance is to be expected when the fault transmissivity exceeds about 10^{-8} m^2/s.

The configuration with the fault normal to the axes of the HLW drifts (scenario *FLTHLWN*; Fig. 6-21b+d+f) leads to a different retardation and retention behaviour. An early tracer breakthrough to the Malm aquifer is observed, caused by advective transport in the fault. At the intersections of the 20 HLW drifts with the vertical fault, the tracer is released from the nearest HLW canisters into the fault, from where it is carried by advection towards the Malm aquifer. Only the nearest canisters contribute to the increased lateral tracer flux to the fault, whereas the more distant canisters remain more or less unaffected, because lateral transport through the bentonite in the HLW drifts is diffusion dominated. At late times, the general regime of diffusion-dominated vertical transport from the HLW drifts to the upper and lower aquifer system prevails, indicating that the drift sections in the immediate vicinity of the fault are leached out.

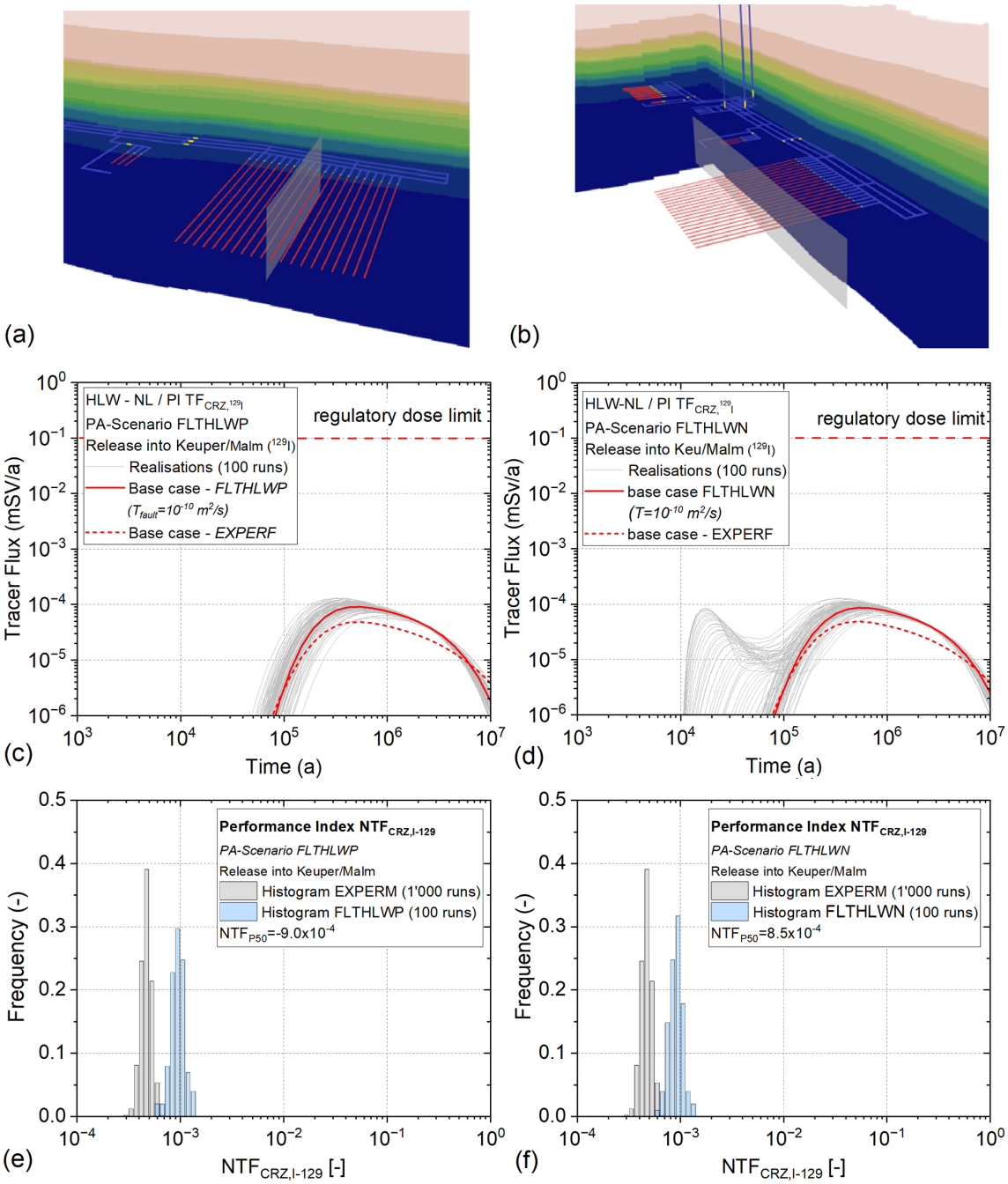

Fig. 6-21: Deviations from expected barrier performance – PA-Scenarios *FLTHLWP* and *FLTHLWN* for the evaluation of the CRZ of the HLW repository section

(a) Configuration with a fault parallel to HLW emplacement drifts; (b) fault perpendicular to HLW emplacement drifts; (c+d) transients of tracer flux $TF_{CRZ,I-129}$ and (e+f) histogram of performance index $NTF_{CRZ,I-129}$.

The existence of steeply dipping faults in the Opalinus Clay with a transmissivity $T_{f,max} \leq 10^{-10}$ m^2/s cross-cutting the HLW repository section cannot be ruled out. *FLTHLWP* and *FLTHLWN* can be classified as likely alternative scenarios with limited relevance for repository safety. Note that a distinct hydraulic gradient between the regional aquifer systems is required to activate the fault as an advective transport path, the effects of which are observed in the vicinity of the repository area.

Steeply dipping faults through the L/ILW repository field

Again according to the current design and implementation plan, the L/ILW caverns will also be placed a minimum lateral distance of 200 m from any major fault systems. Undetected minor tectonic features within and around the L/ILW repository section would exhibit very low transmissivities of less than 10^{-10} m^2/s due to the self-sealing capacity of the Opalinus Clay. However, the effects of undetected vertical faults on the post-closure evolution of the L/ILW repository section in terms of resaturation and pore pressure build-up in the backfilled L/ILW repository structures cannot be excluded. They could give rise to a different mode of functioning of the multi-barrier system, which must be addressed from the PA perspective. Key aspects to evaluate are (i) the volatile radionuclide ^{14}C, which could be released through the fault into the Malm aquifer in an early stage after repository closure and (ii) the enhanced release of the dissolved radionuclide ^{36}Cl due to the fast saturation of the L/ILW emplacement caverns.

For the L/ILW, repository section, the effect of undetected vertical faults on the barrier performance of the CRZ has been evaluated with a single PA-Scenario *FLTLILW*, assuming a fault which intersects the 7 L/ILW emplacement caverns near their V1 seals (Fig. 6-22a). As in the corresponding HLW scenario, it was assumed that the transmissivity of the fault does not exceed 10^{-10} m^2/s. It was further assumed that the reference gas source term applies. Pore pressure conditions in the regional aquifer systems were assumed to be hydrostatic.

Fig. 6-20b illustrates the evolution of gas pressure in the L/ILW emplacement caverns for the base case of the *FLTLILW* scenario with a fault transmissivity of 10^{-10} m^2/s, representing the upper bound of the range of the fault transmissivities observed in Opalinus Clay. The capillary strength of the fault $P_o = 1.075$ MPa, indicating that entry of the gas phase into the fault occurs soon after the gas reaches the hydrostatic pressure level. The comparison with the base case of the *EXPERF* scenario (Fig. 6-7d) shows that the fault causes a much faster pressure recovery, with hydrostatic conditions established after less than 10,000 years (base case in Fig. 6-7: ≈ 20,000 years) and a peak gas pressure which is close to hydrostatic. Fig. 6-22c presents snapshots of gas saturation in the fault plane around the L/ILW emplacement cavern at times of 100, 1,000, 5,000 and 10,000 years after repository closure. After 100 years, the cavern is still unsaturated (note: $S_w = 1\text{-}S_g$). Full water saturation of the lower part of the cavern is reached after 1,000 years; only the rooves of the backfilled caverns remains unsaturated. Gas starts to invade the faults after around 5,000 years. After 10,000 years, when hydrostatic pressure is reached, the gas phase reaches the Malm aquifer. Buoyancy effects prevent the propagation of the gas front below the caverns towards the Keuper aquifer. The gas saturation in the faults stabilises quickly and a quasi-steady state gas flow develops into the Malm aquifer.

Three L/ILW performance indicators were analysed in the context of the probabilistic assessments, namely $TF_{CRZ,Cl\text{-}36}$, $TF\text{-}_{CRZ,C14}$, and $P_{Gas,L/ILW}$ (Fig. 6-23). The tracer flux $TF_{CRZ,Cl\text{-}36}$ is significantly higher than in the *EXPERF* scenario, reaching peak values in the order of 10^{-7} mSv/year (Fig. 6-23a). More detailed analyses indicate that this is caused by some limited displacement of contaminated porewater from the L/ILW caverns towards the Keuper aquifer. Nevertheless, the total release remains around 6 OoM below the regulatory dose limit. Another aspect to consider is the release of ^{14}C along the fault, which is covered by the performance indicator $TF\text{-}_{CRZ,C14}$ (Fig. 6-23b). The tracer flux of volatile ^{14}C along the vertical fault is significantly higher than in the *EXPERF* scenario, reaching leading to peak dose rate values in the order of 10^{-5} mSv/year, but still 4 OoM below the regulatory dose limit. The transients of gas pressure build-up, $P_{Gas,L/ILW}$, depicted in Fig. 6-23d do not indicate pressures sigificantly above hydrostatic. Furthermore, transport of ^{14}C along the backfilled underground structures towards the V3 seal is insignificant.

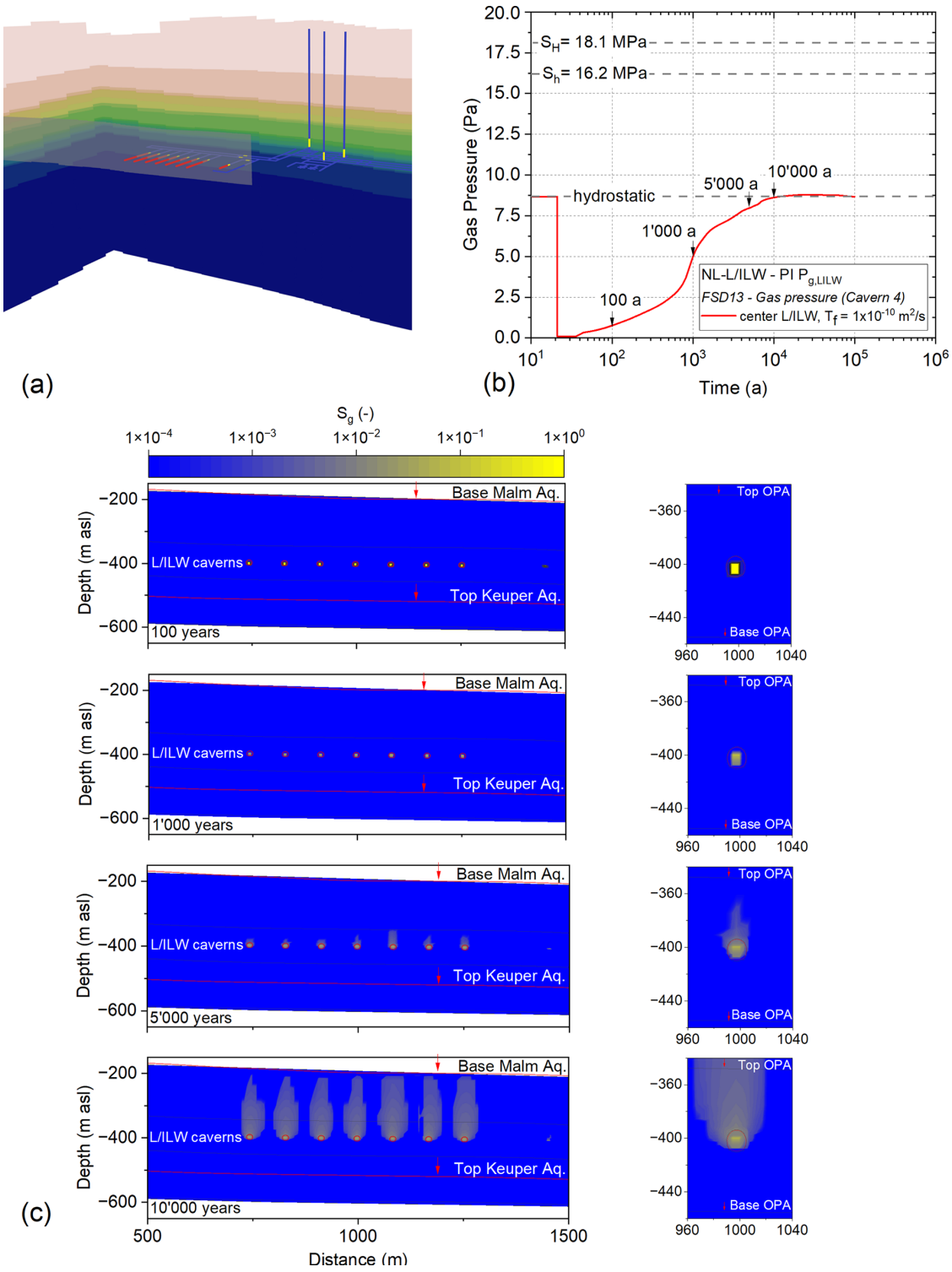

Fig. 6-22: Deviations from expected barrier performance – PA-Scenario *FLTLILW* for the assessment of the CRZ of the L/ILW repository section (case TSD13 in NAB 24-25 Nagra 2024m)

(a) Schematic sketch of L/ILW repository section with a steeply dipping fault; (b) gas pressure evolution in the L/ILW emplacement caverns for the base case with a fault transmissivity of 10^{-10} m^2/s, (c) snapshots of gas saturation in the fault after 100, 1,000, 5,000 and 10,000 years.

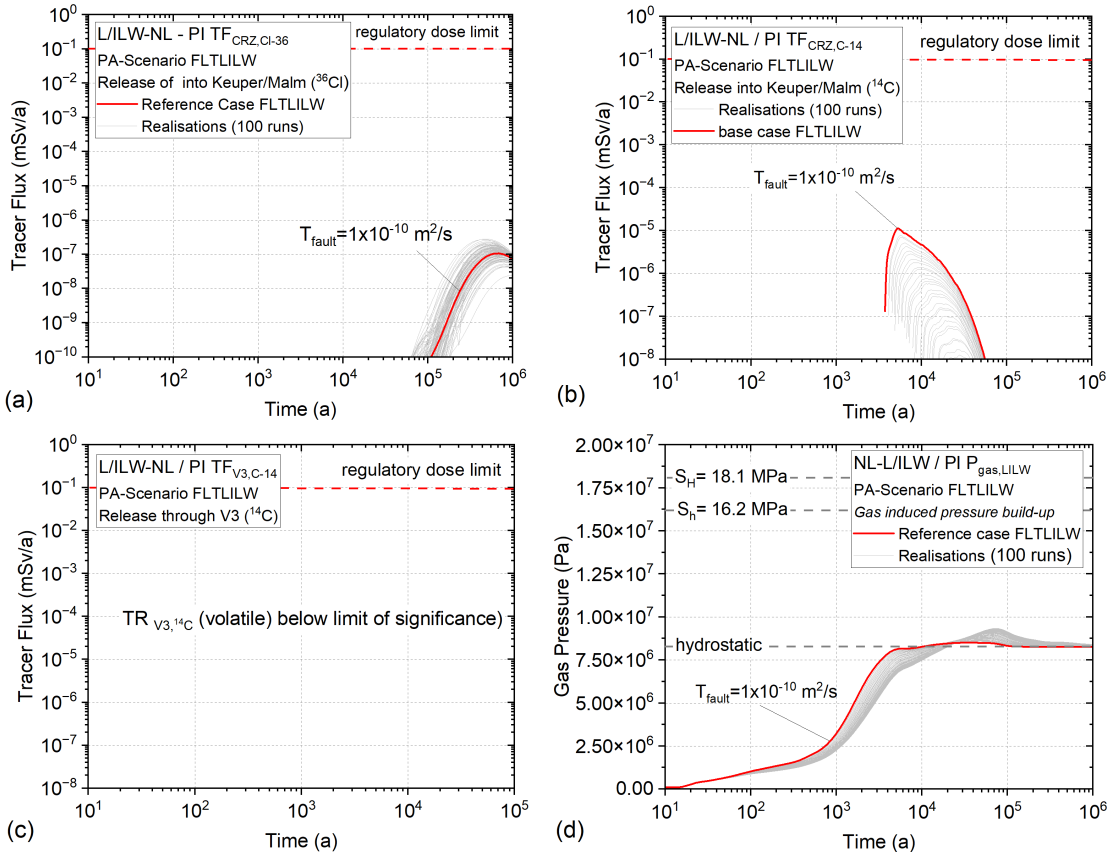

Fig. 6-23: Deviations from expected barrier performance – PA-Scenario *FLTLILW* for the assessment of the CRZ of the L/ILW repository section

Evaluation of the performance indicators (a) tracer flux TF-$_{CRZ-Cl36}$; (b) tracer flux TF$_{CRZ-C14}$; (c) tracer flux TF$_{V3-C14}$; (d) gas pressure in the L/ILW emplacement cavern.

The existence of steeply dipping faults in the Opalinus Clay with a transmissivity less than around 10^{-10} m^2/s cross-cutting the L/ILW repository section cannot be ruled out. *FLTLILW* is a likely alternative scenario with limited impacts on repository safety. Nevertheless, it is of some relevance from the viewpoint of general repository evolution as described in the "storyboard" report (NAB 24-20 Rev. 1, Nagra 2024n), because the rapid saturation of the L/ILW caverns changes the mode of operation of the multi-barrier system. In this sense, the *FLTLILW* scenario is assessed in greater detail in the context of the radiological consequence analysis.

Thermally- and gas-induced faults (HLW repository)

The likelihood of occurrence of thermally- and gas-induced faults has been addressed as part of the PA-Scenarios *EXPERF*, *UBHEAT and UBGAS* with the performance indicators FPH$_{HLW}$, FPG$_{HLW}$. The probabilistic assessments confirmed that, for all scenarios, thermally- and gas-induced faults are unlikely to occur, and may be classified as hypothetical under the expected geomechanical conditions at the repository level. Under unfavourable stress conditions and assuming unexpectedly low rock strength, it is, however, conceivable that thermally- or gas-induced rock failure could occur.

The PA-Scenario *RIEHLW* thus evaluates the impact of thermally- or gas-induced fractures on the transport barrier performance for releases from HLW with a focus on dissolved radionuclides (performance indicator $TF_{CRZ,I\text{-}129}$). The pessimistic assumption [11] is made that a thermally- or gas-induced vertical fracture develops along the axis of an HLW emplacement drift in the centre of the HLW repository section, as shown in Fig. 6-24a, which also shows the 2-D mesh used in the assessment model. The fault extends to the Malm and Keuper aquifers. Hydrostatic pore pressure conditions are assumed in the regional aquifer systems. Source terms of heat and gas correspond to the scenario of expected performance and the release of ^{129}I starts after 10,000 years, corresponding to the canister lifetime assumed in the scenario. The scenario *RIEHLW* evaluates phenomena that include the impact of buoyancy along the fault and gas-driven porewater displacement.

Fig. 6-24b shows a snapshot of tracer release after 500,000 years. Contour plots of tracer concentration are shown, indicating a very minor effect of the fault in the centre of the HLW repository on diffusion-dominated tracer transport. This is also confirmed by the transients of the tracer flux $TF_{CRZ,I\text{-}129}$ (Fig. 6-24c) and by the histograms of the performance index $NTF_{CRZ,I\text{-}129}$ (Fig. 6-24d), which are comparable to those evaluated for the *EXPERF* scenario.

The *RIEHLW* scenario related to a steeply dipping thermally- or gas-induced fault is an unlikely scenario of low significance to repository safety.

[11] A vertical fracture induced by thermal or gas-related porewater overpressures and extending from the Keuper to the Malm aquifer is unlikely to occur. Thermally induced fractures are a local phenomenon associated with undrained conditions and caused by thermal expansion of the porewater in a low-permeability porous medium. Gas-induced fractures propagate preferentially along the EDZ, which represents a zone of weakness in the immediate vicinity of the HLW emplacement drifts.

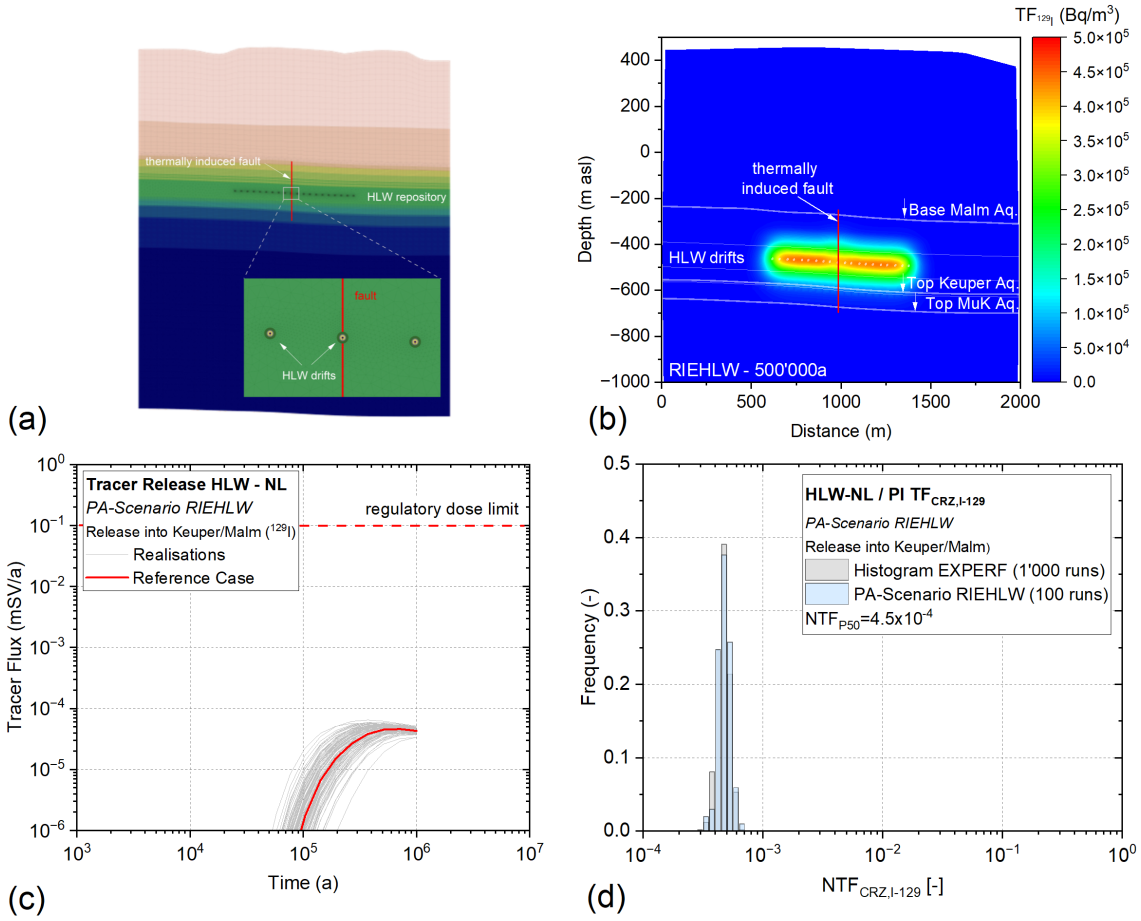

Fig. 6-24: Deviations from expected barrier performance – PA-Scenario *RIEHLW* for the assessment of the CRZ of the HLW repository section

(a) Mesh of the 2-D transport model with a vertical fault through the drift axis in the centre of the HLW repository section; (b) snapshot of tracer concentration after 500,000 years; (c+d) transients of tracer flux $TF_{CRZ,I\text{-}129}$ and histogram of performance index $NTF_{CRZ,I\text{-}129}$.

Gas induced faults in the (L/ILW repository)

The likelihood of occurrence of gas-induced faults in the L/ILW repository section has been addressed with the performance indicator FPG_{LILW} as part of the PA-Scenarios *EXPERF* and *PESSGAS*. The probabilistic assessments revealed that, in both scenarios, gas-induced faults are very unlikely to occur under the expected geomechanical conditions at repository level. Only under very unfavourable stress conditions and assuming unexpectedly low rock strength is it conceivable that gas-induced rock failure could occur in the L/ILW repository section.

The PA-Scenario *RIELILW* is dedicated to evaluating the safety relevance of gas-induced fractures for the L/ILW repository under these unlikely conditions. For this scenario, the transport barrier performance of the L/ILW repository system is evaluated, with a focus on dissolved and volatile radionuclides (performance indicators $TF_{CRZ,Cl\text{-}36}$, $TF_{CRZ,C\text{-}14}$). No additional simulations are required, because the PA-Scenario *EXPERF, PESSGAS* and *FLTLILW* provide all relevant information to draw safety-relevant conclusions for the *RIELILW* scenario:

- Gas-induced fracturing, with the release of dissolved ^{36}Cl and volatile ^{14}C along the newly created fracture, cannot occur before hydrostatic pressure is reached in the L/ILW emplacement caverns. This occurs only after more than 10,000 years in the *PESSGAS* scenario and after around 20,000 years in the *EXPERF* scenario.
- Consequently, the release of dissolved ^{36}Cl along the newly created fracture must be comparable to that in the *FLTLILW* scenario, giving rise to dose rates that are more than 5 OoM below the regulatory dose limit (see Fig. 6-23a).
- The onset of the release of volatile ^{14}C along the newly created fracture is significantly delayed compared with the *FLTLILW* scenario, which, due to radioactive decay, leads to significantly lower ^{14}C dose rates, at least 4 OoM below the regulatory dose limit (*FLTLILW* scenario: see Fig. 6-23b).

It can be concluded that *RIELILW* is a scenario of low safety relevance with a very low likelihood of occurrence.

6.3.7 Deep underground location

A favourable geological setting and a repository depth of 850 – 950 m b.g.l. ensures long-term stability of the repository system with respect to long-term geological and climatic evolution. Accordingly, the impacts of geological long-term evolution are disregarded in the PA-Scenario of expected performance (*EXPERF* – Section 6.2), both for the HLW and the L/ILW repository sections.

Deviations from expected performance of the repository system in response to the impacts of long-term geological evolution are mainly related to earthquakes and erosion process. Four PA-Scenarios are formulated to address detrimental effects associated with the long-term geological evolution (PA-Scenarios *SEISHLW*, *SEISLILW*, *LOSSOB* and *LOSSFLT*; see Tab. 6-1).

Earthquake impact on the deep geological repository (HLW and L/ILW repository sections)

As stated in NAB 24-28 (Nagra 2024i), earthquakes can perturb the multi-barrier system of a geological repository in two main ways. The first is the actual static displacement on the rupture surface of the activated fault zone. The second is the shaking which translates to the cyclic loading of structures through the passing wave train. Nagra (2024i) develops geological scenarios that describe the potential occurrence of seismicity during the post-closure period at the Haberstal site. The geological scenarios are required for the post-closure safety assessment to determine if

earthquakes have the potential to compromise post-closure safety. Four geologic scenarios are presented; two of them postulate a rupture through elements of the L/ILW and HLW repository sections, with a fault size in the hectometre to km-range. The other scenarios address seismic events at the periphery of the repository associated with shaking of the backfilled repository structures. In Nagra (2024i, NAB 24-28), empirical relationships are presented between earthquake magnitude and fault size and are discussed in the context of probabilistic assessments of earthquake frequency. According to these relationships, an earthquake of magnitude 3.4 would correspond to a fault size in the hectometre range and have an annual frequency of occurrence of between 10^{-4} and 10^{-5} events per year and km^2. From this, the likelihood of occurrence such an earthquake with its hypocentre at repository depth can be inferred to be 1 – 2 orders of magnitude lower still (i.e., 10^{-5} and 10^{-6} events per year, with the activated fault zone cross-cutting the repository and connecting the regional aquifer systems above and below the CRZ). Note that these assessments are pessimistic in that they assume no prior information about the distribution or presence of potentially seismogenic faults, even though one paradigm of site selection has been the identification of a zone free of faulting.

The PA-Scenarios *SEISHLW* (Fig. 6-25a) and *SEISLILW* (Fig. 6-25b) involve rupture through elements of the HLW and the L/ILW repository sections. The impacts of shaking are of minor relevance from a post-closure safety perspective. Emphasis is on the performance of the CRZ as a transport barrier for dissolved and volatile radionuclides (safety function IMS). No additional Monte Carlo simulations are required to assess the earthquake impacts; it is sufficient to use the results of the *FLTHLWN* and *FLTL/ILW* scenarios, including their Monte Carlo simulations, as bounding cases.

The PA-Scenario *SEISHLW* postulates a vertical rupture plane intersecting the HLW repository section, as illustrated in Fig. 6-25a. After the earthquake event, it is assumed that a vertical groundwater flow develops along the newly activated fault plane, which is driven by the induced pore pressure disequilibrium in the regional aquifer systems above and below the CRZ. This flow decreases with progressive pressure equilibration in the regional aquifer systems above and below the CRZ. Furthermore, considerable empirical and experimental evidence has been collected (NAB 24-10 Rev. 1, NTB 24-17: Nagra 2024j, 2024k), which provides confidence in an efficient transmissivity reduction of the newly created fault due to self-sealing processes in the in the clay-rich sequences of the CRZ. Comprehensive databases from packer testing in the recent TBO programme and from previous site investigations confirm that fault transmissivities in the Opalinus are generally less than $10^{-10} m^2/s$. In the Monte Carlo simulations of the *FLTHLWN* scenario, 10^{-10} m^2/s is taken as an upper bound for fault transmissivity. This implies that the simulations can be regarded as a pessimistic formulation of the *SEISHLW* scenario, assuming the earthquake happens at the time of repository closure. Recalling that the likelihood of occurrence of an earthquake of magnitude 3.4 with its hypocentre at repository depth in the order of 10^{-5} and 10^{-6} events per year, the *SEISHLW* scenario can be classified as a scenario with a very low likelihood of occurrence.

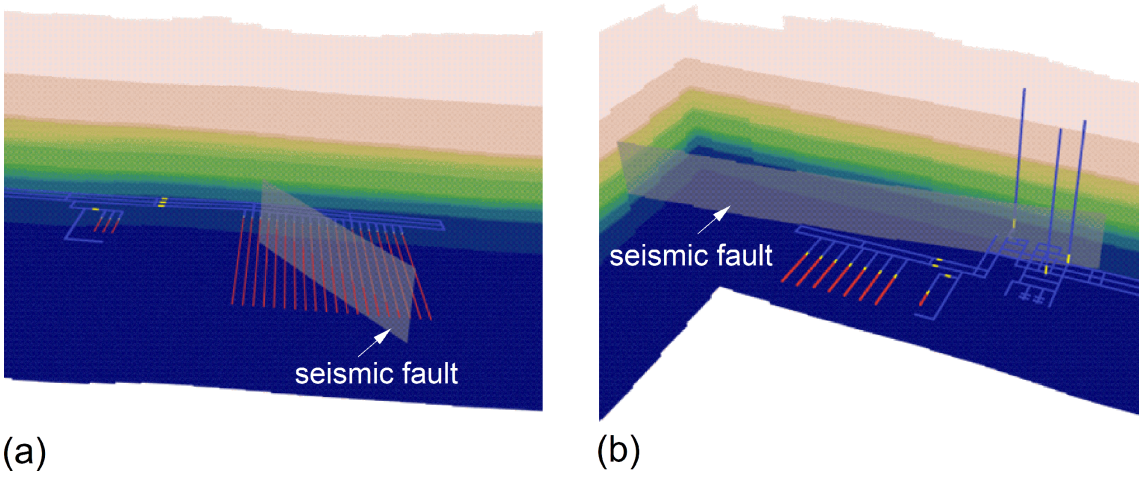

Fig. 6-25: Deviations from expected barrier performance – PA-Scenarios *SEISHLW* and *SEISLILW* for the evaluation of the impact of an earthquake on repository performance

Illustration of (a) rupture surface through the HLW repository section; (b) rupture surface through the L/ILW repository section.

The PA-Scenario *SEISLILW* postulates a vertical rupture plane intersecting the L/ILW repository section, as illustrated in Fig. 6-25b. Similarly to the *SEISHLW* scenario, it is assumed that a vertical groundwater flow develops along the newly activated fault plane. Self-sealing processes in the clay-rich sequences of the CRZ ensure that fault transmissivities are generally less than 10^{-10} m^2/s, except for a short period after the earthquake. The Monte Carlo simulations of the *FLTLILW* scenario can be regarded as a pessimistic formulation of the *SEISLILW* scenario, assuming the earthquake occurs at the time of repository closure. Again, recalling that the likelihood of occurrence of an earthquake of magnitude 3.4 with its hypocentre at repository level has been estimated to be in the order of 10^{-5} and 10^{-6} events per year, *SEISLILW* can be classified as a scenario with a very low likelihood of occurrence.

Landscape evolution and loss of overburden (HLW repository section)

Chapter 7 in NTB 24-17 (Nagra 2024k) presents a synopsis of the geological processes that may affect radionuclide release from a nuclear waste repository into the regional aquifer systems. It points out that a critical reduction of the host rock overburden above the repository is of potential relevance to post-closure safety as it could lead to a significant change in the key barrier properties of the CRZ (hydraulic conductivity, diffusion properties, self-sealing capacity). Fig. 6-26 shows a schematic diagram narrating the anticipated long-term geological evolution of the NL siting region over the next million years, defined as the 5 – 95% uncertainty band in erosion assessment. Multiple aspects related to the changes in the barrier efficiency of the Opalinus Clay and the confining units in response to a reduction of the overburden by erosion processes have been analysed. In particular, hydraulic properties are known to depend on overburden (stress). In the case of the over-consolidated Opalinus Clay, high values of hydraulic conductivity of up to around 10^{-4} m/s are reported only in locations with overburden thicknesses of a few decametres (Fig. 6-27a) due to rock weathering and decompaction. With increasing overburden thickness, the hydraulic conductivity decreases by many orders of magnitude, e.g., in the Mont Terri rock laboratory typical values are in the range of 10^{-12} to 10^{-13} m/s. The best estimates of the hydraulic conductivities from hydraulic packer tests carried out in the JO, NL and ZNO boreholes vary over

a narrow range of 10^{-13} to 10^{-14} m/s. At these depths, no depth dependence is visible (Fig. 6-27a), i.e., the hydraulic properties of the Opalinus Clay are considered to be identical among the siting regions considered in SGT Stage 3.

The PA-Scenario *LOSSLOB* evaluates the effect of mechanical unloading caused by the loss of overburden due to erosion processes on the hydraulic conductivity of the host rock. It is assumed that a hydraulic head difference of 1 MPa exists between Keuper and Malm aquifers, resulting in an upwardly directed porewater flow through the CRZ and through the HLW repository section. The dependence of hydraulic conductivity in the Opalinus Clay on overburden thickness is represented by a power law relationship (blue line in Fig. 6-27a), which can be regarded as an upper bound based on the observed overburden stress dependence of hydraulic conductivity. The expected loss of overburden over the next million years is implemented in terms of a simple functional relationship in which the overburden thickness decreases monotonically with time (Fig. 6-27b). 100 realisations of the time-dependent loss of overburden are generated. For this, the free parameters of the functional relationship are calibrated to match the P05, P50, and P95 percentiles of the site-specific probability density distribution of loss of overburden, which was provided in Section 6.4.4 of NTB 24-17 (Nagra 2024k; see also Fig. 6-26). The realisations are combined with the depth-dependent hydraulic conductivity to form 100 realisations of a time-dependent hydraulic conductivity of the Opalinus Clay as input to transport modelling.

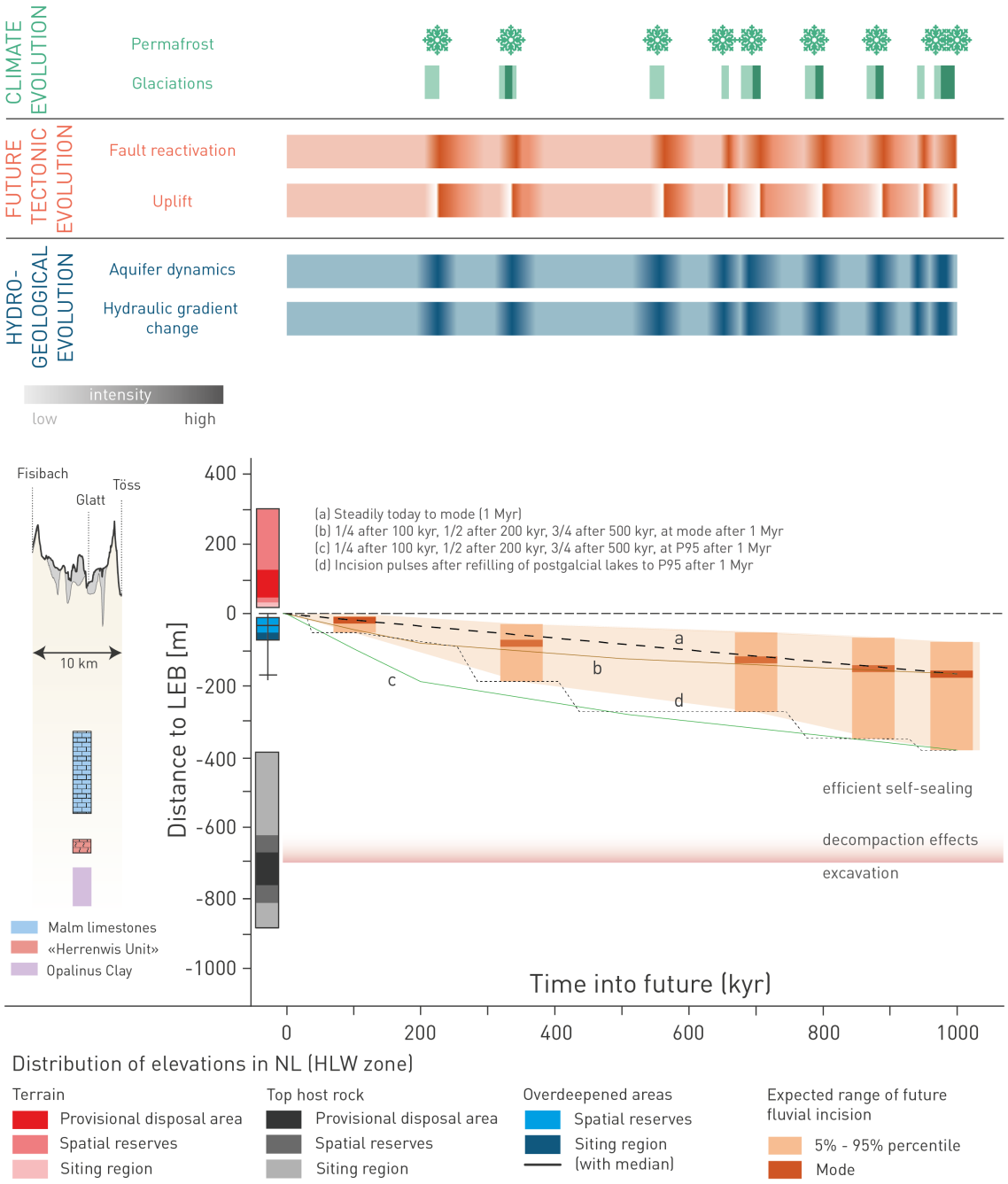

Fig. 6-26: Schematic diagram summarising the long-term geological evolution of the NL site

Figure 6-48 from NTB 24-17 Nagra (2024k).

The diagram summarises the key elements that describe expected long-term geological evolution over the next million years for the Nördlich Lägern siting region. The local erosion base (LEB) constitutes the reference for the depicted present-day elevations and the future evolution.

Fig. 6-27c shows the transients of the performance indicator $TF_{CRZ,I\text{-}129}$, representing the release of dissolved ^{129}I into the Malm and Keuper aquifer. The simulations were stopped when the upper confining units were eroded completely, resulting in exposure of the top of the Opalinus Clay. The great depth of the repository in the NL siting region ensures that this occurs only for a few cases with the highest loss of overburden rates, long after the end of the period for assessment. The spread in the tracer releases calculated in the 100 simulations is conspicuously low. This is because the transition from a diffusion-dominated to an advective transport regime in the CRZ occurs in all simulation cases after more than a million years, with modest effects on the tailings of the breakthrough curves. The corresponding histogram of the performance index $NTF_{CRZ,I\text{-}129}$ (Fig. 6-27d) confirms this, showing practically the same barrier performance as in the base case of the *EXPERF* scenario. For the repository site in NL, it can be concluded that the *LOSSOB* scenario is an alternative scenario with low relevance to safety.

The assessment of fault reactivation by uplift requires profound knowledge of the present-day stress field. The present-day stress field in Northern Switzerland across the Mesozoic sediments and the pre-Mesozoic basement rocks has been evaluated in Section 4.4 of NTB 24-27 (Nagra 2024k). Experimental evidence from microhydraulic fracturing tests in the TBO boreholes, as well as extensive geomechanical modelling, confirms that the stress regime can be considered similar in all three site regions. It changes with depth from a thrust faulting stress regime closer to the surface to a strike-slip and normal faulting stress regime at greater depth. Thus, where the Opalinus Clay is located at a shallower position (e.g., in the JO siting region), a stress regime causing normal to strike-slip faulting is to be expected, whereas, where it is deeper (e.g., in the NL siting region), there is a high probability that it is subjected to a normal faulting stress regime. The loss of overburden due to erosional processes is accompanied by a reduction of vertical stress and can lead to the reactivation of existing faults or even to the formation of new faults in the repository area.

The PA-Scenario *LOSSFLT* evaluates the (re-)activation of a steeply dipping fault, cross-cutting the HLW repository section and connecting the regional aquifer systems above and below the CRZ. The assumed loss of overburden corresponds to the functional relationship in Fig. 6-27b, in which the cover decreases monotonically with time. In the period for assessment, the expected loss of overburden is in the range 100 to 450 m and consequently the dominant stress regime at repository level changes from normal faulting to strike slip faulting. In the event of fault (re-)activation due to mechanical unloading, the upper limit of fault transmissivities is assumed to be 10^{-10} m^2/s, accounting for the self-sealing capacity of fractures in the clay-rich Mesozoic sequences and, in particular, in the Opalinus Clay.

No additional Monte Carlo simulations are required to assess fault (re-)activation in response to mechanical unloading. It is sufficient to refer to the results of the scenarios *FLTHLWN* and *FLTHLWP*, which indicate that radionuclide release along faults has only a limited impact on the barrier function of the CRZ, even when the fault is activated immediately after repository closure. In the *LOSSFLT* scenario, fault activation due to mechanical unloading would be expected to occur only at the end of the period for assessment, if at all. Therefore, the PA-Scenario *LOSSFLT* can by classified as an alternative scenario with low likelihood of occurrence and low relevance to repository safety.

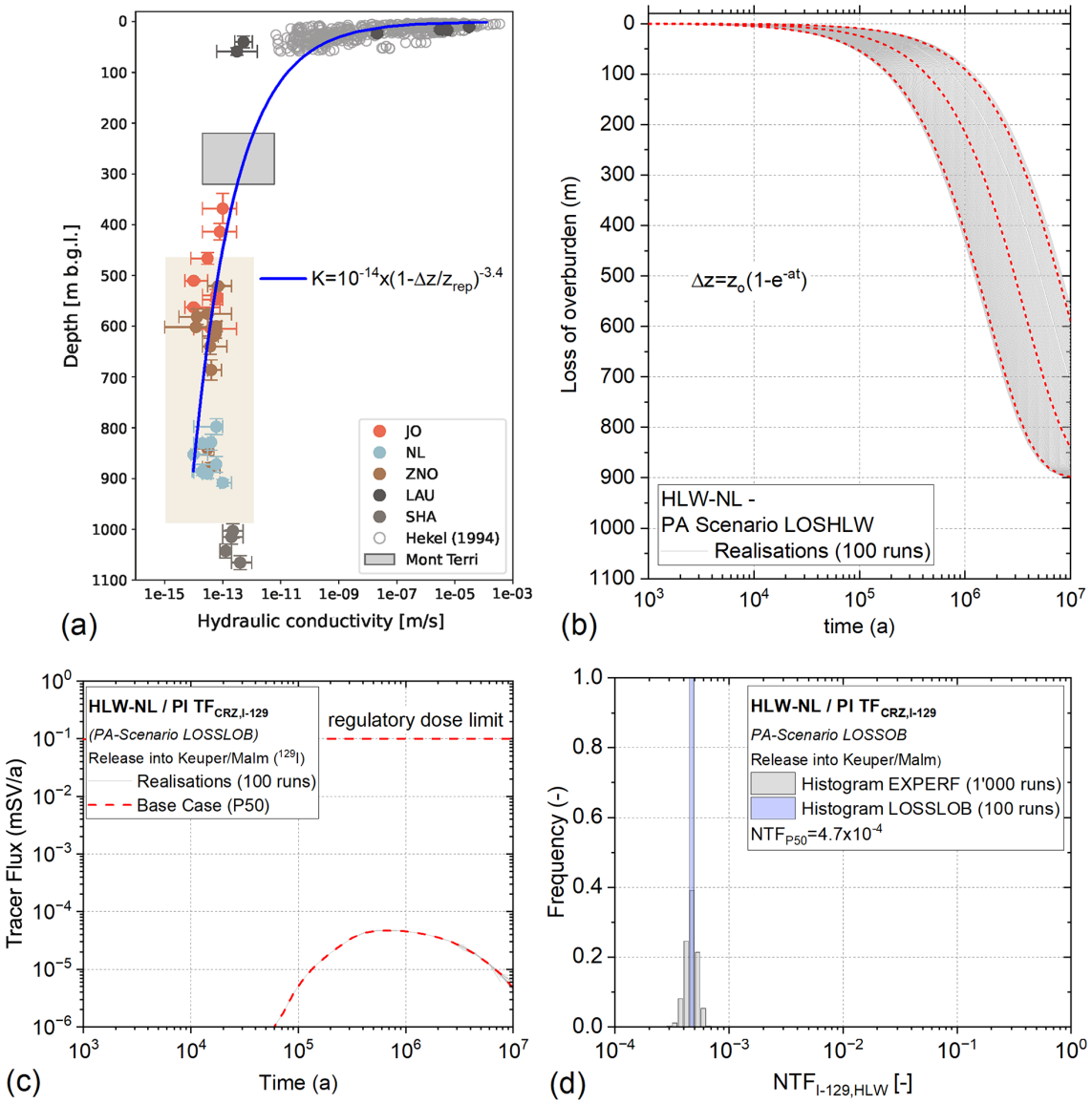

Fig. 6-27: Deviations from expected barrier performance – PA-Scenario *LOSSOB* for the evaluation of the CRZ of the HLW repository section

(a) Hydraulic conductivities of the Opalinus Clay as a function of depth (adapted from Figure 5-38 in NTB 24-17, Nagra 2024k) with power-law relationship representing the depth-dependence of hydraulic conductivity (blue line); (b) 100 realisations of expected loss of overburden over the next million years, implemented in terms of a simple functional relationship in which the cover decreases monotonically with time; (c) transients of tracer flux $TF_{CRZ,I\text{-}129}$ and (d) histogram of performance index $NTF_{CRZ,I\text{-}129}$.

6.4 Deviations from expected performance – the total system perspective

The indicator-based assessment of deviations from expected repository performance at the component level provides valuable insights into the robustness of the repository system as a whole. A total of 22 PA-Scenarios were defined to analyse the impacts of deviations from the expected repository performance for each barrier component in a comprehensible manner. For each PA-Scenario, probabilistic simulations were carried out with a focus on the effect of parametric uncertainties on barrier performance. The evaluation procedure encompassed a comparison of the eight performance indicators specified in Section 6.2.3 with their corresponding performance targets. In particular, it was checked whether the performance margins were changed significantly in the PA-Scenarios compared with the PA-Scenario of expected performance (*EXPERF* scenario). The final step of the evaluation process, described in the following paragraphs, comprises a systematic screening of the PA-Scenarios addressed in the previous sections with regard to the following aspects:

- What is the likelihood that the assumed deviations from expected performance could occur (Section 6.4.1)?
- What is the relevance of the deviations at component scale to repository safety in terms of safety margins between the evaluated the performance indicators and their respective performance targets (Section 6.4.2)?

Both aspects provide input to safetey scenario development, which specifies the safety scenarios for the radiological consequence analysis (see Section 6.4.3).

6.4.1 Likelihood of deviations from expected performance

The provisional repository design and implementation plan on which the PA is based should comply by design with the assigned functionality of the multi-barrier system in most foreseeable circumstances, both at the component scale and at the scale of the entire repository. The indicator-based evaluation of the PA-Scenario of expected barrier performance (*EXPERF* scenario, see Section 6.2) confirms the robustness of the safety concept, showing large safety margins for all addressed performance indicators. In the probabilistic assessments shown in Section 6.2.3, the large safety margins are expressed in terms of an almost negligible risk of violating the performance targets.

The PA-Scenarios described in Section 6.3 address the effects of *conceptual uncertainties* on the performance of the multi-barrier system. Conceptual uncertainties originate from the model abstraction process as detailed in Chapter 5 and from internal and / or external perturbations which may impair the performance of the entire repository system. Typical examples of conceptual uncertainties are related to the geological and hydrogeological setting (e.g., scenarios HARDBED, MKALK), the prevailing transport regimes (e.g., scenarios UPFLOW, DWNFLOW, EXPERF / diffusion only) and the source terms associated with the repository-induced effects (e.g., scenarios UBHEAT, UBGAS). While probabilistic analyses allow the *quantitative assessment* of the impact of *parametric uncertainties* on barrier performance, the assessment of *conceptual uncertainties* must be *based on qualitative arguments*, including consistency with

independent evidence or design requirements, which show that deviations from expected performance are unlikely to occur. In this sense, the process of PA-Scenario screening addresses their likelihood of occurrence, by assigning one of the four categories of likelihood to each PA-Scenario:

- hypothetical deviations from expected performance;
- unlikely deviation from expected performance;
- likely deviations from expected performance;
- expected performance (*PA-Scenario EXPERF*).

Such a qualitative assignment of a likelihood of occurrence must be substantiated with convincing technical arguments. Tab. 6-3 summarises all the investigated PA-Scenarios together with the assigned likelihood of occurrence and the arguments this categorisation.

Tab. 6-3: Screening of the PA-Scenarios for their likelihood of occurrence

PA-Scenario	**Likelihood of occurrence / arguments**
HLW matrix	
PA-Sc01 (IRMAX):	*Hypothetical:* simultaneous failure of all canisters followed by instantaneous release of entire activity can be ruled out.
HLW canister	
PA-Sc02 (WPFAIL):	*Hypothetical:* see PA-Scenario IRMAX.
PA-Sc03 (UBHEAT):	*Hypothetical:* By design, MOX canisters with the highest thermal output are spread evenly across the HLW emplacement drifts. Careful quality assurance procedures prevent clustering of the MOX canisters.
PA-Sc04 (UBGAS):	*Unlikely alternative:* Nagra's dedicated laboratory programme on steel corrosion does not support the high gas generation rates assumed in the UBGAS scenario. The low rate of ingress of porewater from the low-permeability host rock restricts the corrosion process (porewater consumption by anaerobic corrosion; see Sections 4.4.2 and 4.4.4). Gas-induced fracturing in the HLW drifts occurs preferentially along the EDZ by re-opening of existing EDZ features.
Sealing system	
PA-Sc05 (V3PERM):	*Hypothetical:* By design, the V3 shaft seal is gas/water-tight (intrinsic permeability $k = 1 \times 10^{-20}$ m^2). The EDZ around the sealing section can be removed if significant convergence is prior to seal installation.
L/ILW matrix	
PA-Sc06 (ZEROGAS):	*Hypothetical:* The low rate of ingress of porewater from the host rock and the prevailing hydrochemical conditions in the L/ILW near-field restrict gas production by corrosion and degradation processes. The ZEROGAS scenario represents a hypothetical bounding case assuming that all gas produced by these processes is dissolved immediately in the porewater, without forming a free gas phase or creating gas overpressures in the L/ILW emplacement caverns.
PA-Sc07 (PESSGAS):	*Unlikely alternative:* see PA-Scenario UBGAS.

Tab. 6-3: Cont.

PA-Scenario	Likelihood of occurrence / arguments
Containment-providing rock zone (CRZ)	
PA-Sc08 (UPFLOW):	*Likely alternative:* Artesian conditions in the Keuper aquifer were observed in the Benken borehole of the siting region ZNO, but not in NL. In the Keuper aquifer of NL, moderate pore pressures above hydrostatic (<1 MPa) are conceivable from a regional hydrogeological perspective. Long-term monitoring of hydraulic heads in STA3-1 indicates hydrostatic head in the Keuper aquifer and moderate subhydrostatic heads in Muschelkalk and Malm.
PA-Sc09 (DWNFLOW):	*Unlikely alternative:* The Malm and Keuper aquifers share the same recharge and discharges areas, so that distinct head differences with downwards directed porewater flow towards the Keuper aquifer are unlikely. This is confirmed by the results of long-term monitoring (STA3-1). Modest sub-hydrostatic conditions in the Muschelkalk aquifer are conceivable, but not relevant for safety.
PA-Sc10 (HARDBED):	*Unlikely alternative:* According to Section 5.6 of NTB 24-17 (Nagra 2024k), no indications are found of elevated matrix conductivities related to hard beds in the Lias – Dogger section. Long-term monitoring in STA3-1 shows heads in the upper confining units below the water table in local discharge areas, suggesting that formation pressure in upper confining units is controlled by the prevailing site-specific geomechanical conditions rather than by the hydrogeological setting. Anomalous formation pressures are indicative for low-permeability structures.
PA-Sc11 (HERWIS):	*Unlikely alternative:* Hydraulic heads in the «Herrenwis Unit» are the lowest in the upper confining units, significantly below the water table in local discharge areas (based on long-term monitoring in STA3-1). These anomalous heads are an indication of very low hydraulic conductivity (see Sections 4.5.3.7 and 5.6.5 in NTB 24-17, Nagra 2024k).
PA-Sc12 (MKALK):	*Likely alternative:* The Keuper aquifer consists of spatially limited and partly isolated local groundwater flow systems with often stagnant conditions (Section 4.5.3.10 in NTB 24-17, Nagra 2024k). In the NL siting region, the isolated and local character of the water-conducting features in the Keuper aquifer gives reason for assessing the favourable alternative scenario in which the entire Keuper formation is part of the lower confining units and the Muschelkalk represents the lower regional aquifer system.
PA-Sc13 (HETOPA):	*Likely alternative*: The lateral and vertical lithological variability of the Opalinus Clay is generally small compared with other Mesozoic formations (e.g., Section 4.5.3.8 in NTB 24-17, Nagra 2024k. The formation can be subdivided in 6 six facies with minor differences in the mineralogical composition.

Tab. 6-3: Cont.

PA-Scenario	Likelihood of occurrence / arguments
Undetected Fault HLW FLTHLW	
PA-Sc14 / PA-Sc15 (FLTHLWP / FLTHLWN):	*Likely alternative*: Based on structural logs in the TBO boreholes (NAB 24-10 Rev. 1, Nagra 2024j), it cannot be ruled out, that minor tectonic features exist in the vicinity of the HLW repository, which were not detected during the seismic surveys. Such features in the near-field of the HLW section, if they exist at all, would exhibit very low transmissivities $\leq 10^{-10}$ m^2/s, due to the effective self-sealing capacity of the host rock (Section 5.7 in NTB 24-17, Nagra 2024k; see also Fig. 6-20).
PA-Sc16 (FLTLILW):	*Likely alternative*: see PA-Scenario FLTHLWN.
PA-Sc17 (RIEHLW):	*Unlikely alternative:* Thermally- or gas-induced faults in and around the HLW repository section are very unlikely to occur under the expected geomechanical conditions (see Click or tap here to enter text.NAB 24-10 Rev. 1, Nagra 2024j). Only under very unfavourable stress conditions and assuming unexpectedly low rock strength is it conceivable that thermally- or gas-induced rock failure could occur.
PA-Sc18 (RIELILW):	*Unlikely alternative*: see PA-Scenario RIEHLW.
Gelogical Longterm Evolution	
PA-Sc19 (SEISHLW):	*Unlikely alternative:* The likelihood of occurrence of an earthquake on a fault with a size in the hectometre to kilometer range and with its hypocentre at repository level is in the order of 10^{-5} and 10^{-6} events per year (NAB 24-28, Nagra 2024i).
PA-Sc20 (SEISLLW):	*Unlikely alternative*: see PA-Scenario FLTLILW.
PA-Sc21 (LOSSOB):	*Likely alternative*: Nagra (2024k, NTB 24-17, Chapter 6) presents a comprehensive probabilistic assessment of the geological processes that may affect repository safety in the three siting regions considered in SGT Stage 3. At the Haberstal site in the NL siting region, the inferred loss of overburden due to erosion processes over the next million years (the period for assessment) is in the range 100 and 450 m.
PA-Sc22 (LOSSFLT):	*Unlikely alternative*: As noted above, over the period for assessment, the expected loss of overburden at the Haberstal site is in the range 100 and 450 m. As a consequence, the dominant stress regime in the CRZ changes from normal faulting to strike-slip faulting at the end of the period for assessment (see also Section 4.4.5 in NTB 24-17, Nagra 2024k). Due to the great repository depth, the likelihood of fault activation associated with mechanical unloading is deemed low, because a stable stress regime prevails in the CRZ. Fault (re-)activation, if any, would be expected to occur only at the end of the period for assessment.

6.4.2 Relevance to safety

Indicator-based probabilistic assessments of the 23 PA-Scenarios (*EXPERF* scenario, representing the expected performance plus 22 deviations from expected performance) allow performance indicators to be evaluated in terms of their implications for repository performance and safety for each PA-Scenario and safety margins to be assessed. Evaluation scales were formulated for each performance indicator in Tab. 2-2, aimed at quantifying the safety margins provided in each PA-Scenario against the corresponding performance targets. The safety margins were divided in 4 rating levels as follows:

- Very favourable – unconditionally favourable repository performance is ensured over the full range of parametric uncertainties.
- Favourable – robust repository performance is ensured over the full range of parametric uncertainties.
- Less favourable – sufficient repository performance is provided over a wide range of parametric uncertainties.
- Unfavourable – safety margins are low or absent.

Unfavourable conditions exist when the performance target is exceeded (not depicted in the evaluation scales). The four evaluation levels can be viewed as a pragmatic classification scheme that is tailored to the limited scope of the probabilistic analyses. Recalling the number of Monte Carlo simulations, typically between 100 and 1,000 runs, carried out for each of the 23 PA-Scenarios, the modelling results are more indicative rather than substantiated by a rigorous statistical assessment workflow. Accordingly, the Monte Carlo simulations should be viewed more as probabilistic sensitivity analyses, aimed at screening the impact of conceptual uncertainties (formulated in terms of alternative PA-Scenarios) and parametric uncertainties (expressed through the probability density functions of the uncertain input parameters) on the performance of the multi-barrier system. The rating levels which are assigned to the performance indicators of the PA-Scenarios provide guidance for the development of the safety scenarios and in-depth analyses of radiological consequences.

6.4.3 Performance screening and input for scenario development

As described above, performance screening of the 23 PA-Scenarios entailed the compilation of qualitative arguments for the likelihood of occurrence (Tab. 6-3) and an evaluation of their safety relevance, based on the quantitative performance indicators and the corresponding performance indices, targets and evaluation scales. Fig. 6-28 presents the results of the screening process of all PA-Scenarios and the relevant performance indices in the form of a bubble chart. The likelihood of occurrence of the scenarios is indicated by the bubble size and the relevance to safety is indicated by colour coding of the performance indices for each scenario. Several bubbles are marked with a red edge. This indicates deviations from expected performance of the repository system could give rise to a significant impact on the general repository evolution as described in the report of the expected phenomenological evolution of the repository system (NAB 24-20 Rev. 1, Nagra 2024n). In depth assessment of such scenarios are to be performed as part of safety scenario development (NTB 24-21, Nagra 2024e) and radiological consequence analysis (NTB 24-18, Nagra 2024r).

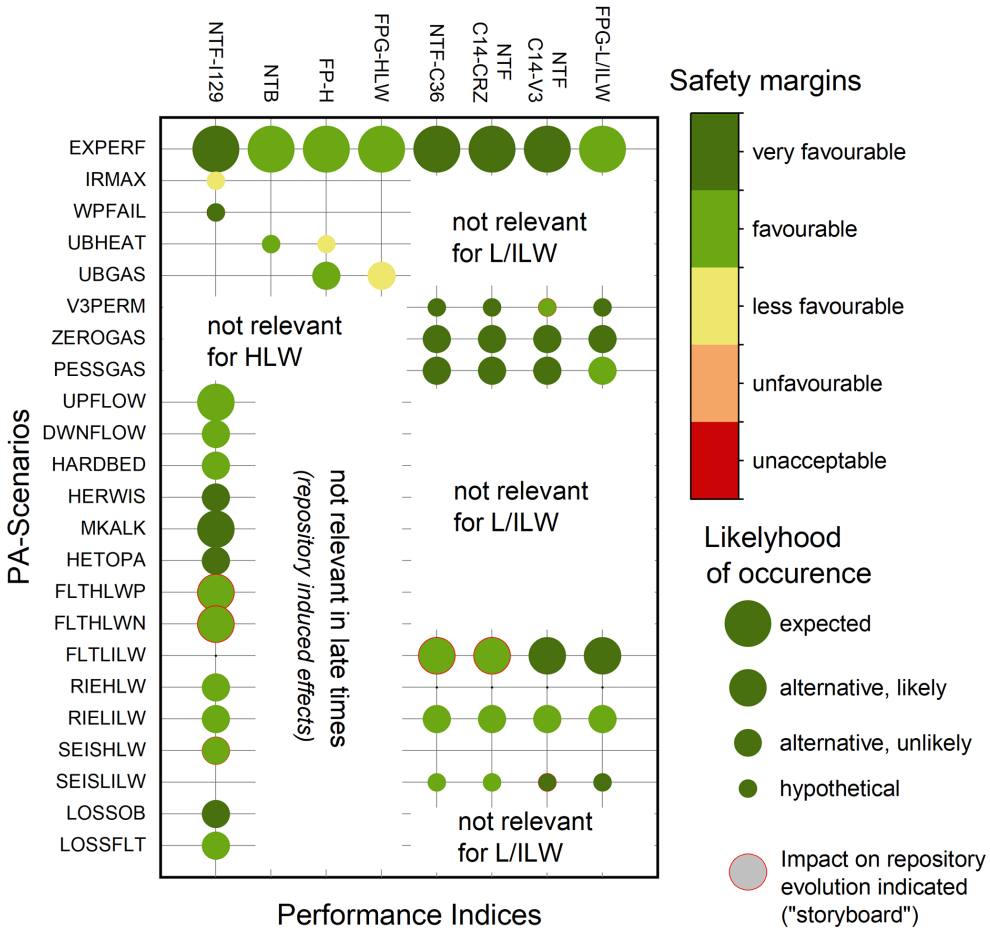

Fig. 6-28: Results of performance screening of all scenarios and the relevant performance indices in form of a bubble chart

The likelihood of occurrence of the scenarios is depicted by the bubble size. The sizes of the safety margins for each scenaio are indicated by colour coding of the performance indices for each scenario. Bubbles which are marked with a red edge indicate deviations from expected performance of the repository system associated with a significant impact on the general repository evolution.

The evaluation chart gives a clear illustration of the robustness of the safety concept. The expected performance scenario *EXPERF* shows, by design, favourable and very favourable safety margins for all performance indices (first row of bubbles in Fig. 6-28). The same applies to almost all other scenarios. Deviations from expected performance of a single barrier component, such as premature canister failure (PA-Scenario *WPFAIL*) or permeable V3 seals (PA-Scenario *V3PERM*) do not lead to an adverse loss of performance of the entire repository system, because the multi-barrier safety concept ensures redundancy in the contributions to the safety functions of individual barrier components. Inherent limitations of the geological database, which lead to conceptual uncertainties about the geological setting (PA-Scenarios *UPFLOW*, *DWNFLOW*, *HARDBED* etc.) have only a moderate impact on the barrier performance of the repository system as a whole. The same applies to the effects of geological long-term evolution, as demonstrated by the analysis of the scenarios *SEISHLW*, *SEISLILW*, *LOSSOB* and *LOSSFLT*.

Overall, only two hypothetical PA-Scenarios, *IRMAX* and *UBHEAT*, and the unlikely alternative scenario *UBGAS* give rise to a less favourable performance. The *IRMAX* scenario leads to a loss of barrier performance of the CRZ by a factor of 10, but nonetheless provides a safety margin for the $NTF_{CRZ,I\text{-}129}$ index that is more than 2 OoM below the regulatory dose limit (Fig. 6-9). It evaluates the hypothetical case that all HLW canisters breach at the same time after 10,000 years and that the entire ^{129}I inventory is released instantaneously into the HLW near-field, which would imply instantaneous dissolution of the UO_2 pellets after canister failure and porewater ingress. Such a behaviour is neither supported by experimental evidence nor by the results of near-field modelling, which indicate that the canister will saturate only slowly after breaching and that spent fuel degradation occurs very slowly, over a timesale of many millions of years. The accumulation of corrosion gases inside the canister will keep gas pressure in the HLW near-field above hydrostatic for several hundred thousands of years, preventing the ingress of liquid water.

The hypothetical *UBHEAT* scenario indicates less favourable safety margins against thermally induced rock shear failure which is expressed by the performance index FPH (Fig. 6-11c and d). The scenario will be avoided by careful canister placement, as discussed in Section 6.3.2. Furthermore, the PA-Scenario *RIEHLW* clearly shows that, even in the unlikely event of a thermally induced fault, the performance of the CRZ as a transport barrier is not significantly impaired.

The unlikely alternative scenario *UBGAS* indicates less favourable safety margins against gas-induced rock shear failure which is expressed by the performance index FPG_{HLW} (Fig. 6-11e, f). The PA-Scenario *RIEHLW* clearly shows that, even in the unlikely event of a gas-induced fault, the performance of the CRZ as a transport barrier is not significantly impaired.

The scenarios *V3PERM*, *FLTHLW*, *FLTLILW*, *SEISHLW* and *SEISLILW* have in common that they represent deviations from expected performance of the repository system associated with an increased rate of resaturation of the backfilled repository structures. Possible impacts on the safety functions of the individual components of the multi-barrier system must be considered.

The *V3PERM* scenario with permeable V3 seals leads to a quite rapid saturation of the backfilled repository structures. As a consequence, the effective gas and water permeabilities of the L/ILW-V2 seal and, to a lesser extent, of the L/ILW-V1 seal are reduced. The probabilistic simulations demonstrate that gas pressure build-up in the L/ILW emplacement caverns remains moderate (Fig. 6-12b). However, the release of volatile ^{14}C along the backfilled repository structures moderately increases (Fig. 6-12d). Note that the safety margins of the performance index $NTF_{V3,C14}$ are still more than 3 orders of magnitude below the regulatory dose constraint, even for a very unfavourable seal permeability of 10^{-16} m^2.

The scenarios *FLTHLW*, *FLTLILW*, *SEISHLW* and *SEISLILW* are related to steeply dipping faults of various origin (pre-existing faults, thermally- and gas-induced faults, seismic faults), cross-cutting the HLW and L/ILW emplacement drifts and caverns. Faults through the repository structures, especially prior to re-sealing, represent preferential transport paths for dissolved radionuclides. Furthermore, they are associated with an enhanced release of repository gases and may affect the water saturation of the engineered barrier systems, including the closure system, the HLW near-field and the L/ILW nearfield. The *FLTHLW* scenario (fault parallel and perpendicular to the HLW drifts) indicates that favourable barrier performance of the CRZ is ensured for fault transmissivities $\leq 10^{-10}$ m^2/s, whereas unfavourable conditions may be faced in the hypothetical case of fault transmissivity exceeding a value of 10^{-8} m^2/s.

In this context, the *FLTLILW* scenario is of special interest, because it may lead to a relatively rapid saturation of the L/ILW repository section, depending on the fault transmissivity (Fig. 6-23c). While the function of the CRZ as a transport barrier for dissolved radionuclides is not significantly impaired (Fig. 6-23a), the impact on the retention of volatile radionuclides is more pronounced (Fig. 6-23b). Note that the release of ^{14}C from the L/ILW emplacement caverns through a highly transmissive fault ($T_{fault} \leq 10^{-10}$ m^2/s) into the Malm aquifer leads to dose rates that are still more than 3 OoM below the regulatory dose constraint.

In-depth assessment of such scenarios with a significant impact on the general repository evolution is the subject of the safety scenario development (NTB 24-21, Nagra 2024e) and radiological consequence analysis (NTB 24-18, Nagra 2024r). This includes the superposition of several deviations from expected performance with qualitatively similar impacts on the repository barriers in single safety scenarios and the use of wider parameter ranges in probabilistic analyses.

6.5 Robustness of the multi-barrier system – concluding remarks

The provisional repository design and implementation plan that forms the basis for the performance assessment and for the wider safety assessment and safety case, has been founded on a well-constrained assessment basis and therefore corresponds in concept with the assigned functionality of the multi-barrier repository system. Its expected performance has been assessed by extensive model-based analyses, which confirm that each individual barrier component, and the multi-barrier system as a whole fulfil the assigned safety functions with large safety margins.

Performance screening is the special process in the PA workflow that focusses on analysing deviations from expected barrier performance. Probabilistic assessment tools are used to quantify the safety margins of deviating PA-Scenarios and to compare their performance with the scenario of expected performance. The sensitivities of the calculated safety margins to parametric and conceptual uncertainties were explored, providing confidence in the robust performance of the individual barrier components and in the robustness of the multi-barrier system as a whole.

The redundancy and diversity of the individual barrier components, a principle that is in accordance with international safety standards (SSR-5, IAEA 2011), has been shown to be important in the numerical assessments of the PA-Scenarios. The assessments carried out for the PA-Scenarios of premature canister failure and thermally induced failure of the host rock have demonstrated that a reduced performance of a single barrier component does not lead to an unacceptable performance of the entire system. Rather, the assessments indicate that the reduced performance of a single component is partially compensated for by the other elements of the multi-barrier system, so that the overall performance of the system is only slightly reduced. The favorable and complementary effects of the diversity of the individual barriers is also illustrated by the interaction of the sand/bentonite seals V1 and V2 of the L/ILW repository and the bentonite-based V3 shaft seals. The sand/bentonite seals enable the gas phase accumulated in the L/ILW caverns to be distributed in the backfilled access structures and the central area at moderate gas overpressures while, on the other hand, a rapid release of the volatile radionuclides (^{14}C) is prevented by the gas tight V3 seal. Several PA-Scenarios are dedicated to the assessment of deviations from expected seal performance, indicating a favorable overall performance of the sealing system, even in case of reduced performance of individual sealing components.

The aim of performance screening is to identify and consolidate the safety-relevant paths of repository performance and to formulate them in a format that can provide a suitable basis for safety scenario development and for radiological consequence analysis. The assessment of 23 PA-Scenarios provides clear evidence of the robustness of the repository system, with only one unlikely and two hypothetical scenarios that could lead to less favorable performance. Finally, the PA-Scenarios *V3PERM*, *FLTHLW*, *FLTLILW*, *SEISHLW* and *SEISLILW* were identified as cases worthy of further evaluation in the radiological consequence analysis. The motivation for

complementary in-depth analyses is the fact that these scenarios deviate significantly from the expected repository evolution (NAB 24-20 Rev. 1, Nagra 2024n), which formed the basis for the provisional repository design, although there was no evidence of a relevant loss of barrier performance.

7 Summary and conclusions

The assessment of the repository performance for both high-level waste (HLW) and low- and intermediate-level waste (L/ILW) in Opalinus Clay is presented here as a high-level synthesis. The assessment framework is based on a multi-barrier concept, including geological and engineered barriers, forming the core of the post-closure safety concept. Each barrier is assigned specific safety functions, and together, they ensure the long-term containment and isolation of radioactive materials to protect human and environment from ionising radiation.

The assessment of the repository performance follows a systematic, transparent, and traceable workflow that ensures the auditability of the results. The assessment first evaluates the performance of individual barrier components before moving on to assess the interactions between the components and their cumulative impact on the repository system as a whole. This total system performance evaluation accounts for potential thermo-hydro-mechanical interactions that could occur between the different elements of the multi-barrier system. An important aspect of the assessment methodology is the integration of uncertainty quantification, which addresses parametric, conceptual, and scenario-based uncertainties. This allows the assessment to accurately represent the range of possible outcomes and ensures that the uncertainties in the system's behaviour are rigorously managed and tracked throughout the abstraction process.

In addition to evaluating the expected performance of the repository, the assessment investigates potential deviations thereof. These deviations are classified and analysed at both the component level and the total system level, with particular emphasis on their likelihood of occurrence and relevance to overall safety. This approach allows for systematic identification and bundling of safety-relevant paths, which are then used to develop safety scenarios and event trees. These scenarios serve as the basis for subsequent radiological consequence analyses, providing a robust framework for understanding the long-term implications of any deviations in system performance. The ability to trace the evolution of repository performance through clearly defined safety scenarios enhances confidence in the system's robustness under all conceivable conditions.

Performance assessment by barrier

The performance assessments carried out at the scale of the barrier components reaffirm that the safety-oriented repository design, with its multiple layers of defense, offers significant safety margins and is capable of meeting both national and international safety standards. The systematic book-keeping of claims, arguments and evidence at the component level confirms the performance of the barrier components with respect to their assigned safety functions. The arguments comprise empirical knowledge, project specific databases from site investigations, dedicated experiments, and a safety-oriented repository layout, based on model-supported designs. The consistency of different lines of argument and wide-ranging evidence from independent data sources provides confidence in the general safety concept. For the sake of traceability, the compilation in this synthesis report focusses on the key arguments and evidence for the claims made for each pillar of safety to convey a clear ranking of the safety relevance of the collected evidence. In order to meet the requirement for completeness of arguments and evidence, technical documents are referenced for in-depth reading.

Performance assessment at system scale

The performance assessment at the system level concentrates predominantly on TH^{2}M phenomena and processes that occur along the backfilled and sealed underground structures. Repository-scale modelling reveals that the HLW and L/ILW sections of the repository are hydraulically and thermally decoupled from each other. The thermal- and gas-induced perturbations in the HLW repository section occur at different times, which means that detrimental superposition of the thermal- and gas-related impacts on the safety functions of the engineered and geological barriers can be excluded. Neither the thermal- nor the gas-related disturbances lead to an increased pore-water flow along the sealed and backfilled repository structures, which could otherwise give rise to increased radionuclide release. Likewise, the impact of thermal- and gas-induced perturbations on the mechanical and chemical integrity of the engineered and geological barriers of the HLW repository is modest. The layout of the repository provides large gas storage volumes, which are crucial for reducing the gas pressure build-up in the L/ILW repository section. The resulting moderate gas overpressures in the repository structures of up to 2 – 3 MPa are not expected to impair the mechanical integrity of the engineered and geological barriers. Volatile radionuclides (mainly ^{14}C) are safely contained until they finally disappear due to radioactive decay. At the same time, the unsaturated conditions in the L/ILW emplacement caverns, with moderate gas overpressures, ensure that the release of dissolved radionuclides from the waste packages into the host rock is strongly retarded for very long times, because the mortar backfill around the waste containers represents a capillary barrier for dissolved radionuclides.

Performance Screening

The provisional repository design and implementation plan that forms the basis for the performance assessment and for the wider safety assessment and safety case corresponds in concept with the assigned functionality of the multi-barrier repository system. Its expected performance has been assessed by extensive model-based probabilistic analyses, which confirm that each individual barrier component and the multi-barrier system as a whole fulfil the assigned safety functions with large safety margins.

A wide range of potentially relevant deviations from expected barrier performance were specified as part of the performance screening process. The assessment of 23 PA-Scenarios in a probabilistic modelling framework provided clear evidence of the robustness of the repository system. Thus, extensive sensitivity studies, exploring the calculated safety margins to parametric and conceptual uncertainties provided confidence in the robust performance of the multi-barrier system. The redundancy and diversity of the individual barrier components has been shown to be important. Several PA-Scenarios confirmed a favorable overall performance of the repository system as a whole, even in case of reduced performance of individual sealing components.

None of scenarios assessed indicated a significant reduction of safety margins of repository at the system scale. Finally, only a handful of PA-Scenarios were identified as cases worthy of further evaluation in the radiological consequence analysis. The motivation for complementary in-depth analyses is the fact that these scenarios deviate significantly from the expected repository evolution, which formed the basis for the provisional repository design, although there was no evidence of a relevant loss of barrier performance.

Concluding remarks

The performance assessments presented in this synthesis report confirm that the geological repository for HLW and L/ILW at the Haberstal site is safe over the entire assessment period, with significant safety margins under both expected and adverse conditions. The concept relying on a multi-barrier system, combined with a robust, evidence-based assessment of its performance, ensures that the repository will meet its safety objectives even considering internal or external perturbations, some of which are of hypothetical nature. By meticulously addressing uncertainties and thoroughly evaluating each element of the system, the performance assessment builds a strong case for the repository's long-term safety. The transparent and traceable workflow further strengthens the conclusions, ensuring that the safety case is both credible and verifiable.

8 References

Alcolea, A. (2018): Hydraulic significance of the EDZ around underground structures of a geological repository for radioactive waste A sensitivity study for the repository configurations L/ILW and SF/HLW in the siting regions JO, NL and ZNO. Nagra Arbeitsbericht NAB 18-17.

Alcolea, A., Marschall, P., Damians, I.P., Olivella, S., Gens, A., Madaschi, A., Bosch, J., Laloui, L., Shao, H., Wang, W., Kolditz O. & Nagel, T. (2021): FE-Modelling Task Force / Task 1: Validation of thermally induced THM effects in the rock around the FE-tunnel. Subtask 1.1: Code and calculation verification. Subtask 1.2: Back-analyses. Nagra Arbeitsbericht NAB 19-40.

Bagnoud, A., Bruijn, I., Andresson, A.F., Diomidis, D., Leupin, O.X., Schwyn, B. & Bernier-Latmani, R. (2015): A minimalistic microbial food web in an excavated deep surface clay rock. FEMS Microbiology Ecology 92/1, fiv138. DOI: 10.1093/femsec/fiv138.

Bernard, E., Jenni, A., Fisch, M., Grolimund, D. & Mäder, U. (2020): Micro-X-ray diffraction and chemical mapping of aged interfaces between cement pastes and Opalinus Clay. Applied Geochemistry 115, 104538. DOI: 10.1016/j.apgeochem.2020.104538.

Berner, U., Kulik, D.A. & Kosakowski, G. (2013): Geochemical impact of a low-pH cement liner on the near field of a repository for spent fuel and high-level radioactive waste. Physics and Chemistry of the Earth, Parts A/B/C 64, 46-56. DOI: 10.1016/j.pce.2013.03.007.

BFE (2008): Sachplan Geologische Tiefenlager: Konzeptteil. BFE 2. April 2008 (Revision vom 30. November 2011). Departement für Umwelt, Verkehr, Energie und Kommunikation UVEK, Bern.

Blanc, P., Bourbon, X., Lassin, A. & Gaucher, E.C. (2010a): Chemical model for cement-based materials: Temperature dependence of thermodynamic functions for nanocrystalline and crystalline C–S–H phases. Cement and Concrete Research 40/6, 851-866. DOI: 10.1016/j.cemconres.2009.12.004.

Blanc, P., Bourbon, X., Lassin, A. & Gaucher, E.C. (2010b): Chemical model for cement-based materials: Thermodynamic data assessment for phases other than C–S–H. Cement and Concrete Research 40/9, 1360-1374. DOI: 10.1016/j.cemconres.2010.04.003.

Blanc, P., Lassin, A., Piantone, P., Azaroual, M., Jacquemet, N., Fabbri, A. & Gaucher, E.C. (2012): Thermoddem: A geochemical database focused on low temperature water/rock interactions and waste materials. Applied Geochemistry 27/10, 2107-2116. DOI: 10.1016/j.apgeochem.2012.06.002.

Bock, H., Dehandschutter, B., Martin, C.D., Mazurek, M., Haller, A. de, Skoczylas, F. & Davy, C. (2010): Self-sealing of fractures in argillaceous formations in the context of geological disposal of radioactive waste. Review and synthesis. OECD/NEA, Paris.

Bosch, J.A., Ferrari, A., Leupin, O. & Laloui, L. (2023): Modelling the density homogenisation of a block and granular bentonite buffer upon non-isothermal saturation. International Journal for Numerical and Analytical Methods in Geomechanics 47/11, 1979-2002. DOI: 10.1002/nag.3547.

Buchwald, J., Grunwald, N., Wang, W., Shao, H., Kolditz, O. & Nagel, T. (2025): The relevance of two-phase flow in the thermo-hydro-mechanical evolution of clay formations exposed to high temperatures by heat-emitting waste. Applied Thermal Engineering 264, 125379. DOI: 10.1016/j.applthermaleng.2024.125379.

Cloet, V., Lothenbach, B., Lura, P., Kosakowski, G., Curti, E., Wieland, E., Lanyon, G.W., Diomidis, N. & Leupin, O.X. (2019): Cementitious backfill for a high-level waste repository: impact of repository-induced effects. Nagra Arbeitsbericht NAB 18-41.

Cloet, V., Pekala, M., Smith, P., Wersin, P. & Diomidis, N. (2017): An Evaluation of sulphide fluxes in the near field of a HLW repository. Nagra Technical Report NTB 17-04.

Cloet, V., Schwyn, B., Baeyens, B., Curti, E., Diomidis, N., Johnson, L., Leupin, O.X., Mibus, J., Van Loon, L. & Wieland, E. (2014): Einfluss der Salinität des Porenwassers der Wirtgesteine auf die Langzeitsicherheit der Tiefenlager. Nagra Arbeitsbericht NAB 14-09.

Courdouan, A., Christl, I., Meylan, S., Wersin, P. & Kretzschmar, R. (2007): Characterisation of dissolved organic matter in anoxic rock extracts and in situ pore water of the Opalinus Clay. Applied Geochemistry 22/12, 2926-2939. DOI: 10.1016/j.apgeochem.2007.09.001.

Curti, E. (2022): Aqueous Corrosion of Vitrified Nuclear Waste: Current Process Understanding, Literature Review and Recommended Rates. Nagra Arbeitsbericht NAB 23-09.

Diomidis, N., Cloet, V., Leupin, O.X., Marschall, P., Poller, A. & Stein, M. (2016): Production, consumption and transport of gases in deep geological repositories according to the Swiss disposal concept. Nagra Technical Report NTB 16-03.

Diomidis, N., Guillemot, T. & King, F. (2023): Definition of Reference Corrosion Rates for Performance and Safety Assessments. Nagra Arbeitsbericht NAB 23-22.

Diomidis, N. & Reddy, B. (2022): Corrosion of Canister Materials in Anaerobic Saturated Bentonite: In Situ and Ex Situ Experiments. Part 1. Nagra Arbeitsbericht NAB 20-10.

Dixon, D.A., Stone, J., Birch, K. & Kim, C.S. (2023): Sealing materials for a deep geological repository: evaluation of swelling pressure and hydraulic conductivity data for bentonite-based sealing materials proposed for use in placement rooms. Canadian Geotechnical Journal 60/7, 951-965. DOI: 10.1139/cgj-2021-0609.

ENSI (2011): Sicherheitstechnische Klassierung für bestehende Kernkraftwerke. Richtlinie für die schweizerischen Kernanlagen ENSI-G01/d. ENSI, Villigen.

ENSI (2018a): Anforderungen an die Konditionierung radioaktiver Abfälle, Ausgabe Februar 2007 (Änderung 20. Dezember 2018). Richtlinie für die schweizerischen Kernanlagen ENSI-B05/d. ENSI, Brugg.

ENSI (2018b): Präzisierungen der sicherheitstechnischen Vorgaben für Etappe 3 des Sachplans geologische Tiefenlager. Sachplan geologische Tiefenlager, Etappe 3. ENSI 33/649. Eidgenössisches Nuklearsicherheitsinspektorat ENSI, Brugg.

ENSI (2020a): Geologische Tiefenlager. Erläuterungsbericht zur Richtlinie ENSI-G03/d. Eidgenössisches Nuklearsicherheitsinspektorat ENSI, Brugg.

ENSI (2020b): Geologische Tiefenlager. Richtlinie für die schweizerischen Kernanlagen ENSI-G03/d. Eidgenössisches Nuklearsicherheitsinspektorat ENSI, Brugg.

ENSI (2023): Geologische Tiefenlager. Ausgabe Dezember 2020 (Änderung vom 1. November 2023). Richtlinie für die schweizerischen Kernanlagen ENSI-G03/d. Eidgenössisches Nuklearsicherheitsinspektorat ENSI, Brugg.

Geomechanica Inc., Toronto (2018): Extent and shape of the EDZ around underground structures of a geological repository for radioactive waste – A sensitivity study for the repository configurations L/ILW and SF/HLW in the siting regions JO, NL and ZNO. Nagra Arbeitsbericht NAB 18-12.

Giroud, N., Tomonaga, Y., Wersin, P., Briggs, S., King, F., Vogt, T. & Diomidis, N. (2018): On the fate of oxygen in a spent fuel emplacement drift in Opalinus Clay. Applied Geochemistry 97, 270-278. DOI: 10.1016/j.apgeochem.2018.08.011.

Glaus, M.A., Kulik, D.A., Miron, G.D., Van Loon, L.R., Wüst, R., Becker, J. & Li, X. (2024): Diffusion Databases for Opalinus Clay, Confining Geological Units and Bentonite: Methods, Concepts and Upscaling of Data. Nagra Technical Report NTB 23-08.

Grambow, B., Lemmens, K., Minet, Y., Poinssot, C., Spahiu, K., Bosbach, D., Cachoir, C., Casas, I., Clarens, F., Christiansen, B., Pablo, J. de, Ferry, C., Giménez, J., Gin, S., Glatz, J.P., Gago, J.A., Gonzalez, R.E., Hyatt, N.C., Iglesas, E., Kienzler, B., Luckscheiter, B., Martinez-Esparza, A., Metz, V., Ödegaard-Jensen, A., Ollila, K., Quiñones, J., Rey, A., Ribet, S., Rondinella, V.V., Sarnemark, G., Wegen, D., Serrano-Purroy, D. & Wiss, T. (2008): RTDC-1 Final Synthesis Report, Dissolution and release from the waste matrix. EU NF-PRO Project FI6W-CT-2003-02389 [see EUR 23730]. European Commission, Brussels, Belgium.

Granet, S. (2021): Modèles de comportement THHM. Code_Aster R7.01.11, available online at www.code-aster.org, status as of October 1, 2024.

Guillemot, T., Wieland, E., Mosberger, L. & Warthmann, R. (2023): Degradation of Organic Materials in a L/ILW Repository. Nagra Technical Report NTB 23-11.

Hesketh, J., Haynes, H., Reddy, B., Rance, A., Bevas, C., Padovani, C. & Diomidis, N. (2023): Carbon steel corrosion in a bentonite buffer: A comparison between in situ exposure and lab based experiments. Materials & Corrosion 74/11-12, 1728-1745. DOI: 10.1002/maco.202313767.

Hofstetter, T.B., Sosedova, Y., Gorski, C., Vögelin, A., Sander, M. & Eawag (2014): Redox properties of iron-bearing clays and MX-80 bentonite - electrochemical and spectroscopic characterization. Nagra Technical Report NTB 13-03.

Hummel, W., Kulik, D.A. & Miron, G.D. (2022): Solubility of radionuclides and influence of EDTA for use in the development of the cement sorption database (SDB 2022). Nagra Arbeitsbericht NAB 22-38.

IAEA (2011): Disposal of radioactive waste. Specific safety requirements IAEA Safety Standards Series No. SSR-5. International Atomic Energy Agency, Vienna.

Idiart, A., Laviña, M., Kosakowski, G., Cochepin, B., Meeussen, J.C., Samper, J., Mon, A., Montoya, V., Munier, I., Poonoosamy, J., Montenegro, L., Deissmann, G., Rohmen, S., Damiani, L.H., Coene, E. & Naves, A. (2020): Reactive transport modelling of a low-pH concrete / clay interface. Applied Geochemistry 115, 104562. DOI: 10.1016/j.apgeochem.2020.104562.

Jacobs, F., Mayer, G. & Wittmann, F.H. (1994): Hochpermeable, zementgebundene Verfüllmörtel für SMA Endlager. Nagra Technischer Bericht NTB 92-11.

Jacops, E. & Kolditz, O. (2024): Gas transport mechanisms: diffusion, retention and advection processes. Task 2. Final technical report: EURAD-GAS Deliverable 6.7, available online at https://researchportal.sckcen.be/en/publications/gas-transport-mechanisms-diffusion-retention-and-advection-proces, status as of 24-09.2024.

Jenni, A., Gimmi, T., Alt-Epping, P., Mäder, U. & Cloet, V. (2017): Interaction of ordinary Portland cement and Opalinus Clay: Dual porosity modelling compared to experimental data. Physics and Chemistry of the Earth, Parts A/B/C 99, 22-37. DOI: 10.1016/j.pce.2017.01.004.

Jenni, A. & Mäder, U. (2021): Reactive Transport Simulation of Low-pH Cement Interacting with Opalinus Clay Using a Dual Porosity Electrostatic Model. Minerals 11/7, 664. DOI: 10.3390/min11070664.

Jenni, A., Wersin, P., Thoenen, T., Baeyens, B., Ferrari, A., Gimmi, T., Mäder, U., Marschall, P., Hummel, W. & Leupin, O. (2019): Bentonite backfill performance in a high-level waste repository: a geochemical perspective. Nagra Technical Report NTB 19-03.

Johnson, L.H., Curti, E. & Spahiu, K. (2023): A Radionuclide Release Model for Spent UO2 and MOX Fuel for Safety Assessment with Application to Waste to be Disposed of in a Deep Geological Repository in Switzerland. Nagra Arbeitsbericht NAB 23-10.

Johnson, L.H. & Tait, J.C. (1997): Release of segregated nuclides from spent fuel. Technical Report TR 97-18. Swedish Nuclear Fuel and Waste Management (SKB), Stockholm.

Jung, Y., Pau, G.S.H., Finsterle, S. & Doughty, C. (2018): TOUGH3 User's Guide. Version 1.0 LBNL 2001093. Energy Geosciences Division, Lawrence Berkeley National Laboratory, University of California.

Karnland, O., Olsson, S. & Nilsson, U. (2006): Mineralogy and sealing properties of various bentonites and smectite-rich clay materials. Technical Report 06-30. Swedish Nuclear Fuel and Waste Management SKB, Stockholm.

KEG (2003): Kernenergiegesetz (KEG) vom 21. März 2003, Stand am 1. Januar 2024. Systematische Sammlung des Bundesrechts SR 732.1, Schweiz.

Kenney, T.C., van Veen, W.A., Swallow, M.A. & Sungaila, M.A. (1992): Hydraulic conductivity of compacted bentonite–sand mixtures. Canadian Geotechnical Journal 29/3, 364-374. DOI: 10.1139/t92-042.

KEV (2004): Kernenergieverordnung (KEV) of December 10, 2004, status as of January 1, 2024. Systematische Sammlung des Bundesrechts SR 732.11, Schweiz.

King, F. & Briggs, S. (2024): FE-G gas modelling. Phase 28 report. Mont Terri Project internal report (unpublished).

King, F., Kolàř, M., Briggs, S., Behazin, M., Keech, P. & Diomidis, N. (2024): Review of the Modelling of Corrosion Processes and Lifetime Prediction for HLW/SF Containers – Part 2: Performance Assessment Models. Corrosion and Materials Degradation 5/2, 289-339. DOI: 10.3390/cmd5020013.

Kober, F., García-Siñeriz, J.L., Villar, M.V., Lanyon, B., Cloet, V., Mäder, U., Wersin, P., Leupin, O., Sellin, P., Gens, A. & Schneeberger, R. (2021): FEBEX-DP Synthesis Summary of the Full-Scale Engineered Barriers Experiment – Dismantling Project. Nagra Technical Report NTB 17-01.

Kolditz, O., Bauer, S., Bilke, L., Böttcher, N., Delfs, J.O., Fischer, T., Görke, U.J., Kalbacher, T., Kosakowski, G., McDermott, C.I., Park, C.H., Radu, F., Rink, K., Shao, H., Shao, H.B., Sun, F., Sun, Y.Y., Singh, A.K., Taron, J., Walther, M., Wang, W., Watanabe, N., Wu, Y., Xie, M., Xu, W. & Zehner, B. (2012a): OpenGeoSys: an open-source initiative for numerical simulation of thermo-hydro-mechanical/chemical (THM/C) processes in porous media. Environmental Earth Sciences 67/2, 589-599. DOI: 10.1007/s12665-012-1546-x.

Kolditz, O., Görke, U.-J., Shao, H. & Eds. (2012b): Thermo-Hydro-Mechanical- Chemical Processes in Porous Media. Springer, Berlin, Heidelberg.

Kosakowski, G. (2023): Reactive Transport Modellling of Material Interface Evolution in the HLW Near-field. Nagra Arbeitsbericht NAB 23-33.

Kosakowski, G., Churakov, S.V., Glaus, M., Guillemot, T., Hummel, W., Kulik, D., Ma, B., Martin, L., Miron, D. & Prasianakis, N.L. (2023): Geochemical Evolution of the L/ILW Near-Field. Nagra Technical Report NTB 23-03.

Kosakowski, G., Huang, Y. & Wieland, E. (2020): Influence of material heterogeneities, process couplings and aggregate reactivity on the geochemical evolution of the L/ILW repository. Nagra Arbeitsbericht NAB 20-11.

Kosakowski, G. & Smith, P.A. (2014): Long-term Evolution of the Engineered Gas Transport System. Nagra Arbeitsbericht NAB 14-16.

Kosakowski, G. & Watanabe, N. (2014): OpenGeoSys-Gem: A numerical tool for calculating geochemical and porosity changes in saturated and partially saturated media. Physics and Chemistry of the Earth, Parts A/B/C 70-71, 138-149. DOI: 10.1016/j.pce.2013.11.008.

Kosakowski, G. & Wieland, E. (2022): Assessing the impact of chemical processes on the long-term evolution of waste packages by geochemical modelling. NUWCEM 2022 - International Symposium on Cement-Based Materials for Nuclear Wastes May 4-6 2022, Avignon, France, CEA, 4.

Kulik, D.A., Wagner, T., Dmytrieva, S.V., Kosakowski, G., Hingerl, F.F., Chudnenko, K.V. & Berner, U.R. (2012): GEM-Selektor geochemical modeling package: revised algorithm and GEMS3K numerical kernel for coupled simulation codes. Computational Geosciences 17/1, 1-24. DOI: 10.1007/s10596-012-9310-6.

Lam, P.-S., Sindelar, R.L., Duncan, A.J. & Adams, T.M. (2009): Literature Survey of Gaseous Hydrogen Effects on the Mechanical Properties of Carbon and Low Alloy Steels. Journal of Pressure Vessel Technology 131/4 August, 041408. DOI: 10.1115/1.3141435.

Leupin, O.X., Birgersson, M., Karnland, O., Korkeakoski, P., Sellin, P., Mäder, U. & Wersin, P. (2014): Montmorillonite stability under near-field conditions. Nagra Technischer Bericht NTB 14-12.

Leupin, O.X., Smart, N.R., Zhang, Z., Stefanoni, M., Angst, U., Papafotiou, A. & Diomidis, N. (2021): Anaerobic corrosion of carbon steel in bentonite: An evolving interface. Corrosion Science 187, 109523. DOI: 10.1016/j.corsci.2021.109523.

Leupin, O.X., Zeyer, J., Cloet, V., Smith, P., Bernier-Latmani, R., Marschall, P., Papafotiou, A., Schwyn, B. & Stroes-Gascoyne, S. (2016): An assessment of the possible fate of gas generated in a repository for low- and intermediate-level waste. Nagra Technical Report NTB 16-05.

Levasseur, S., Collin, F., Daniels, K., Dymitrowska, M., Harrington J., Jacops E., Kolditz O., Marschall, P., Norris, S., Sillen, X., Talandier, J., Truche, L. & Wendling, J. (2021): Initial state-of-the-art on gas transport in clayey materials. Deliverable D6.1 of the HORIZON 2020 project EURAD. EC Grant agreement no: 847593.

Levasseur, S., Collin, F., Dymitrowska, M., Harrington, J., Jacops, E., Kolditz, O., Marschall, P., Norris, S., Sillen, X., Talandier, J., Truche, L. & Wendling, J. (2023): State of the art on gas transport in clayey materials – Update. Deliverable D6.2 of the HORIZON 2020 project EURAD, Work Package Gas EC Grant agreement no: 847593.

Lisjak, A., Garitte, B., Grasselli, G., Müller, H.R. & Vietor, T. (2015): The excavation of a circular tunnel in a bedded argillaceous rock (Opalinus Clay): Short-term rock mass response and FDEM numerical analysis. Tunnelling and Underground Space Technology 45, 227-248.

Lothenbach, B., Kulik, D.A., Matschei, T., Balonis, M., Baquerizo, L., Dilnesa, B., Miron, G.D. & Myers, R.J. (2019): Cemdata18: A chemical thermodynamic database for hydrated Portland cements and alkali-activated materials. Cement and Concrete Research 115, 472-506. DOI: 10.1016/j.cemconres.2018.04.018.

Lothenbach, B., Pelletier-Chaignat, L. & Winnefeld, F. (2012): Stability in the system CaO–Al2O3–H2O. Cement and Concrete Research 42/12, 1621-1634. DOI: 10.1016/j.cemconres.2012.09.002.

Ma, B. & Lothenbach, B. (2020a): Synthesis, characterization, and thermodynamic study of selected Na-based zeolites. Cement and Concrete Research 135, 106111. DOI: 10.1016/j.cemconres.2020.106111.

Ma, B. & Lothenbach, B. (2020b): Thermodynamic study of cement/rock interactions using experimentally generated solubility data of zeolites. Cement and Concrete Research 135, 106149. DOI: 10.1016/j.cemconres.2020.106149.

Ma, B. & Lothenbach, B. (2021): Synthesis, characterization, and thermodynamic study of selected K-based zeolites. Cement and Concrete Research 148, 106537. DOI: 10.1016/j.cemconres.2021.106537.

Madaschi, A. & Laloui, L. (2019): EBS – Task Force / Task 7: Gas Transport in Bentonite - Modelling activities of LMS-EPFL (Final Report - October 2019). Nagra Arbeitsbericht NAB 19-37.

Mäder, U., Jenni, A., Lerouge, C., Gaboreau, S., Miyoshi, S., Kimura, Y., Cloet, V., Fukaya, M., Claret, F., Otake, T., Shibata, M. & Lothenbach, B. (2017): 5-year chemico-physical evolution of concrete–claystone interfaces, Mont Terri rock laboratory (Switzerland). Swiss Journal of Geosciences, Special Issue: Mont Terri rock laboratory, 20 years of research 110, 307-327. DOI: 10.1007/s00015-016-0240-5.

Mäder, U. & Wersin, P. (2023): Reference porewaters for SGT Stage 3 of the Opalinus Clay for the siting regions Jura Ost (JO), Nördlich Lägern (NL) and Zürich Nordost (ZNO). Nagra Arbeitsbericht NAB 22-47.

Manca, D. (2016): Gas Transport and related Chemo-Hydro-Mechanical Response of Sand Bentonite Mixture. Nagra Technical Report NTB 16-07.

Marschall, P., Talandier, J., Kolditz, O., Kucerova, M., Mokni, N., Grgic, D., Agboli, D., Zhang C.-L., Cuss, R., Wiseall, A., Gonzales-Blanco, L., Romero, E., Llabjani, Q., Ferrari, A. & Keller, L. (2024): Barrier integrity: gas-induced impacts and model-based interpretation. EURAD-GAS: Work Package GAS (Mechanical understanding of gas transport in clay-based materials) of the HORIZON 2020 project EURAD. EC Grant agreement N°847593. Task 3. Final Technical Report. Deliverable 6.8 (D6.8).

Martikainen, J., Laurila, T., Kumpulainen, S. & Leupin, O.X. (2024): Bentonite swelling pressure response to temperature change. Applied Clay Science 260, 107504. DOI: 10.1016/j.clay.2024.107504.

Martin, L., Jacobs, F., Loser, R., Lothenbach, B., Leemann, A. & Winnefeld, F. (2024): Using Calcareous Aggregates in the Backfill Mortar M1: A Suitability Assessment. Nagra Arbeitsbericht NAB 22-44.

Martin, L., Kosakowski, G., Papafotiou, A. & Smith, P.A. (2023): Evolution of the sealing system porosity and its impact on performance. Nagra Arbeitsbericht NAB 23-21.

Masurat, P., Eriksson, S. & Pedersen, K. (2010): Microbial sulphide production in compacted Wyoming bentonite MX-80 under in situ conditions relevant to a repository for high-level radioactive waste. Applied Clay Science 47, 58-64.

Matsunaga, H., Yoshikawa, M., Kondo, R., Yamabe, J. & Matsuoka, S. (2015): Slow strain rate tensile and fatigue properties of Cr–Mo and carbon steels in a 115 MPa hydrogen gas atmosphere. International Journal of Hydrogen Energy 40/16, 5739-5748. DOI: 10.1016/j.ijhydene.2015.02.098.

Mayer, G., Moetsch, H.A. & Wittmann, F.H. (1999): Large-scale Experiment for water and gas transport in cementitious backfill materials (Phase 1) : COLEX I. Nagra Technical Report NTB 98-03.

Millington, R.J. & Quirk, J.P. (1961): Permeability of porous solids. Transactions of the Faraday Society 57, 122-1207.

Miron, G.D., Marques Fernandes, M., Kulik, D.A., Marinich, O., Baeyens, B., Wüst, R., Becker, J. & Li, X. (2024): Sorption Databases for Opalinus Clay, Confining Geological Units and Bentonite: Methods, Concepts and Upscaling of Data. Nagra Technical Report NTB 23-06.

Müller, H., Garitte, B., Vogt, T., Köhler, S., Sakaki, T., Weber, H., Spillmann, T., Hertrich, M., Becker, J., Giroud, N., Cloet, V., Diomidis, N. & Vietor, T. (2017): Implementation of the Full-Scale Emplacement (FE) Experiment at the Mont Terri rock laboratory. Swiss Journal of Geosciences, Special Issue: Mont Terri rock laboratory, 20 years of research 110, 287-306. DOI: 10.1007/s00015-016-0251-2.

Nagra (1985): Project Gewähr 1985: Nuclear Waste Management in Switzerland: Feasibility Studies and Safety Analyses. Nagra Project Report NGB 85-09.

Nagra (2002): Project Opalinus Clay: Safety report: Demonstration of disposal feasibility for spent fuel, vitrified high-level waste and long-lived intermediate-level waste (Entsorgungsnachweis). Nagra Technical Report NTB 02-05.

Nagra (2008): Effects of post-disposal gas generation in a repository for low- and intermediate-level waste sited in the Opalinus Clay of Northern Switzerland. Nagra Technical Report NTB 08-07.

Nagra (2014): SGT Etappe 2: Vorschlag weiter zu untersuchender geologischer Standortgebiete mit zugehörigen Standortarealen für die Oberflächenanlage: Geologische Grundlagen Dossier IV Geomechanische Unterlagen. Nagra Technischer Bericht NTB 14-02 Dossier IV.

Nagra (2016): Entsorgungsprogramm 2016 der Entsorgungspflichtigen. Nagra Technischer Bericht NTB 16-01 D.

Nagra (2019): Implementation of the Full-scale emplacement Experiment at Mont Terri: Design, Construction and Preliminary Results. Nagra Technical Report NTB 15-02.

Nagra (2021a): Entsorgungsprogramm 2021 der Entsorgungspflichtigen. Nagra Technischer Bericht NTB 21-01.

Nagra (2021b): Methodik zur Definition des Mindestabstands zwischen den HAA- und SMA-Lagerteilen im Kombilager. Nagra Arbeitsbericht NAB 20-31.

Nagra (2021c): The Nagra Research, Development and Demonstration (RD&D) Plan for the Disposal of Radioactive Waste in Switzerland. Nagra Technical Report NTB 21-02.

Nagra (2021d): Verschlusskonzept für ein geologisches Tiefenlager. Nagra Arbeitsbericht NAB 21-12 Rev. 1.

Nagra (2022): Beherrschung möglicher karstbedingter Wasserzutritte während des Baus und Betriebs eines geologischen Tiefenlagers. Nagra Arbeitsbericht NAB 22-41.

Nagra (2023a): Bautechnisches Dossier. Nagra Arbeitsbericht NAB 23-01 Band 1-9.

Nagra (2023b): Bautechnisches Dossier Standortvergleich – Band 6: Technischer Beschrieb und Pläne Lagerprojekte. Nagra Arbeitsbericht NAB 23-01 Band 6.

Nagra (2023c): Bautechnisches Dossier Standortvergleich – Band 8: Tunnelstatik. Nagra Arbeitsbericht NAB 23-01 Band 8.

Nagra (2023d): Modellhaftes Inventar für radioaktive Materialien MIRAM-RBG. Nagra Technischer Bericht NTB 22-05.

Nagra (2024a): Abfallzuteilung und Betrachtungszeitraum für den Standortvergleich und Nachweiszeitraum für den Sicherheitsnachweis für das geologische Tiefenlager. Nagra Arbeitsbericht NAB 24-05.

Nagra (2024b): Anlagen- und Betriebskonzept für das geologische Tiefenlager. Nagra Technischer Bericht NTB 24-11.

Nagra (2024c): Definition der Bewertungsobjekte für den sicherheitstechnischen Vergleich der Standorte in Etappe 3 des Sachplans geologische Tiefenlager. Nagra Arbeitsbericht NAB 24-01 Rev. 1.

Nagra (2024d): Design and Performance Assessment of HLW Disposal Canisters. Nagra Technical Report NTB 24-20.

Nagra (2024e): Development of Safety Scenarios. Nagra Technical Report NTB 24-21.

Nagra (2024f): Gas related property distributions in the proposed host rock formations of the candidate siting region in Northern Switzerland – Updated database 2024. Nagra Arbeitsbericht NAB 24-27.

Nagra (2024g): GAST Flow Test Data Report. Nagra Arbeitsbericht NAB 23-15.

Nagra (2024h): GAST – Gas Flow Test Preliminary Interpretation. Nagra Arbeitsbericht NAB 23-40 Rev. 1.

Nagra (2024i): Geologic Scenarios for the Evaluation of Earthquake Impact on the Deep Geological Repository. Nagra Arbeitsbericht NAB 24-28.

Nagra (2024j): Geological Properties of the Jura Ost, Nördlich Lägern and Zürich Nordost Siting Regions for Safety Assessment. Nagra Arbeitsbericht NAB 24-10 Rev. 1.

Nagra (2024k): Geosynthesis of Northern Switzerland. Nagra Technischer Bericht NTB 24-17.

Nagra (2024l): Model Supported Assessment of the Containment-Providing Rock Zone in Support of the Site Selection. Nagra Arbeitsbericht NAB 24-26.

Nagra (2024m): Model-Based Performance Assessment for a Combined Repository. Nagra Arbeitsbericht NAB 24-25.

Nagra (2024n): Phenomenological Description of the Evolution of a Geological Repository for Radioactive Waste in Opalinus Clay. Nagra Arbeitsbericht NAB 24-20 Rev. 1.

Nagra (2024o): Post-closure safety report. Nagra Technical Report NTB 24-10 Rev. 1.

Nagra (2024p): Production and Fate of Gases in the Geological Repository. Nagra Technical Report NTB 24-23.

Nagra (2024q): Qualitative Bewertung für den sicherheitstechnischen Vergleich in Etappe 3 des Sachplans geologische Tiefenlager. Nagra Arbeitsbericht NAB 24-23 Rev. 1.

Nagra (2024r): Radiological Consequence Analysis for a Deep Geological Repository in Northern Switzerland. Nagra Technical Report NTB 24-18.

Nagra (2024s): Safety and Repository Concept and Provisional Design. Nagra Arbeitsbericht NAB 24-18 Rev. 1.

Nagra (2024t): Safety Assessment Methodology. Nagra Technical Report NTB 24-19.

Nagra (2024u): Synthesis of the Performance Assessment for a Combined Repository. Nagra Technical Report NTB 24-22 Rev. 1.

Nagra (2024v): The Geochemical Evolution of the HLW Repository Near-Field. Nagra Technical Report NTB 23-02 Rev. 1.

Nagra (2024w): Thermo-hydraulic modelling of the temperature distribution in the siting regions JO, NL and ZNO. Nagra Arbeitsbericht NAB 24-24.

Nagra (2024x): Treatment of ^{14}C in the Post-Closure Safety Assessments. Nagra Arbeitsbericht NAB 24-07.

Nagra (2025a): Rahmenbewilligungsgesuch für das geologische Tiefenlager – Begründung der Standortwahl. Nagra Technischer Bericht NTB 24-03.

Nagra (2025b): Rahmenbewilligungsgesuch für das geologische Tiefenlager – Sicherheitsbericht. Nagra Technischer Bericht NTB 24-01.

OECD/NEA (2002): Establishing and communicating confidence in the safety of deep geologic disposal: Approaches and arguments = Etablir et faire partager la confiance dans la sûreté des dépôts en grande profondeur: Approches et arguments. OECD/NEA, Paris.

OECD/NEA (2004): Geological disposal: Building confidence using multiple lines of evidence. First AMIGO (Approaches and methods for integrating geologic information in the safety case) workshop proceedings, Yverdon-les-Bains, 3-5 June 2003.

Papafotiou, A. & Senger, R.K. (2014a): Sensitivity analyses of gas release from a L/ILW repository in the Opalinus Clay in the candidate siting regions of Northern Switzerland. Nagra Arbeitsbericht NAB 13-92.

Papafotiou, A. & Senger, R.K. (2014b): Sensitivity analyses of gas release from a SF/HLW repository in the Opalinus Clay in the candidate siting regions of Northern Switzerland. Nagra Arbeitsbericht NAB 14-10.

Papafotiou, A. & Senger, R.K. (2016a): Sensitivity analyses of gas release from a L/ILW repository in the Opalinus Clay including the microbial consumption of hydrogen. Nagra Arbeitsbericht NAB 16-07.

Papafotiou, A. & Senger, R.K. (2016b): Sensitivity analyses of gas release from a SF/HLW repository in the Opalinus Clay. Nagra Arbeitsbericht NAB 16-08.

Pinder, G.F. & Gray, W.G. (2008): Essentials of multiphase flow and transport in porous media. Wiley, Hoboken, NJ.

Prasianakis, N.I., Kosakowski, G., Gimmi, T., Luraschi, P., Miron, G.D., Pfingsten, W. & Churakov, S.V. (2022): Cement - Clay : Synthesis of transport across the cement-clay interface. Nagra Arbeitsbericht NAB 22-34.

Reddy, B., Padovani, C., Smart, N.R., Rance, A.P., Cook, A., Milodowski, A., Field, L., Kemp, S. & Diomidis, N. (2021): Further results on the in situ anaerobic corrosion of carbon steel and copper in compacted bentonite exposed to natural Opalinus Clay porewater containing native microbial populations. Materials and Corrosion 72/1-2, 268-281. DOI: 10.1002/maco.202011785.

Romero, E. & Gonzalez-Blanco, L. (2019): Hydro-mechanical processes associated with gas transport in MX-80 Bentonite in the context of Nagra's RD&D programme (results by May 2019). Nagra Arbeitsbericht NAB 19-16.

Seiphoori, A. (2015): Thermo-hydro-mechanical characterisation and modelling of Wyoming granular bentonite. Nagra Technischer Bericht NTB 15-05.

Seiphoori, A. (2019): The effects of burial diagenesis on Opalinus clay behavior: a multiscale study of the pore structure and mechanical properties. Nagra Arbeitsbericht NAB 19-06.

Senger, R., Marschall, P. & Finsterle, S. (2008): Investigation of two-phase flow phenomena associated with corrosion in an SF/HLW repository in Opalinus Clay, Switzerland. Physics and Chemistry of the Earth, Parts A/B/C 33, S317-S326. DOI: 10.1016/j.pce.2008.10.034.

Senger, R.K. & Papafotiou, A. (2013): Effects of salt enrichment in SF/HLW tunnels and L/ILW caverns due to water consumption by iron corrosion. Nagra Arbeitsbericht NAB 13-72.

Senger, R.K., Papafotiou, A. & Marschall, P. (2014): Thermo-hydraulic simulations of the near-field of a SF/HLW repository during early- and late-time post-closure period. Nagra Arbeitsbericht NAB 14-11.

Stroes-Gascoyne, S. (2011): Microbiological characteristics of compacted bentonite fo a dry density of 1450 kg/m3: A literature review. Nagra Arbeitsbericht NAB 11-05.

Taniguchi, N., Kawasaki, M. & Naito, M. (2010): Corrosion behavior of carbon steel in compacted bentonite saturated with simulated groundwater under anaerobic conditions. Zairyo To Kankyo 59/11, 418-429. DOI: 10.3323/jcorr.59.418.

Thacker, B.H., Doebling, S.W., Hemez, F.M., Anderson, M.C., Pepin, J.E. & Rodriguez, E.A. (2004): Concepts of Model Verification and Validation. LA-14167-MS. Los Alamos National Laboratory, Los Alamos, NM.

Thoenen, T., Hummel, W., Berner, U. & Curti, E. (2014): The PSI/Nagra Chemical Thermodynamic Database 12/07. PSI Bericht Nr. 14-04. PSI/LES, Villigen.

Tits, J. & Wieland, E. (2023): Radionuclide Retention in the Cementitous Near-field of a Repository for Low- and Intermediate-level Waste: Development of the Cement Sorption Database. Nagra Technical Report NTB 23-07.

Turnbull, A. (2009): A review of the possible effects of hydrogen on lifetime of carbon steel nuclear waste canisters. Nagra Technical Report NTB 09-04.

Turrero, M.J. & Cloet, V. (2017): FEBEX-DP Concrete ageing, concrete/bentonite and concrete/rock interaction analysis. Nagra Arbeitsbericht NAB 16-18.

Wendling, J., Norris, S. & editors (2024): Modelling of a generic geological disposal: evaluation of various approaches to model gas transport through geological disposal systems. EURAD-GAS: Work Package Gas (Mechanical understanding of gas transport in clay-based materials) of the HORIZON 2020 project EURAD. EC Grant agreement no: 847593. Task 4. Final technical report. Deliverable 6.9 (D6.9).

Wieland, E., Kosakowski, G., Lothenbach, B., Kulik, D.A. & Cloet, V. (2018): Preliminary assessment of the temporal evolution of waste packages in the near field of a L/ILW repository. Nagra Arbeitsbericht NAB 18-05.

Wigger, C., Hanusova I., S., Hausmannova L., C.T., Heino, V., Lavikainen, L., Leupin, O.X., Marshall, P., Mayor, J.C., Meleshyn, A., Pusch, R., Sellin, P., Swahn, J., Talandier, J., Wendling, J. & Wieczorek, K. (2017): BEACON – Bentonite Mechanical Evolution State-of-the-Art Report. Nagra Arbeitsbericht NAB 18-07.

Wilson, J., Bateman, K. & Tachi, Y. (2021): The impact of cement on argillaceous rocks in radioactive waste disposal systems: A review focusing on key processes and remaining issues. Applied Geochemistry 130, 104979. DOI: 10.1016/j.apgeochem.2021.104979.

Wojnarowicz, M., Madaschi, A. & Laloui, L. (2024): A methodology to optimize complex models in the context of nuclear waste repositories. Computers and Geotechnics 173, 106579. DOI: 10.1016/j.compgeo.2024.106579.

Xu, K. (2012): Hydrogen embrittlement of carbon steels and their welds. *In:* Gangloff, R.P. & Somerday, B.P. (eds.): Gaseous Hydrogen Embrittlement of Materials in Energy Technologies. The problem, its characterisation and effects on particular alloy classes. (Woodhead Publishing Series in Metals and Surface Engineering, 2). Woodhead Publishing, Oxford, 526-561.

Xu, K. & Rana, M. (2008): Tensile and Fracture Properties of Carbon and Low Alloy Steels in High Pressure Hydrogen. *In:* Somerday, B.P., Sofronis, P., Jones, R. & Somerday, B. (eds.): Effects of Hydrogen on Materials. Proceedings of the 2008 International Hydrogen Conference. Jackson, WY, September 7-10, 2008. American Society for Metals ASM, Materials Park, Ohio, 349-356.

Yokoyama, S., Shimbashi, M., Minato, D., Watanabe, Y., Jenni, A. & Mäder, U. (2021): Alteration of Bentonite Reacted with Cementitious Materials for 5 and 10 years in the Mont Terri Rock Laboratory (CI Experiment). Minerals 11/3, 251. DOI: 10.3390/min11030251.

Yoshikawa, H., Gunji, E. & Tokuda, M. (2008): Long term stability of iron for more than 1500 years indicated by archaeological samples from the Yamato 6th tumulus. Journal of Nuclear Materials 379/1-3, 112-117. DOI: 10.1016/j.jnucmat.2008.06.009.

App. A Assessment basis – data sources and relevant parameters

A.1 Key PA inputs from the MIRAM database

The radionuclide inventory and a description of the waste forms, masses and volumes are provided by the MIRAM (Model Inventory of Radioactive Materials) database for the general licence application (NTB 22-05, Nagra 2023d). Thermal and gas-related source terms, derived from the waste inventory, represent a key input for the assessment of repository-induced effects (NTB 24-23, NAB 24-25: Nagra 2024p, 2024m). A compilation of important PA inputs from the MIRAM database is given in the following paragraphs.

A.1.1 Gas source terms

Gas generation associated with the corrosion of metals and degradation of organic waste may give rise to pore pressure perturbations in the repository near-field. An overview of the mass fractions of the gas producing metals (hydrogen only) in the L/ILW and HLW repository sections are given in Fig. A-1. Gas-producing organic wastes are disposed of only in the L/ILW repository. The main gas species generated from organics are CO_2 and CH_4. The CO_2 will be largely bound by the cementitious material, which means that the mass fraction of free gas from the degradation of organic matter is mainly CH_4, amounting to around 8% of total gas volume produced in the L/ILW repository (from NTB 24-23, Nagra 2024p).

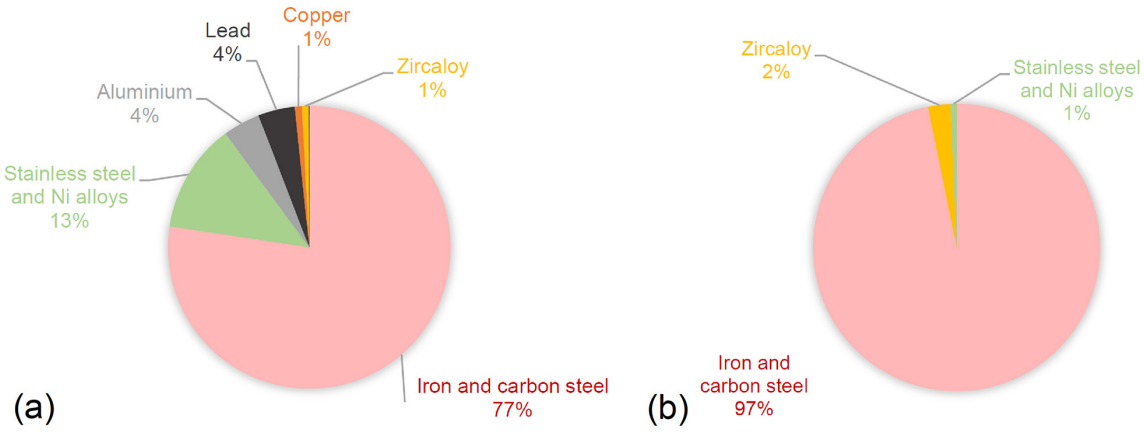

Fig. A-1: Mass distribution of the corrosion groups disposed of in (a) L/ILW emplacement caverns (including metals from waste matrix and containers) and (b) HLW emplacement drifts (including metals from waste matrices and canisters)

The total mass of metals in L/ILW is 4.2×10^7 kg. The total mass of metals in HLW is 4.3×10^7 kg. From NTB 24-23 (Nagra 2024p).

For the estimation of gas production in the deep geological repository over time, it is necessary to define the stoichiometry of the involved chemical reactions. NTB 24-23 (Nagra 2024p) details the corresponding reactions associated with the corrosion and degradation processes in the HLW and L/ILW repository sections. The resulting time-dependent gas generation rates calculated per waste emplacement room for the L/ILW and HLW repository sections are given in Fig. A-2a and b. The transients of the total cumulative volume of gas per waste emplacement room are given in Fig. A-2c. The total volume of gas produced in the entire L/ILW repository is 24.5×10^6 m^3 SATP and in the entire HLW repository 25.2×10^6 m^3 SATP.

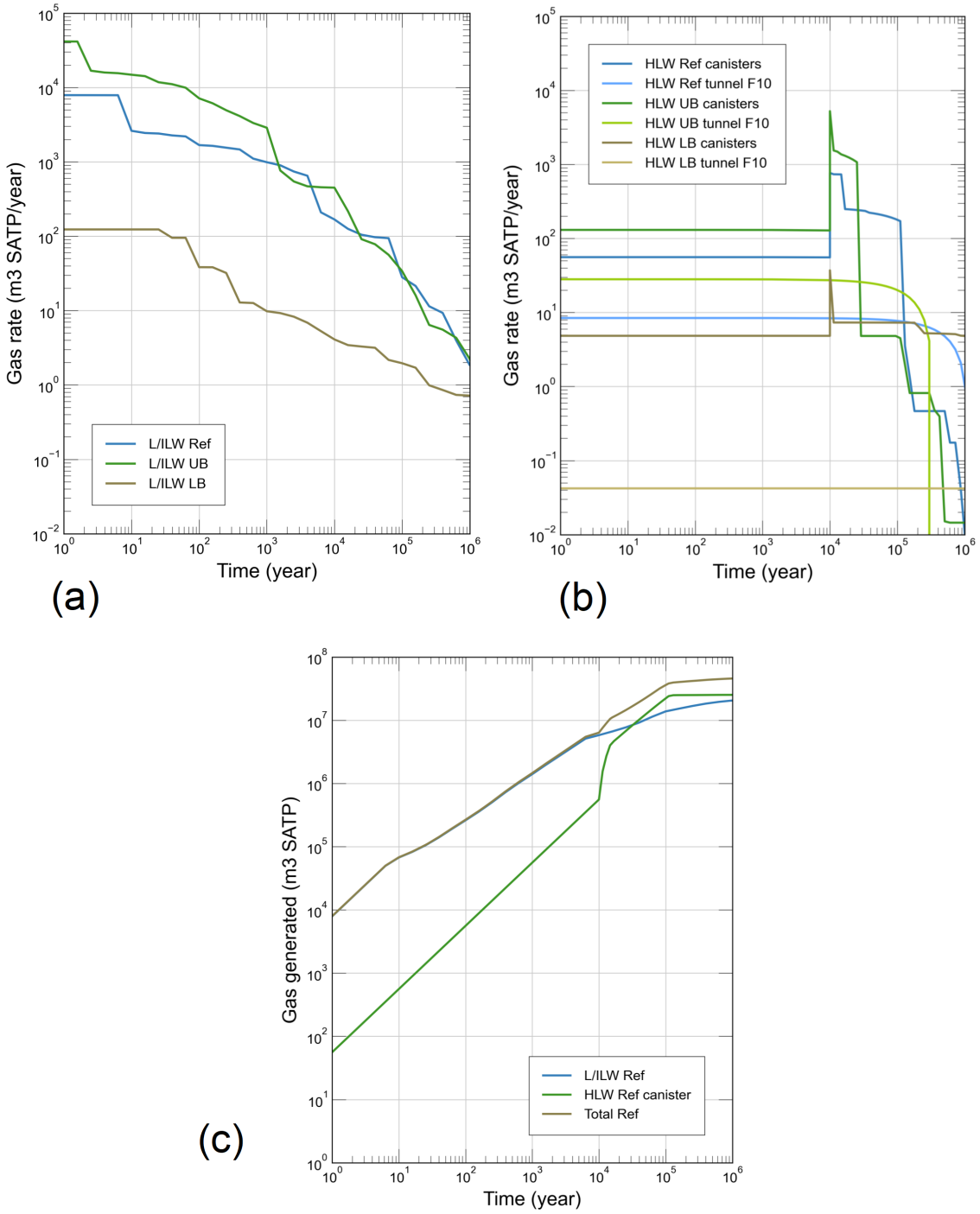

Fig. A-2: Best estimate (Ref), upper bound (UB) and lower bound (LB values of gas generation rates and cumulative gas volumes

Calculated with the gas generation tool for the (a) L/ILW, (b) HLW repository sections, and (c) respective cumulative volume (from NTB 24-23, Nagra 2024p).

A.1.2 Heat source terms

Thermal effects associated with the heat generated in the HLW repository are of relevance in the early time after emplacement of the HLW canisters. The type and the number of HLW canisters has been specified in MIRAM-RBG (NTB 22-05, Nagra 2023d) as a design basis for the current repository project at the Haberstal site (SF: 1,045 PWR canisters, 891 BWR canisters; RP-HLW: 211 canisters). Note that the type and number of waste canisters correspond to the NPP operation time and emplacement schedule adopted in NTB 22-05 (Nagra 2023d) and NTB 24-11 (Nagra 2024b). In the PA calculations average heat rates (Fig. A-3) were specified for PWR-MOX, PWR-UO_2, and BWR canisters due to the different loadings and decays of the SF canisters (see also NAB 24-25, Nagra 2024m) and a weighted average was derived for the entire inventory (called "Kombi"), representing the thermal source term for the PA-Scenario of expected evolution (see Section 6.2.1). To the other end, the heat generation rates PWR-MOX were used to represent the thermal source term for the PA-Scenario UBHEAT (see Section 6.3.2).

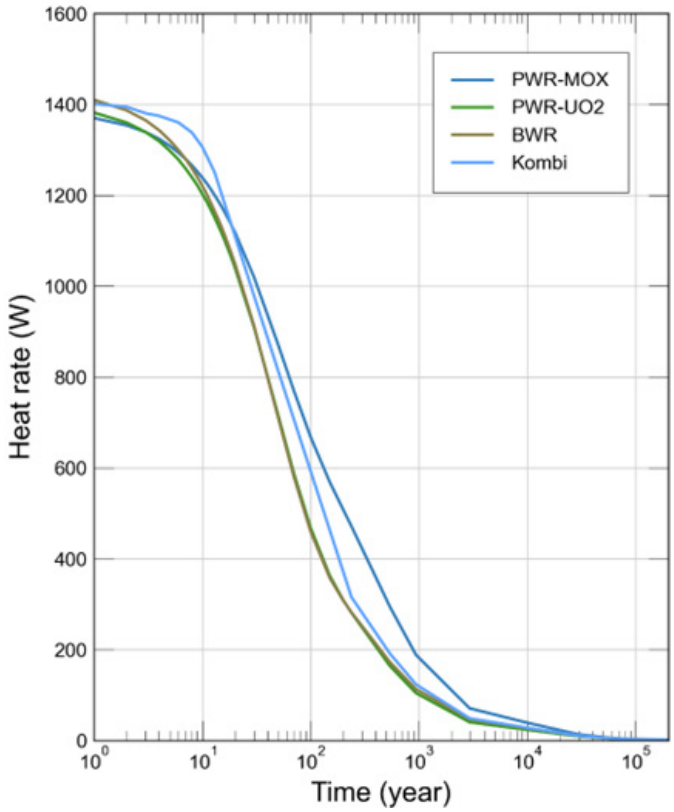

Fig. A-3: Heat generation rates per SF canister type (PWR-MOX, PWR-UO_2, BWR) and average used for PA-Scenario of expected evolution

A.1.3 Source terms of dissolved and volatile radionuclides

Tracer flux of a conservative tracer was introduced in Section 2.5.4 as a category of performance indicators for the HLW and the L/ILW repository. It was assumed that the radionuclide is dissolved in the porewater and released as an instantaneous pulse from the near-field into the host rock, from where it migrates towards regional aquifer systems at the top and bottom of the CRZ. The dose-relevant radionuclide for the HLW repository section is ^{129}I, whereas the representative nuclides for the L/ILW section are ^{36}Cl and ^{14}C.

Accurate source terms are derived in the context of the radiological consequence analysis (NTB 24-18, Nagra 2024r). They are based on the MIRAM inventory and on a detailed modelling of the release rates from the different waste forms. Fig. A-4 presents for the three radionuclides ^{129}I, ^{36}Cl and ^{14}C the source terms as provided in NTB 24-18 (Nagra 2024r). The release rates are given in [Bq], based on initial activities as given in the MIRAM report (NTB 22-05, Nagra 2023d).

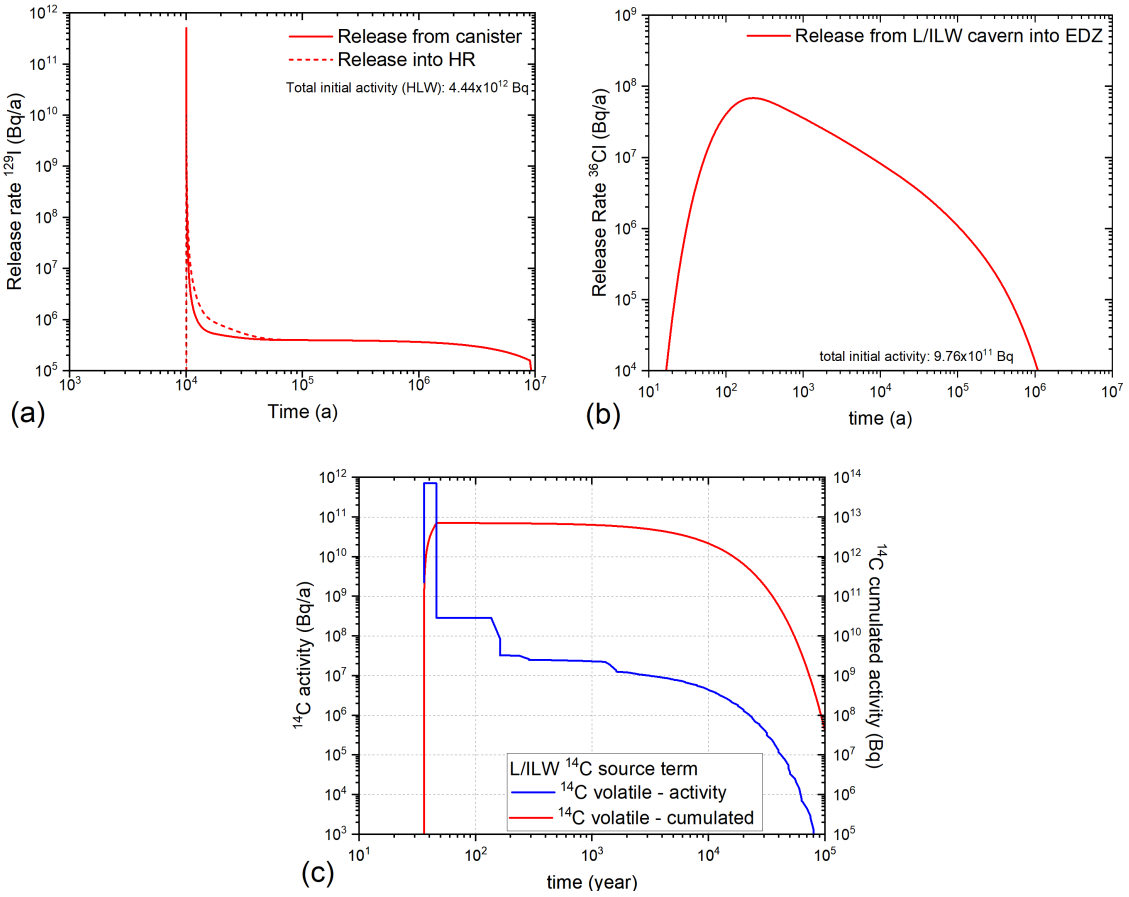

Fig. A-4: Source terms of dissolved and volatile radionuclides, derived in the context of the radiological consequence analysis

From NTB 24-18 (Nagra 2024r).

(a) ^{129}I, (b) ^{36}Cl and (c) ^{14}C.

A.2 Key PA inputs from the engineering database

The provisional technical layout and operation of the current project of a deep geological repository for HLW and L/ILW at the Haberstal site has been documented in NTB 24-11 (Nagra 2024b; Fig. A-5). The engineering dossier (NAB 23-01 Bd. 1 – 9, Nagra 2023a) provides the detailed designs of the individual repository structures. Information about the lengths, cross-sectional areas and backfill materials needed for the development of the PA models at repository scale and component scale were extracted from the engineering dossier. The geometric data of the individual repository components as described in the engineering dossier are given in Tab. A-1. In the PA models with a simplified representation of the repository structures, modifications of the geometric data and the material properties of the backfill material were made (see Section 5.2.2); the corresponding modifications of the engineering databases for the purpose of PA modelling are described in NAB 24-25 (Nagra 2024m).

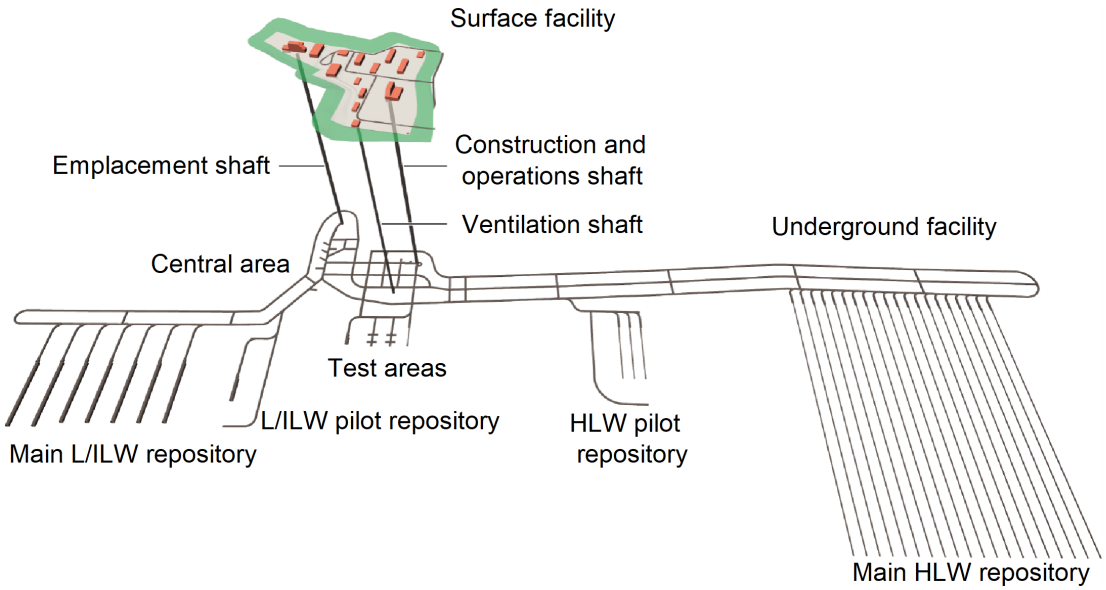

Fig. A-5: Illustration of the current repository project at the Haberstal site

From NTB 24-11 (Nagra 2024b).

Geometric data of the individual repository components as described in the engineering dossier are given in Tab. A-1. Furthermore, reference values of porosity and specific heat of the backfill materials are provided.

Tab. A-1: Geometric data of repository sections

Based on NAB 23-01 Bd. 1 – 9 (Nagra 2023a).

Repository tunnel	**Average cross-section for gas storage[1]** [m^2]	**Length[1]** [m]	**Volume** [m^3]	**Porosity[2]** [-]	**Specific heat[2]** [J/kg/°C]	**Void space volume[3]** [m^3]
HLW drifts	6.605	17,997.2	118,875.1	0.25	964	29,718.8
HLW V1 seals (incl. pilot)	6.605	230.0	1,519.2	0.30	964	455.8
HLW branching tunnels (incl. pilot repository)	52.688	1,870.9	98,576.4	0.35	920	3,4501.7
HLW operations tunnel (incl. V2[4])	49.185	2,947.4	144,967.8	0.35	920	50,738.7
HLW ventilation tunnel (incl. V2[4])	49.514	2,504.3	1,239,98.7	0.35	920	43,400.0
HLW construction tunnel (incl. V2[4])	49.625	3,008.2	149,281.4	0.35	920	52,248.5
HLW connecting tunnels	48.585	720.0	34,981.1	0.35	920	12,243.4
HLW operations tunnel for pilot repository (incl. V2[4])	49.514	322.1	15,946.1	0.35	920	5,581.1
HLW observation drift	43.008	516.8	22,228.5	0.35	920	7,780.0
HLW pilot repository drift	6.605	603.8	3,988.3	0.30	964	997.1
L/ILW caverns	152.184	1,640.0	249,581.4	0.20	920	49,916.3
L/ILW caverns V1 seals (incl. pilot repository)	48.275	240.0	11,586.0	0.30	920	3,475.8
L/ILW branching tunnels (excl. pilot repository)	53.635	1,216.9	65,271.2	0.35	920	22,844.9
L/ILW operations tunnel (incl. V2[4])	49.072	1,166.9	57,260.4	0.35	920	20,041.1
L/ILW ventilation tunnel (incl. V2[4])	48.275	2,119.1	102,299.5	0.35	920	35,804.8
L/ILW connecting tunnels	48.275	180.0	8,689.5	0.35	920	3,041.3
L/ILW operations tunnel for pilot repository (incl. V2[4])	49.514	107.1	5,303.0	0.35	920	1,856.0
L/ILW observation drift	43.008	467.5	20,107.7	0.35	920	7,037.7
L/ILW pilot repository cavern	152.184	85.0	12,935.6	0.20	920	2,587.1
Central area	42.919	2,122.1	112,297.3	0.35	920	39,304.1
Access tunnel	63.588	87.7	5,574.1	0.35	920	1,951.0
Facilities for test areas	47.897	795.4	38,094.8	0.35	920	12,776.1
Total below V3	**-**	**40,984.4**	**1,403,363**	**-**	**-**	**438,301.3**
V3 (access)	91.609	82.0	7,511.9	0.30	964	2,253.6
V3 (ventilation)	54.106	47.0	2,543.0	0.30	964	762.9
V3 (construction)	109.359	50.0	5,467.9	0.30	964	1,640.4

Tab. A-1: Cont.

Repository tunnel	Average cross-section for gas storage[1] [m²]	Length[1] [m]	Volume [m³]	Porosity[2] [-]	Specific heat[2] [J/kg/°C]	Void space volume[3] [m³]
Access shaft (excl. V3)	102.429	758.0	77,641.0	0.35	920	27,174.4
Ventilation shaft (excl. V3)	51.614	762.0	39,329.9	0.35	920	13,765.5
Construction shaft (excl. V3)	123.200	757.0	93,262.1	0.35	920	32,641.7

[1] Extracted from NAB 23-01 Bd. 1 – 9 (Nagra 2023a)
[2] From NTB 24-23 (Nagra 2024p)
[3] Product of porosity and volume
[4] Porosity of V2 seals is 0.3, specific heat of HLW-V2 is 964 J/kg/°C

A.3 Key PA inputs from the geoscientific database

The interpretation of the geoscientific databases gathered during site-specific investigation programmes and the synthesis of the geoscientific interpretations in the context of the regional geological setting has been documented in (NTB 24-17, Nagra 2024k). This process led to the development of site-specific geoscientific reference datasets, encompassing a geological layer model, as well as mineralogical, geochemical, hydrogeological and geomechanical rock properties and relevant hydro-chemical and hydro-mechanical state conditions in the siting regions (NAB 24-10 Rev. 1 and NTB 24-17: Nagra 2024j, 2024k). 3-D numerical models of the of the geological layer stack were developed (NAB 24-10 Rev. 1, NAB 24-24, NAB 24-27: Nagra 2024j, 2024w, 2024f), representing in a simplified manner the detailed lithostratigraphy described in NAB 24-10 Rev. 1 and NTB 24-17 (Nagra 2024j, 2024k). A 2-D vertical cross-section through the centre of the HLW repository area at the Haberstal site is shown in Fig. A-6 providing an overview of the implemented lithostratigraphic units (see also Tab. A-2).

A set of baseline properties, namely hydraulic conductivity and porosity, is taken from the geosynthesis (Nagra 2024k, see also Nagra 2024j) and assigned to the modelled formations as shown in Tab. A-3 and Tab. A-4. In addition, simulations of diffusion of solutes require input parameters for diffusivity. The effective diffusion coefficients for Iodine are summarised in Tab. A-5.

The baseline properties of the site model are complemented with two-phase and TH parameters for the geologic formations. These parameters, summarised in Tab. A-6, are required input for modelling gas and heat transport problems. Capillary strength is calculated from hydraulic conductivity through Leverett scaling using the values for Opalinus Clay as reference (Nagra 2024j, 2024w, 2024f). Similarly, pore compressibility is scaled for each formation using the corresponding porosity value. Thermal conductivity is calculated as described in Nagra (2024j, 2024w, 2024f). Grain density corresponds to the best estimates from Nagra (2024j, 2024k). Additional, less sensitive parameters are assumed constant across all formations as given in Tab. A-6.

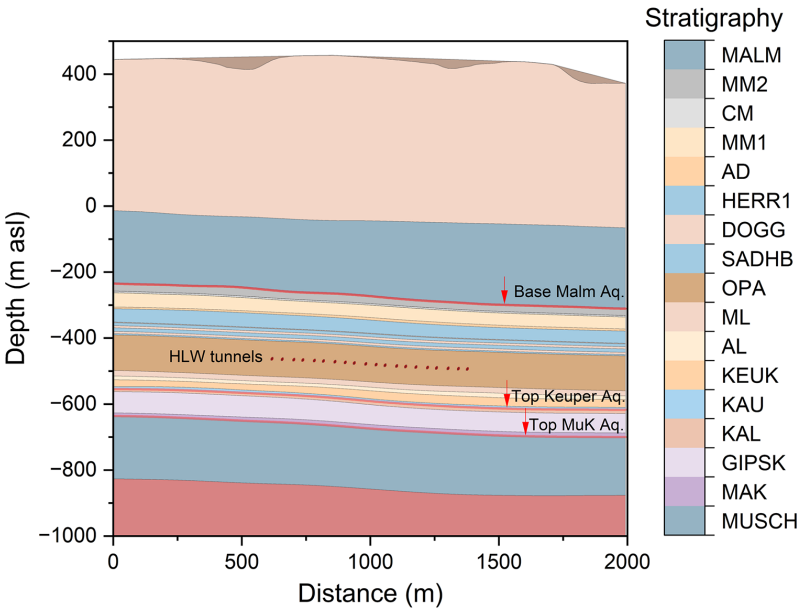

Fig. A-6: Vertical cross-section through the centre of the HLW repository area

The simplified representation of the lithostratigraphic units was documented in NAB 24-10 Rev. 1 and NTB 24-17 (Nagra 2024j, 2024k).

Tab. A-2: Stratigraphic units respectively formations represented in the model for the NL siting region

Stratigraphic units / formation	**PA material code**
Bottom Boundary	BOTBC
Permo-Carboniferous	PERM
Muschelkalk	MUSCH
Dolomitic-Anhydritic Keuper (DAK) & Massive Anhydritic Keuper (MAK) of Bänkerjoch Formation	MAK
Anhydritic-Argillaceous Keuper (AAK) of Bänkerjoch Formation	GIPSK
Argillaceous Keuper (AK1) & Sandy Keuper (SK) & Dolomitic Keuper (JO-DK) of Klettgau Formation	KAL
Argillaceous Keuper (NL-AK2 – "lower" Gruhalde Member) & Dolomitic Keuper (NL-DK2 – Seebi Member)	KAU
Argillaceous Keuper (JO-AK2/3 – Klettgau and Staffegg Formations) & Calcareous Lias (CL) of Staffegg Formation	KEUK
Argillaceous Lias (AL) of Staffelegg Formation	AL
Marly Lias (ML) of Staffelegg Formation	ML
Opalinus Clay (OPA)	OPA/OPAM
Sandy-Argillaceous Dogger (SAD) & Sandy-Calcareous Dogger (SCD) of Passwang Formation	DOGG
«Herrenwis Unit»: in the eastern part (Stadel-3-1 and Bülach-1-1 boreholes) Calcareous Dogger (NLE-CD), towards the west (Stadel-2-1 and Weiach boreholes) the NLE-CD is neighboured by the stratigraphic unit Calcareous Dogger (NLW-CD)	HERRE/HERRW
Argillaceous Dogger (AD)	AD
Marly Malm (NL-MM1)	MM1
Calcareous Malm (NL-CM – Gerstenhübel Beds)	CM
Marly Malm (NL-MM2)	MM2
Malm	MALM
Tertiary (TERT) / Quarternary (QUAT)	TERT
Top Boundary (TOP-BC)	TOPBC

Tab. A-3: Porosity of stratigraphic units respectively formations and their representation in the PA

Unit	Porosity n						PA material code	Thickness for averaging
	NL (East and West)			PA modelling				
	Min. [-]	**Best** [-]	**Max.** [-]	**Min.** [-]	**Best** [-]	**Max.** [-]		[m]
CM (Malm aquifer)	-	-	-	-	0.09	-	MALM	-
MM2	0.031	0.063	0.109	0.031	0.063	0.109	MM2	25.30
NL-CM	0.024	0.030	0.043	0.024	0.030	0.043	CM	4.79
MM1	0.044	0.074	0.104	0.044	0.074	0.104	MM1	42.61
AD	0.084	0.120	0.154	0.084	0.120	0.154	AD	5.67
E/W-CD («Herrenwis Unit»)	0.012/ 0.021	0.026/ 0.043	0.085/ 0.067	0.012/ 0.021	0.026/ 0.043	0.085/ 0.067	HERRE/ HERRW	40.33
NL-ARD	0.117	0.130	0.147	0.071	0.123	0.165	DOGG	-
SCD	-	-	-					28
SAD	0.071	0.123	0.165					12
OPA	0.078	0.115	0.136	0.078	0.115	0.136	OPA	108.56
ML	0.037	0.075	0.161	0.037	0.075	0.161	ML	13.68
AL	0.071	0.083	0.096	0.071	0.083	0.096	AL	11.80
CL	0.028	0.054	0.141	0.072	0.108	0.166	KEUK	2.70
AK3 and JO-AK2/3	0.078	0.115	0.169					19.70
NL-DK2	0.041	0.082	0.106	0.047	0.087	0.116	KAU	6.40
AK2	0.068	0.103	0.150					1.90
NL-DK1	0.020	0.079	0.127	0.077	0.121	0.182	KAL	1.80
AK1	0.095	0.134	0.199					5.87
SK	0.116	0.144	0.170					
AAK	0.038	0.091	0.149	0.038	0.091	0.149	GIPSK	67.73
MAK	0.009	0.009	0.024	0.009	0.017	0.052	MAK	4.10
DAK	0.008	0.026	0.086					3.40
DM	-	-	-	-	0.120	-	MUSCH	-

Tab. A-4: Hydraulic conductivity of stratigraphic units respectively formations and their representation in PA

Unit	Horizontal hydraulic conductivity K_h							Estimated K_h/K_v
	NL (East and West)			PA modelling			PA material code	
	Min. [m/s]	**Best** [m/s]	**Max.** [m/s]	**Min.** [m/s]	**Best** [m/s]	**Max.** [m/s]		[-]
CM (Malm aquifer)	1.E-10	1.E-09	1.E-07	1.E-10	1.E-09	1.E-07	MALM	1
MM2	1.E-14	1.E-12	5.E-10	1.E-14	1.E-12	5.E-10	MM2	1 to 10
NL-CM	1.E-14	1.E-12	1.E-08	1.E-14	1.E-12	1.E-08	CM	1
MM1	1.E-14	1.E-12	5.E-10	1.E-14	1.E-12	5.E-10	MM1	1 to 10
AD	1.E-14	1.E-13	1.E-11	1.E-14	1.E-13	1.E-11	AD	5 (1 to 10)
E/W-CD («Herrenwis Unit»)	1.E-14	1.E-12	1.E-07	1.E-14	1.E-12	1.E-07	HERRE/ HERRW	1
NL-ARD	1.E-14	1.E-13	1.E-11	1.0E-14	8.5E-14	1.5E-10	DOGG/ SADHB	5 (1 to 10)
SCD	1.E-14	5.E-14	5.E-10					1
SAD	1.E-14	1.E-13	1.E-12					5 (1 to 10)
OPA	1.E-14	5.E-14	5.E-13	1.E-14	5.E-14	5.E-13	OPA	5 (1 to 10)
ML	1.E-14	5.E-14	5.E-13	1.E-14	5.E-14	5.E-13	ML	1
AL	1.E-14	1.E-13	1.E-12	1.E-14	1.E-13	1.E-12	AL	5 (1 to 10)
CL	1.E-14	1.E-12	5.E-10	1.0E-14	2.1E-13	6.9E-11	KEUK	1
AK3 and JO-AK2/3	1.E-14	1.E-13	1.E-11					5 (1 to 10)
NL-DK2	1.E-14	1.E-12	5.E-10	1.0E-14	7.9E-13	3.9E-10	KAU	1
AK2	1.E-14	1.E-13	1.E-11					5 (1 to 10)
NL-DK1	1.E-14	1.E-12	5.E-10	1.0E-14	1.0E-12	8.8E-10	KAL	1
AK1	1.E-14	1.E-12	1.E-09					5 (1 to 10)
SK	1.E-09	1.E-07	1.E-05					1
AAK	1.E-14	1.E-13	1.E-11	1.0E-14	1.0E-13	1.0E-11	GIPSK	1
MAK							MAK	
DAK								
DM	1.E-08	5.E-07	1.E-06	1.0E-08	5.E-07	1.E-06	MUSCH	1

Tab. A-5: Effective diffusion coefficient for Iodine of stratigraphic units respectively formations and their representation in the PA

Effective diffusion coefficient D_{eff} (Iodine)							
Unit	**NL (East and West)**			**PA modelling**			**PA material code**
	Min. [m^2/s]	**Best** [m^2/s]	**Max.** [m^2/s]	**Min.** [m^2/s]	**Best** [m^2/s]	**Max.** [m^2/s]	
CM (Malm aquifer)	-	-	-	-	-	-	MALM
MM2	1.81E-12	6.05E-12	1.59E-11	1.81E-12	6.05E-12	1.59E-11	MM2
NL-CM	1.24E-12	4.72E-12	1.33E-11	1.24E-12	4.72E-12	1.33E-11	CM
MM1	1.96E-12	6.15E-12	1.58E-11	1.96E-12	6.15E-12	1.58E-11	MM1
AD	1.58E-12	3.66E-12	8.27E-12	1.58E-12	3.66E-12	8.27E-12	AD
E/W-CD («Herrenwis Unit»)	9.00E-13/ 1.53E-12	3.40E-12/ 5.57E-12	9.76E-12/ 1.52E-11	9.00E-13/ 1.53E-12	3.40E-12/ 5.57E-12	9.76E-12/ 1.52E-11	HERRE/ HERRW
NL-ARD	1.43E-12	3.14E-12	6.93E-12	1.43E-12	3.35E-12	7.25E-12	DOGG
SCD	1.86E-12	6.47E-12	1.72E-11				
SAD	1.43E-12	3.35E-12	7.25E-12				
OPA	1.22E-12	2.65E-12	5.48E-12	1.22E-12	2.65E-12	5.48E-12	OPA
ML	1.96E-12	5.76E-12	1.45E-11	1.96E-12	5.76E-12	1.45E-11	ML
AL	1.80E-12	4.28E-12	1.05E-11	1.80E-12	4.28E-12	1.05E-11	AL
CL	1.66E-12	5.02E-12	1.24E-11	1.54E-12	3.87E-12	8.59E-12	KEUK
AK3 and JO-AK2/3	1.53E-12	3.72E-12	8.16E-12				
NL-DK2	1.46E-12	5.20E-12	1.42E-11	1.56E-12	5.32E-12	1.42E-11	KAU
AK2	1.81E-12	5.61E-12	1.44E-11				
NL-DK1	1.05E-12	3.85E-12	1.08E-11	1.23E-12	2.97E-12	6.51E-12	KAL
AK1	1.12E-12	2.45E-12	5.10E-12				
SK	1.97E-12	5.36E-12	1.34E-11				
AAK	1.63E-12	5.17E-12	1.35E-11	1.63E-12	5.17E-12	1.35E-11	GIPSK
MAK	3.48E-13	1.33E-12	3.94E-12	3.48E-13	1.33E-12	3.94E-12	MAK
DAK	4.84E-13	1.83E-12	5.37E-12				
DM	-	-	-	-	-	-	MUSCH

Tab. A-6: Additional parameters assigned to formations considered in the PA models

Material	**P_0** [Pa]	**C_p** [1/Pa]	**λ** [W/m K]	**ρ_s** [g/cm^3]
TERT	1.45E05	1.67E-09	4.27	2,700
MALM	1.52E05	1.67E-09	2.74	2,700
MM2	1.08E07	2.38E-09	2.74	2,707
CM	4.81E06	5.00E-09	2.74	2,706
MM1	1.08E07	2.03E-09	2.74	2,708
AD	3.40E07	1.25E-09	2.74	2,708
HERRE/HERRW	4.81E06	5.77E-09/ 3.49E-09	2.74	2,704/ 2,715
DOGG	3.08E07	1.22E-09	2.53	2,715
OPA	4.81E07	2.10E-09	wet: 2.10 dry: 1.40	2,700
ML	2.15E07	2.00E-09	1.98	2,689
AL	3.40E07	1.81E-09	1.98	2,684
KEUK	3.19E07	1.39E-09	1.98	2,774
KAU	1.68E07	1.73E-09	1.98	2,799
KAL	1.52E04	1.24E-09	1.98	2,810
GIPSK	1.52E07	1.65E-09	1.98	2,808
MAK	1.52E07	9.00E-09	6.26	2,920
MUSCH	6.81E03	1.25E-09	6.26	2,700
PERM	1.45E06	1.25E-09	2.58	2,700

Additional parameters (same value for all formations):

- specific heat capacity (J/kg K): 995.0
- thermal expansion coefficient (1/K): 1.70E-05
- residual water saturation in water retention curve (-): 0.01
- residual water saturation in relative permeability (-): 0.50
- residual gas saturation (-): 0.0
- van Genuchten shape parameter n (-): 1.67

App. B Repository components – complementary information

B.1 Provisional design of the L/ILW emplacement cavern

According to the provisional design, the L/ILW caverns (Fig. B-1) will reach about 230 – 250 m in length, ca. 11.5 m in width and ca. 12.5 m in height and will be supported by two shells. The outer shell comprises various shotcrete layers for rock support and gliding arches which take up the convergence. After the intial convergence has ceased, a massive inner-shell tunnel support made of in-situ concrete will be installed, which serves to take up the mechanical stresses during the operational phase (NAB 23-01 Bd. 6, Nagra 2023b).

The L/ILW to be disposed of in the L/ILW emplacement caverns is low in radiotoxicity but heterogeneous in its composition as a result of its numerous sources (e.g., operation and decommissioning of nuclear power plants, research, industry and medicine). The major materials that comprise the waste and waste packages are hardened cement paste, aggregates, metallic components and organic substances. Operational waste will be disposed of in waste packages and is mostly embedded in cementitious material. The waste packages are placed into a concrete disposal container and the void space will be filled with cementitious material. Metallic decommissioning waste, such as activated metal pieces or activated concrete blocks, are directly disposed of into the disposal container and filled with a flowable cementitious suspension. Disposal containers will be stacked into the L/ILW emplacement cavern and the void space filled with a backfill mortar according to the provisional design.

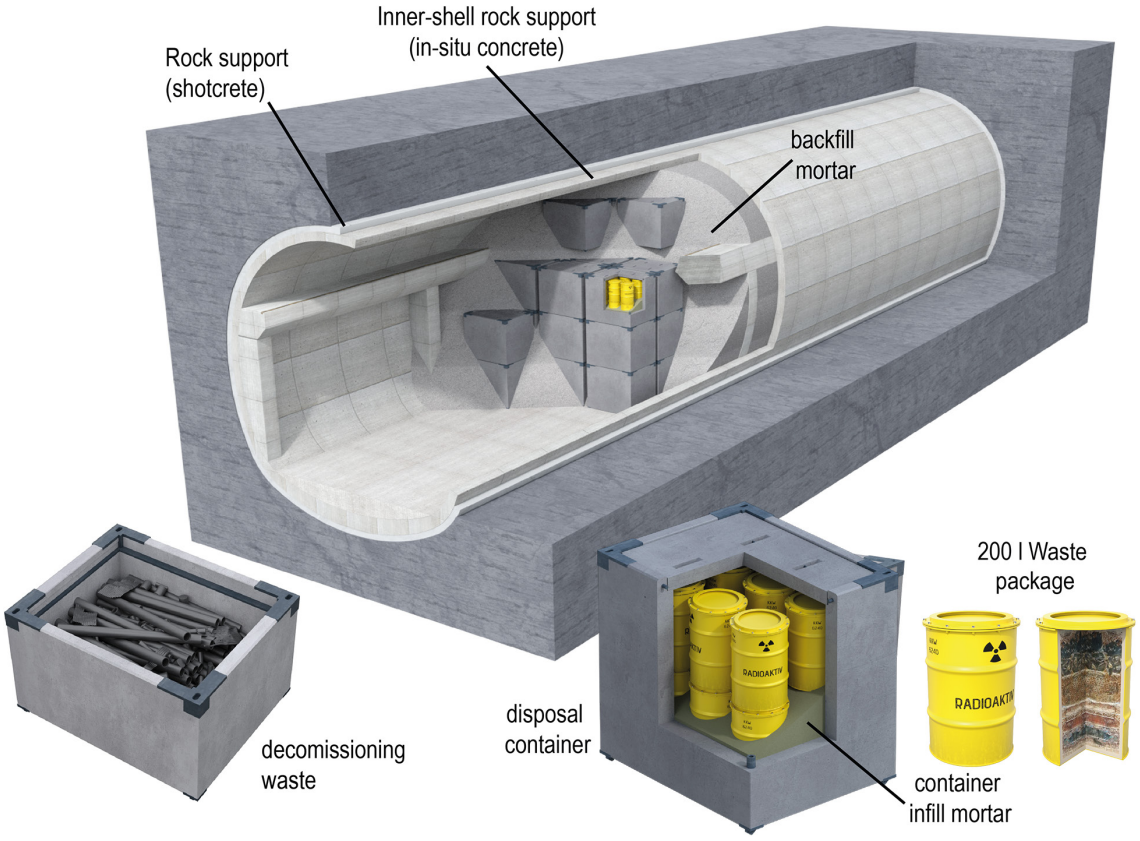

Fig. B-1: Illustration of the provisional design of an L/ILW emplacement cavern and its components

Containers and container infill materials have to fulfill various requirements related to post-closure safety, handling, interim storage, operational safety, costs, retrievability and regulatory measures (ENSI Guideline B05, ENSI 2018a). Despite no credit in safety assessment is taken for the integrity of the waste packages, by design, the concrete container is massively reinforced and is constructed of high-quality concrete. For transport of these container on the road, they had to been approved as Type A packages, conforming to the European Agreement concerning the International Carriage of Dangerous Goods by Road (ADR) and, thus, selected container had to pass drop tests (cf. NTB 21-02, Nagra 2021c). This indicates that – despite no credit is taken in post-closure safety assessment – the strongly reinforced container, backfilled with cementitious material which is reducing void space and providing an alkaline chemical near-field to the waste/waste packages within the containers – are expected to mechanically protect the emplaced waste at least for some time and retard the release of radionuclides.

B.2 Extent and hydraulic characteristics of the EDZ-field for PA/SA modelling

The excavation-damaged zone (EDZ) around the backfilled underground structures of a geological repository represents a release path for radionuclides, which needs to be addressed in the assessment of post-closure safety. Additionally, the EDZ may form a highly efficient escape route for corrosion and degradation gases, thus limiting the gas overpressures in the backfilled repository structures. The efficiency of this release path depends not only on the shape and extent of the EDZ, but also on the self-sealing capacity of the host rock formation and the prevailing state conditions, such as in situ stresses and pore pressure. The hydro-mechanical phenomena associated with the formation and temporal evolution of the EDZ are complex, thus precluding a detailed representation of the EDZ in conventional modelling tools for safety assessment. Therefore, simplified EDZ models, able to mimic the safety-relevant functional features of the EDZ in a traceable manner are required.

B.2.1 Fracture network approach for general licence application

A novel numerical approach has been developed in NTB 14-02 Dossier IV (Nagra 2014) with special emphasis on an adequate representation of the hydro-mechanical conditions in the EDZ, covering the full range of hydraulic regimes, from the fracture dominated flow, with localised pore-water flow during early times, to the matrix-dominated distributed flow in the late times. The workflow consists of three main steps carried out sequentially (Fig. B-2). First, a hybrid finite-discrete element method (FDEM; Lisjak et al. 2015) is used to simulate the geometry and geomechanical conditions of the discrete fracture networks forming the EDZ (Fig. B-2a). The FDEM simulations are purely mechanical and mimic the excavation and emplacement processes only. Second, the geometric properties simulated by the FDEM are mapped onto a finite element mesh (Fig. B-2b), which allows to solve the fluid motion equations in the excavation near-field. A salient feature of the suggested approach is that hydraulic parameters of both fracture and matrix evolve over time as a response to re-saturation of the tunnel surroundings. Finally, an abstraction of the complex model is made based on the late time behaviour (after full re-saturation) of the system (Fig. B-2c). The main outputs of the model are the spatio-temporal distributions of hydraulic parameters and the corresponding specific fluxes towards the tunnel, with special emphasis on the late time behaviour. Finally, the abstraction of the EDZ is implemented by defining a piece-wise homogeneous “shell-like” model with hydraulic behaviour identical to that of the complex model.

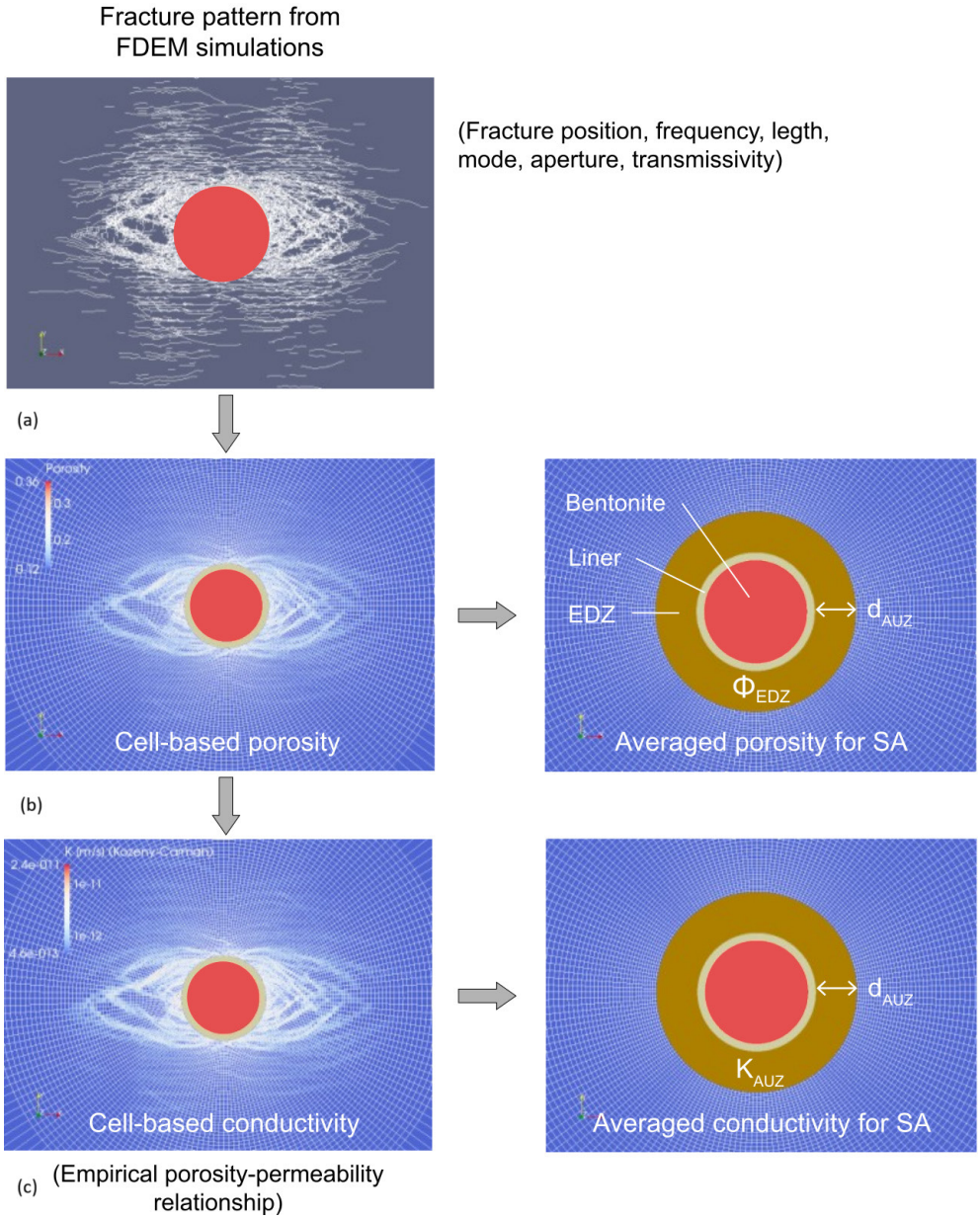

Fig. B-2: Concept of the EDZ abstraction procedure for safety assessment (SA) applicable for a circular tunnel

After NTB 14-02 Dossier IV (Nagra 2014). (a) representative fracture patterns are simulated for relevant repository configurations with a discrete element model (FDEM); (b) the discrete fracture patterns are converted in heterogeneous porosity and hydraulic conductivity distributions; (c) in a final abstraction process, the heterogeneous porosity and conductivity distributions are converted into a shell defined by a radius and homogeneous porosity and conductivity.

Based on empirical and experimental evidence, the hydraulic significance of the EDZ during tunnel construction and its evolution during the operational phase and after backfilling of the underground structures was formulated in NTB 14-02 Dossier IV (Nagra 2014) in terms of a heuristic EDZ closure model. The creation of the EDZ is a brittle process, i.e., the increase of the void volume in the damaged rock zone around the excavation is solely attributed to fracture

opening, whereas the porosity of nonfractured rock remains essentially unchanged during the early times after excavation. The initial transmissivity of the EDZ fractures is controlled by the fracture aperture and can be very high. The matrix conductivity remains essentially unchanged, i.e., it is the same as the conductivity of the intact rock. With time, pore-water uptake from the non-fractured rock zones is associated with swelling and consequently with an increase of matrix porosity. This porosity increase occurs at the expense of a decrease of fracture aperture (and correspondingly, of fracture transmissivity), i.e., fractures start to close and fracture transmissivity reduces drastically, whereas the hydraulic conductivity of the non-fractured matrix zones increases slightly as a consequence of the porosity increase. This process continues until the equilibrium of effective stresses is reached. This is essentially the case, when pore pressure reaches the static formation pressure.

It is assumed that complete disaggregation of the Opalinus Clay has been reached in the equilibrium state, associated with swelling pressures that correspond to the swelling pressure of normally consolidated Opalinus Clay. Comprehensive laboratory tests were conducted on remoulded Opalinus Clay, aimed at determining hydraulic conductivity of the rock matrix under a wide range of effective stresses and the corresponding porosities in the normally consolidated state. Fig. B-3 presents a compilation of hydraulic conductivity measurements on remoulded and recompacted Opalinus Clay from different sites. The following power law relationship is derived, representing the dependency of hydraulic conductivity on porosity for the Opalinus Clay samples from the deep investigation boreholes in Northern Switzerland:

$$K\left[\frac{m}{s}\right] = 1 \cdot 10^{-15} \cdot exp^{27.37 \cdot \emptyset[-]}$$

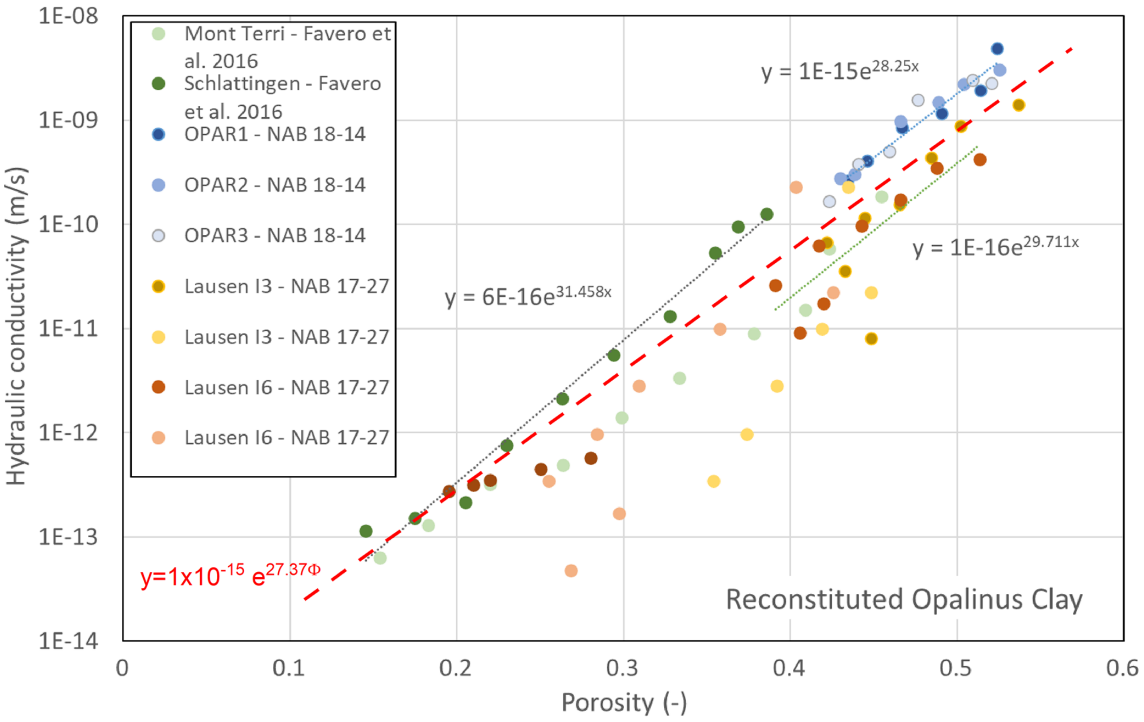

Fig. B-3: Hydraulic conductivity measurements on remoulded and recompacted Opalinus Clay samples from various locations in Northern Switzerland

After NTB 24-17, NAB 19-06 (Nagra 2024k, Seiphoori 2019) and Marschall et al. (2024).

B.2.2 Simulation of fracture network patterns

Fracture network simulations on the EDZ formation for L/ILW and HLW emplacement rooms and the operations shaft were carried out for repository for HLW and L/ILW at the Haberstal site. The modelling activities refer to previous workflows which are documented in NAB 18-12 (Geomechanica Inc., Toronto 2018). The general procedure for modelling excavation advance and support installation in FDEM consisted of two main steps, graphically summarised in Fig. B-4.

The EDZ was simulated for 6 cases of the HLW / L-ILW emplacement rooms and for the shaft, with varying horizontal in-situ stress, rock strength, core softening ratio, and core softening scheme. For each HLW model, the core softening ratio was adjusted such that the maximum deformation at one of the four monitoring points converges approximately 6.1 cm before the liner is installed. For all models, an initial pore pressure of 9 MPa is applied to the rock mass, with the liner being prescribed zero pore pressure (see Tab. B-1).

Tab. B-1: Summary of HLW emplacement drift simulations performed in this study

Case	Total horizontal stress, σ_h [MPa]	Initial effective horizontal stress, $\sigma_{h'}$ [MPa]	Rock strength properties	Core softening scheme	Core softening ratio, α_s
1	17.5	8.5	Lower limit	Anisotropic	0.0025
2	17.5	8.5	Upper	Anisotropic	0.0010
3	22.5	13.5	Lower	Anisotropic	0.0020
4	22.5	13.5	Upper	Anisotropic	0.0015
5	29.25	20.25	Lower	Anisotropic	0.0040
6	29.25	20.25	Upper	Anisotropic	0.0030

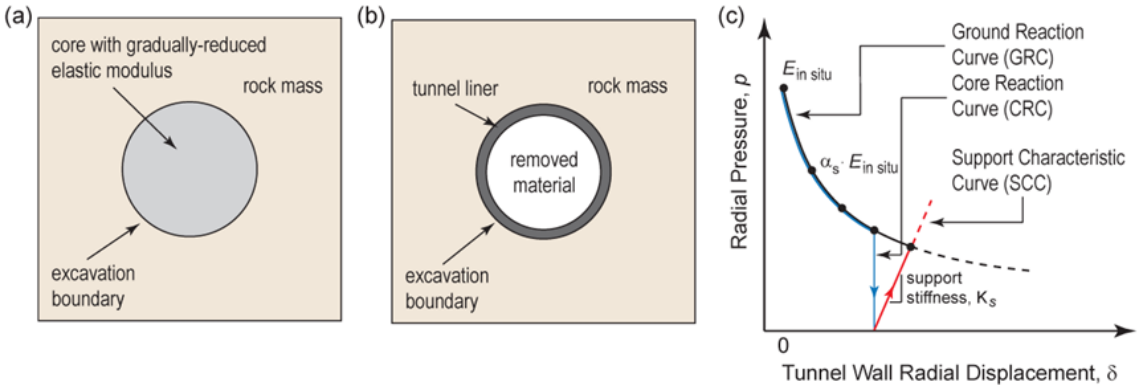

Fig. B-4: Modelling procedure for excavation advance and support installation using the core replacement technique

(a) Replacement of core with reduced elastic modulus material. (b) Installation of tunnel lining. (c) Qualitative example of ground reaction curve simulated by modulus reduction and support characteristic curve for a linear elastic lining.

Exemplarily, the simulated aperture and slip of the fractures for the two simulation cases are shown in Fig. B-5. As observed in the plot, the region near the excavation boundary has the greatest aperture and slip. Regions of significant shear displacement are bedding parallel fractures above/below the crown/floor and conjugate shear fractures in the sidewalls.

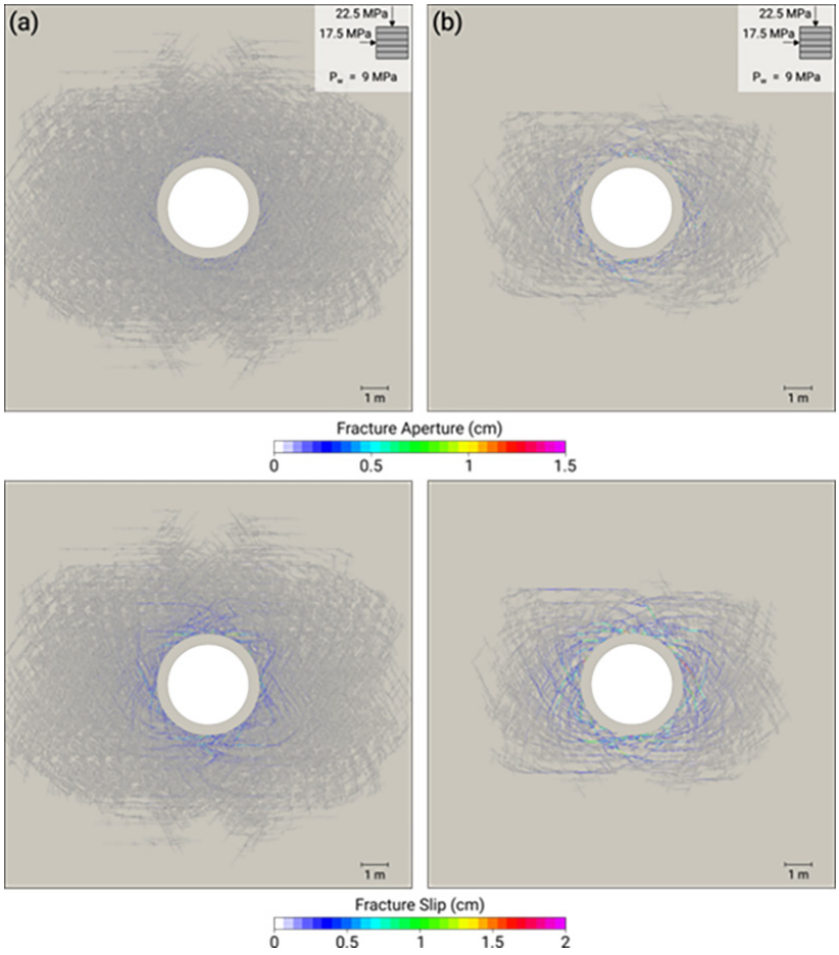

Fig. B-5: Fracture aperture (top) and slip (bottom) contours for HLW tunnel models with minimum horizontal in-situ stress (σ_h = 17.5 MPa) for (a) lower bound and (b) upper bound strength calibrations

B.2.3 Calculation of effective hydraulic EDZ properties (late time properties)

The outputs of the fracture pattern simulations were analysed with the numerical approach in NAB 18-07 (Wigger et al. 2017). Here we focus on the derivation of the late time hydraulic conductivities. For this cell-based porosity values $\Phi(r,\varphi)$ were calculated by box counting the fracture apertures. Radial porosity profiles $\Phi(r)$ were derived by summing up the cell porosities for a given radial distance. In a second step, the porosity profiles were used to calculate the corresponding hydraulic conductivity profile with the power law function given in Fig. B-3.

In a final abstraction process, the radial porosity and radial conductivity profiles were converted into a shell defined by a radius and equivalent homogeneous porosity and conductivity (Fig. B-6).

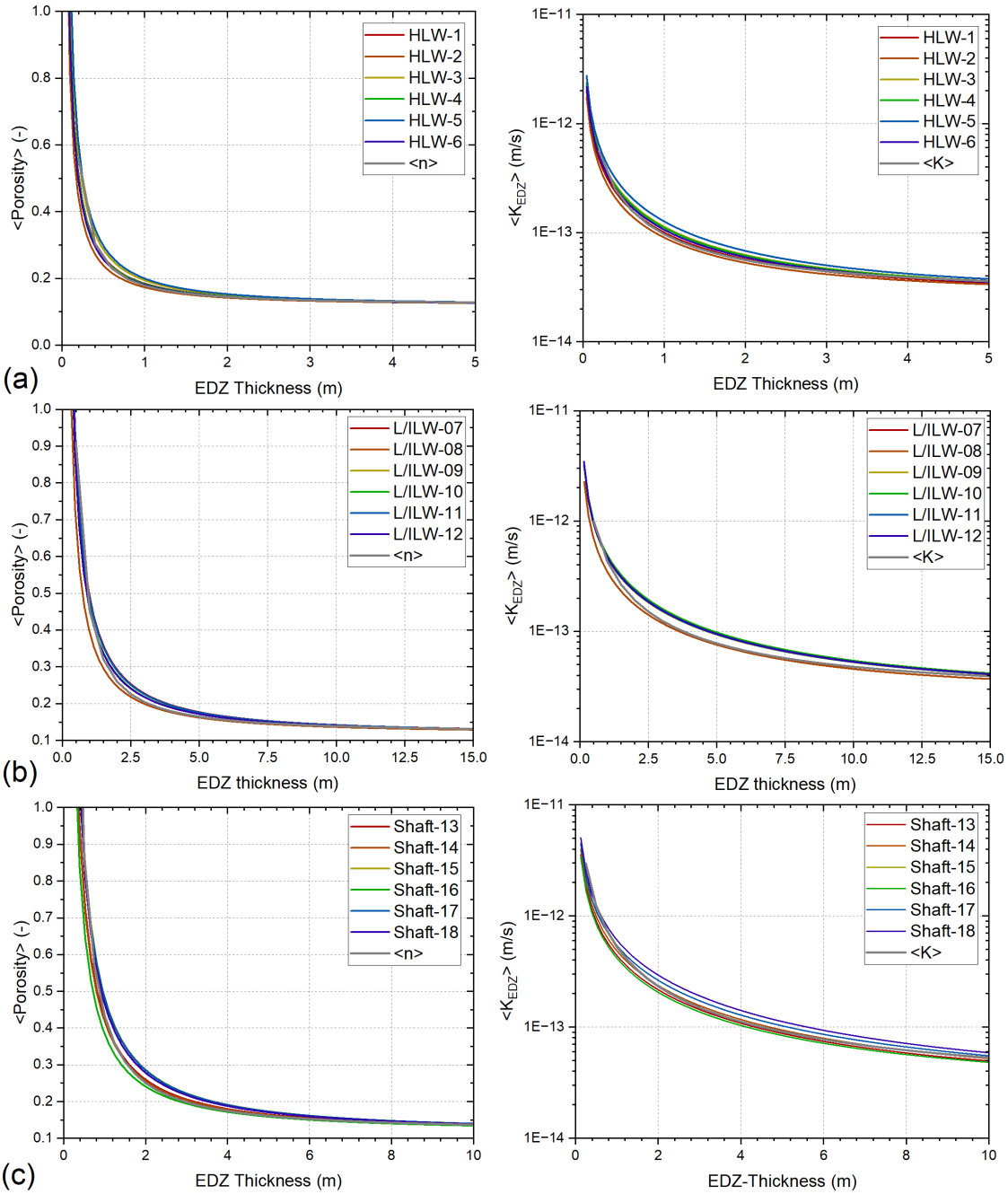

Fig. B-6: Radial profiles of equivalent porosity and equivalent hydraulic conductivity derived from the corresponding radial profiles

HLW emplacement drifts (top), L/ILW emplacement caverns (middle) and shaft (bottom).

App. C Performance indicators for quantitative assessment of the multi-barrier system

C.1 Tracer Flux TF

Tracer flux TF of a conservative tracer, dissolved in the porewater and released from the repository field into the regional aquifer systems is the performance indicator for the model-supported assessment of the IMS safety function ("immobilisation, retention and slow release of radionuclides"). The indicator is indicative for dose-relevant, non-sorbing radionuclides such as ^{129}I released from the HLW emplacement drifts or ^{36}Cl from the L/ILW emplacement caverns. Further performance indicators of interest are tracer fluxes of gaseous tracers (indicative for the volatile radionuclide ^{14}C), released from the L/ILW repository through the host rock and along the sealed and backfilled repository structures.

In the PA indicator workflow all model-based analyses are carried out with the TH-code family TOUGH3 (Jung et al. 2018). Parametric uncertainty of input parameters is assessed in a probabilistic framework with Monte Carlo simulations. This calls for model set-ups of moderate size (typically 2-D models or so-called 2.5-D models) and simplified representations of the complex THM processes in the repository near-field to limit computational efforts. Model set-ups, boundary conditions and source terms required for the indicator-based assessment of barrier performance are described in the following paragraphs. Performance indicators, performance indices and performance targets are defined and the corresponding evaluation tables are discussed.

Tracer flux $TF_{CRZ,I-129}$

Tracer flux $TF_{CRZ,I-129}$ is the performance indicator for the evaluation of the CRZ for the HLW repository. Tracer flux is calculated with a 2-D transport model (TOUGH3/EOS 1), representing a vertical cross-section through the centre of the HLW repository in Nördlich Lägern and comprising the entire Mesozoic layer stack (Fig. C-1).

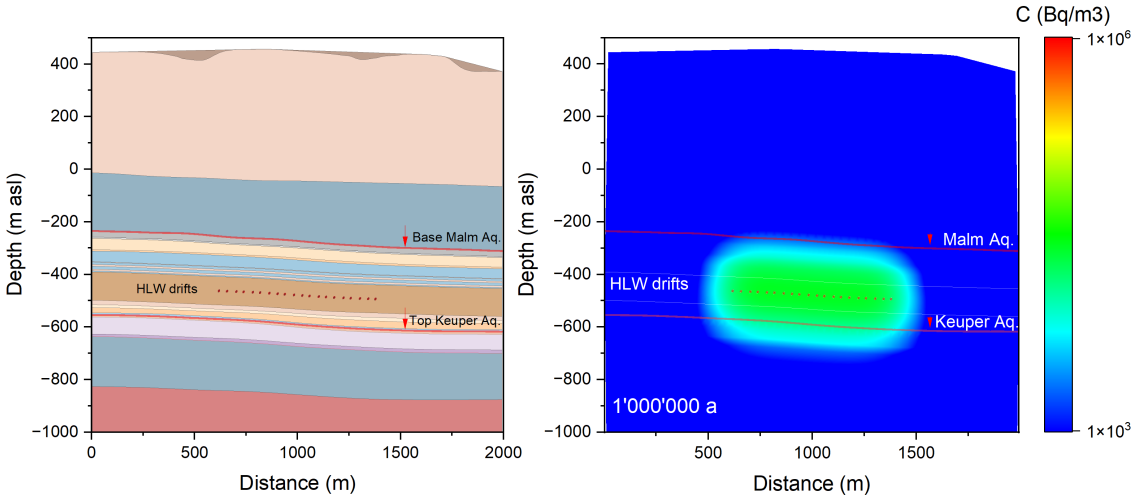

Fig. C-1: Model set-up for the derivation of the HLW performance indicator $TF_{CRZ,I-129}$

Left: vertical cross-section through the centre of the HLW repository in Nördlich Lägern, comprising the entire Mesozoic layer stack. Right: simulation of tracer transport from the repository structures towards the top and base of the CRZ.

A conservative tracer is released from the HLW canisters in the emplacement drifts into the bentonite buffer, assuming fully saturated conditions in the HLW near-field and the surrounding host rock (Fig. C-1 right). Transport of the tracer from the repository structures towards the top and bottom of the CRZ (base Malm aquifer, top Keuper aquifer) is controlled by diffusion and advection. Further details about the model set-up and the implementation of the source term in the 2-D HLW repository model are given in NAB 24-25 (Nagra 2024m).

After canister failure when water gets in contact with the spent fuel cladding and pellets only few percent of the total radionuclide inventory are instantaneously released ("Instantaneous Release Fraction" – IRF). The rest of the inventory, termed as "congruent release" – CR, dissolves at low rates in the porewater, which seeps slowly into the canister. The IRF of ^{129}I, representing a dose relevant radionuclide with long half-live time and low sorption capacity on the mineral phases of the bentonite buffer comprises less than 10% of the entire ^{129}I inventory. Fig. C-2 (left) displays the ^{129}I source term (^{129}I released from the HLW near-field into the host rock) as used in safety analysis (NTB 24-18, Nagra 2024r), expressed both, in terms of released activity [Bq/yr] and as cumulated activity [Bq]. The total initial activity is ≈ 4.4 × 10^{12} Bq, of which 2.7 × 10^{11} Bq are released instantaneously (corresponding to 6.5% of the total initial activity). The rest of the ^{129}I inventory, termed as "congruent release", dissolves at low rates (2 × 10^{5} – 2 × 10^{6} Bq/a) over a time period which spans many times more than the period for assessment.

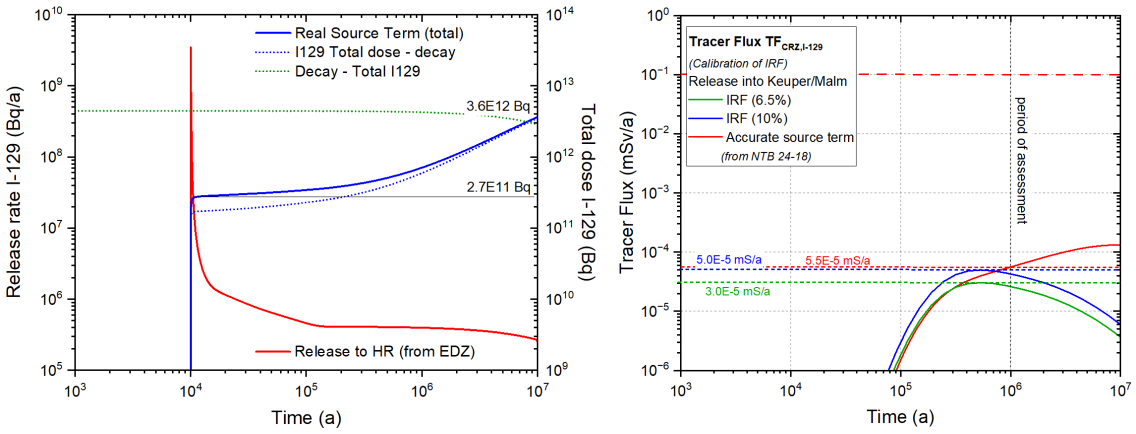

Fig. C-2: Calibration of source terms for indicator-based PA (HLW repository – ^{129}I)

Left: accurate source term ^{129}I as used in the context of the radiological consequence analysis (NTB 24-18, Nagra 2024r). Source term (^{129}I released from the HLW near-field into the intact host rock) expressed in terms of released activity [Bq/y] (red curve) and as cumulated activity [Bq] (blue curve). The green curve displays the decay of the total initial activity of 4.4 × 10^{12} Bq) over a period of 10 mio years. Right: deterministic simulations of tracer flux representing the three cases: (I) instantaneous release of 6.5% of total ^{129}I inventory (green); (II) instantaneous release of 10% of total ^{129}I inventory (blue); (III) accurate source term according to NTB 24-18 (Nagra 2024r) (red).

For simplicity, the indicator-based PA calculations assume a pulse-like tracer release ("instantaneous release") from the HLW near-field, while the more precise source term used in the radiological consequence analysis consists of an IRF and a CR component. Simulations of tracer flux towards the regional aquifer systems at the top and bottom of the CRZ over a period of 10 million years are shown in Fig. C-2 (right). The graph shows a steadily increasing tracer flux for the accurate source term (red line), while the pulse-like source terms with a IRF of 6.5% (green line) and 10% (blue line) exhibit a tracer peak after several 100,0000 years, followed by a monotonous

decrease. To make the results obtained with the simplified pulse-like source term comparable to those obtained with the accurate source term, the following simple calibration scheme was adopted. For this, the tracer flux which corresponds to the accurate source term is extracted after 1 million years (i.e., at the end of the period of assessment) and compared to the peak tracer fluxes which correspond to the pulse-like source terms. The peak tracer flux which corresponds to the IRF of 10% matches well, while the IRF of 6.5% leads to a lower peak flux (see Fig. C-2 right). It was therefore decided to perform the PA calculations with the performance indicator $TF_{CRZ,\ I\text{-}129}$ using an IRF of 10%.

In this context, it should be noted that the tracer flux $TF_{CRZ,\ I\text{-}129}$ is a simple indicator of barrier performance rather than a precise estimator of dose rates. Reliable estimates of dose rates are obtained in NTB 24-18 (Nagra 2024r), which takes into account the entire radionuclide inventory of the repository and represents the time dependent source terms in a more sophisticated manner. Simple benchmarks were carried out, aimed at comparing the results of the PA- and SA-models. Differences of tracer fluxes up to a factor of two were observed, which can be attributed to the differences in model set-ups and the implemented phenomena and processes (1-D / 2-D layer stack; implementation of HLW drifts; isothermal / non-isothermal)

The tracer flux $TF_{CRZ,\ I\text{-}129}$ is calculated as follows: first, the 2-D model simulates tracer transport from the HLW drifts towards the regional aquifer systems, accounting only for the IRF, which is 10% of the entire ^{129}I inventory. Transients of the lateral profiles of tracer flux $F(y,z_{top/base\ CRZ},t)$ in [Bq/(a·m)] at top / base CRZ are extracted from the model. The total tracer flux $TF_{CRZ,\ I\text{-}129}$ released from the CRZ into the aquifer systems is calculated by spatial integration of the tracer profiles $F(y,z_{top\ CRZ},t)$ and $F(y,z_{base\ CRZ},t)$ along the lateral extent w of the model and multiplication with the decay factor:

$$TF_{CRZ,I-129}(t) = \left[\int_0^w \left(F\left(y, z_{top\ CRZ}, t\right) + F\left(y, z_{base\ CRZ}, t\right)\right) dy\right] \cdot e^{-\lambda \cdot t} \qquad \text{(C-1)}$$

in [Bq/a], where λ represents the decay time of ^{129}I ($\lambda_{I\text{-}129} = 4.41 \times 10^{-8}\ a^{-1}$). The dimensionless performance indicator $NTF_{CRZ,I\text{-}129}$ is derived by conversion and normalisation of $TF_{CRZ,\ I\text{-}129}$:

$$NTF_{CRZ,I-129}(t) = \frac{TF_{CRZ,I-129}(t)\left[\frac{Bq}{a}\right] \times BDCF\ [\frac{Sv}{Bq}] \times 1000}{0.1[\frac{mSv}{a}]} \qquad \text{(C-2)}$$

where

$$BDCF_{I-129} = 6.32 \cdot 10^{-13}\left[\frac{Sv}{Bq}\right] \qquad \text{(C-3)}$$

represents the biosphere dose conversion factor for the present-day climate and the normalisation factor 0.1 mSv/a corresponds to the regulatory dose limit. Finally, the maximum value of the transient of normalised flux is calculated, representing the performance index $NTF_{CRZ,I\text{-}129}$:

$$NTF_{CRZ,I-129} = \left\{NTF_{CRZ,I-129}(t)\right\}_{max} \qquad \text{(C-4)}$$

Probabilistic simulations of the performance indicator $TF_{CRZ,I\text{-}129}(t)$ are an essential element in the PA workflow, aimed at quantifying parametric and conceptual uncertainties associated with the performance of the CRZ as a transport barrier. Fig. C-3 (left) displays a typical example of Monte

Carlo simulations of tracer flux $TF_{CRZ,I\text{-}129}$ in response to the IRF (representing 10% of the total initial activity of ^{129}I). The maximum value of the normalised tracer flux represents the performance index $NTF_{CRZ,I\text{-}129}$. Fig. C-3 (right) exhibits the histogram, based on 1001 samples of the performance index $NTF_{CRZ,I\text{-}129}$, representing the base case and 100 probabilistic realisations of the input parameters corresponding the the PA-Scenario *EXPERF* (see Section 6.2.4).

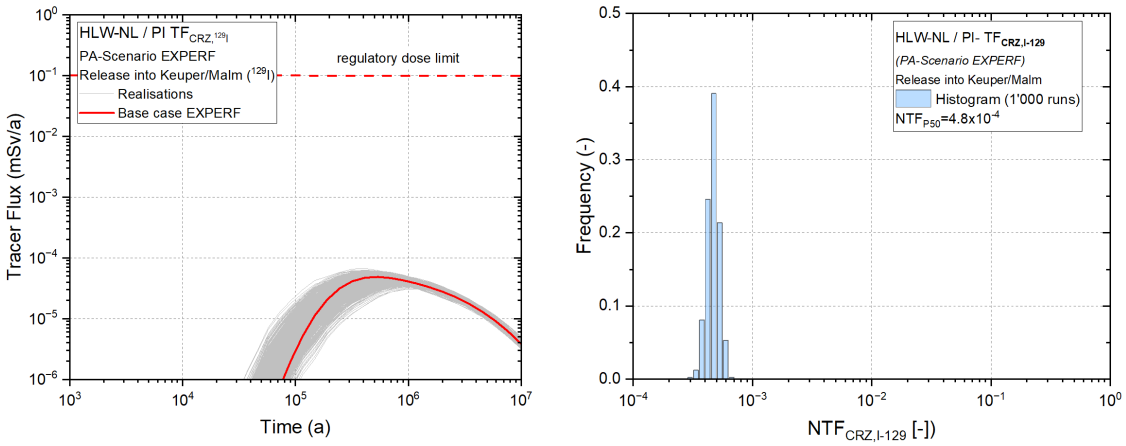

Fig. C-3: Evaluation of the dimensionless performance index $NTF_{CRZ,\ I\text{-}129}$ in a probabilistic workflow

Left: Transients of tracer flux $TF_{CRZ,\ I\text{-}129}$ released from the CRZ into Keuper- and Malm aquifer. Right: histogram of the performance index $NTF_{CRZ,\ I\text{-}129}$, encompassing the reference case and 1,000 realisations of the uncertain input parameters.

The performance index $NTF_{CRZ,\ I\text{-}129}$ is defined in such a way that a value greater than one indicates a CRZ that is deemed unacceptable with respect to the regulatory dose limit. Lower index values imply an increasingly favourable performance of the CRZ. The evaluation scale in Tab. C-1 is adopted for the for assessment of the performance of the CRZ of the HLW repository as a transport barrier using the 95th percentile of the frequency distribution NTF_{P95} (Fig. C-3 right).

Tab. C-1: Evaluation scale for assessing the performance of the CRZ of the HLW repository with the 95th percentile of the dimensionless performance index NTF_{P95}

Unacceptable	$NTF_{P100} \geq 1$
Unfavourable	$1 > NTF_{P95} \geq 0.1$
Less favourable	$0.1 > NTF_{P95} \geq 0.01$
Favourable	$0.01 > NTF_{P95} \geq 0.001$
Very favourable	$NTF_{P95} < 0.001$

Tracer flux $TF_{CRZ,\ Cl\text{-}36}$

^{36}Cl is a dose relevant non-sorbing radionuclide of the L/ILW inventory and tracer flux $TF_{CRZ,\ Cl\text{-}36}$ is the performance indicator for the evaluation of the CRZ of the L/ILW repository. Tracer flux is calculated with a 2-D transport model (TOUGH3/EOS 5), representing a vertical cross-section through the centre of the L/ILW repository in Nördlich Lägern and comprising the entire Mesozoic layer stack (Fig. C-4a).

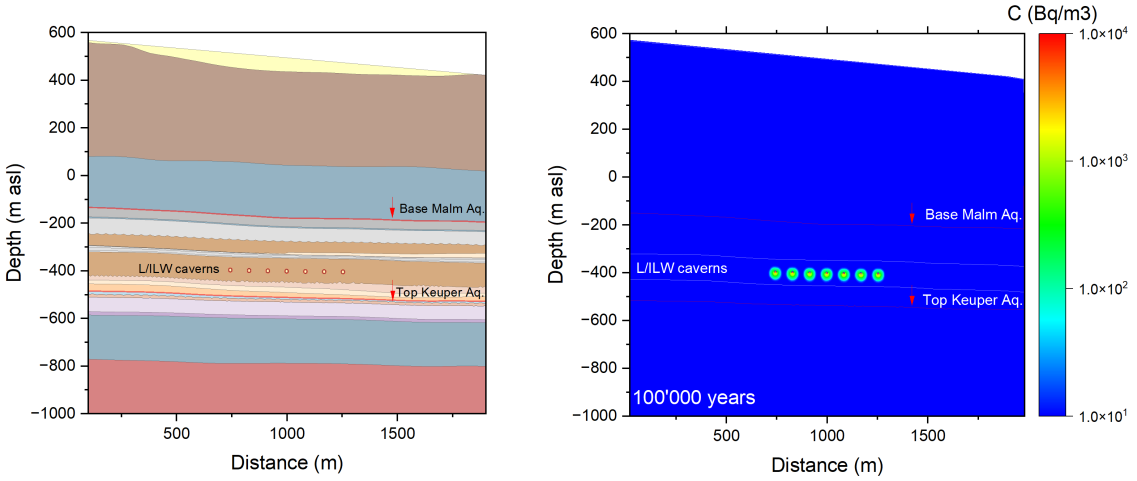

(a) (b)

Fig. C-4: Model set-up for the derivation of the HLW performance indicator $TF_{CRZ,\ Cl\text{-}36}$

(a) Vertical cross-section through the centre of the L/ILW repository in Nördlich Lägern, comprising the entire Mesozoic layer stack; (b) simulation of tracer transport from the repository structures towards the top and base of the CRZ.

A non-sorbing tracer, representing the dose relevant radionuclide ^{36}Cl is released from the L/ILW near-field in the emplacement caverns into the partially saturated cement near-field and the surrounding host rock. Transport of the tracer from the repository structures towards the top and bottom of the CRZ (base Malm aquifer, top Keuper aquifer) is controlled by diffusion and advection in the porewater under the action of gas pressure build-up in the caverns (Fig. C-4b).

After emplacement of the waste in the L/ILW cavern, it is assumed that the radionuclide inventory will be released with time, depending on the local saturation conditions around the conditions. Fig. C-5 shows the time dependent source term for ^{36}Cl as used in the safety assessment (NTB 24-18, Nagra 2024r). The red curve indicates the release rates from the L/ILW nearfield in [Bq/a], while the blue curve shows the cumulated release in [Bq]. The total initial activity of ^{36}Cl is $\approx 9.76 \times 10^{11}$ Bq and the decay time $\lambda_{Cl\text{-}36} = 2.31 \times 10^{-6}\ a^{-1}$. Correspondingly, the calculated activity after 100,000 years is still $\approx 2.90 \times 10^{11}$ Bq as indicated in Fig. C-5 (green line). Further details about the implementation of the source terms in the 2.5-D L/ILW repository model are given in NAB 24-25 (Nagra 2024m).

The normalised performance indicator $NTF_{CRZ,Cl\text{-}36}$ is derived according to equations C-1 and C-2 using the biosphere dose conversion factor for the present-day climate:

$$BDCF_{Cl-36} = 1.65 \cdot 10^{-14} \left[\frac{Sv}{Bq}\right] \qquad \text{(C-5)}$$

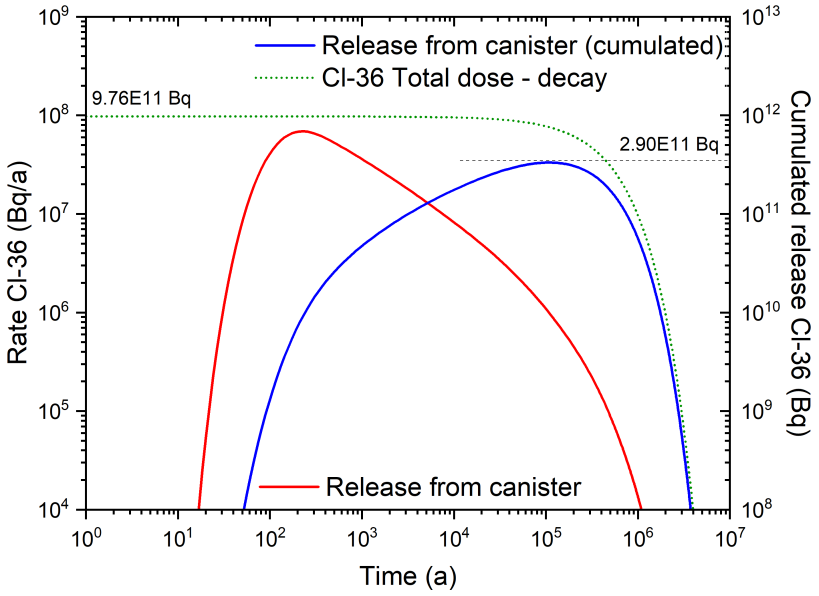

Fig. C-5: Source term for indicator-based PA (L/ILW repository – ^{36}Cl)

The accurate source term ^{36}Cl as used in the context of the radiological consequence analysis (NTB 24-18, Nagra 2024r) exhibits a distinct time dependence. The simplified source term for the probabilistic PA calculations assumes conservatively that the entire inventory of ^{36}Cl is released instantaneously.

The workflow for the probabilistic simulations of the performance indicator $TF_{CRZ,Cl\text{-}36}(t)$ and concept of evaluation scales is the same as for the assessment of the HLW repository (see above).

Tracer flux $TF_{CRZ,\,C\text{-}14}$ and Tracer flux $TF_{V3,\,C\text{-}14}$

After closure of the L/ILW repository the emplacement caverns are unsaturated, and air at atmospheric pressure is the dominating gas species. Hydrogen originating from corrosion of metallic waste, accumulates in the air-filled pore space and replaces the air as the dominant species in the gas phase after several hundred years. ^{14}C originating from degradation of organic waste, in the form of CO_2 or CH_4, represents a minor component. The hydrogen can act as a carrier gas transporting ^{14}C out of the repository system when pressure builds up in the L/ILW emplacement caverns. Possible gas escape routes are discontinuities in the host rock and the backfilled repository structures across the V3 seal. The intact host rock does not represent an efficient release path.

The Monte Carlo simulations of the release of volatile radionuclides (^{14}C) from the L/ILW near-field through the CRZ and along the backfilled repository structures are carried out with a 2.5-D transport model implemented in the two-phase flow simulator TOUGH3/EOS 5. The calculations are time consuming and require a slightly modified indicator workflow compared to the ^{36}Cl simulations. The ^{14}C is not simulated as a separate species but it is assumed that it is homogeneously distributed in the hydrogen. Details about the model set-up and the implementation of the source terms in the 2.5-D L/ILW repository model are given in NAB 24-25 (Nagra 2024m). The derivation of the performance indicators $TF_{CRZ,\,C\text{-}14}$ and $TF_{V3,\,C\text{-}14}$ is briefly summarised in the following paragraphs.

Two-phase flow simulations of the post closure evolution of the L/ILW repository are carried out using the realistic gas source term $GST_{L/ILW}(t)$ in [kg/a] derived from Fig. A-2 and assuming that the entire ^{14}C is released instantaneously (conservative assumption). The initial gas-filled pore volume of the unsaturated L/ILW repository (including the access tunnels, central unit etc.) is estimated at 1.5×10^5 m^3, based on the volumetry of the repository structures (Tab. A-1). The initial total activity $A_{tot}^{C14}(t = 0)$ is 7.1×10^{12} Bq; it decays as shown graphically in Fig. A-4 ($\lambda = 1.21 \times 10^{-4}$ a^{-1}). The gas release into the upper and lower aquifer systems and the release through the V3 seal is extracted from the modelling results as total gas fluxes $GF_{KEU}(t)$ $GF_{Malm}(t)$ and $GF_{V3}(t)$ in [kg/a]. The simulations cover a time period of 1 mio years (period of assessment).

The performance indicator $TF_{CRZ,C\text{-}14}$ is calculated as follows:

$$TF_{CRZ,C14}(t) = \frac{\partial}{\partial t}\frac{\int_0^t GF_{KEU}\cdot dt + \int_0^t GF_{Malm}\cdot dt}{M_{ini} + \int_0^t GST_{L-ILW}(t)\cdot dt} \cdot A_{tot}^{C14}(t) \cdot BDCF_{C14} \quad \text{(C-6)}$$

using the biosphere dose conversion factor for the present-day climate $BDCF_{C\text{-}14} = 3.55 \times 10^{-16}$ Sv/Bq. M_{ini} represents the mass of the gas phase in the initial unsaturated state after repository closure (here we assume $M_{ini} = 1.3 \times 10^4$ kg by converting the initial gas volume into the corresponding mass of hydrogen).

Likewise, the performance indicator $TF_{V3,C\text{-}14}$ is calculated with the total $GF_{V3}(t)$ across the V3 seal in [kg/a]:

$$TF_{V3,C14}(t) = \frac{\partial}{\partial t}\frac{\int_0^t GF_{V3}\cdot dt}{M_{ini} + \int_0^t GST_{L-ILW}(t)\cdot dt} \cdot A_{tot}^{C14}(t) \cdot BDCF_{C14} \quad \text{(C-7)}$$

Fig. C-6 shows an example of the derivation of $TF_{CRZ,C14}$, representing the base case simulation of the *FLTLILW* scenario (see Section 6.3.6). The red curve in Fig. C-6a displays the total mass of gas generated in a single cavern, while the blue curve shows the total mass (per cavern) released into the Malm aquifer (note, there is no gas released into the Keuper). The decay of the total dose of ^{14}C in [mSv/a] in the L/ILW repository is given in Fig. C-6b. Finally, Fig. C-6c presents the calculated tracer flux $TF_{CRZ,C14}$ according to equation (C-6).

The workflow for the probabilistic simulations of the performance indicator $TF_{CRZ,C14}(t)$ and the concept of evaluation scales is the same as for the assessment of the HLW repository (see above).

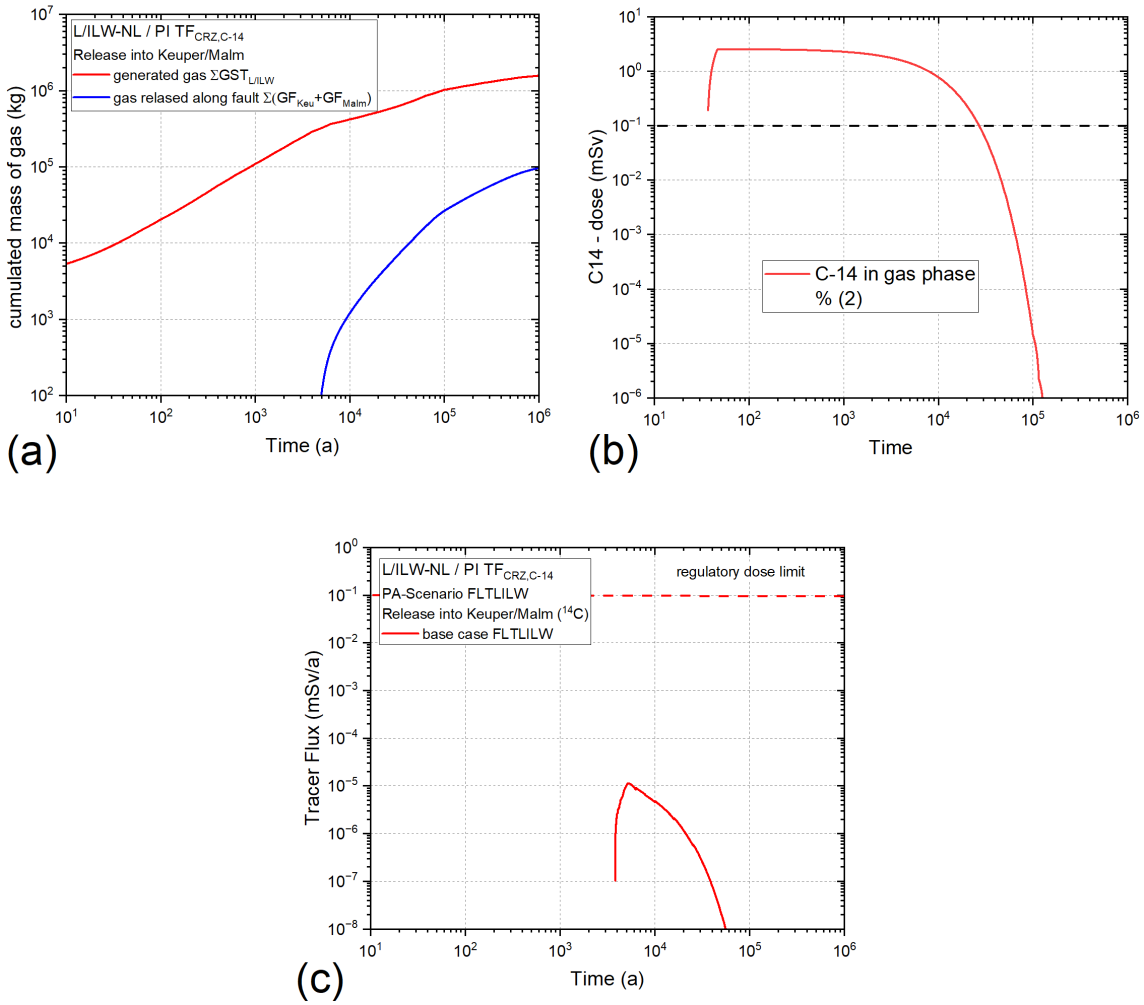

Fig. C-6: Derivation of the performance indicator $TF_{CRZ,C14}$ for indicator-based PA from two-phase flow simulations, representing the base case of the *FLTLILW* scenario

See Section 6.3.6.

(a) cumulated mass of gas generated by corrosion and degradation processes (red curve) and released mass of gas along the vertical fault (blue line); (b) decay curve representing the total ^{14}C inventory in the L/ILW repository; (c) calculated transient of tracer flux $TF_{CRZ,C14}$ for the base case of PA-Scenario *FLTILW*.

C.2 Temperature TB in the HLW near-field

Decay heat from SF and HLW will increase temperatures within and around the repository for long periods of time (see Fig. 4-7). The maximum temperature reached in the bentonite buffer and the surrounding host rock depends on the thermal properties of the buffer which are a function principally of its saturation state and of the ambient (site-specific) rock temperature. At temperatures of 150 °C and above, the swelling pressure of the bentonite buffer is reduced, and the hydraulic conductivity increases. Furthermore, exposure of compacted bentonite to temperatures of 150 °C and above may alter the plastic properties due to cementation effects. In NTB 14-12 (Leupin et al. 2014), the temperature value of 150 °C was specified as a pragmatic performance target for dry bentonite, which ensures that the buffer material does not experience significant HM-C alterations in response to heating.

In the PA indicator workflow, the performance indicator TB is used for evaluating the impact of heat-emitting SF/HLW canisters on the barrier performance of the bentonite buffer, addressing the CMP safety function ("compatibility of the components of the repository system"). The evolution of temperature distribution in the HLW near-field is calculated with a 2-D transport model (TOUGH3/EOS 5), representing a vertical cross-section through the centre of the HLW repository in Nördlich Lägern and comprising the entire Mesozoic layer stack. Temperature transients are calculated at the control point TB in the bentonite buffer at the rim of the canister (5 cm above the canister surface), representing the hottest area in the entire buffer (Fig. C-7). Normalisation of the temperature transients with the performance target for bentonite temperature results in:

$$NBT(t) = \frac{T_B(t)[°C]}{150[°C]} \tag{C-8}$$

Finally, the maximum value of the normalised temperature evolution at the control point T_B is calculated, representing the performance index NBT, which ensures that the buffer material does not experience significant HM-C alterations in response to heating:

$$NBT = \{NBT(t)\}_{max} \tag{C-9}$$

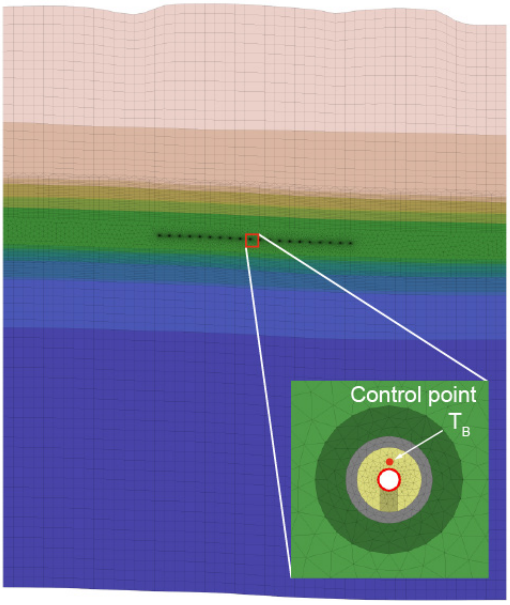

Fig. C-7: Model set-up for the derivation of the HLW performance indicator TB

Temperature is taken at the control point T_B.

The performance index NBT is defined in such a way that a value greater than one indicates that the zone of the bentonite buffer in the immediate vicinity of the SF/HLW canisters may experience significant HM-C alterations in response to heating, entailed by a reduced sorption and radionuclide retention capacity of the buffer. Lower index values imply an increasingly favourable performance of the buffer. The evaluation scale in Tab. C-2 is adopted for the for assessment of the performance of the CRZ of the HLW repository as a transport barrier. The percentiles P75, P95, P99 and P99.9 of the calculated frequency distributions are used to formulate the levels of performance.

Tab. C-2: Evaluation scale for assessing the performance of the HLW near-field with the dimensionless performance index NBT

Unacceptable	$NBT_{P75} \geq 1$
Unfavourable	$NBT_{P95} < 1$
Less favourable	$NBT_{P99} < 1$
Favourable	$NBT_{P99.9} < 1$

C.3 Thermally and gas induced pore pressure perturbations

Pore pressure in the repository nearfield defines three performance indicators for the model-supported assessment of the safety function CMP ("Compatibility of the components of the repository system"). Thermally induced overpressures in the HLW repository nearfield and gas induced overpressures in both, the HLW and L/ILW repository sections could increase the risk of shear failure in the host rock. In PA the pore pressure in the host rock is used as a performance indicator for thermally / gas induced shear failure and the failure potential FPI ("failure potential of the intact rock") is the corresponding performance index. The failure potential associated with thermally induced overpressures, indicated by the acronym FPH, and the gas induced failure potential FPG are derived in the following sections.

C.3.1 Derivation of the performance index FPI (failure potential of the intact rock)

From a long-term safety perspective, it is desirable to avoid shear (or tensile) failure in the host rock due to gas-induced and thermally induced overpressures. The possibility of shear/tensile failure can be assessed using the performance indicator FPI. In case of thermally induced pore-water overpressures the indicator is called FPH, gas-induced overpressures are associated with the indicator FPG.

Assuming the applicability of the Mohr-Coulomb criterion for shear failure, the FPI can be expressed as:

$$FPI = \frac{\tau}{\tau_{max}} = \frac{q}{q_{max}} \tag{C-10}$$

where τ is the shear stress, τ_{max} is the maximum shear stress that can be accommodated by the rock without failure and q, q_{max} are the corresponding deviator stresses. For stress path analyses it is convenient to use the mean effective stress p' and the deviator stress q, which are formulated here as octahedral stresses:

$$q = \sqrt{\frac{(\sigma_H-\sigma_h)^2+(\sigma_H-\sigma_v)^2+(\sigma_h-\sigma_v)^2}{2}} \tag{C-11}$$

$$p' = \frac{\sigma_H+\sigma_h+\sigma_v}{3} - p_w \tag{C-12}$$

where σ_H, σ_h and σ_v are the principal stress components and p_w represents the pore pressure. The Mohr-Coulomb criterion is formulated in terms of a deviator stress q_{max} using:

$$q_{max} = a + M \cdot p' \tag{C-13}$$

where the slope M and the intercept a from the drained friction angle φ' and cohesion c' as:

$$M = \frac{6 \cdot sin\varphi'}{3-sin\varphi'} \tag{C-14}$$

and

$$a = c' \cdot \frac{6 \cdot cos\varphi'}{3 - sin\varphi'} \quad \text{(C-15)}$$

In cases when non-isothermal conditions apply (e.g.; thermally induced porewater overpressures), temperature changes ΔT do not only affect the porewater pressure (thermal expansion of the fluid) but create also a change of total stress $\Delta\sigma_T$. In the TOUGH code, the impact of temperature changes on the fluid and the rock skeleton is addressed by the temperature dependence of fluid viscosity and fluid density and by the thermal expansion of the rock.

In the stress path analysis, temperature dependence of total stress can be considered in the effective stress formulation:

$$p'(T) = \left(\frac{\sigma_H + \sigma_h + \sigma_v}{3}\right)_{ini} - p_w(T) + \Delta\sigma_T \quad \text{(C-16)}$$

with:

$$\Delta\sigma_T = \frac{3 \cdot E \cdot \alpha_s \cdot \Delta T}{1 - 2 \cdot \nu} \quad \text{(C-17)}$$

and

$$\alpha_s = \frac{\alpha_T \cdot n}{3 \cdot (1 - n)} \quad \text{(C-18)}$$

where E is the Young's modulus, α_s is the thermal expansion coefficient of the solid, ν is Poisson's ratio, α_T is thermal pore expansivity and n is porosity. Note that the thermal stress component assumes constant volume conditions. In the case of gas induced porewater overpressures, temperatures do not significantly affect the stress path.

A graphical representation of the Mohr circle used to evaluate the failure potential is given in Fig. C-8. The increase of porewater pressure in the host rock due to gas production or thermal expansion of the porewater will shift the Mohr circle towards low effective stress. If a significant change of total stress $\Delta\sigma_T$ must be considered, this would cause a shift towards higher effective stresses. Shear failure occurs when the Mohr circle hits the Mohr-Coulomb failure line, corresponding to the performance target / performance limit FPI = 1. Shear failure is omitted when FPI < 1.

The evaluation scale in Tab. C-2 is adopted for the for assessment of the different variants of the failure potential FPI (FPH, FPG_{HLW}, $FPG_{L/ILW}$). The percentiles P75, P95, P99 and P99.9 of the calculated frequency distributions are used to formulate the levels of performance.

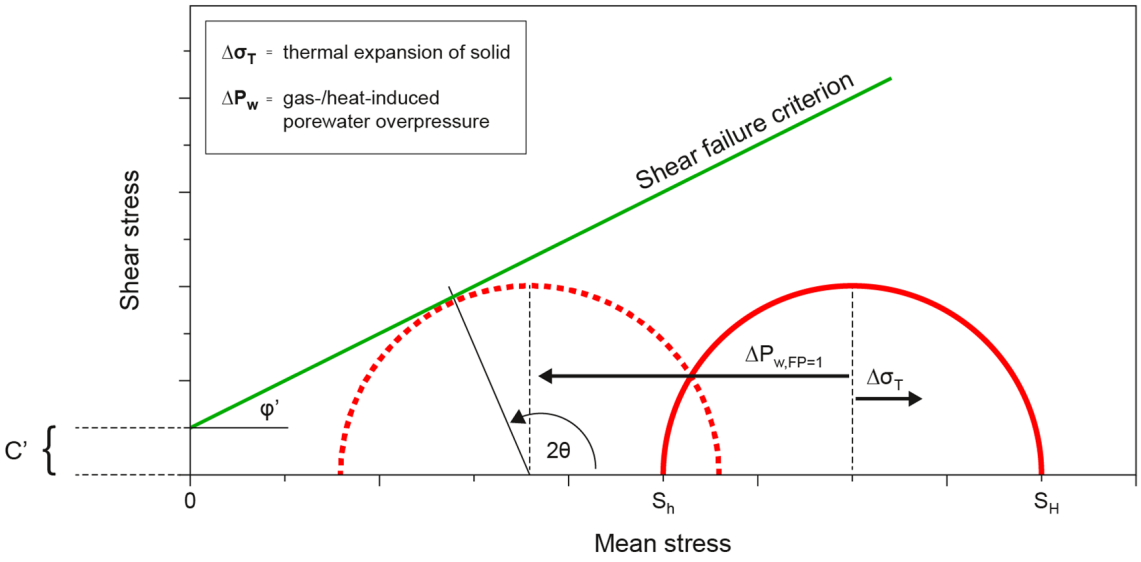

Fig. C-8: Shear failure of the intact host rock in response to gas- and heat induced porewater overpressures presented in the Mohr diagram

C.3.2 Indicator based assessments using of FPI_{Heat} and FPI_{Gas}

Model-based assessment using the performance index FPI were carried out for the assessment of:

- Thermally induced overpressures in the host rock above the HLW emplacement drifts (FPH);
- Gas induced overpressures in the host rock above the HLW emplacement drifts (FPG_{HLW});
- Gas induced overpressures in the host rock above the L/ILW emplacement caverns ($FPG_{L/ILW}$).

The calculation workflow for each version of the FPI index is described in greater detail in the following paragraphs.

Thermally induced overpressures in the host rock above the HLW drifts (FPH)

TH-simulations of pore pressure evolution in the HLW repository nearfield were carried out with the 2-D models presented in Fig. 6-3. The control point for calculating the FPI index was located 20 m above the HLW emplacement drift in the centre of the repository as shown in Fig. C-9.

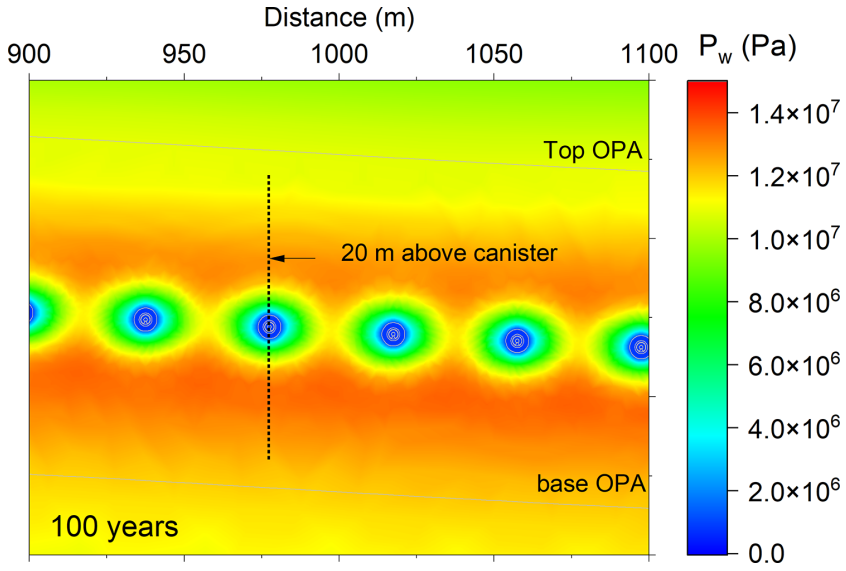

Fig. C-9: Control point for calculating the performance indicator FPH, located 20 m above the HLW emplacement drift in the centre of the repository

The maximum pore pressure at the control point and the corresponding temperature value is extracted from the simulation results. The FPH index is calculated as described in App. C.3.1. The strength parameters of the Opalinus Clay refer to post peak strength (c' = 1.3 MPa, φ' = 24°) according to NAB 24-10 Rev. 1 (Nagra 2024j). The principal components of initial stress at the location of the control point were also derived from the best estimate values in NAB 24-10 Rev. 1 (Nagra 2024j) (S_v = 20.9 MPa; S_H = 18.8 MPa; S_h = 16.8 MPa). The estimation of the change of total stress $\Delta\sigma_T$ with temperature was carried out with the following parameters: E = 7 GPa, ν = 0.27, α_T = 1.7E-5 1/°C, n = 0.12.

Gas induced overpressures in the host rock above the HLW emplacement drifts (FPG_{HLW})

TH-simulations of gas-related pore pressure evolution in the HLW repository nearfield were carried out with the 2-D models presented in Fig. 6-3. The control point for calculating the FPG_{HLW} index is at the interface between EDZ and host rock in the centre of the repository as shown in Fig. C-10.

The maximum pore pressure at the control point was extracted from the simulation results. The FPG_{HLW} index were calculated as described in App. C.3.1. The strength parameters of the Opalinus Clay refer to post peak strength (c' = 1.3 MPa, φ' = 24°) according to NAB 24-10 Rev. 1 (Nagra 2024j). The principal components of initial stress at the location of the control point were also derived from the best estimate values in Nagra (2024j) (S_v = 21.9 MPa; S_H = 19.2 MPa; S_h = 17.2 MPa). The estimation of the change of total stress $\Delta\sigma_T$ with temperature was omitted, because temperature changes at late times are small.

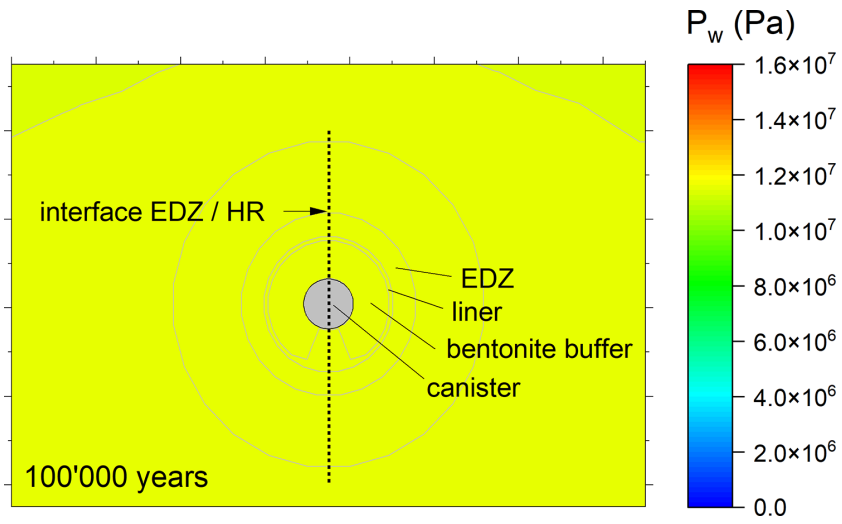

Fig. C-10: Contol point for calculating the performance indicator FPGHLW, located at the interface between EDZ and host rock in the centre of the repository

Gas induced overpressures in the host rock above the L/ILW emplacement caverns (FPI_{Gas})

TH-simulations of gas-related pore pressure evolution in the L/ILW repository nearfield were carried out with the 2.5-D models presented in Fig. 6-3. The control point for calculating the FPI_{Gas} index is at the interface between EDZ and host rock in the centre of the repository as shown in Fig. C-11.

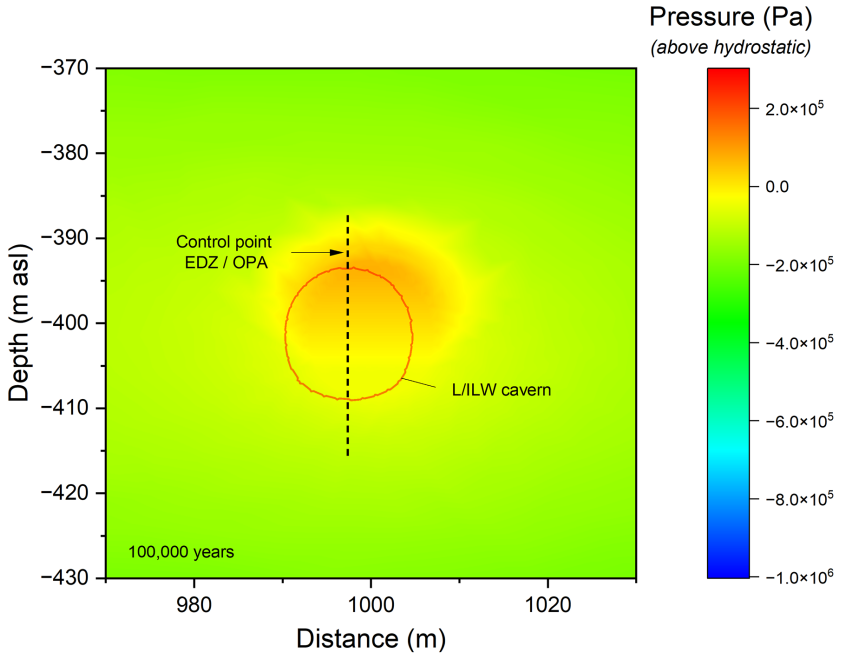

Fig. C-11: Contol point for calculating the performance indicator FPGL/ILW, located at the interface between EDZ and host rock in the centre of the L/ILW repository

The maximum pore pressure at the control point was extracted from the simulation results. The $FPG_{L/ILW}$ index were calculated as described in Section C.3.1. The strength parameters of the Opalinus Clay refer to post peak strength (c' = 1.3 MPa, φ' = 24°) according to NAB 24-10 Rev. 1 (Nagra 2024j). The principal components of initial stress at the location of the control point were also derived from the best estimate values in Nagra (2024j) (S_v = 20.4 MPa; S_H = 18.1 MPa; S_h = 16.2 MPa). The estimation of the change of total stress $\Delta\sigma_T$ with temperature was omitted, because temperature changes at late times are small.

App. D Process abstractions – examples

D.1 TH^{2}M to TH^2-Abstraction

The evolution of the near-field around an HLW emplacement drift depends on complex coupled thermal-hydrological-mechanical processes. TH^{2}M numerical codes have been developed and validated in the past for the simulation of the coupled non-isothermal two-phase flow and hydro-mechanical phenomena associated with repository-induced effects in the near-field of an HLW repository. The TH^{2}M codes are based on formulations of physical conservation laws and constitutive laws described in Section 5.3.1. However, it is most practical to perform the computationally expensive performance assessment calculations using a simpler conceptual model that only explicitly accounts for thermal-hydrological processes (termed TH^2 if separate gas and liquid phases are considered). This simplification requires a TH^{2}M-to-TH^2 abstraction and model validation step.

The numerical implementation of TH^{2}M-processes using simplified TH^2 models must be validated specifically for the intended purpose, which includes a traceable quantification of the uncertainties associated with the abstraction process. Process-related uncertainty quantification is carried out in the context of numerical benchmarks, demonstrating that TH^{2}M processes can approximately be represented by determining effective TH^2 parameters. These effective parameters are estimated by the inversion of data reflecting TH^{2}M processes using a TH^2 model. The following example describes the validation workflow for simplified representation of the TH^{2}M evolution of the HLW near-field in a 2-D TH^2 numerical model.

For this application, a coupled two-phase flow and mechanical numerical model was developed using the TH^{2}M module of Code_Aster (Granet 2021). The numerical model is a 2-D plain-strain finite element model, representing the stack of geological formations at the location of the HLW component model in Nördlich Lägern. The model comprises the 22 sequences of Mesozoic formations from the Permocarboniferous to the Malm, as shown in Fig. D-1a. Only half of the tunnel drift needs to be considered due to symmetry. The distance between the axes of two adjacent tunnels is 40 m. The geometry has therefore been chosen to consist of a rectangle of half of that distance, i.e., 20 m width, representing a vertical section from the top surface to the Permocarboniferous across half of an excavated drift. The centre of the drift is located on the left boundary of the model, and the emplacement tunnel is in the middle of the host rock layer “Opalinus Clay” (OPA) with a drift depth of 910 m. The drift has a radius of 1.925 m. The drift contains a canister placed on a pedestal of bentonite blocks; the rest of the drift is filled with bentonite pellets. After the excavation of the drift, a concrete liner is emplaced, and a circular excavation-damaged zone (EDZ) is explicitly defined. The model mesh discretises the drift as a semi-circular cavity with a finer mesh that transitions to a coarser mesh away from the drift.

The TH^2 model was developed using the iTOUGH2 code with a modified integrated finite difference (IFD) grid, as shown in Fig. D-1b. The HLW drift was represented by a 2-D radial grid that was merged with rectangular grids, representing the bentonite blocks and surrounding stack of geologic formations using Voronoi tessellation. The grid nodes are carefully placed to position observation locations and interfaces between formations and tunnel materials such that they are consistent with the Code_Aster THM grid (Fig. D-1a).

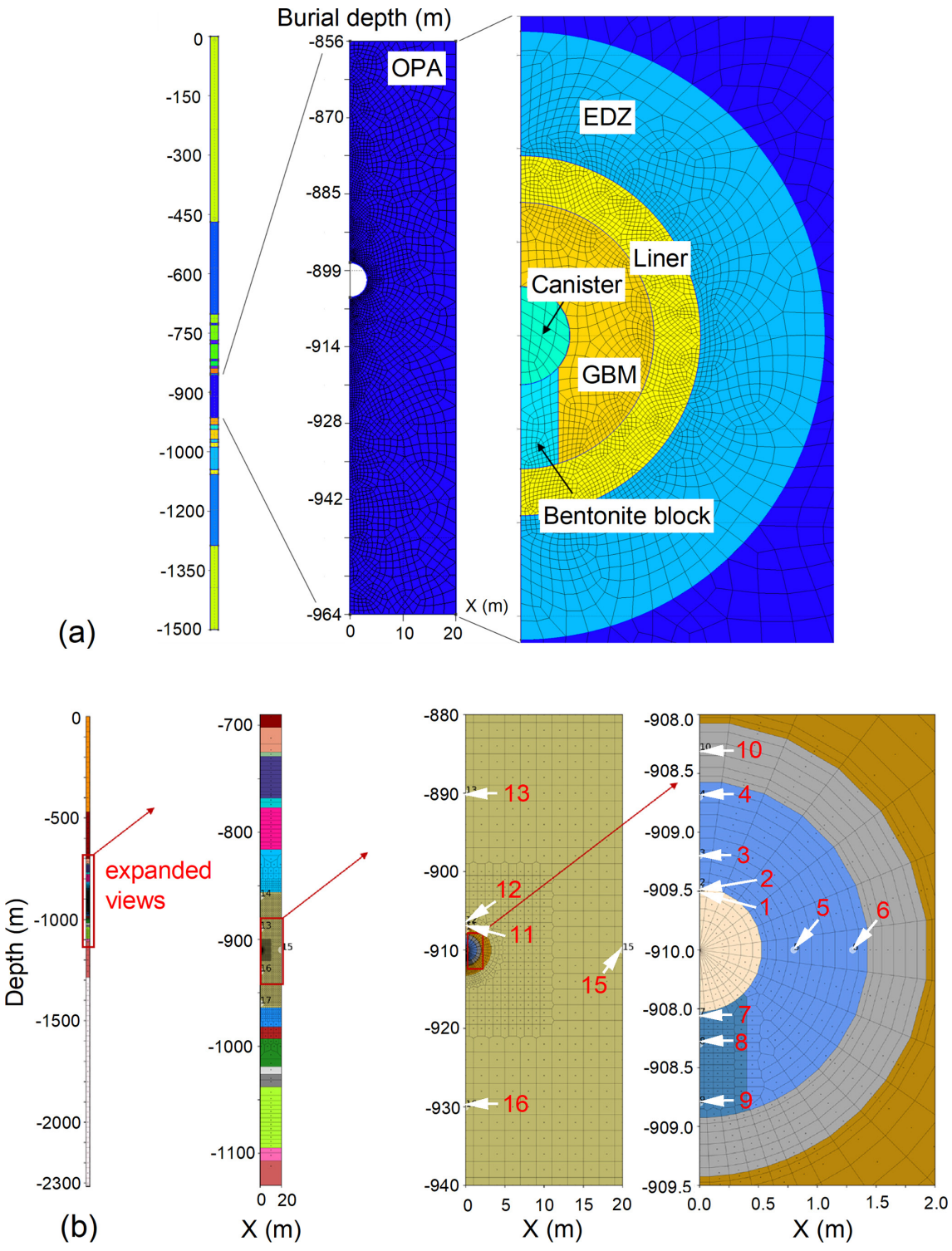

Fig. D-1: Modelling of the HLW near-field evolution: benchmark for the validation of the TH^{2}M-to-TH^2 abstraction workflow

Model set-up implemented in (a) Code_Aster and (b) iTOUGH2, representing an HLW emplacement drift in a repository in the siting region NL with the stratigraphic layer stack and the dimensions of HLW near-field elements. The observation points 1-16, marked in the iTOUGH2 mesh are used for inverse modelling of the outputs of the Code_Aster simulations (transients of pore pressure and temperature).

Assuming ideal elastic material behaviour in a cross-isotropic configuration, the effective stress, $\boldsymbol{\sigma}'$ – strain, $\boldsymbol{\varepsilon}$ relationship in the HLW near-field can be expressed as $\boldsymbol{\varepsilon} = \mathbf{D} : \boldsymbol{\sigma}'$ (see also NTB 14-02 Dossier IV, Nagra 2014), where the compliance tensor **D** is expressed as follows:

$$\boldsymbol{D} = \begin{bmatrix} 1/E_h & -n_{hh}/E_h & -n_{vh}/E_v & 0 & 0 & 0 \\ -n_{hh}/E_h & 1/E_h & -n_{vh}/E_v & 0 & 0 & 0 \\ -n_{vh}/E_v & -n_{vh}/E_v & 1/E_v & 0 & 0 & 0 \\ 0 & 0 & 0 & 1/2G_{vh} & 0 & 0 \\ 0 & 0 & 0 & 0 & 1/2G_{vh} & 0 \\ 0 & 0 & 0 & 0 & 0 & 2(1+n_{hh})/E_h \end{bmatrix} \quad \text{(D-1)}$$

The indices *h* and *v* represent the horizontal and vertical directions, respectively. E_i is the Young's modulus in the direction of *i*, G_{ij} is the shear modulus in direction *j* on the plane whose normal is in direction *i*, and v_{ij} is the Poisson's ratio that corresponds to a contraction in direction *j* when a compression is applied in direction *i*.

In the present example, it is assumed that all materials in the HLW near-field exhibit linear elastic and isotropic properties, which allows a simplified representation to be made of the compliance tensor, expressed in terms of stress invariants, mean effective stress p' and deviatoric stress q with isotropic Young's modulus E and Poisson ratio v:

$$\begin{Bmatrix} \varepsilon_v \\ \varepsilon_s \end{Bmatrix} = \begin{bmatrix} 1/K & 0 \\ 0 & \sqrt{3}/6G \end{bmatrix} \begin{Bmatrix} p' \\ q \end{Bmatrix}, K = \frac{E}{3(1-2\cdot v)} \text{ and } G = \frac{E}{3(1+v)} \quad \text{(D-2)}$$

where ε_v and ε_s are the volumetric and deviatoric strain components, respectively, and *K* and *G* represent the bulk modulus and shear modulus, respectively. The mean effective stress p' and deviatoric stress q are defined as:

$$q = \sqrt{\frac{(S_1'-S_3')^2+(S_1'-S_2')^2+(S_2'-S_3')^2}{2}} \quad \text{(D-3)}$$

$$p' = \frac{(S_1'+S_2'+S_3')}{3} \quad \text{(D-4)}$$

with S_1', S_2', and S_3' representing the effective principal stresses at the repository site.

The validity of TH^{2}M-to-TH^2 abstraction is examined by generating synthetic THM data – calculated by a THM simulation of a two-dimensional cross-section of an HLW disposal drift (Fig. D-1a) – and inverting the synthetic THM data using a TH model of the same cross-section (Fig. D-1b). The TH^2 simulations are carried out with the multiphase flow simulator iTOUGH2. Geometric representation of the HLW near-field is practically identical with the implementation in Code_Aster. A simplified formulation of the geomechanical behaviour of the porous medium is, however, required, because iTOUGH2 does not explicitly address the tensorial character of the stress-strain relationship, as formulated in Equation (D-2). Instead, only volumetric behaviour of the porous medium is taken into account in response to pore pressure changes (∂P), i.e., the porosity (φ) changes as a function of the pressure changes, $\partial\varphi = \mathrm{C_p}\partial P$. The $\mathrm{C_p}$ is the pore compressibility, an effective parameter to account for hydromechanical coupling which can be derived from the bulk modulus of the material $\mathrm{C_p} = 1/(\varphi K)$. Similarly, the TH^{2}M formulation includes a full description of thermo-poroelasticity formulation, i.e., the changes in porosity in

response to temperature variations, which depend on the thermal stress development and solid grain expansion. iTOUGH2 adopts a formulation analogous to the HM coupling, expressed as $\partial\varphi = \alpha_T \partial T$, where α_T is the pore thermal expansivity. Note that the TH^2 approach inherently assumes a constant total stress condition with no deviatoric component, meaning that all pore pressure changes are directly transferred to changes in mean effective stress, thereby affecting porosity. In contrast, in the in TH^{2}M approach, total stress is influenced by thermal stress development and mechanical constrains at the boundaries. These changes in total stress further affect the deviatoric stress and mean effective stress, which in turn affect the porosity change in addition to pore pressure variations. This highlights the key abstraction mechanism from TH^{2}M to TH^2, which is demonstrated in the following paragraph by approximating TH^{2}M processes through the determination of effective TH parameters and their associated uncertainties.

The pressure and temperature observations that are calculated using the Code_Aster TH^{2}M model and included as synthetic data for model calibration are shown as symbols in Fig. D-2a and Fig. D-2b, respectively. Also shown are the calculated pressures and temperatures using the initial iTOUGH2 model (solid lines). The pore compressibility was set to 10^{-10} [1/Pa] for both the bentonite blocks and granular bentonite. The initial estimates based on the elastic data yielded much higher values, which caused a significant misfit of late-time pressure responses and were not suitable as a starting point for model calibration. The temperature responses at the different monitoring locations showed good agreement between those calculated using the Code_Aster TH^{2}M model and those using the TH^2 model (Fig. D-2b).

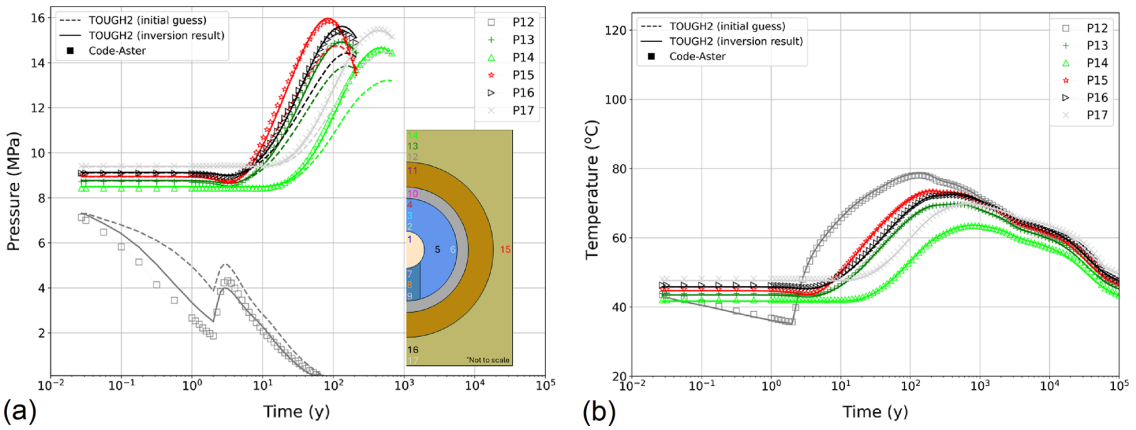

Fig. D-2: Simulated (a) pressures and (b) temperatures with the Code_Aster THM model compared with the initial iTOUGH2 model and calibrated model using the best fit parameters

Sensitivity analyses using the Code-Aster TH^{2}M model and the iTOUGH2 TH^2 model revealed not only the relevant, i.e., influential parameters, but also the timing when the calculated pressures and temperature exhibited a more sensitive response as well as the monitoring locations where the sensitivities of the responses were most pronounced. The focus was on the pressure and temperature responses (rather than saturation and porosity), because they are more directly related to the main performance indicators. This defined the synthetic data and limited the adjustable parameters used for the calibration with the iTOUGH2 inversion to the effective pore compressibility and pore expansivity used in the TH^2 model.

The sensitivity analysis demonstrated that the pressure response (i) is sensitive to only a few parameters at “early” times (i.e., less than approximately 1,000 years) during which the maximum pressures occur, and (ii) at later times (i.e., beyond 1,000 years) is complicated by additional

sensitivity to pressure reflections from deeper geological layers and model boundaries, as well as to bentonite properties. Therefore, for model calibration, only pressure observations that occur up to and slightly after the maximum pressures (i.e., the "first peaks" in pressure) at their respective control points P13 through P17 are included as synthetic data; a more limited time range is used for P12 (see Fig. D-2a). For temperature observations, all times are included as synthetic data for model calibration (see Fig. D-2b).

An iTOUGH2 inversion was conducted with 12 successful iterations/parameter updates that reduced the objective function from its initial value of 5.8×10^4 (corresponding to the initial parameter guesses) to a value of 1.54×10^3, or 2.7% of the initial value (for the final estimated parameter set). The estimated error variance, which is a composite goodness-of-fit measure, is only slightly larger than 1.0, indicating that the quality of the match is consistent with prior expectations.

In Fig. D-2, the pressure and temperature observations, respectively, are shown for the initial iTOUGH2 model (dashed lines), the final calibrated model (solid lines), together with the respective synthetic data (symbols). The calibrated model generally gives a very good fit to the synthetic data.

The means and standard deviations of the residuals for each pressure and temperature data set are listed in Tab. D-1 and are mostly in line with expectations. The average of the mean residuals for the pressure data sets P13 to P17 is -0.03 MPa, indicating that no significant bias exists. The higher average residual of 0.18 MPa at P12 (see Fig. D-1a) is a result of its proximity to the unsaturated bentonite buffer, where pressures are affected by uncertainties in two-phase flow parameters, which are not adjusted during the inversion.

The average of the standard deviations of the temperature residuals for P12 through P17 is 0.48, which is less than the assumed value of 1.0 °C, suggesting an acceptable fit. However, there is a slight bias in the residuals (with temperatures overpredicted on average by about 0.24 °C); this bias may be related to slight differences in the implementation of boundary conditions between the Code_Aster and iTOUGH2 models.

The estimated parameter values and standard deviations are summarised in Tab. D-1. Notably, the uncertainty estimates are low, ranging between 0.001 and 0.027. For the host rock: the estimated value of log pore expansivity is increased substantially compared to its initial value (from -4.77 to -3.86), while the log pore compressibility is decreased from -8.8 to -9.1. The estimated pore compressibility values for most of the remaining materials (KEUK, AL, ML, HERRE, DOGG) are not dramatically different from their original values, while the value for the EDZ is reduced substantially from -8.352 to -10.8.

Tab. D-1: Calibration of the iTOUGH2 model, using the Code_Aster simulations as input data: estimated parameters and uncertainties

Parameter	Material	Initial	Estimate	Std. Dev.
$\log_{10}$ (pore expansivity [1/°C])	HOST	-4.770	-3.856	0.001
$\log_{10}$ (pore compressibility [1/Pa])	HOST	-8.766	-9.128	0.001
	EDZ	-8.352	-10.80	0.027
	KEUK	-9.032	-8.92	0.010
	AL	-8.840	-8.99	0.012
	ML	-8.796	-8.833	0.004
	HERRE	-8.336	-8.321	0.024
	DOGG	-8.853	-9.059	0.003
	BLOCK	-10.0	*fixed*	N/A
	PELL	-10.0	*fixed*	N/A

D.2 TH²C Abstraction

Modelling the geochemical evolution of the multi-barrier system at the repository scale using fully coupled TH²C models is neither computationally feasible nor scientifically warranted. Multiple types of empirical and experimental evidence have been used in the past to demonstrate that repository-induced chemical and biological processes, such as the propagation of redox fronts, alkaline plumes or chemical alteration of interfaces between barrier components, are limited to the immediate vicinity of the repository structures. In performance assessment, TH²C models and simplifications thereof are mainly needed to evaluate hydro-chemical interactions at the component scale.

A common approach adopted in geochemical models is to use abstracted representations of the two-phase flow transport problem, postulating that chemical reactions predominantly depend on the availability of water. Hydraulics are therewith approximated, e.g., assuming stationary conditions or using proxy state variables, mainly fluid saturation and/or flows, in the form of boundary conditions or source terms.

Accordingly, the essence of geochemical effects in the TH² consideration is captured in a simplified manner. The abstraction follows two main assumptions:

- Chemical reactions that result in changes in the chemical composition of fluids can be approximated as species source and sink terms that are variable in time and space.
- Chemical reactions that result in mineral precipitation/dissolution can be approximated as porosity and permeability changes that are variable in space and time.

In turn, variants of source/sink terms and porosity are assigned to specified sections of the repository in performance assessment modelling, e.g., in the waste emplacement rooms. These feed directly into the mass conservation formulations adopted for the TH² problem. The TH² model outcomes feed back into the geochemical analyses to check assumptions and inform variants related to the hydraulic evolution of repository components.

The geochemical evolution of individual components of the multi-barrier system has been the subject of previous PA modelling activities. This includes studies on water consumption associated with steel corrosion in the HLW near-field (Senger et al. 2008), salt enrichment in the backfilled L/ILW emplacement caverns (NAB 13-72, Senger & Papafotiou 2013), and consumption of repository-produced gases caused by chemical reactions and microbial activity (NTB 16-05, Leupin et al. 2016, NTB 16-03, Diomidis et al. 2016). Three examples related to the safety case are discussed in the subsequent paragraphs.

Kosakowski (2023, NAB 23-33), as summarised in NTB 23-02 Rev. 1 (Nagra 2024v), has performed reactive transport calculations (TH-C, assuming fully saturated conditions), to study the evolution of the clay and cement-based materials in the HLW emplacement drift. For the calculations, the coupled code OpenGeoSys-GEMS (Kosakowski & Watanabe 2014) has been employed, which has been bench (Idiart et al. 2020)marked against various codes in the scope of the CEBAMA project (Idiart et al. 2020). The results of the benchmark modelling study (Idiart et al. 2020) showed that different reactive transport codes can be used to quantify the geochemical interaction between a low-pH concrete and a claystone to essentially obtain the same results, despite of inherent differences between modelling approaches. In all modelled cases, the differences observed between models do not have significant consequences for the description of the governing processes and system evolution. This builds confidence in the application of these types of models. In the scope of the study by Kosakowski (2023), the thermal pulse from heat output of the spent fuel canister was accounted for. Chemical reactions are calculated with GEMS3K with the set-up used in NAB 18-41 (Cloet et al. 2019). To this end, PSI/Nagra TDB 07/12 (Thoenen et al. 2014) is used together with CEMDATA 18 (Lothenbach et al. 2019). According to Lothenbach et al. (2019), the two databases contain thermodynamic data on common cement minerals that are valid over temperatures up to 120 °C in Cloet et al. (2019). Temperatures in this study (only) reach 120 °C near the canister-bentonite boundary. The near-field peak is mostly slightly above 100 °C (Kosakowski 2023). Based on this, solid solution C-S-H data included in CEMDATA are replaced by crystalline C-S-H phases from Blanc et al. (2010a, 2010b) that can potentially form in the long-term at elevated temperatures (see Section 4.1.3 in Cloet et al. 2019). The zeolite phases included in CEMDATA 18 were replaced by the new Zeolite21 DB (Ma & Lothenbach 2020a, 2020b, 2021) valid for temperatures up to 100 °C. In addition, for the bentonite and Opalinus Clay set-up, two cation exchanger phases were employed with parameters identical to those used by PSI for the calculations of the Opalinus Clay and bentonite porewaters (NTB 23-02 Rev. 1, Nagra 2024v). The Opalinus Clay cation exchanger was extended with amphoteric pH buffering sites taken from Berner et al. (2013). The data for clay minerals were imported by Thermoddem DB / Thermochimie and are valid for even higher temperatures (Blanc et al. 2012). Further information on the employed Debey-Hückel equation and parametrisation, as well as for kinetic data for dissolution and precipitation reactions, are given in Kosakowski (2023).

The models implemented the near-field geometry and materials of the currently envisaged rock support concept with a segmental liner and cement-based annular gap filling material. In the scope of this model, heat transport is coupled to solute transport via temperature dependent diffusion coefficients. Temperature is considered for the calculation of chemical equilibria and the kinetics control of mineral dissolution/precipitation. As a result of the high temperature, the geochemical evolution of the near-field is accelerated. In the scope of the model, the internal degradation of the liner system by kinetically controlled silica-aggregate dissolution is faster and can occur within the first hundred years. As shown by the model, the rapid degradation of the cementitious material lowers the pH of the porewater below 10 reducing the pH difference to the adjacent clay media (Kosakowski 2023). The decreased pH contrast between clay and cement materials slows down or even suppresses cement clay interaction and related porosity changes. As a result of this pH decrease and mass fluxes, a carbonation front is forming at the grout interface towards the

Opalinus Clay. Due to this process, the further progression of an alteration front comes to a halt. As a result, the extension of the alteration rim towards the bentonite as well as to the Opalinus Clay is limited (Fig. D-3).

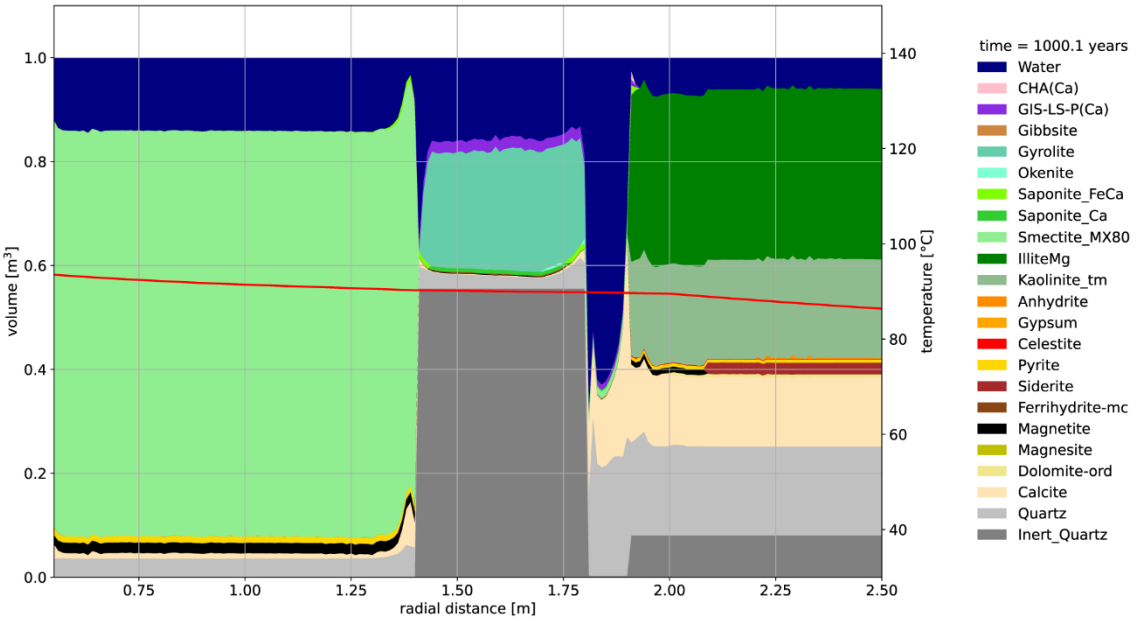

Fig. D-3: Spatial mineralogical profile after 1,000 years accounting for the temperature variation associated with heat generation of HLW canisters

The x-axis starts at the contact between canister and bentonite at 0.55 m from the drift centre, the bentonite extents from 0.55 to 1.4 m, tubing concrete between 1.4 and 1.8 m, the annular grout between 1.8 and 1.9 m, and Opalinus Clay beyond 1.9 m. The model accounts for the temperature-influenced reaction kinetics and for porosity coupling. From NTB 23-02 Rev. 1 (Nagra 2024v).

Further modelling studies were dedicated to the geochemical evolution of the L/ILW sealing systems (L/ILW-V1 seal) with special emphasis on the chemical interaction between cement-material (as part of the abutment) and the sand/bentonite mixture (NAB 14-16, Kosakowski & Smith 2014 and Fig. D-4). The general purpose FE code OpenGeoSys (Kolditz et al. 2012a) was used to solve the flow and transport equations. Verification and application examples for single and coupled thermal-hydraulic-mechanical-chemical processes (THMC) can be found in Kolditz et al. (2012b). Details of the applied methods are given in Kosakowski & Smith (2014). In the scope of the models of Kosakowski & Smith (2014), solutes from the sand/bentonite mixture and from the concrete interact and mix within the transition layer. Several reaction fronts caused by solutes migrating from one zone into another are formed and gradually migrate. In the concrete, monocarbonate and portlandite progressively dissolve and some ettringite and small amounts of calcite are formed. This is triggered by the in-situ diffusion of SO_4^{2-} from the transition and sand-bentonite layers saturated with host rock porewater, resulting in a small decrease in porosity between the dissolving monocarbonate and portlandite front (NAB 23-21, Martin et al. 2023). The decrease in porosity is, however, a transient feature that migrates and does not build up over time. Therefore, there is no risk of clogging if inert $CaCO_3$ gravel is used for the transition layer. Overall, the 1D calculation for the example seal design indicates that porosity changes are

relatively minor and the newly formed mineral have a smaller molar volume then the dissolved phases. Therefore, the porosity changes are far less than would be required for pore clogging to occur, as summarised in Martin et al. (2023, NAB 23-21).

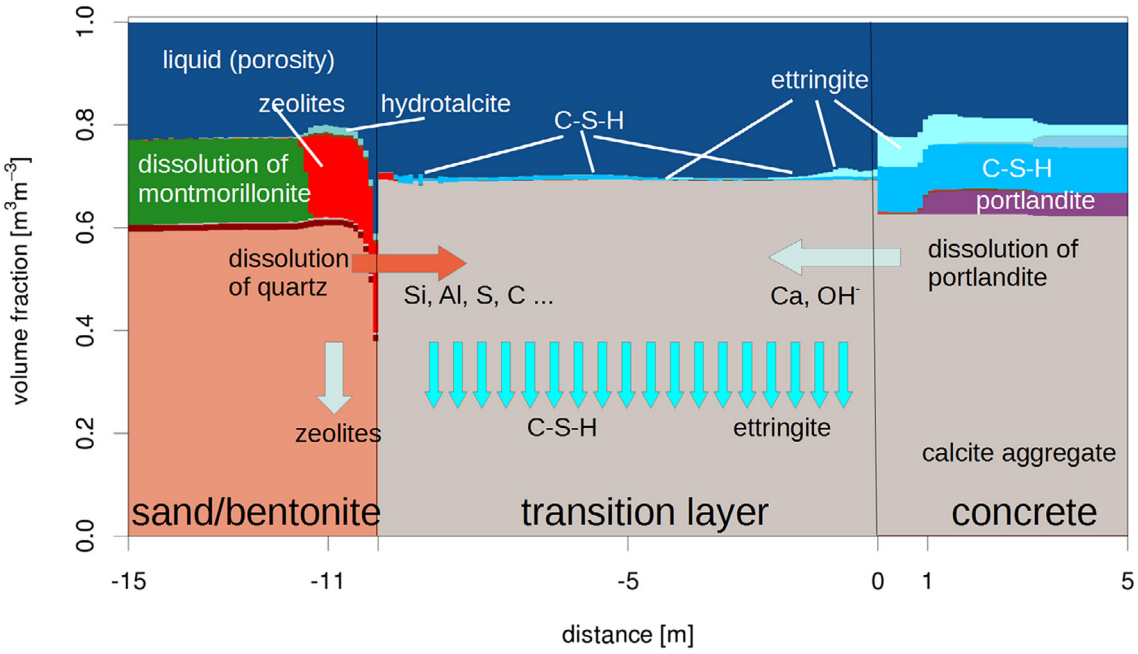

Fig. D-4: Schematic illustration of major processes in a seal after 100,000 years of evolution, where a sand/bentonite sealing element and concrete abutment are separated by a 10 m transition layer of calcite gravel under assumed fully liquid saturated conditions

From NAB 14-16 (Kosakowski & Smith 2014).

Furthermore, simplified representations of the relevant geochemical phenomena and processes were made in the scope of NAB 18-05 (Wieland et al. 2018) and NAB 20-11 (Kosakowski et al. 2020), modelling the chemical evolution of various waste types. Details of the modelling approach are presented in the corresponding reports. In brief, to model the temporal chemical evolution of the waste types using the GEM-selektor (GEMS) v.3.3 (Kulik et al. 2012), the Nagra-PSI database (NAB 22-38, Hummel et al. 2022 and Thoenen et al. 2014) and the well-established CEMDATA 14.01 (Lothenbach et al. 2012) have been employed. Further details of the thermodynamic data implemented are given in NAB 18-05 (Wieland et al. 2018). For the model implementation, the composition of various waste types from the MIRAM 14 database were modelled as a homogenised material, based on the so-called mixing tank approach (cf. Wieland et al. 2018 and Kosakowski et al. 2020). In the scope of the model the carbonation of the degradation of the contained organic material, the aggregate-cement interaction as well as the amount of gas generated by corrosion and by the degradation of organic materials was accounted for. What could be shown in the scope of model (Kosakowski et al. 2020) is that, for operational waste sorts, which contain large amounts of fast degrading organic materials (e.g., cellulose) and/or slowly degrading materials (e.g. polystyrene, PVC), the types of aggregates (siliceous vs. carbonaceous) has only a minor effect on the temporal evolution of the chemical conditions of the operational waste sorts. That is in these waste types, the temporal evolution of the chemical conditions is mainly determined by the degradation of the organic material and the subsequent carbonation of cementitious materials (cf. Kosakowski et al. 2020). However, what has a strong

impact on the extent of the chemical reaction is the water present in the waste, which is getting consumed by chemical reactions (in particular by metal corrosion). However, water, gas and humidity transport will set the long-term boundary conditions for the reactivity of individual waste packages (Kosakowski et al. 2020).

Furthermore, in the scope of Wieland et al. (2018) and Kosakowski et al. (2020) the chemical evolution of a decommissioning waste type (SA-L-MX), essentially consisting of metallic waste from decommissioning emplaced in a concrete container that contains a mortar with silica fume, has ben modelled. Interaction between the silica fume and the cement paste will lead to the dissolution of portlandite. Furthermore, interaction between the siliceous aggregates and the cement paste is assumed to occur. As a result of the cement-aggregate interaction, pH decreases successively as long as water is available. At a pH below 10.5, which is, according to the model, reached within a few thousand years, it is assumed that the steel corrosion and the related H_2 generation by anaerobic corrosion will be strongly accelerated (Wieland et al. 2018). By contrast, the newly conceived CEM II/B-T, which is envisaged for the conditioning of metallic waste, is a cementitious suspension without any aggregates. According to the model-based assessment, this material does not show internal degradation due to the lack of a silica source, and provides long-term stable pH conditions (NTB 23-03, Kosakowski et al. 2023; blue line in Fig. D-5).

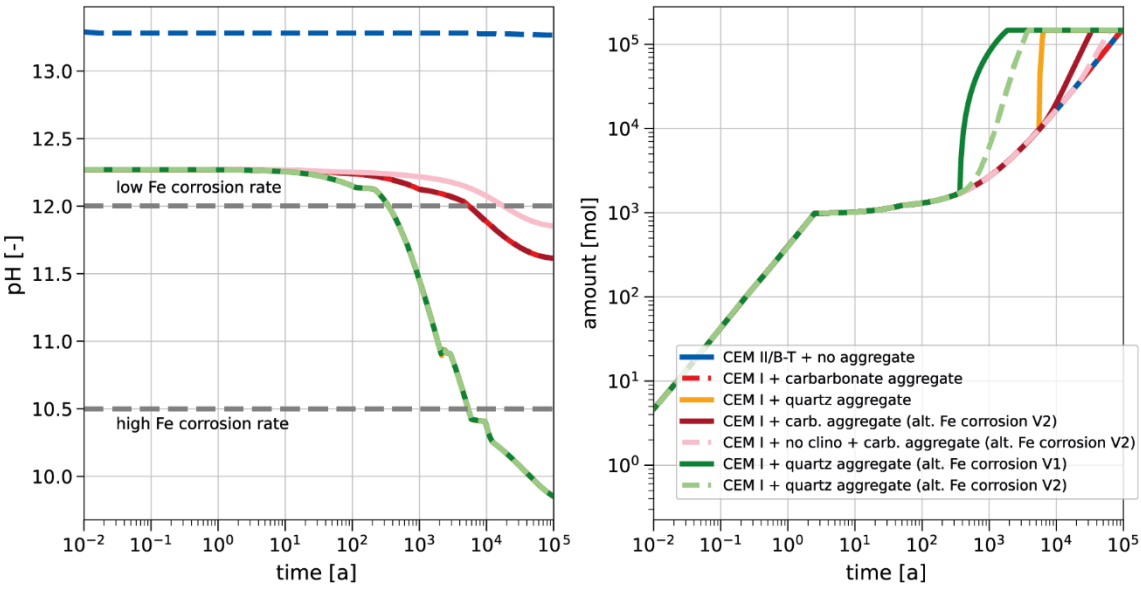

Fig. D-5: pH evolution of the pore solution in an SA-L-MX container with time for different modelled scenarios (left) and cumulative hydrogen gas release by metal corrosion (right)

Scenarios differ in terms of cementitious infill and the rate law used for iron corrosion (clino: clinoptilolite) (Kosakowski & Wieland 2022).

Each of these modelling studies, are each tailored to the intended use of the models. Considerations about the validity of the TH^{2}C abstractions are given in the aforementioned references.

App. E Probabilistic assessments – input parameters

Monte Carlo simulations are performed to evaluate the influence of uncertainty of key input parameters on performance indicators and estimate the confidence intervals around the base case simulations for each of the PA-Scenarios, specified in Chapter 6. For gas and heat simulations, parameters are selected based on their sensitivity to maximum pressures and temperatures in the Opalinus Clay and inside the caverns (NAB 16-07 & 16-08, Papafotiou & Senger 2016a, 2016b). These are the permeability, porosity, pore compressibility, and saturated thermal conductivity of the Opalinus Clay, and the saturated thermal conductivity of the EDZ. The distributions of the parameters considered, together with the "hardwired" correlations of the uncertain input parameters with other model parameters are discussed briefly in NAB 24-25 (Nagra 2024m). The distributions are used to generate a set of 100 – 1,000 Latin Hypercube samples, as depicted in Fig. E-1.

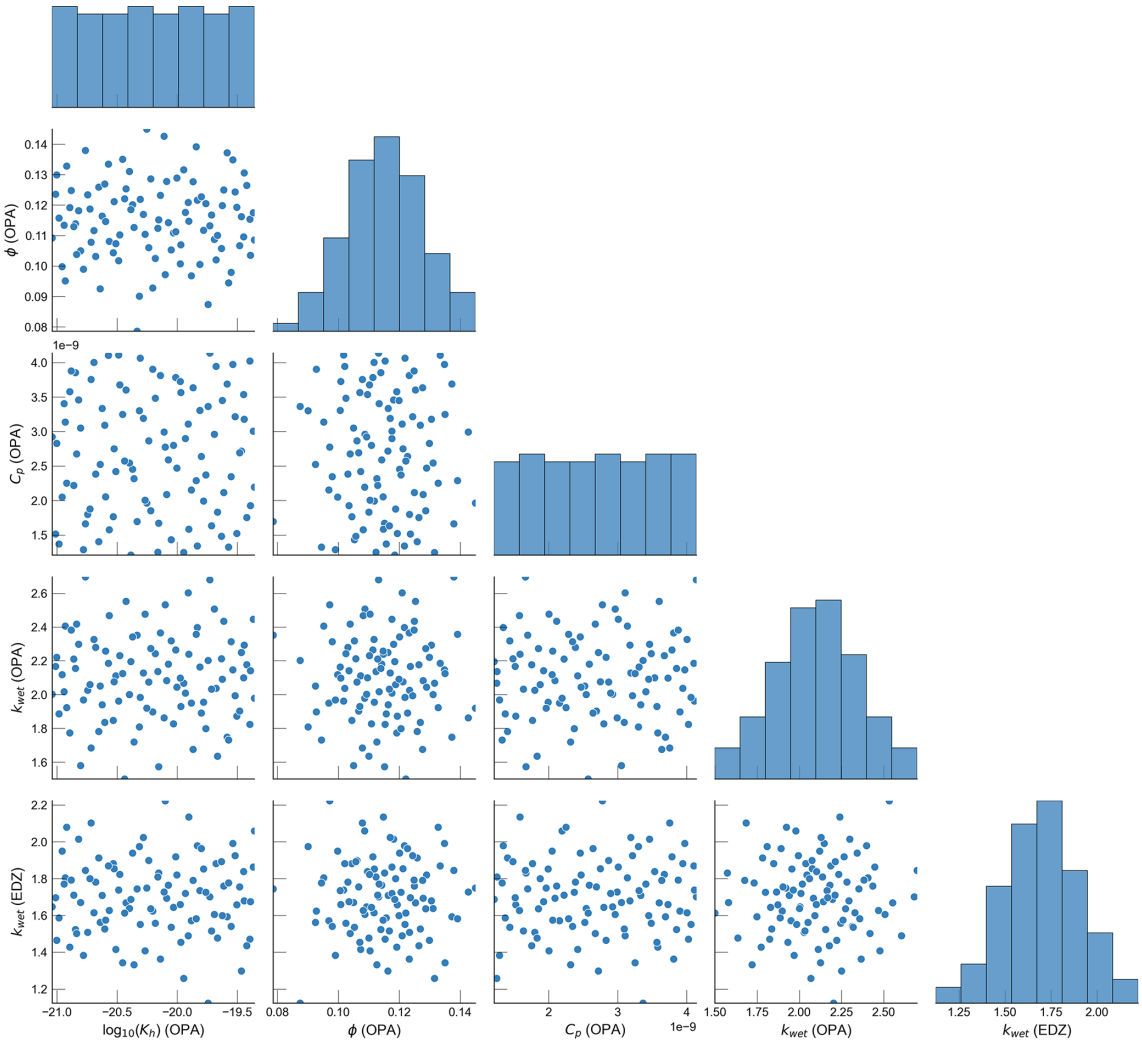

Fig. E-1: Scatter-plot matrix of 100 Latin Hypercube samples for all TH^2 model parameters

The subplots along the diagonal show the marginal distributions (as a histogram) of the samples, while the off-diagonal subplots of the matrix represent a pairwise scatter plot between the different model parameters.

Monte Carlo simulations of gas pressures in the L/ILW models are performed to evaluate the influence of uncertainty of key parameters on the maximum pressures in the Opalinus Clay and inside the L/ILW emplacement caverns, in particular the permeability, porosity, and pore compressibility of the Opalinus Clay. The distributions of the parameters considered, together with the "hardwired" correlations of the uncertain input parameters with other model parameters are discussed briefly in NAB 24-25 (Nagra 2024m). The distributions are used to generate a set of 100 – 1,000 Latin Hypercube samples, as depicted in Fig. E-2.

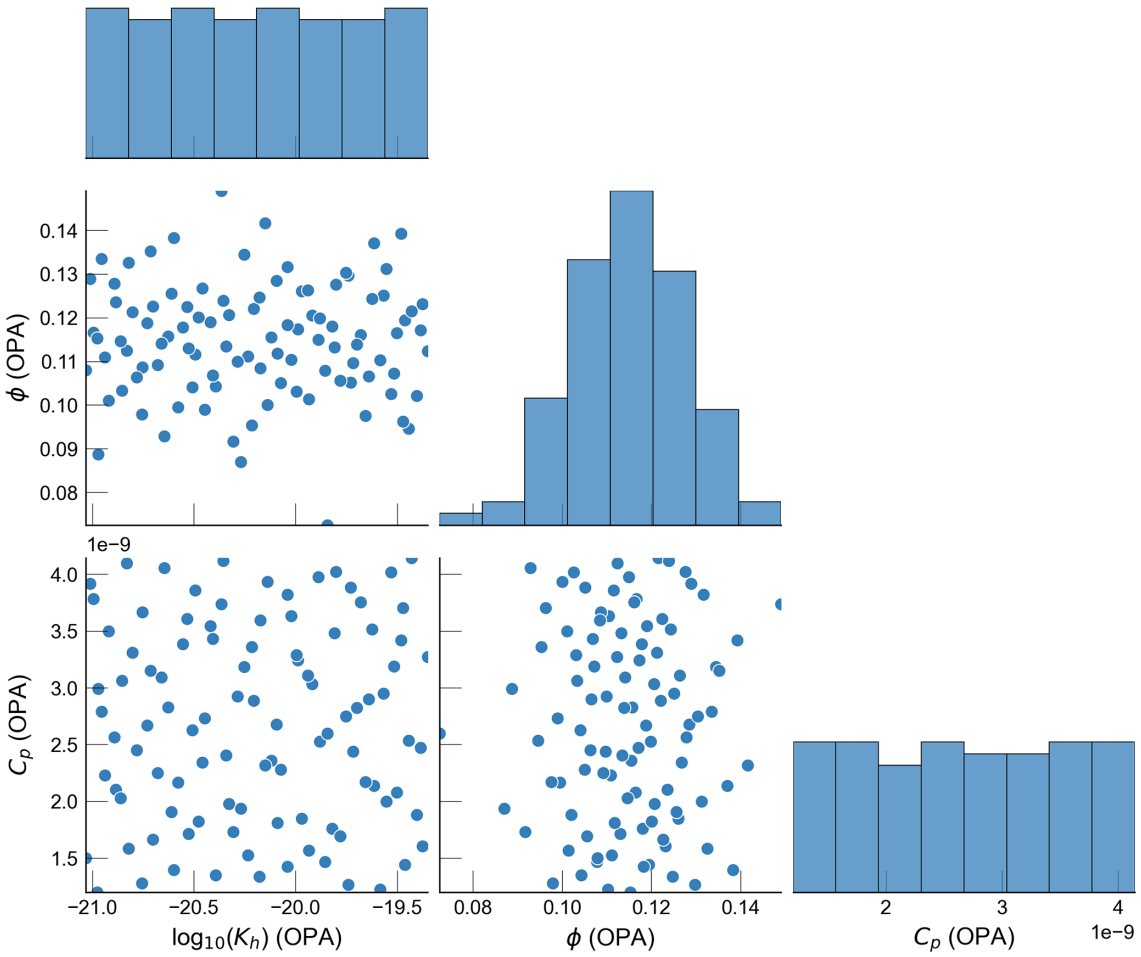

Fig. E-2: Scatter-plot matrix of the 100 Latin Hypercube samples for all model parameters

The subplots along the diagonal show the marginal distributions (as a histogram) of the samples, while the off-diagonal subplots of the matrix represent a pairwise scatter plot between the different model parameters.

Finally, Monte Carlo simulations were performed to evaluate the influence of uncertainty of key parameters on the performance index NTF and estimate the confidence intervals around the best estimate. The uncertain flow and transport parameters considered were used to generate a set of 100 Latin Hypercube samples, as depicted in Fig. E-3 (see also Tab. A-4 and Tab. A-5). Further details about parameter correlations and the assumed property distributions are given in NAB 24-25 (Nagra 2024m).

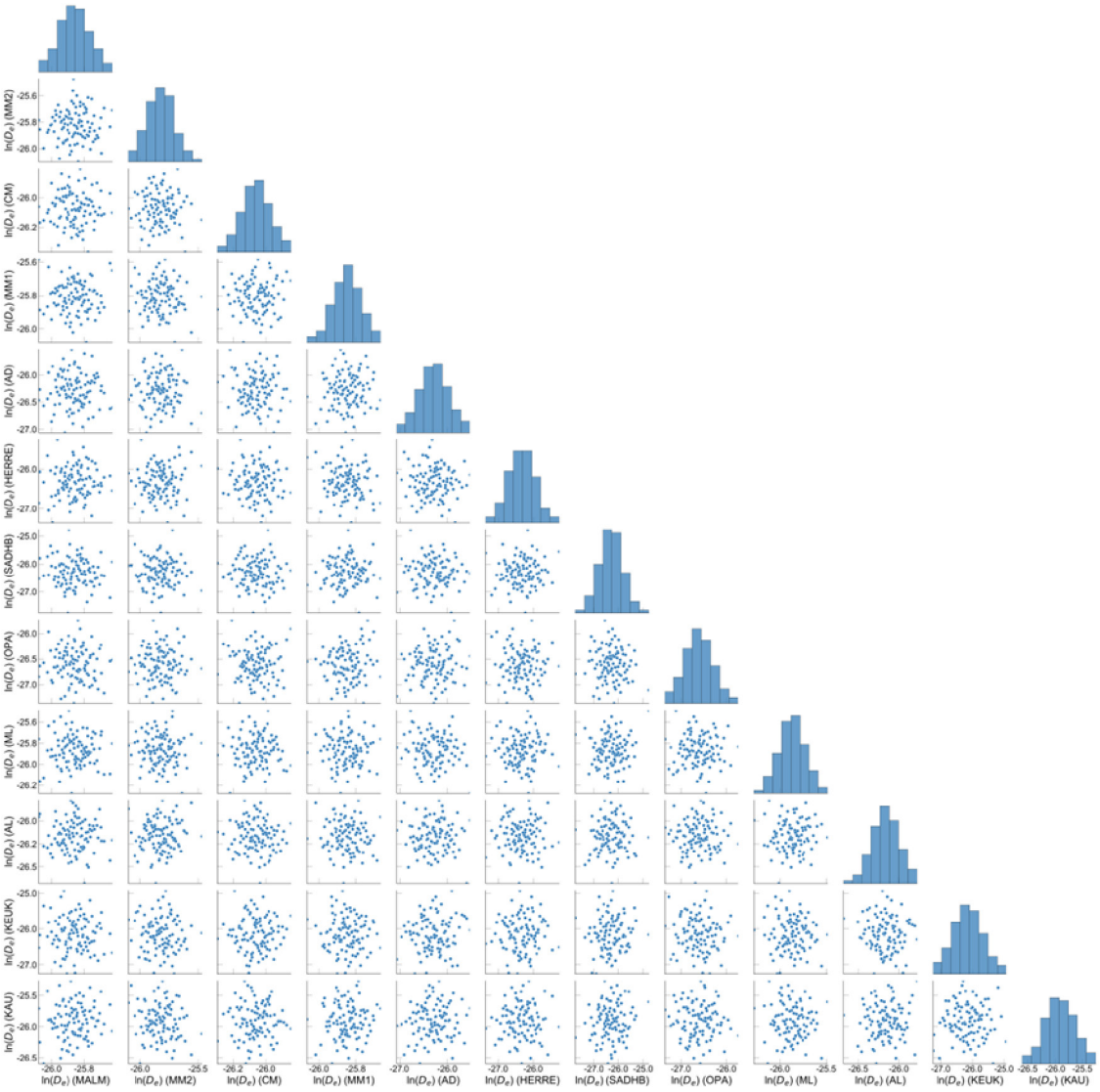

Fig. E-3: Scatter-plot matrix of the 100 Latin Hypercube samples for effective diffusion coefficient for Iodine for various stratigraphic units respectively formations and their representation in the PA

The subplots along the diagonal show the marginal distributions (as a histogram) of the samples, while the off-diagonal subplots of the matrix represent a pairwise scatter plot between the different model parameters.